UNIVERSITY OF LIVERPOOL

Numerical Modelling of Impacts from Horizontal Axis Tidal Turbines

Thesis submitted in accordance with the requirements of the University of Liverpool for the degree of Doctor in Philosophy

By

Sufian Fuad Sufian

01 Nov 2016

Abstract

It has become essential to consider alternative sources of energy since the CO_2 related issues to the global warming and climate changes as well as energy source shortages. Horizontal Axis Tide Turbines (HATT) are one of the alternative renewable solutions that is reliable, predictable and has a lot of potential in UK waters. Many studies and tests have looked into the design, performance and loading related issues of the turbine. However, not many have actually considered their impact on stream flow dynamics, i.e. wake characteristics and implication on the surrounding environment.

A 3D CFD model was developed to simulate tidal turbine operation in realistic natural conditions. The flow module is based on FLUENT 14.5 CFD package to resolve the flow using the Reynolds Averaging Navier-Stoke (RANS) equations for steady and unsteady state flow conditions. A new module based on Virtual Blade Model (VBM) is developed to represent the turbine operation. The free surface effects are simulated through the Volume of Fluid method to allow both current and surface wave modelling. The turbulence characteristics were simulated by shear stress transport (SST) $k-\omega$ model to ensure accuracy as well as computationally efficient. The model was solved based on Finite Volume method using an implicit method for temporal solutions. The computational mesh was generated with high resolution near the turbine, channel bed and the free surface. Extensive validation was carried out based on a series of experimental data available for various conditions. Overall, the model validations produced an accuracy of approximately 88% for flow velocities in the x, y and z directions as well as turbulence kinetic energy measurements across the channel in both steady and unsteady state flow conditions, i.e., upper surface layer; turbine-affected region and bed boundary layer.

Then the model was used to examine potential near wake impacts to the environment using different turbine configurations and natural hydrodynamic conditions. The computed results show that the distribution of the wake is asymmetrical across the channel behind the turbine, e.g., it tends to shift towards the highest deficit side in the horizontal plane and towards the channel bed in the vertical direction. The flow velocity distribution changes from “W” to “U” shape when moving downstream. The highest turbulent energies are produced in the wake region. The turbulence kinetic energy (TKE) generated by a yawed turbine is found to be

higher in comparison with the normal angle (0˚) condition. With higher background turbulence energy, the turbine operation tends to generate more energy. For the cases simulated in the study, the wave effects are relatively weak in comparison with that due to current. The results show that the wave-period averaged flow has similar features as that in the steady current along condition in both streamwise and opposing waves. However, there are many distinct differences between these different wave conditions in flow hydrodynamics, turbulence energy distribution and wave dynamics. The presence of waves enhances the wake recovery across the depth and width of the channel. They encourage stronger TKE generation in the flow regime, where the highest TKEs are found in the upper surface layer. Opposing waves produce higher TKE values in the upper surface layer, however, streamwise waves produce higher TKEs in turbine-affected and bed boundary layers. In both cases, the turbine-induced TKE extends to the upper surface layer to interact with the upper layer under the free surface.

It was found at the channel centre that the wave height reduces by 10% in adjacent to the turbine and the bed shear stresses increases by approximately 14% for waves following the current. For waves opposing the current, it is found that the wave height increase by 11% and the bed shear stress increases by 12%.

Acknowledgments

I would like to thank my supervisor, Dr Ming Li, for all his efforts and support in guiding me throughout these research.

Many thanks to Prof Rob Poole and his PhD students, Miss Sian Tedd's and Mr Tiago De Jesus Henriques, for providing me with essential laboratory data. In addition, many thanks to Miss Laura-Beth from the University of Hull for providing me with essential experimental data.

I would like to dedicate my work to my rock and backbone, my wife Yemenat Al-madhagi who was constantly supporting me with love, care and patience. I couldn't have done this without her. To my blessing Jenna, my beautiful daughter, her smiles and laughter gave me strength which kept me going.

Also, many thanks to The University of Liverpool for partially funding the current research.

Content Table

List of Figures

List of Tables

Notation

x	Axial coordinate
x_n	Aligned axial coordinate
z	Lateral coordinate
z_n	Aligned lateral coordinate
y	Vertical coordinate
y_n	Aligned vertical coordinate
r	Radial coordinate
u	Horizontal velocity
v	Vertical velocity
w	Lateral velocity
P	Static pressure
p'	Pressure correction
T	Time
g	Gravitational force
F_i	External body force
τ_{ij}	Stress tensor
μ	Dynamic viscosity
ν	Kinematic viscosity ($=\frac{\mu}{\rho}$)
μ_t	Turbulent eddy viscosity
ρ	Density
c_l	Coefficient of lift
c_d	Coefficient of drag
q	Dynamic pressure
a	Axial induction factor
a'	Rotational induction factor
u'	Velocity fluctuation

u^*	Shear velocity
a_p	Under relaxation factor for pressure
a_{nb}	Under relaxation factor for adjacent cell
A	Wave amplitude
A_c	Stream cross-section area
A_t	Turbine swept area
A_i	Interfacial area density for phase i
Δn	Cell height normal to interface
w_m	Gaussian weights
ω	Specific dissipation rate
f	Angular wave frequency
f_e	Effective wave frequency
D_ω	Cross diffusion term
S	User defined source term
K_s^+	Roughness Reynolds number
k_s	Roughness height
κ	Von Kármán
C_s	Roughness constant
z_0	Roughness length
$\dot{m}$	Mass transfer
α_w	Water fraction
h_d	Hydraulic diameter
K	Wave number
C	Damping resistance
c_2	Pressure jump
α	Face permeability
α'	Blade twist angle
α^*	Damping coefficient

ϵ	Void fraction
ε	Turbulent dissipation
V_s	Superficial velocity
D_p	Sphere diameter
Γ	Effective diffusivity
R_v	Viscous resistance
R_i	Inertial resistance
D	Diameter
e	Porosity
ϕ	Sphericity
AOA	Angle of attack
Ω	Blade rotational speed
Ω_w	Wake rotational speed
β	Relative flow angle
λ	Tip speed ratio
θ	Azimuthal angle
Ψ	Tip loss factor
B	Number of blades
B	Damping factor
σ'	Local solidity
c	Chord length
C_u	Currant number
T_i	Turbulent intensity
L	Wavelength
L_c	Characteristic length (hydraulic diameter in open channels)
h	Water depth
D	Turbine diameter
H	Wave height = 2A

Ur	Ursell number
CFD	Computational fluid dynamics
Re	Reynolds number
VBM	Virtual blade element
k (TKE)	Turbulent kinetic energy
RANS	Reynolds averaging Navier-stokes
VOF	Volume of fluid
Fr	Froude number
HATT	Horizontal axis tidal turbine
SST	Shear stress transport
MWL	Mean water level
PISO	Pressure-Implicit with Splitting of Operators
SIMPLE	Semi-Implicit Method for Pressure-Linked Equation
PRESTO	PREssure STaggering Option

Chapter 1 - Introduction

1.1 Tidal Turbines

Tidal turbines are devices that operate in streams and convert kinetic energy of tidal flow into electricity. They are similar to wind turbines but are fitted with shorter and thicker blades. The number of blades may vary between two or three, depending upon the design of the turbine. They are usually installed underwater on stream beds using gravity base (large concrete blocks) or are pile mounted (Thake, 2005). The tide moves enormous volumes of water twice daily, with the direction depending on the time of day. When the flow speed exceeds a certain limit, the turbine blades will experience sufficient lift force that causes rotation. Their rotors are mounted on a gearbox shaft, which generates electricity by electromagnetic induction (Fig 1.1). Underwater cables transfer the electricity to shore, which is then fed through high voltage transformers into a grid. These tidal devices function similarly as wind turbines. However, due to the higher density of water tidal turbines are capable of extracting more power than a similarly rated wind turbine. To achieve economic performance, tidal turbines normally operate in multiple groups called farms. The turbine arrangement within a farm itself is a critical aspect that allows efficient utilisation of the obtainable energy.

So far, several types of tidal stream generators have been proposed. Some of the examples will include, horizontal and vertical axis, flow augmented and oscillating devices (EMEC, 2015). This particular study, horizontal axis tidal turbines (HATT) are considered as they are one of the most popular turbine types and have been evaluated in many experimental investigations. Many international companies such as SeaGen (Fig 1.2) and Scottish Power Renewable (Fig 1.3) have developed a variety of designs to introduce more efficient and easily installable turbines. SeaGen is the world's first large scale commercial tidal stream generator. Their first generator was installed in Strangford Narrow and can create 1.2 MW for approximately 18 to 20 hours a day (SeaGen, 2007).

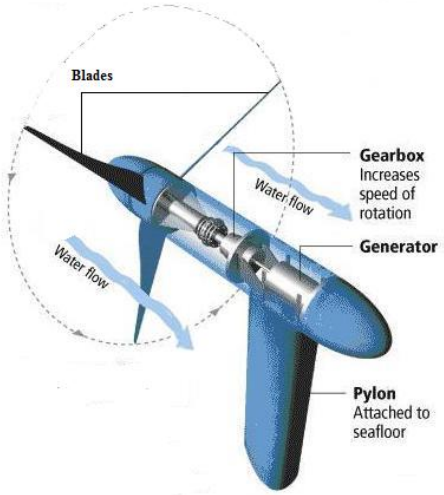

Figure 1-1- Turbine structure (after Ghode and Kukkar, 2001)

Figure 1-2 – SeaGen double and single rotor HATT (after Dubey, 2008).

Figure 1-3 - Scottish Power Renewable, 3 bladed HATT (after Press Office, 2008).

1.2 Turbine Effects

Tidal stream converters are considered as one of the proceeding technologies in the renewable energy sector. They have rapidly developed as the theoretical principals are very similar to those found in wind turbines (Douglas, 2008) which have been developed over many years. However, the remarkable difference is the transition from air to water flow which leads to fundamental changes that have to be considered and carefully controlled. Water differs from air in terms of compressibility, density and viscosity. Unlike wind turbines, tidal turbines are typically bounded by walls and a free water surface. This confined region allows turbines to create a blockage effect favourable to energy production. As a result, extra turbulence is generated from the turbine operation and the boundaries that are typically significant to the surrounding environment.

Due to presence of a tidal turbine and its separation effects, a wake region will be generated behind the structure, which has significant influences on the surrounding environment. Typically, depending on the distance to the structure and the influence on the hydrodynamics and turbulence, the wake region is further divided into near wake and far wake. The near wake usually refers to region where the effect of the rotor is major i.e. high turbulence, bed shear stresses and velocity deficit ($x/D < 10$). However, far wake usually refers to beyond the near wake and is frequently concentrated in farms (El-Kasmi and Masson, 2008). The size of impact of a tidal turbine varies significantly depending on many factors, some of which arise from turbine configuration and others from natural occurring processes. Configuration aspects include turbine blockage ratio, turbine yawing angle in relation to the flow direction and the turbine elevation. Natural processes include flow behaviour in terms of velocity, background turbulence, bed roughness and sea states. Surface waves and tidal current introduce strong unsteadiness effects which have not been investigated in great detail yet. It is critically important to improve current understanding by quantitative analysis of how each of the above factors would influence the wake characteristics and the surrounding environment (stream bed).

1.3 Aim and Objectives

Aim

The aim of the present study is to characterise the horizontal axis tidal turbine (HATT) effects on the surroundings in the near wake region under realistic conditions and different turbine configurations. The aim will be accomplished through the following objectives:

Objectives

1. Develop a realistic representation of tidal stream turbine in a CFD model for waves with current simulations.
2. Investigate turbine impacts to the surrounding environment under steady flows and surface wave conditions e.g., streamwise and opposing waves.
3. Investigate turbine impacts including different yawing angles, elevations, blockage ratio effects and background turbulences to the surrounding environment.
4. Compare the influence of different factors by carrying out quantitative analyses.

1.4 Scope

This study will mainly focus on the hydrodynamics of flow in the near wake region (x/D = 0 ~ 10). The physical processes will mainly be analysed in terms of streamwise, vertical and cross-stream velocities and Turbulent Kinetic Energy (TKE). The fact that different flow and rotor configuration conditions will influence the characteristics of wake (Bahaj et al., 2007); as a result, the bed shear stresses and the free surface elevations may well be affected. Therefore, it is also sensible to consider their changes due to the turbine operation.

The fundamental understanding of turbine impact on the water flows in the near wake region is still far from satisfactory. The majority of up to date studies are more focused on power production, turbine performance and loadings (Frost et al., 2015) and (Batten et al., 2008). In many cases, the investigations were restricted to idealised steady flow conditions and without surface effect (Masters et al. 2013). With more likelihood of commissioning tidal stream at industrial scale in recent years, it has become increasingly important to better understand the

impacts of turbine operations on the flow dynamics and associated environment at realistic conditions.

There are many methods used for representing turbines. These methods differ in terms of accuracy, computational costs and convergence speed. Selecting a method also depends on the turbine geometry adopted i.e. uniform porous disk or actual rotor-blades. In studies where the wake is investigated, it is found that the flow is dominant in the streamwise direction (Mozafari, 2010) and (Harrison et al., 2009). Hence, the flows in vertical and cross-stream directions become overpowered by the dominant flow and therefore are neglected. This assumption puts forward the porous disk approach and in many cases is favoured. In contrast, this assumption is avoided when assessing the performance and designing turbine. Creating actual blades correlate to high accuracy but on the other hand is very time consuming and computationally expensive.

In this study, the computation facility is limited and a porous disk is used in order to keep costs at minimum. However, the assumption of neglecting overpowered flows is avoided by taking into account each vector component. The disk will be able to implement a rotatory motion by introducing a virtual blades method. In addition, the disk will be improved by introducing a hub feature. Two numerical methods, Actuator Disk Model (ADM) and Virtual Blade Model (VBM), are tested. These two methods adapt similar rotor mesh (Porous Disk), which make them preferable due to their simplicity and faster convergence. The pros and cons of each method will be highlighted. The VBM method is then further tested under different experimental conditions that will help evaluate the strengths and weaknesses of the method.

The 3D CFD package Fluent 14.5 is selected as the basis of the present model, which is calibrated with experimental measurements, due to its availability and robustness. Both steady and unsteady flows are considered, including waves and tides.

In addition to the flow conditions, the present work also examines several important aspects in relation to turbine operation, including the yaw angle, elevation, blockage ratio and the background turbulence intensity. All of these different aspects not only influence turbine performance but also impact the environment differently, which is often critical to the protection of the marine environment.

1.5 Outline of Thesis

The following chapters are organised as follows:

In chapter 2: The literature reviews of previous and current published researches are described. As an overview, tidal stream energy potential sites around the UK are identified in addition to their marine nature. The physical flow processes created when employing a turbine in a stream are highlighted. The different numerical methodologies that exist to represent a turbine are defined and compared. This chapter will highlight the gaps in knowledge and raise their importance.

In chapter 3: An introduction of the CFD package FLUENT 14.5 is explained. It will identify and explain the theories and governing equations that will be used to resolve the flow under realistic conditions (turbulence model, free surface tracing model, boundary and zone conditions).

In chapter 4: The theories and equations of the two numerical representation of turbines Actuator Disk Model (ADM) and Virtual Blade Model (VBM) are described. The limitations of the 2 approaches as well as their setups are also discussed. A detailed description of the geometry and meshes conducted is presented here.

In chapter 5: The calibration of the CFD models with several experimental data sets is described. The results are further explored beyond the experimental measurements.

In chapter 6: It will summarise the various study conditions that are used in this study. A cross comparison of the different cases is discussed.

Chapter 7 summarises all the major findings discussed in Chapters 5 and 6. Recommendations for future works are specified too.

1.6 Major Research Questions

Several important research questions raised based on previous studies are going to be examined in detail in the present study:

1. How does the rotational motion (VBM) of a turbine influence the wake characteristics and the surroundings e.g., flow dynamics, induced turbulence and streambed, when compared to a static turbine (ADM)?
2. Do turbines have significant impact on the environment i.e., bed shear stresses?
3. What are the additional/different effects from turbine high-low blockage ratios, yawing angle, background turbulence intensity and elevations on the turbine-induced impacts?
4. How would the presence of a turbine affect the propagation of waves e.g., waveform, alignment and wave-induced turbulence?
5. How do waves e.g., streamwise and opposing waves, influence the wake characteristics and the streambed?

1.7 References

Bahaj, A.S., Meyers, L. E., Thomsan, M. D. and Jorge, N. (2007) Characterising the wake of horizontal axis marine current turbines, *Proceedings of the 7th European Wave and Tidal Energy Conference,* Porto, Portugal.

Batten, W.M.J., Bahaj, A.S., Molland, A.F. and Chaplin, J.R. (2008) The prediction of the hydrodynamic performance of marine current turbines. *Journal of Renewable Energy,* vol. (33), Issue: 5. pp.1085-1096.

Douglas, C.A., Harrison, G. P. and Chick, J. P. (2008) Life cycle assessment of the Seagen marine current turbine *Proceedings of the Institution of Mechanical Engineers, Part M: Journal of Engineering for the Maritime Environment,* vol. (222), Issue: 1. pp.1-12.

Dubey, K. (2008) SeaGen – The first tidal powered turbine in world from Marine Current Turbines [Homepage of Techshout], [Online]. Available from: http://www.techshout.com/general/2008/21/seagen-the-first-tidal-powered-turbine-in-world-from-marine-current-turbines/ [accessed March 03, 2016].

El Kasmi, A. and Masson, C. (2008) An extended model for turbulent flow through horizontal-axis wind turbines. *Journal of Wind Engineering and Industrial Aerodynamics,* vol. (96), Issue: 1. pp.103-122.

EMEC, (2015) Tidal Devices [Homepage of The European Marine Energy Centre Orkney], [Online]. Available from: http://www.emec.org.uk/marine-energy/tidal-devices/.

Frost, C., Morris, C. E., Jones, A., O'Doherty, D. M. and O'Doherty, T. (2015) The effect of tidal flow directionality on tidal turbine performance characteristics. *Journal of Renewable Energy,* vol. (78), pp.609-620.

Ghode, A. R. and Kukkar, K. (2001) Tidal Energy Harvesting. Available from: http://www.engineeringcivil.com/tidal-energy-harvesting.html [accessed October 02, 2015].

Harrison, M. E., Batten, W. M. J., Myers, L. E. and Bahaj, A. S. (2009) A comparison between CFD simulations and experiments for predicting the far wake of horizontal axis tidal turbines, *Proceeding of Renewable Power Generation, IET,* vol. (4), Issue: 6. pp.613-627.

Masters, I., Malki, R., Williams, A. J. and Croft, T. N. (2013) The influence of flow acceleration on tidal stream turbine wake dynamics: A numerical study using a coupled BEM–CFD model. *Journal of Applied Mathematical Modelling,* vol. (37), Issue: 16–17. pp.7905-7918.

Mozafari, A. T. J. (2010) *Numerical modelling of tidal turbines: Methodology Development and Potential Physical Environmental Effects,* MSc. Thesis, University of Washington.

Press Office, (2008) Scottish Power Renewables Announce Largest Tidal Stream Projects [Homepage of Scottish Power Renewables], [Online]. Available:

http://www.scottishpowerrenewables.com/news/pages/scottishpower_renewables_announce_largest_tidal_stream_projects.asp [accessed March 15, 2016].

SeaGen, (2007) SeaGen The world's first commercial scale tidal energy turbine deployed in Northern Ireland [Homepage of Marine Current Turbines], [Online]. Available: http://kirstendunst.ga/show.php?url=http://www.marineturbines.com/3/news/article/10/world_s_first_commercial_scale_tidal_power_system_feeds_electricity_to_the_national_grid__/ [accessed April 21, 2016].

Thake, J. (2005) *Development, installation and testing of large scale tidal current turbine.* UK: DTI Technology Programme: New and Renewable Energy.

Chapter 2 – Literature Review

2.1 Introduction

It is important to recognise the conditions at which tidal stream turbines operate. It helps researchers to replicate realistic conditions during investigation and allows them to bring forward recommendations. During a turbine operation, the hydrodynamic processes are affected directly behind the turbine (wake). The flow will experience acceleration, deceleration and recirculation depending on the area of interest. It is important to understand these processes and investigate their impacts on the surrounding environment. In addition, these processes have further impact on turbulence characteristics within the fluid flows.

Furthermore, the various natural conditions at which turbines operate such as steady or unsteady flows, yaw angle, blockage effect, and turbulence intensities etc. also have considerable impact on flow.

This chapter will discuss previously published works on several impact aspects related to tidal stream operation and impact on the surrounding environment, including the potential sites, the natural environment around an offshore site, turbine impacts on natural flow and, more importantly, the developed modelling methods so far. Based on these reviews, the knowledge and understanding gap can be identified which can then be focused on in the following chapters.

2.2 Challenges

There are three critical flow conditions that cause the unsteadiness of a flow. Waves, having different wave lengths and, amplitudes, are accompanied by a transfer of energy from one point to another. Secondly, there are tidal flows, which travel in different directions depending on the time of the day. Finally, turbulence, being the flow irregularities caused by

sudden flow changes and majorly induced by turbines. All aspects of turbulences will be accounted for, i.e., background turbulence, bed and turbine-induced turbulences. There are many inbuilt turbulence models in FLUENT that will be explained later in Chapter 3. Turbine operations have the greatest influence on turbulence and hence should be represented accurately.

One of the challenging conditions is to introduce surface waves; as a result, a multiphase model (Air & Water) will be developed. A numerical technique for tracking and locating the free surface would be introduced by the Volume of Fluid model. The mesh that will characterise the method could either be flat or wavy to entrain the moving shape of the interface. Various wave conditions will be generated in both following and opposing directions of the current. The turbine impact on the wave structure, and vice versa, is still not clear from literature. In many previous simulations, the free surface feature is ignored, even in steady conditions. Consul et al (2011) demonstrated that the free surface effects can be important, as errors tend to occur if a rigid lid approach is adopted. Therefore, a free surface condition will be implemented in all steady and unsteady flow states.

The next challenge is imitating tidal flow routines. It is recognized that tidal flows travel in dissimilar directions due to the flood and ebb movements. To account for multi-directional flows, the turbine will be positioned at different yawing angles to receive the flow at different angles of approach. Most researchers tend not to deviate from flows that are normal to the turbine, whereas in real life there is more variety. This model therefore will explore their influences on wake characteristics, free surface elevation and bed shear stresses.

In addition to tidal flow regimes, it is clear that water levels change continuously during tide phases. This would directly influence the blockage ratio of turbines with a stream cross-section. It has not yet been clearly revealed how blockage ratios would influence the flow behaviour across the water depth and, therefore, it is important to carry out this investigation. This continuous variation of flow behaviour may also influence the flow regime (background turbulence). Employing the turbine will generate significant turbulence and it is important to understand the impact on the background turbulence. It will also be interesting to evaluate the impact of background turbulence on the induced turbine turbulence.

It has not yet been clearly revealed if turbine operations have a direct impact on sea/channel beds. If turbine operations have a significant impact on the flow characteristics, then it is very

likely it will have implications on stream floors if located in areas containing highly mobile sediment sources. The shear stresses enforced by turbines on the bed may cause sediment transport distortion. This might lead to waves starting to break closer to the shore, which could increase coastal erosion and flooding (Neill et al., 2009b). In this study the shear stresses on the channel floor beneath the wake region are measured. The elevation of turbines is another parameter that should be investigated.

2.2 Potential Sites

There are two common techniques for capturing energy from tidal regimes, tidal barrages and tidal streams. Tidal barrages (dams) collect the water during high tides and during low tides this water is released through sluice gates where turbines are placed to capture the energy as the water flows. In tidal streams however, turbines are placed on the stream beds to converter moving masses of water during tides into energy. In this study, tidal stream converters (turbines) are considered, particularly horizontal axis tidal turbines.

Carbon Trust (2011) suggests that a total of 20.6 TWh per year could practically be extracted from 30 key tidal stream sites in the UK. Table 2-1 and Figure 2-1 illustrate the names and locations of 14 sites with high energy potential (Black and Veatch, 2005). These sites are unique in terms of their shape.

Looking at these areas of interest, a set of coastal geometries is reflected from Figure 2-1. Open sea locations feature no side boundaries, such as in channels. The water can flow in and out of the vicinity without any restriction. The head difference remains constant unless turbines are installed. Sites are found at Alderney Race in the English Channel, indicated as site 7, North Sea coast (site 12), site 9, near Sumburgh and Fair Isle, indicated as sites 5 and 6 respectively. Inter-island channels feature side boundaries where the head difference between upstream and downstream directs the flow. The tidal elevation is not affected by these flows and potential sites are found within the Pentland Firth (Scotland) region, indicated as sites 1, 2, 3, 4 and 8 in Figure 2-1. Headlands surrounded by water on three sides feature complex flows with shifting tidal velocity locations. They have fixed head difference and are found in

the English Channel, i.e., Portland Bill, and in the Irish Sea near Holyhead, indicated as sites 13 and 14 respectively in Figure 2-1. Estuaries, coastal vicinities with a river flowing in from one side and open to the ocean from the other side, may become resonant when the tidal stream provokes one of the resonant modes of the geometry. Sites include the Thames Estuary and Severn Estuary (site 11).

From table 2-1, approximately 50% of UK tidal sites correspond to water levels greater than 40m, specified at sites 1, 2, 3, 7, 8, 9 and 10.

Table 2-1 – Available UK tidal sites (after Fujita Research, 2000).

#	**Site Name**	**Width (m)**	**Depth (m)**
1	Pentland Skerries	3200	59
2	Stroma P. Firth	2500	71
3	Duncansby Head	2000	65
4	Casquets	8000	115
5	S. Ronaldsay	2300	58
6	Hoy, Pentland Firth	2000	76
7	Alderney Race	3324	33
8	S. Ronaldsay/ P. Skerries	2300	63
9	Rathlin Island/near Eilean Mhic Coinich	4000	80
10	Mull of Galloway	4807	80
11	Bristol Channel/Severn Estuary	3923	22
12	North Sea/ East coast (Norwich)	-	-
13	Portland Bill, English Channel	1989	33
14	The Skerries of Isle of Anglesey/Irish Sea	-	-

(-) Not given

It is clear from Figure 2-1 that the Pentland Firth consists of many neighbouring sites together (Sites 1, 2, 3 and 8). Furthermore, it is found that site 1, 2 and 6 are linked together in the longitudinal route of the flow stream.

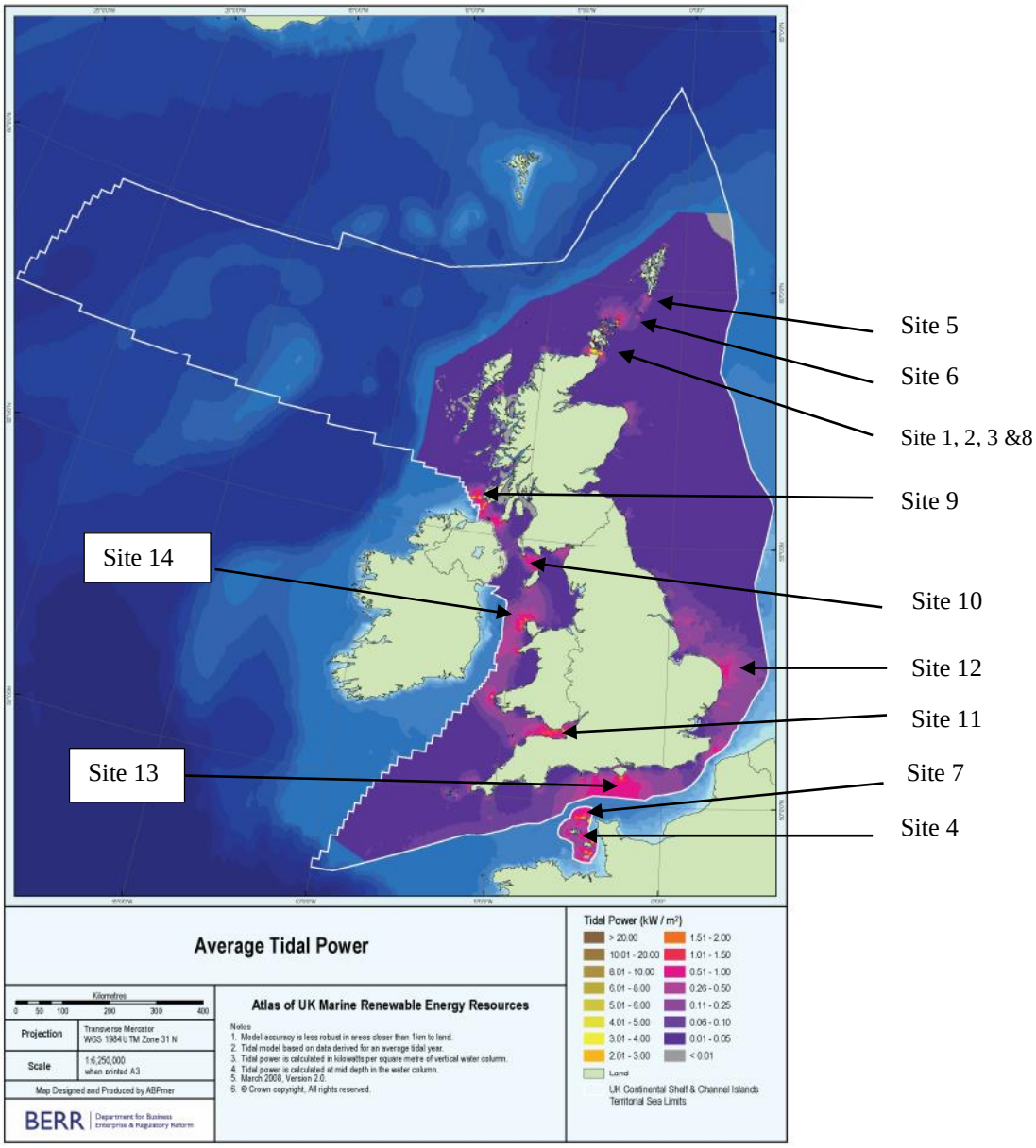

Figure 2-1 - Presents the average tidal stream power at sites in the UK (after BERR, 2008).

It is apparent that there are a large number of tidal stream energy potential sites in the UK, which encourages the exploitation of the technology as well as improving techniques of simulation. It will also be encouraging to document how these turbines would influence flow behaviour in the waters and if they have an impact on the surrounding environment.

2.3 Natural Processes at Potential Sites

At high energy potential sites, it is recognised that water flows undergo many physical processes that are complex in nature. Many of these processes are often significant to the local sustainability of the ecosystem, morphology and other natural resources that need to be conserved. In this section, an overview of these natural occurring processes is highlighted.

2.3.1 Tidal Current

All of the above mentioned UK sites are subjected to continuous tides and changing currents. Black and Veatch (2005) and BERR (2008) stated that tidal streams must have velocity magnitudes of $u \geq 2$ m/s in order to generate adequate energy; this can be accompanied by large tide range, e.g., ≥ 6m.

In general, sites that experience tidal range above 8m are sites of particular interest. These sites are called Mega tidal sites. The BERR (2008) atlas report highlights the mean spring tidal range around UKs waters. The Bristol Channel and Severn Estuary (Site 11) show the largest single area of tidal range resource, recording 10m and above. Sites 4 and 10 also record mega tides measuring between 8m-9m. The remaining sites in the UK waters fall under Macro tides (tidal range 4m-8m). The lowest tidal range (1m-2m) is recorded in the English Channel (site 13) and Rathlin Island (Site 9). It is interesting to point out that Pentland Firth experiences tidal ranges between 2m-3m and also the strongest tidal current velocity in UKs waters (6.18 m/s)

Table 2-2, illustrates the tidal current velocity for each site derived from an average tidal year. In terms of peak flow velocities, it is clear that all sites in the UK during spring tides experience flow velocities ranging between 2.57m/s – 6.18m/s. Maximum velocities are recorded greater than 5 m/s at sites 1, 2, 3 and 8. During neap tides, velocities range between 1.39m/s – 2.64m/s. The flow velocities are measured at mid-depth in the water column.

Table 2-2 - Flow velocities at spring and neap tides at potential sites in the UK waters.

#	Site Name	Velocity m/s (Spring)	Velocity m/s (Neap)
1	Pentland Skerries	6.18	2.64
2	Stroma P. Firth	5.15	2.20
3	Duncansby Head	5.15	2.20
4	Casquets	2.57	1.39
5	S. Ronaldsay	4.89	2.05
6	Hoy, Pentland Firth	4.38	1.80
7	Alderney Race	4.38	2.41
8	S. Ronaldsay/ P. Skerries	4.38	1.79
9	Rathlin Island	2.57	1.44
10	Mull of Galloway	2.57	1.44
11	Bristol Channel/Severn Estuary	3.09	1.43
12	North Sea	2.25	1.13
13	Portland Bill, English Channel	3.86	1.92
14	The Skerries of Isle of Anglesey/Irish Sea	2.75	1.63

It has been concluded that 30% of the UKs tidal energy come from sites of 30-40m depth with flow velocities of 2.5-4.5 m/s. These sites are not too deep and flows are not too fast, which allows feasible installation. 50% of UK tidal energy comes from deep water sites > 40m that have flow velocities of > 3.5 m/s.

2.3.2 Waves

The UK is located on the east side of the Atlantic Ocean, which imposes strong waves onto the coastline. The nature of waves approaching these sites depends on local factors such as site exposure and strength of winds. Seasonal mean wave heights show that the strongest waves are recorded in winter (Black and Veatch, 2005). Wave heights were measured on hourly time scale and recorded over 7 years. Mean annual wave heights range between 3 – 3.5m at sites 5 and 6. The sites 1, 2, 3 and 8 experiences mean annual wave heights in the range of 2.75 – 3m. Rathlin Island (site 9) experiences wave heights around 2.51 – 2.75m. Site 12 in the North Sea experiences mean annual wave heights between 1.75 – 2m. Both Alderney Race (site 7) and Casquets (site 4) in the English Channel experiences mean annual

wave heights of 1.5 - 1.75m. The smallest wave heights are recorded at sites 10 and 11 and show wave heights smaller than 0.75m.

However, storms, tsunamis and other extraordinary events will create strong waves. In the past decade, the UK has experienced a number of strong storms. Storms are typically associated with strong winds that reach up to speeds of 120 miles per hour. These strong winds increase surface wave speeds which consequently increase the wavelength. In 1607, the Bristol Channel and Severn estuary experienced a flood caused by a storm surge combined with high tides. Wave heights were recorded as high as 7.5m during that period.

2.3.3 Wave and Current Interaction

The flow of currents has a considerable effect on the wave dynamic. Waves can propagate opposing and following the direction of flow that can influence the frequency or the wavelength of a wave. The Doppler Effect describes this change when an observer is moving relative to or away from the wave source. When moving towards the wave source, the crest of consecutive waves become closer since it takes less time to reach the observer. Hence, waves with opposing current will reduce the wave length, causing an increase in frequency and amplitude. On the other hand, when moving away from the wave source, the crests of consecutive waves become further apart since it takes longer to reach the observer. Hence, when waves are following the current, the wavelength tends to increase, causing the amplitude and frequency to decrease.

Brevik and Aas (1980) stated that when opposing wave experience high velocities, the wave steepness increases and under certain conditions will break. In addition, opposing currents may result in a nonlinear wave feature. For streamwise waves, increasing the current velocity results in increasing the wavelength and thereby reduces the wave amplitude.

2.3.4 Flow Velocities due to Wave-Current interactions

Hedges (1987) has explained water particle kinematics under a wave motion, see Figure 2-2. The water particles beneath the surface are continuously changing their direction of motion

depending on the wave phase (wave angle). The local particle velocities are presented in the figure as circular motions and decay as moving deeper into the water.

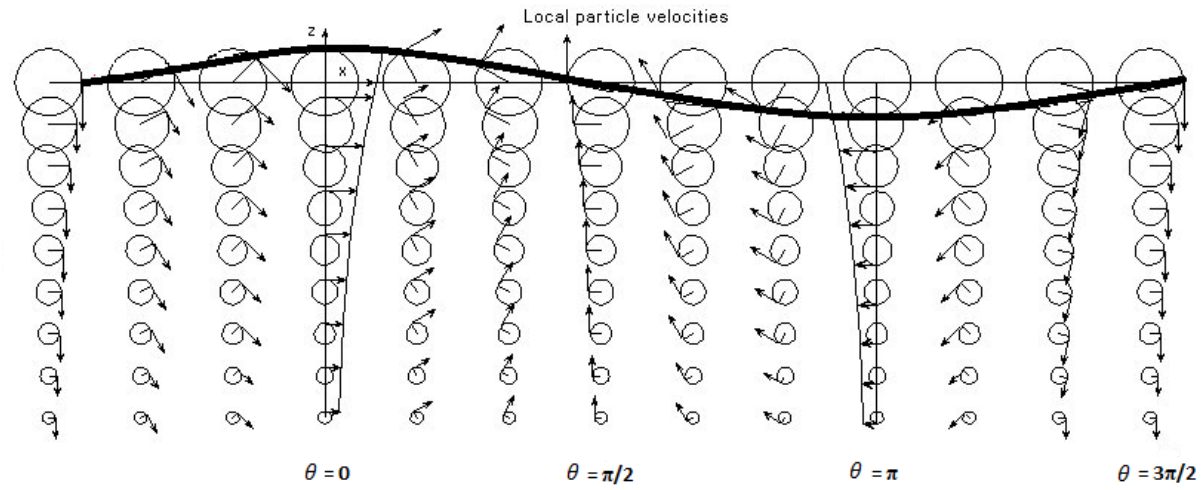

Figure 2-2 - Water particle kinematics under a wave motion http://fgg-web.fgg.uni-lj.si/~/pmoze/ESDEP/master/wg15a/l0200.htm

Maximum horizontal velocities occur at the crest ($\theta = 0$) and minimum horizontal velocities occur at the trough ($\theta = \pi$), when waves are following the current. For maximum and minimum vertical velocities, positive (upwards) and negative (downwards) take place between crest and trough at angles π/2 and 3π/2 respectively. For opposing waves however, an opposite behaviour occurs where maximum and minimum horizontal velocities take place at the trough and the crest respectively. Maximum and minimum vertical velocities, positive (upwards) and negative (downwards) take place at angles 3π/2 and π/2 respectively

Kemp and Simon (1983) have carried out an experiment to examine the influence of waves on the current velocity vertical profile. For smooth beds they found that when the waves are generated in the stream wise direction, the velocity near the bed increases and reduces near the water surface. In contrast, opposing waves will reduce the flow velocity near the bed and increase it near the water surface.

2.3.5 Turbulence due to Waves-Current Interaction and free surface (Interface)

As explained in section 2.3.4, particles beneath the surface undergo orbital motion and usually in any case, are an order of size faster than the current and hence will produce turbulence. In ocean dynamics, normally breaking waves are considered alone since large amounts of energy is released and become the source of turbulence at the upper surface layer (Babanin, 2011). Beyond this layer (normally a wave amplitude length), these turbulences decay quickly (Thorpe, 2005). Lately however, breaking wave-induced turbulence has been challenged by the non-breaking wave-induced turbulence that is introduced by (Babanin, 2006). A number of experimental investigations showed that non-breaking waves do produce turbulence and should be accounted for.

Wind surface wave are another cause for inducing turbulence at the surface (Langmuir circulation). It is a wave related phenomenon that is produced by the unsteadiness of the wave scheme. The horizontal component of the wind creates stresses that generates shear currents and therefore induced turbulence and encourage mixing (Kudryavtsev and Makin, 2002). They form a counter-rotating vortices at the surface that range with the wind.

Marquis and Rice (2009) conducted experiments to determine the impact of surface waves on turbulence in an empty channel (no turbines). It was found that wave-induced turbulence was generated. A similar observation was found by Bahaj et al. (2007) in their experiment. Furthermore, Veron et al. (2009) showed that highest turbulent levels were found at wave crest or slightly behind it.

The presence of free surface is not only important for the generation of waves but also in current only conditions. In many existing studies it is suggested that when the Froude number (Fr) is larger than 0.2, free surface variation will affect the subsurface hydrodynamics considerably (Roulund et al., 2015). The pressure distribution over the depth will not follow a simple linear distribution and hence the surface dynamics should be taken into account when examining the details of flow within the water body. The turbulence generated near the interfaces from both sides (top and bottom) can be significant (Shirani et al. 2006). When the rigid-lid approach is used, the free surface effect is suppressed without allowing deformation; inaccuracies are therefore expected (Consul et al., 2011).

In general, the rotational wave motion in CFD modelling is typically ignored (irrational). It is assumed that there is no surface tension and waves are free; as a result, the wave-induced turbulence and shear stresses are not generated (Komen et al., 1994). This approach ties with the wave motion in linear and nonlinear wave theories which are useful in the analytical solutions. Furthermore, the presence of the free surface will always produce a high velocity gradient at the interface that will produce turbulence. However, this unwanted turbulence will be eliminated by introducing a turbulence damping source at the interfacial area (dissipation (ω) equation seen in Chapter 3).

2.3.6 Bed Shear Stress

It has been confirmed by Chanson (1999) that bed shear stresses are stronger at the centreline of the channel rather than at banks. He also mentioned in his experimental investigation that at wave crest shear stresses are high whereas, at troughs, shear stresses are low. Combining current with waves has small effects on wave-induced velocities near the bed and on oscillatory shear stresses (Simons et al 1994). Elsewhere, wave steepness increases with water surface current. Simons (1992) also found that shear stresses at the bed boundary increase when generated waves are at right angles to the current. Simons et al. (2001) published a paper on the kinematics and shear stresses from combined waves and longshore currents in the UK coastal research facility at Wallingford.

The results showed that the mean shear stress and apparent bed roughness increased when waves were imposed. It was also found that shear stresses are higher at shallow waters than at deeper waters. There was no significant change in shear stresses when current was superimposed. When combining waves with current the shear stress along the bed where found to be greater at crest than trough.

2.4 Tidal Turbine Impact (Wake)

The presence of a turbine in a marine environment will form an obstruction to the water flow, creating a wake. In addition, eddies are created in the turbine-affected regions that contain turbulence, dissipate fairly quick to smaller eddies, then decay. On the other hand, more stable eddies are created behind the turbine about the turbine central axis line, being large in size, maintained over a long distance and not dissipating as fast. Furthermore, reverse flows typically are generated behind blades. The characteristics of wakes generated behind a turbine are an attractive study area that researchers have looked into through many experimental and computational investigations. This section will describe the influences of a tidal turbine on a stream flow during operation and highlight possible impacts on the surrounding environment.

2.4.1 Wake Characteristics

There are two regions in a wake that are often studied, e.g., the near wake and the far wake regions. However, it is not clear from literature how these two regions are to be determined. Maganga et al (2010b) characterise the near wake by high shear gradient and turbulent intensity, and the far wake by its expansion. Myers and Bahaj (2009) on the other hand, define the near wake region as being where vortex shedding cause discontinuity in stream velocity profile. Where these vortices dissipate marks the beginning of a far wake. Among these researches, the typical boundary of these two regions can be found between 4-6 turbine diameters (Xiao et al., 2013 and Maganga et al., 2010a). In this study, the near wake region was determined whereby the flow velocity deficit behind the turbine exceeded 40% of the inlet flow velocity. This region is found to extend over ≈ 5D downstream where D is the diameter of the turbine. Furthermore, the flow in this region shows reversed values of velocity (eddies) that dissipate beyond this region. This adopted near wake boundary will be the main focus for identifying the turbine effects on the physical processes of flow.

The wake is best characterised in terms of detailed three-dimensional velocities and turbulent flow field information. The flow velocity (u_i) describes the velocity of a water particle in a direction ($i = x, y, z$) over time (t). In steady flows, velocity does not change with time ($\frac{\partial u}{\partial t} =$

0) but is time dependent for unsteady flows. Turbulence is the other phenomenon that illustrates irregularities and fluctuations in a flow. They occur when the flow experiences a large enough Reynolds number or a strong change in pressure due to intersection with an object, in this case the turbine, forming a vortex and eddies. There are several ways turbulences are possibly induced, including turbine rotor (motion) and flow boundary interactions. These factors produce vortices and eddies that dissipate when converted to internal energies by viscous shear stress. The Reynolds number (equation 2.1) is the ratio of acceleration forces and viscous shear stress forces acting on a fluid element. The Reynolds number is a parameter that is used to identify the flow regime.

$$Re_{flow} = \frac{\bar{u}h}{\nu} \tag{2.1}$$

where ū is the mean velocity, h is the water depth and ν is the kinematic viscosity coefficient. When Re < 500, the flow is considered as laminar. When Re > 1000, the flow is considered to be turbulent (Chanson, 2004). Figure 2-3 illustrates the impact of two identical cylinders on flow behaviour when the flow is laminar and turbulent.

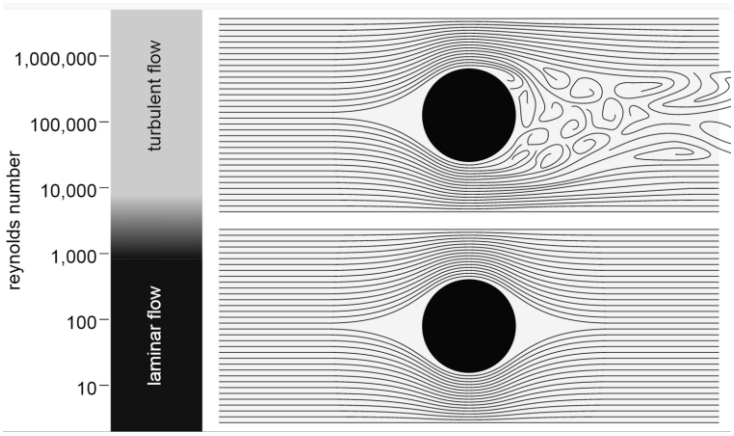

Figure 2-3 - 2D description of laminar and turbulent flow states (after Elert, 2015).

It is clear that, for turbulent regimes, the flow produces von Karman vortices that alternate positions with time whereas in laminar regimes, the flow behaviour is constant in respect to time.

The turbulent kinetic energy is an important characteristic of turbulence and is expressed as the mean kinetic energy per unit mass:

$$TKE = \frac{1}{2}\sqrt{(u'_x)^2 + \left(u'_y\right)^2 + (u'_z)^2} \tag{2.2}$$

where u_i' is fluctuation of velocity (i = x. y and z) and is found as follows:

$$u_i' = u_i - \overline{u_i} \tag{2.3}$$

where u_i is instant velocity at i direction. Tidal streams are known to be highly turbulent due to high flow speeds.

Laboratory experiment

There are many experimental investigations that describe wake characteristics. Bahaj et al. (2007) used a tunnel and a towing tank to conduct an investigation of wake characteristics behind a tidal turbine. A mesh disk of diameter 0.1m was employed in a 21m x 1.37m x 0.5m flume with peak flow rate 2.3m^3/s. Initially, results showed that the velocity profile at the inlet underwent a severe transition due to the turbulent shear layer at the bed. In terms of the wake, this was constrained vertically by the free surface and therefore expansion was restricted compared with lateral expansion. In addition, the wake's centre line was slightly shifted below the centreline of the turbine by 0.1D. This happens due to the higher flow rate over the turbine which tends to push the wake downwards (Venturi effect). In addition, supporting structures will misrepresent real rotor wake behaviours. A suggestion was made to employ long, thin stem supports in the experiment in order to minimise such effects. The velocity deficit continued beyond 20D, recovering 90%. The flow velocity below the wake had greater magnitude which caused stronger mixing.

Rose et al. (2011) conducted three different experiments to investigate techniques for measuring flow in the near wake region. The first experiment employed a four bladed turbine of 0.14m diameter in a 20m x 0.75m x 0.52m flume. The turbine operated in a 0.57m/s flow with a Reynolds number of 25,000. The second experiment employed a two bladed turbine of 0.25m diameter in a 35m x 0.4m x 0.92m flume. Flow speed was 0.42m/s with a Reynolds

number of 27,000. The third experiment employed a four bladed turbine of 1.5m diameter in a 400m x 133m site (Montgomery Lough). The turbine was operating in a 0.57m/s flow with a Reynolds number of 246,000. In all the experiments, maximum velocity deficits were found at the turbine centre.

Tedds et al. (2014) conducted an experiment to measure the flow velocity and the Turbulent Kinetic Energy behind a model turbine in steady flow. The experiment took place at a high speed recirculating flume with high blockage of 16%. The flow speed was uniform at 0.9m/s with ambient inlet turbulences induced. Detailed measurements using an ADV at different locations were taken.

Results reveal that turbulence created behind a turbine in the near wake is of anisotropic nature (the statistical features of turbulence have directional preference and the mean velocity has a gradient). Consequently, isotropic turbulence (perfect disorder, $u' = v' = w'$) models should not be used when investigating near wake dynamics. In addition, using a disk to represent a turbine neglects the swirling effect of flow due to rotating blades. As a result, Turbulent Kinetic Energy will possibly decay at a faster rate, leading to an under-prediction of turbulence energy.

Jordan et al. (2015) conducted an experiment that took into account a blockage ratio of 2.6%. The flume was 11m long, 1.6m wide and 0.6m deep, with a turbine diameter of 0.2m. Detailed measurements of velocity and turbulence were collected when the turbine was set at two different elevations (mid-depth and 2/3 deep). It was found that the closer the turbine was to the bed, the higher TKE was produced. Furthermore, wake length increased and the wake shape become asymmetric. This indicates that the turbine has an important role on bed shear stresses.

Myers and Bahaj (2009) investigated the wake characteristics of a turbine in the near wake region. This region is known to be highly turbulent and flow speeds are low, however it is not clearly known from literature where the boundaries of near and far wake regions appear. The experiment took place in a 1:20 scale facility under a maximum flow of speed 2m/s. A 0.8m diameter turbine was located in a flume of length 18m, breadth 4m and depth 2m. It was found that the supporting structure has a significant impact by inducing high turbulences to the flow, which consequently may misrepresent the actual rotor impact on wakes (Figure

2-4). This is also accompanied by additional velocity reduction in the near wake. The experiment results illustrated 80% wake recovery at 10D behind the turbine.

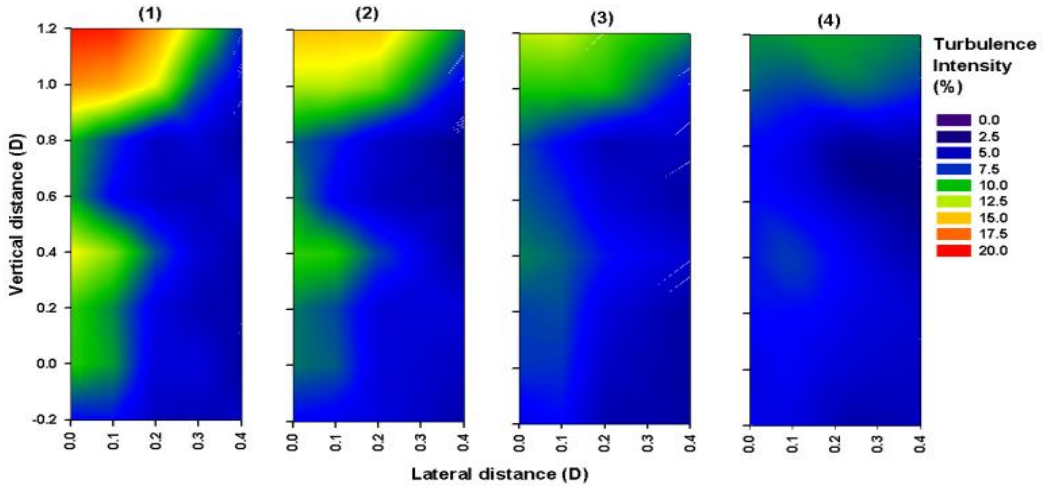

Figure 2-4 – Vertical profile of turbulence intensities behind a HATT at (1) 2.5D, (2) 3D, (3) 4D and (4) 5D (after Myers and Bahaj, 2009).

Maganga et al. (2010b) carried out an experiment to characterise the wake induced by a three bladed horizontal axis turbine. A 0.7m turbine was placed in 18m long, 4m wide and 2m deep flume. The tests were conducted with different background Turbulence Intensities (TI) of 4.6% and 14.6%. They found that the wake recovery rate was faster when higher turbulence intensity was present in the flow. For TI=14.6%, the wake was almost recovered after 5D downstream. However, for TI=4.6%, the velocity deficit was still seen at 10D downstream with higher turbulence intensity than that in the ambient flows.

Numerical modelling

CFD models have become very popular in simulating open channel flow in recent years. Malki et al. (2011) studied the influence of varying flow conditions on wake structure behind a turbine, using a CFD model. The model was used to simulate the turbulence around a 10m diameter turbine. It was found that wake length will increase linearly as the velocity inlet increases. Wake width also increases with increasing upstream velocity. Model results showed that after a certain distance downstream (1.92 diameters), the wake width remained constant.

Harrison et al. (2010) developed a CFD model to predict the far wake (x > 4D) of horizontal axis tidal turbines. The model was created to simulate steady flow in a flume of 1.37m width, 21m long and 0.3m deep. The turbine was represented by a disk of 0.1m diameter located at the mid-depth of the flume. This model's results show similar velocity and turbulence trends to those of experimental data conducted by Myers and Bahaj (2010).

Based on a number of tests, it was suggested that the wake is directly affected by the thrust value created by the turbine. This was obtained by investigating different disk porosities representing different thrusts. Turbulence is another important contributory factor to the rate of wake recovery levels. However, without induced rotation motion, the wake recovery rate was underestimated in the model.

Sufian and Li (2014) have used CFD FLUENT to model the impact of tidal turbines in the near region. The CFD model was successfully validated against experimental data conducted by Tedds et al. (2011). The results showed strong velocity deficit immediately in front of and behind the turbine due to the pressure change. Highest turbulences were recorded behind the blade tips of the rotor.

Masters et al. (2015) carried out a number of simulations to investigate the wake characteristics behind a turbine. Their models showed that 50% drops in flow velocity were found at 4D-5D behind the turbine. The velocity deficit profiles showed almost symmetrical distributions up to 40D downstream. Batten et al. (2013) observed that the higher the turbulence found in the near wake, the shorter the distance the wake recovered. Jones (2009) developed a field scale model where the turbine diameter was 10m, mean velocity 3.08 m/s and TI 5%. He found that on increasing the blade pitch angles, the velocity deficit decreased behind the turbine. In addition, the wake vortex width decreases as the blade pitch angles increase. At 17D, wake streamwise velocity recovery becomes 71% for all pitch angles. 90% of the upstream velocity was reached at 40D downstream.

Previous studies have broadly touched upon wake characteristics, especially in the near wake, with most of the effort being concentrated on performance and loadings. In this study however, wake characteristics are investigated in much more detail, taking into account naturally occurring and turbine related conditions. It will demonstrate the extent of their influence on flow, and potentially the surrounding area, by providing a quantitative analysis.

2.4.2 Importance of a Free Surface effect

There are many researches which have focused particularly on free surface impact of tidal turbine operations. Myers and Bahaj (2007) carried out an experiment of a $1/30^{th}$ scale in a circulating tunnel. They employed a 0.4m diameter turbine at a depth of 0.84m, which represented a blockage ratio of 12% similar to that of a full scale turbine. Three different velocities were used with a maximum speed of 2.35 m/s. One of the major aims was to measure the free water surface elevation profiles. It was found that on increasing the inlet flow velocity, the free surface depth changes also increased.

Bahaj et al. (2007) conducted experimental and theoretical studies to investigate parameters that would influence the wake structure and its recovery to ambient inlet velocity. A rotating disk of 100 mm diameter with a rotation speed of 1500 rpm was used in a 0.5m depth flume. The flume was 1.37m in width, 21m in length and had a blockage ratio of 2%. It was found that the existence of a free surface limits the spreading out of the wake in the vertical direction when compared to the lateral spread.

However, it is important to establish whether this lateral growth continues in the downstream. He also stated that waves will bring about turbulence near the surface with length scales that diminish in a logarithmic way when moving deeper in the water. Beneath the wake, vertical velocity measurements presented greater values which corresponded with the turbulent boundary layer and proposed stronger mixing.

Sun et al. (2008) applied a CFD model to simulate the flow around and behind an actuator disk in order to predict the flow consequences resulting from energy extraction. Both 2D and 3D simulations were employed, to compare with the measurements along the centre of channel and different water depths. It was found that extracting energy via a turbine will cause a free surface elevation change. The surface level slightly rises just before the turbine followed by an immediate drop downstream. This occurs due to the pressure jump caused by the turbine blockage effect. The surface drop persists over a length of a few turbine diameters downstream, which also encompasses a vortex (Smith, 2011). This feature should be considered when operating an array of turbines to avoid the impact on subsequent turbines.

The above studies conclude that the presence of a free surface (open channel) has a great influence on wake characteristics and therefore should be considered. Surface waves are an

additional condition that will require the free surface to be represented. Present work will therefore implement a free surface feature to accommodate waves and to represent a realistic flow.

2.4.3 Waves

It is essential to introduce waves in a tidal flow environment to simulate turbines under realistic conditions. A research by the European Marine Energy Centre (EMEC) employed an Acoustic Doppler Current Profiler (ADCP) to capture the energy potential in a site taking into account wave-induced velocities with the primary current (Norris and Droniou, 2007). The effects of waves are hugely important especially when they are at high states. It has been shown that wave-induced oscillations appear at the upper 66% of the water depth and bed-induced turbulences appear at 40% of the bottom depth of water.

Olczak et al. (2013) set up a wave tank experiment to investigate the influence of opposing waves on ambient flow and wake recovery behind a single turbine. A three-bladed turbine of 0.27m diameter was employed at the mid-depth of the channel. The wave maker was positioned at the outlet in order to generate the opposing waves. In comparison with steady current, introducing waves led to an increase in flow kinetic energy towards the surface, and a slight reduction near the bed. In the presence of waves, the overall distance of the wake region decreased. For deep water waves ($Kd > \pi$), where K is the wave number $\frac{2\pi}{L}$ and L is the wave length, the upper half of wake depth alone experienced reduced velocity deficit i.e., enhanced flow velocity recovery. However, for intermediate water waves ($\pi > Kd > \pi/10$), the recovery in flow velocity improved along the turbine centreline and bottom half of the wake depth. The bypassing flow beneath the wake showed slightly increased velocity deficit when compared to the steady flow condition.

Henriques et al. (2014) set up an experiment in a high speed flume to investigate the effects of wave-current interaction on the performance of HATT. The same experimental setup as Tedds et al. (2011) was used, with a paddle wave maker at the inlet to produce waves in the same direction of flow. Surface wave-induced velocities were captured using an ADV at different depths with two different wave conditions. The presence of the turbine had an overall impact of the wave shape; the wave height was found to decrease behind the turbine

especially on the off shore half of the flow (at trough). On the other hand, overall, the waves improved the flow velocity recovery downstream. It was also found that streamwise waves increase the turbulence kinetic energy behind the turbine which enhances flow mixing.

Lust et al. (2013) examined the impact of surface wave on the performance of a two-bladed 0.8m diameter turbine. It was found that the wave with different phases had different influences on power, rotation speed and thrust of turbine. Maximum impact was observed when crest occurred and minimum impact when trough occurred. On average, the power and thrust coefficients were slightly increased, which suggested that turbines should be carefully positioned at a depth where minimum fatigue and maximum power can be obtained.

There are researches that have considered wave models in single and multiple turbine operations. Buckland (2014) modelled a turbine operation under a tidal flow environment. The model was used to predict the performance of an individual turbine inside an array and its impact on the supporting structure. The stream function wave theory was employed, where the frame of reference moves with the wave. Wave acceleration was also taken into account. Model results suggest that the performance of a turbine is dependent on tip speed ratio profile which is the ratio between the tangential speed of the blade tip and the actual speed of the water. When waves are present, the supporting structure experiences fatigue due to the fluctuating forces formed by waves.

From the above, it is clear that the free surface can be significant in flow hydrodynamics and turbine operation, especially when surface waves are present. However, most existing studies with surface variations and wave dynamics are still very limited. More importantly, the effects of these surface dynamics on the flow turbulence and hydrodynamics are still unclear. In addition, the effects of turbines on wave-currents dynamics are also not investigated sufficiently.

In this study, the CFD model will be developed to investigate the coupling of turbine-current and waves. The study can reveal the flow kinematic and turbulence variations behind a turbine when waves are combined with current, the impact of wave direction on turbine-affected regions, the combined effects on channel beds and the possible impact of turbines on wave shape.

2.4.4 Bed Shear Stress

Bed shear stress is the force of friction from the flowing of water alongside the bed of stream. The velocity gradient near the bed produces shear forces that are parallel to the bed. When the drag force (due to friction) of flowing water against an object is greater than the gravitational force holding it in place it begins to move. Faster flows near the bed cause stronger movements. Sediment transport is a function of shear stress. Turbines are large structures installed on water stream beds. They cause obstruction to flows, changing their magnitude and direction. Swirling, diverted or reversed flows created from turbine rotation will impose additional shear forces on beds. These resulting forces may cause scouring, sedimentation and/or particle suspension. Neill et al. (2009a) investigated the impact of tidal stream turbines on large scale sediment dynamics. Results suggest that tidal stream energy extraction in the Bristol Channel can have a significant impact on the large scale morphodynamics of tidal systems, the magnitude of which depends upon the tidal asymmetry at the point of extraction. These results notwithstanding, energy extraction reduces the overall magnitude of bed level change in comparison with non-extraction case. Simon et al. (2011) covered the impact of tidal stream turbines on sand bank dynamics at Alderney Race, in France. Results suggest small changes to the tidal regime can have a large effect on the residual sediment transport pathways, and hence sand bank evolution, over the life cycle of a tidal energy converter device.

Couch and Bryden (2007) stated in their investigation that extracting energy from a tidal system will lead to an overall reduction in current speed over a larger area. Bryden (2005) also added in a different study that in a tidal channel the impact of energy extraction on current speed becomes noticeable only when the energy extracted reaches around 10% of the available kinetic energy flux. This reduction in flow speed will influence the sediment dynamics in the wake of the tidal turbine.

Given the scour/sediment transport effects around individual turbines, it is very likely that these processes can be accumulated around a large scale farm of turbines and lead to regional impacts.

Ahmadian and Falconer (2012) assessed the impact of certain array arrangements on the environment. One of the findings was that suspended sediment levels were increased along the sides of the array and were reduced both up and downstream of the array. Flood risks

associated with water level changes were very minor. (Mozafari, 2010) modelled the impact of turbines on sediments and fish. He found that sudden fluctuations of static pressure will not necessarily negatively affect small fish. He also shows that possible particles would settle behind the turbine as the flow velocity at the area is reduced. Hakim et al. (2013) used a finite volume community ocean model to assess the impact of tidal stream turbines on the flow and sediment transport in the Muskeget channel. The impacts were minor at that particular site due to low levels of extraction.

Williams et al. (2010) modelled a stream turbine using real site data from the Bristol Channel. Two model simulations were carried out illustrating different bathymetries. One had a flat bed and the other had a defined bathymetry obtained from site measurement. It was observed that flat beds can be used when the nature of a channel bed is fairly uniform. This becomes favoured as it simplifies mesh creation and computational time. Whereas, non-uniform beds, the wake behaviour is bound to be misinterpreted. Non-uniform beds will cause alterations to the vertical velocity profile which will also affect the performance of the turbine and the wake characteristics.

With all these findings from the studies mentioned above, it becomes important to understand the direct influence of a single turbine on bed shear stresses in more detail.

2.4.5 Blockage Ratio

The blockage ratio is the proportion of turbine area to that of a channel cross-section. Different ratios have different effects on flow dynamics, turbulence and power extraction due to the boundary limitation. It is very important to recognise blockage ratios in streams and channels in order to be able to predict the impacts on wake and surroundings, i.e., floor beds and surface fluctuations, and in further studies to provide assistance with power potential estimations. In many studies where blockage ratio impacts were investigated, the impacts in terms of turbine performance and loadings were always the focus, e.g., Takafumi and Willden (2012), Consul et al. (2013) and Kolekar (2015).

It was found that the higher the blockage ratio, the higher the coefficients of power and thrust. Not many researchers have looked into the impact of blockage on wake

characteristics. Consul et al. (2013) conducted an experiment to assess the initial expansion of wake under different blockage conditions. The wake expansion was measured using quantitative dye visualization. It was found that a blockage condition of 25% led to a narrower wake expansion of 50% when compared to that of a 10% blockage condition.

The influence of blockage is also visualised on the tip vortex behaviour. Patil (2008) investigated the influence of different blockage ratios on wakes created from a square cylinder. Results indicate that in higher blockage conditions the velocity of flow bypassing the cylinder increases. On the other hand, in front and behind the cylinder, the flow velocity decreases, showing negative values due to flow recirculation. Griffith et al. (2004) modelled the blockage effect on flow between flat plates. When the blockage ratio was smaller than 0.5, flow separation occurred and when the blockage ratio exceeded 0.5, vortex shedding and unusual patterns occurred.

It is still not clear from literature how the blockage effect would influence the velocity and turbulence distribution profiles, in particular behind a turbine, or how these profiles influence the bed layer when a turbine is employed. Detailed description of wake characteristics, flow path lines and differing magnitudes are yet to be presented. A quantitative analysis will highlight the significance of blockage on wake behaviour and the surrounding environment.

2.4.6 Yaw Angle

In general, tidal currents travel in complex patterns depending on the time of day. The flow misalignment with the turbine will cause yawing loads that create a moment on the rotor, enforcing its realignment to the mean flow direction. However, Hansen (1992) suggested there are other factors that may also cause yawing loads, such as mass, pitch and cyclic pitch imbalances of the turbine, which could be avoided by faultless turbine manufacturing.

The inclusions of yawing flows add complications to the hydrodynamics nature which researches tend to avoid by simplifying flow simulations to unidirectional alone (1D). In many previous studies, flows have been set to strike turbine axes at perpendicular angles. However, Galloway (2014) conducted an experiment using a 1:20th scale turbine in a large towing tank. The investigation looked into the combined effects of yaw and waves on a

turbine. It was found that the maximum bending moment on blades occurred when the flow was at a yawing angle.

Furthermore, the applied load on the turbine blades for a yawed turbine were smaller when compared to the loads applied from waves and, therefore, it was recommended not to include them when waves were present as poor loading predictions would be encountered. He also found in this investigation that power extraction and thrust coefficients were reduced when the flow was at yaw angles.

Bellonim (2013) studies the impact of yawing inflows on three different types of turbines one of which is a horizontal axis turbine. Results suggest that the performance of the turbine reduces with increasing angle of yaw. When the flow collides with the turbine, asymmetric loading distribution appears on the rotor. This asymmetry leads cyclic loads to increase, resulting in higher stresses on the rotor.

Furthermore, a yawing angle of flow would neither cause significant flow separations nor associated drag forces that would affect the efficiency of the channel, whereas for other turbine types such as ducted turbines that might not be the case. Yawing flows could cause complications when an array of turbines is installed.

Blanco (2009) investigated the interaction of multiple turbines for different yaw angles. Three turbines were arranged with one turbine at the front followed by the other. Their performance within the array dropped due to the interaction of the first turbine's wake with subsequent turbines. This means when arranging turbines, it is necessary to consider yaw angle impacts on wake interactions.

It is still not clear from literature that turbine yaws influence the wake, including any wake expansion deflections, velocity deflection, turbulence and vortex profile change downstream. In addition, the impacts on bed shear stress and the free surface elevation also need to be assessed.

2.4.7 Background Turbulence

Turbulence intensity in the background of a flow is an important factor that influences the wake behaviour. Milne et al. (2013) measured the turbulence intensities at a fixed point 5m above the channel bed of the Sound of Islay, UK. The measurements were taken for two complete near spring tidal cycles.

They found that turbulence intensities almost reached 12-13% during non-slack flows varying slightly during ebb and flood tides. With the presence of tidal stream devices, turbulence intensity becomes a critical parameter that influences diffusivity and mixing between wake and free stream. Maganga et al. (2010b) conducted an experiment to investigate the impact of flow properties on the wake structure, employing a three-bladed 0.7m turbine in a free surface circulating tank. Two inflow velocities with different ambient turbulent intensities were produced to investigate the wake characteristics. It found that the wake velocity recovered faster when the inlet turbulence was higher due to enhanced fluid mixing (diffusivity). It was also found that it causes the wake to be narrower.

These results suggest that it is important to understand the influences of not only background turbulence on the wake but also turbine-generated turbulence on the background turbulence. This relation should be tested under realistic conditions of field scale, and quantified.

2.4.8 Elevation

Malki et al. (2013) measured the velocity profile for different turbine immersions to explain wake characteristics. Two different immersions where used, shallow and deep (H=0.15m & 0.44m respectively). The CFD model was validated against measurements collected from a tow tank of 0.37m width, 1.8m depth and 60m length. The turbine had a diameter of 0.1m with a nose of 1m from head to tail (Figure 2-5).

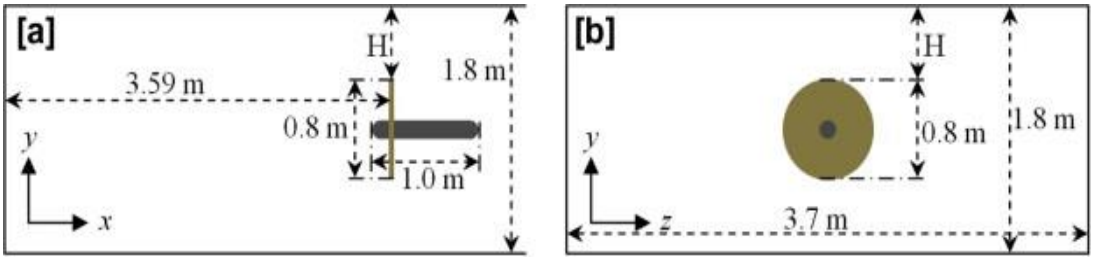

Figure 2-5 – Description of experimental set up [a] side view [b] upstream view (after Malki et al. 2013).

When the turbine was located closer to the free surface (H=0.15), the wake growth limit was constrained along the upper verge of the wake. The symmetry profile, however, remained unaffected by this expansion limitation. When the turbine was located in deep water, the observations indicated similar effects. A reason for this is because a free surface feature was absent, which meant the total flow rate was identical in both cases. Adamaski (2013) tested the impact of turbine elevation on both the free surface and wake. She found that the turbine elevation did not change the average surface drop but caused stronger surface fluctuations when the turbine was closer to the surface. She also stated that the wake length was directly affected by turbine elevation as it showed slower recovery when nearer to the surface. This is due to the lower momentum fluid experienced near the surface.

Turbine elevation is an important factor that influences the turbine wake. In field scales, it would be more realistic to situate a turbine close to the bed rather than the free surface. This would also mean bed shear stresses will be directly influenced by the turbine elevation.

2.5 - Numerical Modelling

Is a method that uses computer techniques to replicate a physical problem by reproducing their processes. This is completed by calculations implemented by a program that solves mathematical models that interpolate scientific theories.

2.5.1 Solvers

This study will implement a software package ANSYS FLUENT to numerically analyse the physics of flow behind a turbine. Computational Fluid Dynamics (CFD) is one of the favoured approaches to resolving the details of flow. The finite volume method (FVM) is used for discretising partial differential equations in the form of algebraic equations, using small controlled volumes bordering each node point defined by the mesh. However, different methods in solving the spatial and temporal discretisation, turbulence generation and dissipation and, more importantly, how to represent tidal turbine in the model, will result in different levels of accuracy. The selection of model approaches therefore needs to take these different aspects into account and will be explained in Chapter 3.

2.5.2 Mesh

In turbines simulations 1, 2 and 3 dimensional models have been developed. These different dimensional types influence the meshing systems in the model. Meshing grids are classified into three types, e.g., structured, unstructured and hybrid mesh. A structured mesh is regularly connected, using quadrilateral (2D) or hexahedra (3D). It is known for its high space efficiency (Castillo, 1991) i.e., storage arrangement and high resolution, and has been used in turbine models (Malki et al., 2013). An unstructured grid is irregularly connected, usually using triangles (2D) and tetrahedral (3D). It is known for space inefficiency and is used in complex geometries (Mavriplis, 1996). This grid type has been commonly used for turbines e.g., O'Doherty et al. (2009) and Jones et al. (2013). A hybrid grid is simply a mixture of structured and unstructured grids. They are very useful when complicated geometries are involved. Papadogiannis et al. (2014) adopted this type of mesh to simulate the Francis turbine. They used hybrid mesh when adopting large eddy simulation of a high pressure turbine.

The number of mesh points is another critical aspect that should be considered. Adopting real turbine geometries requires the use of high mesh counts; typical counts always exceed a million.

2.5.3 Turbulence Closure

There are a number of models can be found in literature for simulating flow around turbines. In this section, all turbulence models will be reviewed in a descending order, beginning with the strongest model for turbulence capturing the Direct Numerical Simulation (DNS). This type model resolves all velocity fluctuations and therefore is computationally expensive and hence is not considered in the present study. Large Eddy Simulation (LES) is the next technique that was proposed by Smagorinsky (1963) and is similarly expensive. It directly resolves eddies with scale larger than mesh size and accounts for the smaller eddies as a sub-grid process and hence reduces computational costs.

The next option solves the Reynolds averaged Navier-Stokes (RANS) equations with a suitable model for turbulent quantities. The RANS equations govern the transport of the time-averaged flow quantities, with less computational costs in comparison with the DNS and LES. Two different models are used in the RANS type of modelling, e.g. the Eddy Viscosity Model (EVM) and Reynolds Stress Models (RSM). In the RSM, the Reynolds stresses derived from the RANS equations are directly solved, taking into account complex properties such as anisotropy.

However, the number of transport equations involved is high (7 equations). EVM, on the other hand, offers a lower order closure that assumes isotropic turbulences. They are divided into sub categories depending on the number of transport equations and linearity state. Starting with the nonlinear model ($\overline{v^2} - f$), which uses velocity to estimate eddy viscosity, the function f can model the anisotropic effect of the wall on the flow. For linear EVMs, common models are $k - \varepsilon$ and $k - \omega$. They are two-equation models that consider convection and diffusion. Taking into account computational costs and time consumption, it is acceptable to use the second approach (RANS).

Harrison (2010) developed a model that used a shear stress transport (SST) $k - \omega$ turbulence model to validate against experimental results conducted by Myers and Bahaj (2010). The model was able to capture the flow turbulence accurately in the far wake with minor discrepancies in the near wake due to turbine related issues. McSherry et al. (2011) modelled the turbulences created from a tidal turbine in the near field. Part of this study was to compare the accuracy of three turbulence models, $k - \varepsilon$, $k - \omega$ and RSM. Results showed that both

$k-\omega$ and RSM were able to capture the turbine performance as well as the flow profiles accurately, however, $k-\varepsilon$ showed under-prediction. Gretton et al. (2009) carried out a comparison on modelling the impact of a turbine wing under a wide range of engineering tests and found that SST $k-\omega$ produces high accuracy in terms of lift and stall characteristics. Overall in this data, the SST $k-\omega$ has been widely used by many other researchers that investigate turbine performance and flow behaviours e.g. McSherry et al (2011) and Gretton et al. (2009). The SST $k-\omega$ turbulence model is suitable when used in inner boundary layers due to its capability to formulate the entire way to the wall via the viscous sub layer. This means that the SST $k-\omega$ requires no extra damping function when low Reynold number regimes are employed. The model is able to change to $k-\varepsilon$ when in the free stream, which is a better approach that avoids extra $k-\omega$ sensitivity to inlet stream turbulence properties.

Based on above considerations, in this study, the SST $k-\omega$ model is adopted for the turbulence modelling due to its acceptable accuracy in near and far wake regions and for its ability to capture boundary layer induced turbulence and flow separation in hostile pressure gradients (Menter et al., 2003). It is also noted that the SST $k-\omega$ turbulence model is the appropriate choice to take forward in this study, where computational resources are limited. The SST combines $k-\varepsilon$ and $k-\omega$, since $k-\varepsilon$ is good to use for initial predictions. SST modified turbulent viscosity formulation to account for the transport effects of the principal turbulent shear stress

2.5.4 Representation of Turbine

There are many different numerical methods available for simulating the rotational behaviour of a turbine. These methods differ in terms of complexity and accuracy. In summary, three different numerical methods are employed: Single/Multi Reference Frame (SRF/MRF), Virtual Blade Model (VBM) and Actuator Disk Model (ADM). Mozafari (2010) illustrated these three numerical approaches when simulating the dynamics of flow around and behind a turbine.

In all cases, the flows were steady and did not take into account a two phase channel (air and water). In this section, a comprehensive comparison in terms of accuracy, computational

costs and limitations for each method is described. Table 2-3 below provides an initial comparison of some important aspects of the three methods.

Table 2-3 – Comparison between different HATT representation methods.

	ADM	**VBM**	**MRF/SRF**
Geometry	Disk	Disk	Turbine
Blades	Non	Virtual	Actual
Motion	Stationary	Rotatory	Rotatory
Comparative Cost	Cheap	Cheap-Moderate	Expensive

2.5.3.1 Moving Reference Frame (MRF)

MRF presents a turbine with actual blade geometry being explicitly described. It computes in the rotating frame of reference, with velocity and fluxes relative to the rotating reference frame, using Cartesian components. These methods are highly accurate and are capable of capturing flow details not only around and after the turbine but also right in front of it.

However, they have their drawbacks in terms of high computational costs and limitations in some usages of boundary conditions. Jones et al. (2013) recommended that at least 200 mesh nodes on each blade span are needed. The turbine was created from 1.75 million cells excluding the channel. O'Doherty et al. (2009) used 1.25 million cells to represent the turbine blades, in addition to ninety thousand for the channel. Furthermore, Craft et al. (2006) developed a model with a total of 4.8 million mesh cells.

There are many researches that have followed this approach when studying turbines. For example, Jones (2009) has assessed a tidal turbine in a high velocity shear environment using a MRF approach. He calibrated his model with the experimental data of Tedds et al. (2011). A singular turbine was used to reduce the total computational costs. Jones et al. (2013) particularly examined the performance of a turbine in terms of torque, power and thrust which required actual blades. They investigated the impacts of various velocity profiles on the performance of a turbine and also considered the impact of different stanchion shapes on

wake. MRF and SRF methods are clearly appropriate in studying loadings and power extractions of turbines.

In the present study however, the details of physical processes behind turbines, including velocity, turbulent kinetic energy and influences on bed shear stresses are investigated. Therefore, the accurate representation of each individual blade becomes less crucial and hence MRF/SRF methods are not important in this study. Alternative representations should be considered given its high computational costs.

2.5.3.2 Actuator Disk Model (ADM)

In the Actuator Disk Model (ADM), the geometry of a porous disk is used to represent a turbine sweeping area. It is a simple method that is computationally cheap and produces faster convergence. Gant and Stallard (2008) modelled a turbine in FLUENT using a porous disk and this model only required total of 700,000 mesh nodes. Williams et al. (2010) used a porous disk to model a turbine under real site data, using in total 350,000 mesh elements in the simulation.

However, ADM demonstrates poor accuracy at near wake regions but then acceptable accuracy at far wake regions as is seen in many studies e.g. Mozafari (2010). This method does not represent the operation of a real turbine; instead, it replaces it with a porous medium that will cause a pressure jump. Due to the absences of rotational motion, this method produces poor angular velocity measurements and therefore is not a strong method for detailed wake characterisation.

Many researchers have favoured this method for its simplicity and fast convergence. The flow velocity is always dominant in the streamwise direction and overrides the flow in the cross stream and vertical directions. Consequently, it is applicable when it is safe to neglect those weak flows and ignore the rotational movement.

Previous studies examined the suitability of the numerical actuator disc approach for modelling the flow behind a tidal stream turbine (Harrison et al., 2009). The far wake of a single turbine was examined. Velocity profiles matched reasonably well with measured data but the turbulent kinetic energy was under predicted.

Sun et al. (2008) applied a CFD model to simulate the flow around an actuator disk in order to examine the flow pattern in the near region. Both 2D and 3D simulations were employed to compare with experimental data. The computed results were poor in comparison with measured data on the area immediately adjacent to the turbine. The accuracy of results gradually improved moving further downstream (far wake region).

The ADM approach has also been extended for simulating a small farm of turbines (Batten et al., 2006). Comparing with other methods, it is clearly favoured in large multiple-turbine modelling due to its lower computational cost and faster convergence. However, it is also recognised by many studies that lacking the detailed representation of turbine motion makes it less accurate in the near wake region

In general, ADM is not the optimal method for simulating near wakes, and it has been shown as such by many researchers (Mozafari, 2010). The benefits of using the Actuator Disk Method are that it requires low computational costs, adopts a simple theory and hence provides fast convergence. ADM is useful where long-scale flow effects are considered, such as in array instabilities (MacLeod and Bryden, 2002).

In this study, the characterisation of the wake in the near region is important. ADM will not be the most appropriate method to employ, however; it will be tested and compared with another method (VBM).

2.5.3.3 Virtual Blade Model (VBM)

The Virtual Blade Model takes advantage of both ADM and MRF methods with acceptable costs. The turbine geometry is represented by virtual blades across the swiped area of a porous disk. It simulates the effect of the rotating blades on the fluid through a body force in the x, y and z direction acting along the blades inside a disk.

In comparison with SRF/MRF, it is able to replicate the rotation movement with less computational cost. VBM does not represent the actual blades. Instead, it takes into account their specifications and simulates the motion of fluid surrounding the blades. The effect of the blade on the flow is temporally averaged over the course of an entire rotation cycle and applied along the whole disk. Such an approach can simulate near wake regions from one

turbine onwards. It provides a compromise solution where reasonably accurate results can be achieved when assessing turbine performance and capturing near wake processes. VBM has proven its flexibility by simulating wind turbines (Makridis et al., 2009), tidal turbines (Mozafari, 2010) and helicopter rotors (Michael, 2005).

These studies show that VBM is a method that can be applied in both water and air. It can be applied to a realistic domain that is influenced by the effects of channel bed and free surface boundaries. Unlike more complicated models such as Sliding Mesh, SRF and MRF, VBM does not require high computational costs and yet the level of accuracy is acceptable.

One of the practical attempts in applying VBM to a turbine was demonstrated by Mozafari (2010), in which three different methods, SRF, VBM and ADM were compared. He built a cylindrical shaped domain which consisted of one single turbine positioned at the centre. The results were validated against the well characterized two-blade wind turbine NREL-VI. He emphasised that the VBM method is an acceptable choice which affords the advantages of acceptable accuracy and low time consumption.

Batten et al (2013) investigated the accuracy of VBM for predicting the wake behind a tidal turbine. He found, when comparing measured data at the turbine centreline, that VBM was capable of predicting the velocity variation up to 94% accuracy, which suggests that VBM is an excellent approach to predicting turbine wake.

Adamaski (2013) used the VBM method to assess the impact of turbine positioning on the turbine-affected region and found slower recovery when the turbine is closer to the surface. She also assessed the turbine impact on the free surface elevation.

VBM is also a suitable method for predicting the performance and impacts of an array of turbines. Harrison et al. (2010) compared computed results of an infinitely wide array of turbines with five rows. He was able to predict the flow field as well as the performance of each turbine, and discovered higher wake velocity recovery within an array.

Turnock et al. (2011) modelled turbine wakes as an implement for analysing the power capture of arrays of turbines. He found that small lateral separation and large longitudinal separation is the most effective combination.

Chime et al. (2014) investigated the likelihood of using a turbine to control the flow and produce energy in a constructed channel by replacing the sluice gates. ADM and VBM methods were employed using ANSYS Fluent and it was found that power dissipated from the flow was under predicted by both methods, at 30% and 10% respectively. In addition, it was found that surface height downstream was lower when the blockage ratio was higher.

Batten and Bahaj (2006) found that VBM can be used as a tool for designing and optimising energy output with tidal data. They demonstrated possible high load factors that could supply better load to the grid. Furthermore, Batten et al. (2008) predicted the hydrodynamic performance of a large diameter turbine in the form of power and thrust curves. The same rotor was assessed on possible cavitation if the rotor tip was immersed. The study concentrated on the aspects of the rotor and how velocity profiles would influence blade loading

The Virtual Blade Model is a compromise method that has been certified by many researchers. It is a robust method that can be adapted in real boundary conditions. However, the main disadvantage of this method is that the effect of the blade on the flow is temporally averaged over the course of an entire rotation cycle; this leads to poor detail in capturing of the flow around the blade. In addition, the real blade geometry is not presented and only the blade specification detail is used. Therefore, it is not suitable in areas very close to the turbine ($x/D < 1$).

In this study, the VBM method will be used to carry out various investigations such as blockage, yaw angle, background turbulence and wave effects. The present review examines several aspects related to tidal stream applications, including the potential sites around UK, the physical processes around typical stream sites, the understanding of the effects of stream devices on the surrounding environment and modelling techniques developed in the literature.

2.6 Conclusions

Based on these reviews, the following conclusions can be drawn:

Firstly, the common aspect of all above mentioned experiments and computations is the typical turbine setup of a flow at an angle normal to the turbine, steadiness of the flow and, in some cases, the absences of water free surface. However, in a natural marine environment, it is rare to see such simple conditions. More often, flow conditions will change across a tide cycle. The tidal flows therefore always strike a turbine from different yaw angles rather than just perpendicular to the front face of a turbine. It is advisable to assess the wake behaviour and the implications of the surrounding area when water strikes at a yawing angle. This application has not been clearly considered previously for tidal turbines and yet the impacts are unexplained.

In previous studies, large farms were considered for assessing environmental impacts. As a result, intermediate approaches of 2D models were employed to carry out the simulations. These studies focused on bed shear stresses in the far field and their influence on sediment transport but by not considering the near field and therefore ignore the small details of turbines. It is important to recognise the environmental impacts in the near field as tidal turbines are occasionally employed at near shore. There is very little research into how turbine operations would affect the bed shear stress when exposed to steady and unsteady flow conditions.

In this study, bed shear stresses will be assessed under several stream and turbine conditions in order to show the influence of tidal turbines on the bed. An improved approach modifying a porous disk with a hub feature is adopted with both ADM and VBM methods. The model predictions are expected to improve especially for the near wake region. Introducing waves in the simulation challenges both FLUENT 14.5 and VBM methods in terms of their applicability and accuracy.

Secondly, in those entire potential stream sites, strong waves are a common feature. Waves travel in different directions in reference with the current and influence the flow dynamics in the stream considerably (Norris and Droniou, 2007). The impact of a turbine on flow behaviour and wave structure is yet unclear. Moreover, the impact of wave kinematics on the turbine-affected region across different phases is also not clear.

Thirdly, there are many gaps in knowledge on how turbine parameters could influence flow processes and bed shear stress at both near and far wake regions, such as blockage ratio and background turbulence. It is not clear how the wake will respond to different blockage ratios when the water depths are the same but the width of the stream differs. It is also not evident from literature how background turbulence will react to turbine-induced turbulences, and vice versa. Understanding the physical processes behind a turbine can be difficult.

Fourthly, numerical methods that represent turbine operations are different in strengths and limitations. However, very few studies consider the free surface effects on the hydrodynamics. The surface wave dynamics are also not investigated systematically, particularly their effects coupling with turbine operation and effects on the surrounding environment. Among the three commonly used approaches, ADM, VBM and SRF, the VBM clearly has advantages in computation efficiency over the others. However, it has not been systematically used under free surface and under surface waves with current conditions.

2.7 References

Adamaski, S. J. (2013) *Numerical Modelling of the Effects of a Free Surface on the Operating Characteristics of Marine Hydrokinetic Turbines*, Masters. Thesis, University of Washington.

Ahmadian, R. and Falconer, R. A. (2012) Assessment of array shape of tidal stream turbines on hydro-environmental impacts and power output. *Journal of Renewable Energy*, vol. (44), pp.318-327.

Babanin, A. V. (2006) On a wave-induced turbulence and a wave mixed upper ocean layer. Geophysical Research. Letter, 33, L20605, doi:10.1029/2006GL027308

Babanin, A. V. (2011) *Breaking and dissipation of ocean surface waves*. Cambridge, UK: Cambridge University Press.

Bahaj, A.S., Meyers, L. E., Thomsan, M. D. and Jorge, N. (2007) Characterising the wake of horizontal axis marine current turbines, *Proceedings of the 7th European wave and tidal energy conference,* Porto, Portugal.

Batten, W. M. J., Harrison, M. E. and Bahaj, A. S. (2013) Accuracy of the actuator disc-RANS approach for predicting the performance and wake of tidal turbines. *Philosophical transactions of the royal society*, vol. (371), Issue: 1985. pp.1-15.

Batten, W.M.J. and Bahaj, A.S. (2006) CFD simulation of a small farm of horizontal axis marine current turbines. In, Sayigh, A.A.M. (eds.), *World Renewable Energy Congress 2006. World Renewable Energy Congress (WREC-IX)*, Elsevier Science.

Batten, W.M.J., Bahaj, A.S., Molland, A.F. and Chaplin, J.R. (2008) The prediction of the hydrodynamic performance of marine current turbines. *Journal of Renewable Energy*, vol. (33), Issue: 5. pp.1085-1096.

Bellonim, C. (2013) *Hydrodynamics of Ducted and Open-Centre Tidal Turbines*, PhD. Thesis, University of Oxford.

BERR (Department for Business Enterprise & Regulatory Reform), (2008) *Atlas of UK Marine Renewable Energy Resource: A Strategic Environmental Assessment Report.* UK: ABPmer, The Met Office and Proudman Oceanographic Laboratory.

Black and Veatch (2005) Phase 2 UK tidal stream energy assessment. The Carbon Trust, http://www.lunarenergy.co.uk/Userimages/PhaseIITidalStreamResourceReport.pdf [accessed 21 June 2014].

Blanco, J. M. (2009) *Investigation of Turbine Interactions in a tidal device*, MSc. Thesis, Cranfield University.

Brevik, I. and Aas, B. (1980) Flume experiment on waves and currents. I. Rippled bed. *Coastal Engineering*, Elsevier Scientific. Netherland: vol. (3), pp.149-177.

Bryden, I.G. and Couch, S.J. (2005) ME1—marine energy extraction: tidal resource analysis. Renewable Energy, vol. (31), issue: 2. pp.133-139. http://www.sciencedirect.com/science/article/pii/S096014810500220X [accessed 01 Sep 2014].

Buckland, H. (2014) *Combined current, wave and turbulent flows and their effects on tidal energy devices*, Swansea University.

Carbon Trust (2011) *UK Tidal Current Resource and Economics Study.* http://www.marineenergypembrokeshire.co.uk/wp-content/uploads/2010/03/CarbonTrustMarineResourceJune2011.pdf [accessed 18 Oct 2016]

Castillo, J.E. (1991) *Mathematical aspects of grid Generation.* 8 edn. San Diego State University, San Diego, California.

Chanson, H. (1999) Boundary Shear Stress Measurements Below Free-Surface Standing Waves: Application to Bed Form Processes. The University of Queensland, Australia. Available from: http://staff.civil.uq.edu.au/h.chanson/reprints/iahr99_2.pdf [accessed 20 Sep 2015].

Chime, A. H. and Malte, P. C. (2014) Hydrokinetic Turbine at High Blockage Ratio. *Proceedings of the 2nd Marine Energy Technology Symposium.* Seattle, Washington. Available from: https://depts.washington.edu/nnmrec/docs/METS_draft_Hoseyni%20Chime.pdf [accessed 5 April 2015].

Consul, C.A., Willden, R. H. J. and McIntosh, S. C. (2011) An investigation of the influence of free surface effects on the hydrodynamic performance of marine cross-flow turbines, *Proceeding of Euro Wave Tidal Energy Conference*.

Consul, C. A., Willden, R. H. J. and McIntosh, S. C. (2013) Blockage effects on the hydrodynamic performance of a marine cross-flow turbine, CrossMark. vol. (371), Issue: 1985. Available from: http://rsta.royalsocietypublishing.org/content/371/1985/20120299 [accessed 3 July 2014].

Couch, S. J. and Bryden, I. G. (2007) Large-scale physical response of the tidal system to energy extraction and its significance for informing environmental and ecological impact assessment, *in IEEE/OES OCeans '07 Marine Challenges: Coastline to Deep Sea.*, pp.5.

Craft, T. J., Gerasimov, A. V., Launder, B. E. and Robinson, C. M. E. (2006) A computational study of the near-field generation and decay of wingtip vortices. *International Journal of Heat and Fluid Flow*, vol. (27), Issue: 4. pp.684-695.

Crown Estate (2012) *UK Wave and Tidal Key Resource Areas Project, summary report.* Version 2.

Elert, G. (2015) The Physics Hyper Textbook. Available from: http://physics.info/turbulence/ [accessed 4 April, 2016].

Fujita Research, (2000) Wave and tidal power [Homepage of Fujita Corporation], [Online]. Available: http://www.fujitaresearch.com/reports/tidalpower.html [accessed 15 March, 2012].

Gant, S. and Stallard. T. (2008) Modelling a Tidal Turbine in Unsteady Flow. *Proceedings of the Eighteenth International Offshore and Polar Engineering Conference,* Canada. pp.473-476.

Gretton, G. I., Bruce, T. and Ingram, D. M. (2009) Hydrodynamic modelling of a vertical axis tidal current turbine using CFD, *In the 8th European Wave and Tidal Energy Conference,* Uppsala, Sweden.

Griffith. M.D., Hourigan, K. and Thompson, M. C. (2004) Numerically Modelling Blockage Effects on the Flow Between Flat Plates, *15th Australasian Fluid Mechanics Conference*, Sydney, Australia.

Hakim, R., Cowles, W. and Churchill, H. (2013) The Impact of Tidal Stream Turbines on Circulation and Sediment Transport in Muskeget Channel, MA. *Marine Technology Society Journal*, vol. (47), Issue: 15. pp.122-136.

Hansen, A. C. (1992) Yaw dynamics of Horizontal Axis Wind Turbines: Final report. *National Renewable Energy Laboratory,* Golden, CO.

Harrison, M. E., Batten, W. M. J. and Bahaj, A. S. (2010) A blade element actuator disc approach applied to tidal stream turbines, *OCEANS 2010*, MTS/IEEE SEATTLE. pp.1-8. Available from: http://ieeexplore.ieee.org/xpl/articleDetails.jsp?arnumber=5664564 [accessed 17 May 2014]

Harrison, M. E., Batten, W. M. J., Myers, L. E. and Bahaj, A. S. (2010) Comparison between CFD simulations and experiments for predicting the far wake of horizontal axis tidal turbines. *Renewable Power Generation, IET*, vol. (4), Issue: 6. pp.613-627.

Harrison, M. E., Batten, W. M. J., Myers, L. E. and Bahaj, A. S. (2009) A comparison between CFD simulations and experiments for predicting the far wake of horizontal axis tidal turbines, *Renewable Power Generation, IET,* vol. (4), Issue: 6. pp.613-627.

Hedges, T. S. (1987) Combination of waves and current: an introduction, *In Proceedings to the Institute of Civil Engineers*, vol. (Part 1), pp.567-585.

Henriques, T. A., Tedds, S. C., Botsari, A., Najafian, G., Hedges, T. S., Sutcliffe, C. J., Owen, I. and Poole, R. J. (2014) The effects of wave-current interaction on the performance of a model horizontal axis tidal turbine. *International Journal of Marine Energy,* vol. (8), pp.17-35.

Jones, A. M. (2009) *Performance assessment of a horizontal axis tidal turbine in a high velocity shear environment*, PhD. Thesis, Cardiff University.

Jones, A. M., O'Doherty, D. M., Morris, C.E. and O'Doherty, T. (2013) Influence of a velocity profile & support structure on tidal stream turbine performance. *Journal of Renewable Energy,* vol. (52), pp.23-30.

Jordan, L.B., Simmons, S., McLelland, S., Murphy, B., Parsons, D. and Vybulkova, L. (2015) The Impact of Tidal Stream Turbines on 3D Flow and Bed Shear Stress Measured with Particle Image Velocimetry in a Laboratory Flume, *Proceedings of the 11th European Wave and Tidal Energy Conference (EWTEC),* Nantes, France.

Kemp, P. H. and Simon's, R. R. (1983) The interaction of waves and a turbulent current: waves propagating against the current. *Journal of Fluid Mechanics,* Issue: 130. pp.73 - 89.

Kolekar, N. and Banerjee, A. (2015) Performance characterization and placement of a marine hydrokinetic turbine in a tidal channel under boundary proximity and blockage effects. *Journal of Applied Energy,* vol. (148), pp.121-133.

Komen, G. I., Cavaleri, L., Donelan, M., Hasselmann, K., Hasselmann, S. and Janssen, P. A. E. M. (1994) Dynamics and Modelling of Ocean Waves. Cambridge University Press, pp.554.

Kudryavtsev, V. N. and Makin, V. K. (2002) Coupled dynamics of short waves and the airflow over long surface waves. Journal of Geophysical Research, vol. (107), Issue: C12. pp. 2-13, doi:10.1029/2001JC001251.

Lust, E.E., Luksa, L., Karen, A. F., Walker, J. M. and Benthem, M. C. V. (2013) The influence of surface gravity waves on marine current turbine performance. *International Journal of Marine Energy,* vol. (3–4), pp.27-40.

MacLeod, A.J., Barnes, S., Rados, K. G. and Bryden, I. G. (2002) Wake effects in tidal current turbine farms, *MAREC International Conference on Marine Renewable Energy,* Institute of Marine Engineering, Science and Technology. Newcastle upon Tyne, United Kingdom. pp.49-53.

Maganga, F., Pinon, G., Germain., G. and Rivoalen, E. (2010a) Wake properties characterisation of marine current turbines. *3rd International Conference on Ocean Energy,* Bilbao.

Maganga, F., Germain, G., King, J., Pinon, G. and Rivoalen, E. (2010b) Experimental characterisation of flow effects on marine current turbine behaviour and on its wake properties. *Renewable Power Generation, IET,* vol. (4), Issue: 6. pp.498-509.

Makridis, A. and Chick, J. (2009) CFD Modelling of the wake interactions of two wind turbines on a Gaussian hill. *In 5th European & African Conference on Wind Engineering,* Florence, Italy.

Malki, R., Masters, I., Williams, A. J. and Croft, T.N. (2011) The variation in wake of a tidal stream turbine with flow velocities. *International Conference on Computational Methods in Marine Engineering,* vol. (29), pp.137-148.

Malki, R., Williams, A. J., Croft, T. N., Togneri, M. and I. Masters. (2013) A coupled blade element momentum – Computational fluid dynamics model for evaluating tidal stream turbine performance. *Journal of Applied Mathematical Modelling,* vol. (37), Issue: 5. pp.3006-3020.

Marquis, G. A., Roy, A. G. and Rice, S. P. (2009) Exploring the impact of flow surface waves on turbulence and bedload transport rates in gravel-bed rivers. American Geophysical Union, Fall Meeting 2009, abstract #EP23B-0640.

Masters, I., Williams, A., Croft, T., Togneri, M., Edmunds, M., Zangiabadi, E., Fairley I. and Karunarathna, H. (2015) A Comparison of Numerical Modelling Techniques for Tidal Stream Turbine Analysis. *Article in Journal of Energies*, vol. (8), pp.7833-7853.

Mavriplis, D. J. (1996) *Mesh Generation and adaptivity for complex geometries and flows.* Handbook of Computational Fluid Mechanics London: Academic Press.417-459. Avaliable from: http://dx.doi.org/10.1016/B978-012553010-1/50000-19780125530101 [accessed 21 June 2013].

McSherry, R., Grimwade, J., Jones, I., Mathias, S., Wells, A., Mateus, A. (2011) 3D CFD modelling of tidal turbine performance with validation against laboratory experiments, *9th European Wave and Tidal Energy Conference,* University of Southampton, UK.

Menter, F. R., Kuntz, M. and Langtry, R. (2003) Ten Years of Industrial Experience with the SST Turbulence Model. *Proceedings of Turbulence, Heat and Mass Transfer 4*, Begell House, Inc.

Michael, R. (2005) Unstructured, Multiplex Rotor Source Model with Thrust and Moment Trimming - Fluent's VBM Model. *23rd AIAA Applied Aerodynamics Conference, Fluid Dynamics and Co-located Conferences,* FLUENT, INC.

Milne, I.A., Sharma, R. N., Flay, R. G. J. and Bickerton, S. (2013) Characteristics of the turbulence in the flow at a tidal stream power site. *Journal of Philosophical Transactions of the Royal Society A,* vol. (371), Issue:1985.

Mozafari, A. T. J. (2010) *Numerical modelling of tidal turbines: Methodology Development and Potential Physical Environmental Effects*, MSc. Thesis, University of Washington.

Myers, L. and Bahaj, A. S. (2009) Near wake properties of horizontal axis marine current turbines. *Proceedings of the 8th European Wave and Tidal Energy Conference,* Uppsala, Sweden. pp.8.

Myers, L. and Bahaj, A. S. (2007) Wake studies of a 1/30th scale horizontal axis marine current turbine. *Journal of Ocean Engineering,* vol. (34), Issue: 5–6. pp.758-762.

Myers, L.E. and Bahaj, A.S. (2010) Experimental analysis of the flow field around horizontal axis tidal turbines by use of scale mesh disk rotor simulators. *Journal of Ocean Engineering,* vol. (37), Issue: 2-3. pp.218-227.

Neill, S. P., Litt, E. J., Couch, S. J. and Davies, A. G. (2009a) The impact of tidal stream turbines on large-scale sediment dynamics. *Journal of Renewable Energy,* vol. (34), Issue: 12. pp.2803-2812.

Neill, S.P., Litt, E.J., Couch, S.J. and Davies, A.G. (2009b) The impact of tidal stream turbines on large-scale sediment dynamics. *Journal of Renewable Energy,* vol. (34), Issue: 12. pp.2803-2812.

Norris, J. V. and Droniou, E. (2007) Update on EMEC activities, resource description and characterisation of wave-induced velocities in a tidal flow, *7th European Wave and Tidal Energy Conference,* Poto, Portugal.

O'Doherty, T., Jones, A., O'Doherty, D. M. and Byrne, C. B. (2009) Experimental and Computational Analysis of a Model Horizontal Axis Tidal Turbine. *Proceedings of the 8th European Wave and Tidal Energy Conference.* Uppsala, Sweden. http://orca.cf.ac.uk/id/eprint/16918 [accessed 15 Feb 2015].

Olczak, A., Stallard, T. and Stansby, P. (2013) The influence of waves on tidal stream turbine wake recovery, *In 10th European Wave and Tidal Energy Conference,* Aalborg, Denmark.

Papadogiannis, D., Duchaine, F., Sicot, F. and Gicquel, L. (2014) Large Eddy Simulation of a High Pressure Turbine Stage: Effects of Sub-Grid Scale Modeling and Mesh Resolution, *Proceedings of ASME Turbo Expo 2014: Turbine Technical Conference and Exposition GT2014,* Düsseldorf, Germany vol. (2B).

Patil, P. P. and Tiwari, S. (2008) Effect of blockage ratio on wake transition for flow past square cylinder. *Journal of Fluid Dynamics Research,* vol. (40), Issue: 11–12. pp.753-778.

Rose, S., Good, A., Atcheson, M., Hamill, G., Johnstone, C., MacKinnon, P., Robinson, D., Grant, A. and Whittaker, T. (2011) Investigating experimental techniques for measurement of the downstream near wake of a tidal turbine, *Paper presented at Ninth European Wave and Tidal Energy Conference,* Southampton, United Kingdom. pp.1-5.

Roulund, A., Sumer, B. M., Fredsøe, J. and Michelsen, J. (2015) Numerical and experimental investigation of flow and scour around a circular pile. *Journal of Fluid Mechanics,* vol. (534), pp.351-401.

Shirani, E., Jafari, A. and Ashgriz, N. (2006) Turbulence Models for Flows with Free Surfaces and Interfaces. *The Journal of AIAA,* vol. (44), Issue: 7

Simon, P., Jordan, J. R. and Couch, S J. (2011) Impact of tidal stream turbines on sand bank dynamics. *World Renewable Energy Congress,* School of Ocean Sciences, Bangor University, Menai Bridge, UK 2 Institute for Energy Systems, The University of Edinburgh. UK.

Simons, R. R., Grass, T. J., Saleh, W. M. and Tehrani, M. M. (1994) Bottom shear stresses under random waves with a current superimposed. *Coastal Engineering Proceedings,* vol. (1), Issue: 24.

Simons, R., MacIver, R. and Saleh, W. (2001) Kinematics and Shear Stresses from Combined Waves and Longshore Currents in the UK Coastal Research Facility. Coastal Engineering. *Coastal Engineering Proceedings,* vol. (1), Issue: 25. pp.3481-3494.

Simons, R. R., Grass, T. J. and Mansour-Tehrani, M. (1992) Bottom shear stresses in the boundary layers under waves and currents crossing at right angles. *Coastal Engineering Proceedings,* vol. (1), Issue: 23.

Smagorinsky, J. (1963) General Circulation Experiments with the Primitive Equations. *Monthly Weather Review,* vol. (91), Issue: 3. pp.99-164.

Smith, J.W. (2011.) *Mechanics of Fluid.* 9th edn. New York, USA: Spon Press.

Sufian, S. F. and Li, M. (2014) 3D-CFD Numerical modelling of impacts from horizontal axis tidal turbines in the near region. *Coastal Engineering Proceedings,* vol. (1), Issue: 34. pp.30.

Sun, X., Chick, J. P. and Bryden. I. G. (2008) Laboratory-scale simulation of energy extraction from tidal currents. *Journal of Renewable Energy,* vol. (33), Issue: 6. pp.1267-1274.

Takafumi N. and Willden, R. H. J. (2012) Effects of 3-D channel blockage and turbulent wake mixing on the limit of power extraction by tidal turbines. *International Journal of Heat and Fluid Flow*, vol. (37). http://www.sciencedirect.com/science/article/pii/S0142727X12000653 [accessed 12 Feb 2015].

Tedds, S. C., Poole, R. J. and Owen, I. (2011) Experimental investigation of horizontal axis tidal stream turbine, *Proceedings of the 9th European Wave and Tidal Energy Conference,* Southampton, UK. http://www.see.ed.ac.uk/~shs/EWTEC%202011%20full/E [accessed 02 April 2013].

Tedds, S. C., Owen, I. and Poole, R. J. (2014) Near-wake characteristics of a model horizontal axis tidal stream turbine. *Renewable Energy,* vol. (63), pp.222-235.

Turnock, R., Phillips, A. B., Banks, J. and Nicholls, R. (2011) Modelling tidal current turbine wakes using a coupled RANS-BEMT approach as a tool for analysing power capture of arrays of turbines. *Journal of Ocean Engineering,* vol. (38), Issue: 11-12. pp.1300-1307.

Veron, F., Melville, W. K. and Lenain, L. (2009) Measurements of ocean surface turbulence and wave–turbulence interactions. *Journal of physics and oceanographic,* vol. (39), pp.2310-2323.

Williams, A. J., Croft, T. N., Masters, I. Willis, M. R. and M. Cross. (2010) Combined BEM-CFD modelling of tidal stream turbines using site data, *Proceedings of the International Conference on Renewable Energies and Power Quality,* Bilbao.

Chapter 3 – CFD model FLUENT

3.1 Introduction

In this study the CFD package ANSYS FLUENT 14.5 is used as the numerical solver for the simulation. It is known for its robustness and high accuracy when employed by researchers e.g., Mozafari (2010) and Consul (2011). It is one of the widely used codes for a range of flow modelling applications. The model is based on a finite volume solver that is used for solving incompressible flows using structured and unstructured grids. It features a set of useful models for free surface tracking. The package also consists of a range of turbulence models that have a wide range of applicability. It is well-known through parallel processing on shared-memory to help increase simulation speeds. The flow field due to turbine-flow interaction is simulated via the Reynolds Averaging Navier Stokes (RANS) equation. This chapter will illustrate the theories and governing equations relevant to the current study within ANSYS FLUENT 14.5. All routines and subroutines for solution development are described in detail. The ADM and VBM representations of the turbine provided in FLUENT with specially designed Blade Momentum Theory details are discussed in Chapter 4.

3.2 Governing Equations

3.2.1 Hydrodynamics

The mass conservation equation is given as:

$$\frac{\partial \rho}{\partial t} + \frac{\partial \rho u}{\partial x} + \frac{\partial \rho v}{\partial y} + \frac{\partial \rho w}{\partial z} = 0 \tag{3.1}$$

where ρ is density of fluid, u, v, w are the velocities along the x, y, z respectively.

The momentum conservation equation is shown below,

$$\frac{\partial}{\partial t}(pv_i) + \nabla.(\rho v_i v_j) = -\nabla p + \nabla.(\tau_{ij}) + \rho g_i + F_i \tag{3.2}$$

where p is the total pressure, ρg_i the gravitational body force and F_i is the external body force in the i direction. τ_{ij} is the stress tensor and is given by:

$$\tau_{ij} = \mu\left[(\nabla v_i + \nabla v_j) - \frac{2}{3}\nabla.v_l I\right] \tag{3.3}$$

where μ is the dynamic viscosity and I is the unit tensor. In the present study, the Volume of Fluid (VOF) approach is used to simulate free surface effects in FLUENT. This approach is based on the concept of mixture velocity.

$$\tilde{u} = \alpha u_w + (1-\alpha)u_a \tag{3.4}$$

where u_w and u_a are the flow velocity in water and air respectively and α is the fluid volume fraction. When α = 0, the cell is fully occupied by air; when α = 1, the cell is full of water and when 0 < α < 1 the cell is partly filled and encloses the interface. Once the domain is defined with the fluid phase through adapting the region of water by registering the initial water level, each cell volume is then assigned with the correct properties and variables.

The VOF model is a surface-tracking technique that solves a single set of momentum equations that share water and air volume fraction of each of the fluids in each computational cell and is tracked throughout the domain. Hence, the momentum equation becomes dependant on the volume fractions of all phases through the properties ρ and μ.

$$\frac{\partial}{\partial t}(\rho v_i) + \nabla.(\rho v_i v_j) = -\nabla p + \nabla.\left[\mu\left(\nabla v_i + \nabla v_j^T\right)\right] + \rho g_i + F_i \tag{3.5}$$

It is important to take into account that at areas near the interface if large velocity differences take place then the accuracy of velocity calculated maybe unfavourably affected.

Equation (3.6) presents the water phase equation that performs by taking the solution of the continuity equation for the phase.

$$\frac{\partial}{\partial t}(\alpha\rho_w) + \nabla.(\alpha\rho_w v_w) = 0 \tag{3.6}$$

where $\alpha_w, \rho_w \; and \; v_w$ are the water fraction, density and velocity respectively. The air phase volume fraction is not considered in equation 3.6; it will instead be computed depending on the following restriction:

$$\alpha_w + \alpha_a = 1 \tag{3.7}$$

3.2.2 Turbulence Modelling

RANS equations

In the present study, the Reynolds Average Navier-Stokes (RANS) equations within FLUENT are used to resolve the flow kinematics and turbulence characteristics. The RANS equations are derived from the instantaneous Navier Stokes equations where the flow variable is separated into mean ($\bar{u}_i$) and fluctuating components (u_i') according to Reynolds' hypothesis for turbulent flow, i.e.

$$u_i = u_i' + \bar{u}_i \tag{3.8}$$

$$\bar{u}_i = \frac{1}{T}\int_0^T u_i dt \tag{3.9}$$

When substituting (3.8) into (3.2) and averaging over a time period longer than the turbulence time scale, the following RANS equations are obtained:

$$\frac{\partial \bar{u}_i}{\partial x_i} = 0 \tag{3.10}$$

$$\frac{\partial}{\partial \mathrm{t}}(\rho \bar{u}_\mathrm{i}) + \frac{\partial}{\partial \mathrm{x_i}}(\rho \bar{u}_\mathrm{i} \bar{u}_\mathrm{j}) = -\frac{\partial \mathrm{p}}{\partial \mathrm{x_i}} + \frac{\partial}{\partial \mathrm{x_j}}\left[\mu\left(\frac{\partial \bar{u}_\mathrm{i}}{\partial \mathrm{x_j}} + \frac{\partial \bar{u}_j}{\partial \mathrm{x_i}} - \frac{2}{3}\delta_\mathrm{ij}\frac{\partial \bar{u}_i}{\partial \bar{u}_i}\right)\right] + \frac{\partial}{\partial \mathrm{x_j}}\left(-\rho\,\overline{u_i' u_j'}\right) \tag{3.11}$$

For simplicity, the over bar is dropped in the following text so that the RANS equation can be closed using different turbulent models based on the Boussinesq hypothesis.

$$-\overline{u_i' u_j'} = \mu_t\left(\frac{\partial \bar{u}_i'}{\partial x_j} + \frac{\partial \bar{u}_j'}{\partial x_i}\right) - \frac{2}{3}k\delta_{ij} \tag{3.12}$$

where μ_t is the turbulence eddy viscosity, $k = \frac{1}{2}\overline{u_i' u_j'}$ is the turbulence kinetic energy and δ_{ij} is the Kronecker delta.

Shear Stress Transport (SST) $k-\omega$

Based on previous literature reviews, a two-equation turbulence model Shear Stress Transport (SST) $k-\omega$ is adopted to simulate turbulence generation and dissipation. It uses the $k-\omega$ formulation for both inner parts and at the wall through the viscous sub layer then switches to $k-\varepsilon$ in the free stream (Menter, 1993). SST $k-\omega$ is favoured taking into account all aspects in comparison with other models (El-Behery, 2009). Since $k-\omega$ is very sensitive and consequently good initial predictions should be used, therefore, $k-\varepsilon$ is automatically adopted. The SST modifies turbulent viscosity formulation to account for the transport effects of the principal turbulent shear stress. The SST model incorporates a damped cross-diffusion derivative term in the ω equation which makes it better for adverse pressure gradient flows.

In the present study, the turbulence is expected to be generated by three different sources, including the perturbation in the flow (background turbulence), the turbine operation and the variation in the flow in the bottom boundary layer. The time scales and spatial scales in the

generation and dissipation in these different sources are very different. Therefore, the SST $k-\omega$ is expected to be able to pick up these different sources and represent them through the following equations:

$$\frac{\partial}{\partial t}(\rho k)+\frac{\partial}{\partial x_i}(\rho k u_i)=\frac{\partial}{\partial x_i}\left(\Gamma_k \frac{\partial k}{\partial x_i}\right)+G_k-Y_k+S_k \tag{3.13}$$

$$\frac{\partial}{\partial t}(\rho \omega)+\frac{\partial}{\partial x_i}(\rho \omega u_i)=\frac{\partial}{\partial x_i}\left(\Gamma_\omega \frac{\partial \omega}{\partial x_i}\right)+G_\omega-Y_\omega+S_\omega+D_\omega \tag{3.14}$$

where G_k and G_ω are the generation of k and ω due to mean velocity gradients respectively, Γ_k and Γ_ω are the effective diffusivity, Y_k and Y_ω are the dissipation due to turbulence, D_ω is the cross diffusion term and S_k and S_ω are user-defined source terms. The effective diffusivity Γ_k and Γ_ω are given by:

$$\Gamma_k=\mu+\frac{\mu_t}{\sigma_k} \tag{3.15}$$

$$\Gamma_\omega=\mu+\frac{\mu_t}{\sigma_\omega} \tag{3.16}$$

where σ_k and σ_ω are the turbulent Prandtl numbers for k and ω. When SST is employed, the turbulent viscosity μ_t is defined as:

$$\mu_t=\frac{\rho k}{\omega}\frac{1}{max\left(\frac{1}{a^*},\frac{SF_2}{a_1\omega}\right)} \tag{3.17}$$

$$\text{where } F_2=tanh\left[\left[max\left(\frac{2\sqrt{k}}{0.09\omega y},\frac{500\upsilon}{y^2\omega}\right)\right]^2\right] \tag{3.18}$$

where S is the strain rate magnitude, F_2 is the blending function and a^* damping coefficient of turbulent viscosity.

The turbulent kinetic energy (k) at inlet is calculated from turbulence intensity as following:

$$k = \frac{3}{2}(\bar{u}T_i)^2 \tag{3.19}$$

where T_i is the initial turbulence intensity [%] given below:

$$T_i = \frac{u'}{\bar{u}} = 0.16Re^{-1/8} \tag{3.20}$$

$$u' = \frac{1}{3}\sqrt{\left(u_x'^2 + u_y'^2 + u_z'^2\right)} \tag{3.21}$$

$$\bar{u} = \sqrt{u_x^2 + u_y^2 + u_z^2} \tag{3.22}$$

The turbulence dissipation rate (ω) is found from the length scale (l):

$$\omega = k^{\frac{1}{2}}c_\mu^{-\frac{1}{4}}l^{-1} \tag{3.23}$$

where c_μ is an experimental constant whose value is typically given as 0.09. The length scale (l) is defined as:

$$l = 0.07 \tag{3.24}$$

where L_c is the characteristic length, taken as the hydraulic diameter which is commonly used when handling flows in channels it is mainly used in calculation involving turbulent flows.

$$L_c = D_h = \frac{4A_c}{P_w} \tag{3.25}$$

where A_c is the stream cross-section area and P_w is the wetted perimeter. The turbulence generated from the bed is explained in section 3.3.1.

3.3 Boundary Conditions

In simulation, there are five different types of boundary conditions involved: inlet, outlet, bed, channel top and side walls. However, there are two different model setups; steady flow and waves setup (Figure 3-1).

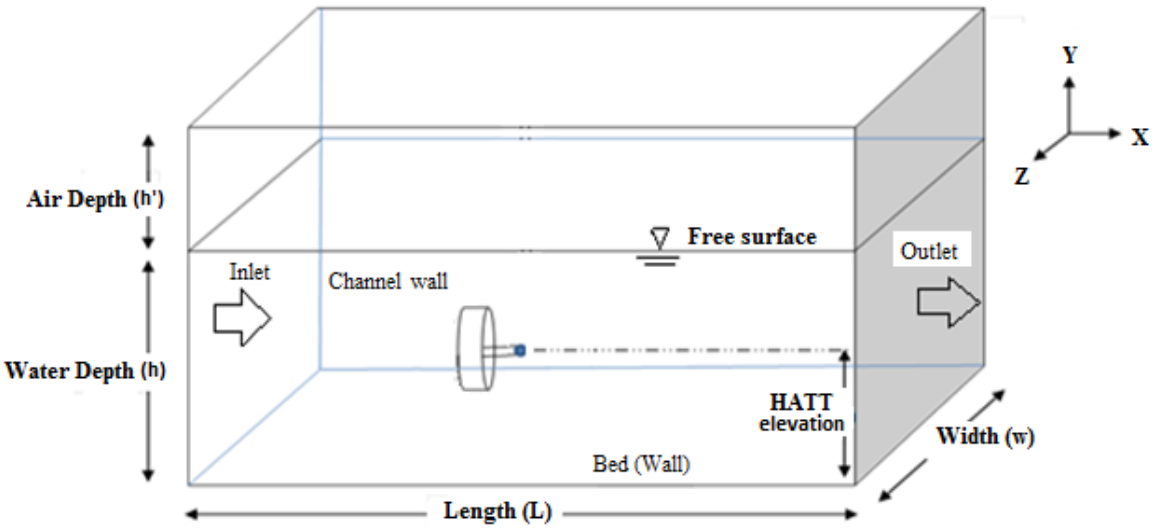

Figure 3-1 – Model boundaries.

In both cases, the operating pressure and density are set to 101325 Pa and 1.225 kg/m^3 respectively. The pressure reference location is set at a position within the air. The gravitational acceleration is also accounted for and all reference values are computed from inlet.

3.3.1 Bed/Channel Sides

The channel bed is set as a stationary wall with a no-slip shear condition. The wall roughness constant and heights values are both prescribed as required. The bed presents a uniform bathymetry inducing a uniform velocity variation

There are two parameters that specify roughness; the non-dimensionless roughness Reynolds number $\mathrm{K_s^+}$ and roughness constant $\mathrm{C_s}$.

$$\mathrm{K_s^+} = \frac{\rho k_s \mathrm{u}^*}{\mu} \tag{3.26}$$

$$\mathrm{C_s} = \mathrm{C_\mu^{\frac{1}{4}} k^{\frac{1}{2}}} \tag{3.27}$$

where k_s is the roughness height that can be taken as the sand-grain height when sand-grain roughness is uniform. For hydrodynamic smooth regimes $\mathrm{K_s^+}$ is smaller than 2.25 and $\mathrm{C_s}$ depends on the type of roughness. The turbulent model SST $k-\omega$ takes into account near wall turbulence (Menter, 1993). Since the wall function boundary is enabled in this simulation, the value of k at the wall adjacent cell is computed on the basis of the local equilibrium hypothesis. The production of k is calculated from the source terms of kinetic energy G_k as follows

$$G_k = \tau_w \frac{\partial u}{\partial y} = \tau_w \frac{\tau_w}{k_p C_u^{1/4} k_p^{1/2} y_p} \tag{3.28}$$

where k_p is the turbulence kinetic energy at point P and y_p is the distance from point P to the wall. For turbulence dissipation at the wall adjacent cell (ω^+) logarithmic region, it is found as follows:

$$\omega^+ = \frac{1}{\sqrt{\beta_\infty^*}} \frac{d\mu_t}{dy^+} \tag{3.29}$$

where β_{∞}^{*} is a model constant 0.09.At the wall however, the boundary condition for k and ω are:

$$\frac{\partial k}{\partial n} = 0 \tag{3.30}$$

$$\frac{\partial \omega}{\partial n} = 0 \tag{3.31}$$

where ∂n is the local coordinate normal to the wall. For high Reynolds number, it is valid to find the velocity parallel to the wall using the logarithmic law:

$$u^{+} = \frac{1}{\kappa}\ln(y^{+}) + C^{+} \tag{3.32}$$

where $$u^{+} = \frac{u}{u^{*}} \tag{3.33}$$

and $$y^{+} = \frac{yu^{*}}{\nu} \tag{3.34}$$

and $$u^{*} = \sqrt{\frac{\tau_w}{\rho}} \tag{3.35}$$

$$\tau_w = \mu \frac{\partial u}{\partial y} \tag{3.36}$$

where u_p is the mean velocity at a point P and κ is the Von Kármán. The side walls of the channel have zero friction since a turbine is typically positioned away for channel banks.

3.3.2 Open air boundary

The top of the channel is assigned with an open air boundary condition where the pressure is set to zero. At the interface however, high velocity gradients are found and produce turbulence. A turbulence damping source term is therefore added to the ω equation (3.23).

$$S_i = A_i \Delta n \beta \rho_i \left(\frac{B6\mu_i}{\beta \rho_i \Delta n^2} \right) \tag{3.37}$$

where A_i is the interfacial area density for phase i, Δn is the cell height normal to interface, β = 0.075 (constant) and B is the damping factor.

3.3.3 Inlet

The velocity inlet boundary condition is assigned at channel inlet. At the boundary, the velocity components as well as the scalar quantise defined. Inlet turbulences are defined at the boundary specified through intensity (%) and hydraulic diameter (m). The velocity set at channel inlet is defined as perpendicular to the boundary with an initial gauge pressure of zero. Fluent uses both the velocity components and the scalar quantities defined at boundary to compute the inlet mass flow rate, momentum fluxes, and fluxes of energy. The static pressure adjusts to accommodate the prescribed velocity distribution.

In terms of generating waves, they are introduced at the inlet boundary condition. The velocity of flow with incoming waves (V) is now calculated using the following equation:

$$V = (U + u)\hat{x} + v\hat{y} + w\hat{z} \tag{3.38}$$

where U is the uniform flow velocity magnitude, $u, v \; and \; w$ are the velocity components of the surface wave in the $\hat{x}, \hat{y} \; and \; \hat{z}$ direction respectively. These velocity components of the surface waves depend on the wave theory and are calculated as shown in equations 3.37, 3.38, 3.44, 3.45 and 3.46.

For setting up wave simulation, the open channel wave boundary condition is assigned at the inlet boundary. The relevant phase is selected where the specified parameters of waves are to be effective.. The wave condition is selected in accordance to the water depth and wave length relation. For shallow waves, the water depth is less than 1/20th of wave length. For short gravity waves (deep water regimes), water depth (h) is greater than 1/4th of wave length. Other wave sizes between these limits are classified as intermediate waves. The free surface level is specified and represented by $y_{local} = -(\vec{a}.\hat{g})$ where $\vec{a}$ is the position vector of any point on the surface and $\hat{g}$ is the unit vector acting downwards.

There are two wave theories provided by FLUENT 14.5, Airy and Stokes. Both theories assume that the wave is inviscid and irrotational and therefore do not induce turbulence. The Airy wave theory is used for small wave heights that demonstrate linear behaviour. The Stokes wave theory is applied for nonlinear waves that have finite wave height. The wave profile for a linear wave is given as:

$$\zeta(X,t) = \mathrm{A}cos\alpha \tag{3.39}$$

$$\alpha = K_x x + K_y y - f_e t + \epsilon \tag{3.40}$$

where x is the space coordinate in the flow and y is the vertical direction. ϵ is the void fraction, A is the amplitude, t is the time and f_e is the effective wave frequency. The effective wave frequency is defined as follows:

$$f_e = f + KU \tag{3.41}$$

where $K = \frac{2\pi}{L}$ is the wave number and f is the angular wave frequency defined as follows:

$$f = \sqrt{gK\tanh(Kh)} \tag{3.42}$$

The wave length property is determined as:

$$L = \left\{ \sqrt{\frac{gL}{2\pi} \tanh\left(\frac{2\pi h}{L}\right) + \bar{u}} \right\} T_a \tag{3.43}$$

The velocity components for shallow/intermediate waves are described as follows:

$$\begin{pmatrix} u \\ v \end{pmatrix} = \frac{gKA\cosh[K(z+h]}{f\cosh(Kh)} \begin{pmatrix} \cos\theta \\ \sin\theta \end{pmatrix} \cos\alpha \tag{3.44}$$

$$w = \frac{gKA\sinh(K(z+h)}{f\cosh(Kh)} \sin\alpha \tag{3.45}$$

where z is the height from the free surface level.

For non-linear waves (Stokes), waves are steeper (H/L > 0.04). The Stokes theory is suitable for waves on intermediate and deep water where it describes regular waves more accurately (Hedges, 1995). The wave profile for different order theories (2^{nd} – 5^{th}) is generalized as:

$$\begin{aligned} \zeta(X,t) = A\cos\alpha + \underbrace{A^2K(b_{22} + A^2K^2b_{24})cos2\alpha}_{2^{\text{nd}}\text{ order}} + \underbrace{A^3K^2(b_{33} + A^2K^2b_{35})cos3\alpha}_{3^{\text{rd}}\text{ order}} \\ + \underbrace{A^4K^3b_{44}cos4\alpha}_{4^{\text{th}}\text{ order}} + \underbrace{A^5K^4b_{55}cos5\alpha}_{5^{\text{th}}\text{ order}} \end{aligned} \tag{3.46}$$

where b_{ij} is a function for liquid height. The potential for shallow/intermediate waves is described as follows:

$$\Phi(X,t) = c\Bigg[A(a_{11} + A^2K^2a_{13} + A^4K^4a_{15})cosshKhsin\alpha + \underbrace{A^2K(a_{22} + A^2K^2a_{24})cosh2Khsin2\alpha}_{2^{\text{nd}}\text{ order}} + \underbrace{A^3K^2(a_{33} + A^2K^2a_{35})cosh3Khsin3\alpha}_{3^{\text{rd}}\text{ order}} + \underbrace{A^4K^3(a_{44})cosh4Khsin4\alpha}_{4^{\text{th}}\text{ order}} + \underbrace{A^5K^4(a_{55})cosh5Khsin5\alpha}_{5^{\text{th}}\text{ order}}\Bigg] \quad (3.47)$$

where a_{ij} is a function of wavelength. The angular wave frequency f is defined as follows:

$$f = \sqrt{gK(1 + A^2K^2c_3 + A^4K^4c_5)tanhKh} \quad (3.48)$$

where c_i is the wave speed. The velocity components for waves are described as follows:

$$u = \frac{\partial\Phi}{\partial x}cos\theta \quad (3.49)$$

$$v = \frac{\partial\Phi}{\partial x}sin\theta \quad (3.50)$$

$$w = \frac{\partial\Phi}{\partial z} \quad (3.51)$$

Choosing an appropriate theory will depend on two wave parameter checks, wave steepness and relative depth. They distinguish between linear and nonlinear waves and as a result mandatory checks for full wave regime within wave breaking limit is required.

Table 3-1 – Mandatory wave checks

Relative Depth	H/h = Maximum theoretical limit = 0.780
Wave Steepness	H/L = Maximum theoretical limit = 0.142

It is important to check if the selected wave theory is within the wave breaking and stability limit. The relative depth is an ideal measure for determining the appropriate wave theory for the simulations. For first order Airy theory, the Relative Depth is ≤ 0.1, otherwise Stokes theory (RD ≥ 0.1) must be used. The wave steepness is another measure for deciding the wave theory. For first order theory, wave steepness is ≤ 0.03; otherwise use Stokes (WS ≥ 0.03). Furthermore, for first order Airy theory, the Ursell Number $Ur = \frac{HL^2}{h^3}$ is ≤ 105, however for Stokes Ur ≤ 26. The overall wave regime is successful when h/L ≤ 1000.

One of the main aspects that should be accounted for in the simulation is the prevention of wave reflections caused by the outlet boundary for passing waves. Thus, a damping zone is introduced to suppress this effect via adding a damping source term in the momentum equation at the zone near the outlet boundary. The source term is show as follows:

$$s = -[c_1 \rho V + 0.5 c_2 \rho |v| v] f(z) f(x) \tag{3.52}$$

where $c_1$is the damping resistance (1/m), c_2 is the quadratic damping resistance, $f(x)$ and $f(z)$ are the damping functions in the x and z directions respectively.

3.2.4 Outlet

Steady Flow Setup

The downstream boundary is set as outflow where the velocity and pressure are extrapolated from the interior. This boundary condition assumes that the flow is fully developed.

Waves Setup

In the cases where waves are involved, the downstream boundary is defined as the pressure outlet where the pressure is specified from the free surface level governed by:

$$p_s = (\rho - \rho_0)|\vec{g}|((\hat{g}.\vec{b}))y_{local} \tag{3.53}$$

$$y_{local} = -(\vec{a}.\hat{g}) \tag{3.54}$$

where $\vec{b}$ is the position vector of the face centroid, $\vec{a}$ is the position vector of any point of the free surface, $\hat{g}$ is the unit vector of gravity and y_{local} is the distance from the reference point to free surface. The density is interpolated from neighbouring cell volume fractions.

3.4 Solver Method

A finite volume method is used to solve the governing equation. The domain is divided into a number of control volumes without overlap. Variables of interest are centred inside these controlled volumes where the differential form of governing equations will integrate. Interpolation is needed to obtain the function values at quadrature points.

The Pressure-Implicit with Splitting of Operators (PISO) pressure-velocity coupling scheme that use the pressure-based segregated algorithm as a solution method. PISO performs corrections to enforce mass conservation and to obtain pressure fields. The algorithm is an extension of the Semi-Implicit Method for Pressure-Linked Equation (SIMPLE) algorithm (see ANSYS (2010) for more details) that provides two extra corrections; momentum and skewness. In terms of momentum, the PISO algorithm removes the repeated calculations inside the solution stage of pressure correction (p').

$$a_p p' = \sum_{nb} a_{nb} p'_{nb} + b \tag{3.55}$$

where b is the net flow rate, a_p under relaxation factor for pressure and a_{nb} under relaxation factor for adjacent cell. In terms of skewness, the pressure correction gradient of skewed mesh faces is recalculated and is used to update the mass flow rate.

The VOF method is adopted since it is a simple method without the complications found in Mixture and Eulerian models. The implicit scheme is used for time discretization, therefore the fluxes at the face of all cells and those close to the water-air interface are found as follows:

$$\frac{\alpha_w^{n+1}\rho_w^{n+1} - \alpha_w^n \rho_w^n}{\nabla t} V + \sum_f \left(\rho_w^{n+1} U_f^{n+1} \alpha_{w.f}^{n+1}\right) = 0 \tag{3.56}$$

where V is the volume of cell, U_f is the volume flux through the face, based on normal velocity, α is the volume fraction, n is the index of previous time step and w is water and f is the cell face.

The Green-Gauss theorem is used for discretization of spatial gradients of scalars at cell centres. Node-based gradient evaluation is recommended when implementing VBM in order to obtain high accuracy (FLUENT 2010).

$$\bar{\phi}_f = \frac{1}{N_f} \sum_n^{N_f} \bar{\phi}_n \tag{3.57}$$

where ϕ_f is the value of scalar at the cell face centroid, $\bar{\phi}_n$ is the nodal value and N_f is the number of nodes.

The pressure discretization scheme PREssure STaggering Option (PRESTO) is used in this simulation as it is known for producing higher accuracy than that of the other schemes and is compatible with the mesh used in this study. It uses separate continuity equilibrium for a staggered control volume around the face to calculate the staggered pressure.

The momentum, volume fraction, turbulent kinetic energy and specific dissipation rate are all computed using the Quadratic Upstream Interpolation for Convective Kinematics (QUICK) scheme, which is based on average weighted and centre interpolation of the variable. This scheme is selected for its higher accuracy when compared with upwind schemes (Leonard, 1979).

The convergence of the numerical scheme is improved by defining under-relaxation factors. They operate by using in values from earlier iterations to cut out sharp fluctuations and dampen the solution to encourage convergence. These factors are known as stabilizers and are defined as: pressure=0.1, momentum=0.4, volume fraction=0.5, turbulence kinetic energy=0.5, specific dissipation rate=0.5 and turbulence viscosity=0.5. All residuals are monitored and checked. The convergence criteria are defined as $< 10^{-5}$.

3.5 Time Step Control

The stability and time of the simulations are significantly influenced by the Courant number (C_u) and the time step defined. For multiphase simulation, the Courant number recommended is 0.5. Although the Courant number is not relevant in implicit numerical analysis, it is used as an indication of the time step size (Brethouwer et al., 1999).

$$C_u = \frac{\bar{u}\Delta t}{\Delta x} \tag{3.58}$$

where Δt is the time step and Δx is the cell size in the path of flow.

3.6 Initialisation

The simulation starts as defined at the inlet boundary. The required water depth is described by specifying the volume of water as 1 for the region below the prescribed water depth.

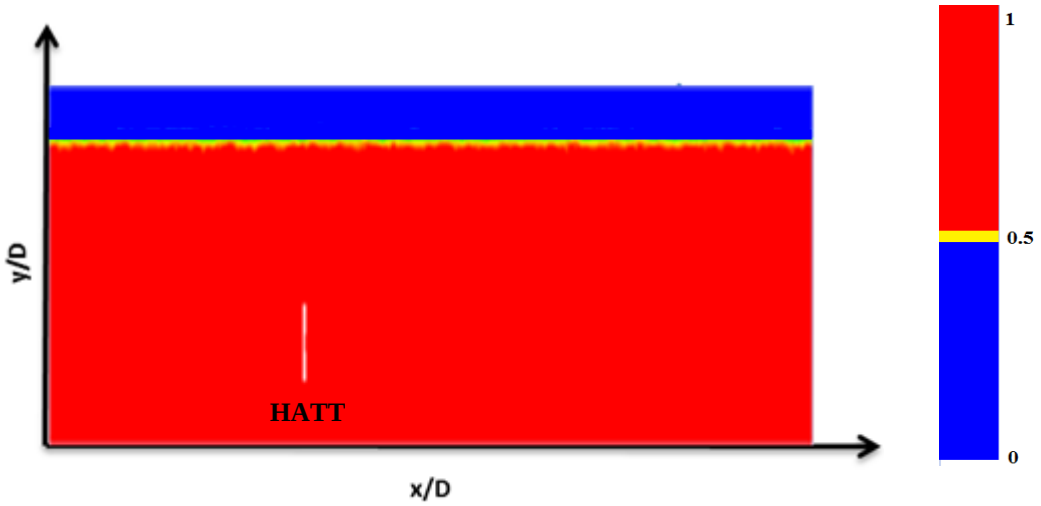

Figure 3-2 - Air and water seperation.

3.7 References

ANSYS, I. (2010) ANSYS Fluent Theory Guide. USA: Issue: 13.

Consul, C. A. (2011) *Hydrodynamic Analysis of a Tidal Cross-Flow Turbine*, Worcester College, UK.

El-Behery, S. M. and Hamed, M. H. (2009) A comparative study of turbulence models performance for separating flow in a planar asymmetric diffuser. *International Journal of mechanical, aerospace, industrial, mechatronic and manufacturing engineering*, vol. (3), Issue: 5.

Brethouwer, G., Boersma, B.J., Pourquié, M.B.J.M. and Nieuwstadt, F.T.M. (1999) Direct numerical simulation of turbulent mixing of a passive scalar in pipe flow. *European Journal of Mechanics - B/Fluids*, vol. (18), Issue: 4. pp.739-756.

Hedges, T. S. (1995) Regions of validity of analytical wave theories. *Proceedings of the ICE - Water Maritime and Energy*, vol. (112), Issue: 2. pp.111-114.

Holton, J. R. (1979) *An Introduction to Dynamic Meteorology*. 2nd edn. New York, USA: Academic Press Inc.10.1119/1.1987371.

Leonard, B. P. (1979) A stable and accurate convective modelling procedure based on quadratic upstream interpolation. *Computer Methods in Applied Mechanics and Engineering*, vol. (19), Issue: 1. pp.59-98.

Menter, F. R. (1993) Zonal Two Equation k-ω Turbulence Models for Aerodynamic Flows. *Turbulence, Heat and Mass Transfer 4*, AIAA 93·2906. Germany.

Chapter 4 – Tidal Turbine Representation

4.1 Introduction

Two different numerical turbine representations, i.e., Actuator Disk Model (ADM) and Virtual Blade Model (VBM) are employed in the present work. Both methods will embrace the same mesh setup for a clearer comparison. This chapter will provide the background theory and the governing equations employed. It will show how these methods are implemented in FLUENT in order to perform the simulation.

4.2 Actuator Disk Model - ADM

4.2.1 Linear Momentum Theory

The linear momentum theory is a simplified approach that substitutes the actual motion of turbine blades with a porous disk of the same area as the turbine. Pressure discontinuity is described across the disk, but not velocity difference (Mikkelsen, 2003). A set of assumptions is taken into account with regards to the flow, i.e., the flow is isentropic, one-dimensional and incompressible. Figure 4-1 below shows the three different positions which are considered in the analysis.

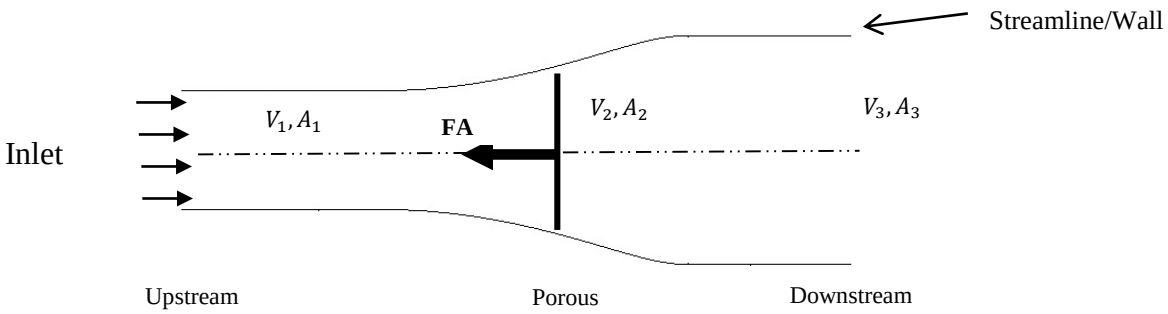

Figure 4-1 - Actuator disk in stream tube.

By considering steady flow past turbines between streamlines and taking into account conservation of mass, the below equation is formed:

$$V_1 A_1 = V_2 A_2 = V_3 A_3 \tag{4.1}$$

Similarly, considering the conservation of momentum for fixed, inertial and non-deformed control volume, the equation below is derived:

$$\rho V_3^2 A_3 - \rho V_1^2 A_1 = FA \tag{4.2}$$

where FA is the force that the turbine exerts on the flow. The conservation of energy is also simplified by neglecting heat transfer, alongside with prior assumptions, giving:

$$P_i + \tfrac{1}{2}\rho V_i^2 = constant \text{ (i=1,2,3)} \tag{4.3}$$

Apply Bernoulli's equation at 1, 2 and 3:

$$P_1 + \frac{1}{2}\rho V_1^2 = P_2^+ + \frac{1}{2}\rho V_2^2 \tag{4.4}$$

$$P_3 + \frac{1}{2}\rho V_3^2 = P_2^- + \frac{1}{2}\rho V_2^2 \tag{4.5}$$

Considering viscous loss (Darcy's law) and inertial loss, the porous media condition in FLUENT defines the pressure change over the thickness of disk as:

$$\Delta p = \left(\frac{\mu}{\alpha} v + C_2 \frac{1}{2}\rho v^2\right)\Delta m \tag{4.6}$$

where μ is the fluid viscosity, α is the face permeability of the media, C_2 is the inertial resistance factor, v is the velocity normal to the porous face and Δm is the thickness of the

media. At the disk, the momentum forces influence the pressure gradient producing a pressure fall that is proportional to the flow velocity in the zone.

Following the Ergun equation, the friction factor in a packed column can be expressed as a function of the Reynolds number:

$$f_p = \frac{150}{Gr_p} + 1.75 \tag{4.7}$$

Friction factor is defined as:

$$f_p = \frac{\Delta p}{L}\frac{D_p}{\rho V_s^2}\left(\frac{\epsilon^3}{1-\epsilon}\right) \tag{4.8}$$

Reynolds number is defined as:

$$Gr_p = \frac{D_p V_s \rho}{(1-\epsilon)\mu} \tag{4.9}$$

where Δp is the pressure drop across the bed, Gr_p is the modified Reynolds number, L is the length of the bed, D_p is the equivalent spherical diameter of the packing, ρ is the density of fluid, μ is the dynamic viscosity, V_s is the superficial velocity and ϵ is the void fraction.

Taking into account the Ergun equations, 1/α (viscous resistance) and C_2 (inertial resistance) in equation 4.6 are found as:

$$1/\alpha = \left[150 * \frac{(1-e)^2}{\phi^2 * D^2 * e^3}\right] \tag{4.10}$$

$$C_2 = \left[2 * 1.75 * \frac{1-e}{\phi * D * e^3}\right] \tag{4.11}$$

where e is porosity of the medium, ϕ sphericity of the particles making the medium (0.75) and D diameter of particles (0.001m). Various values of porosity of the medium were used, i.e., 0.1, 0.3, 0.5, 0.7 and 0.9 in order to achieve the similar resistance (0.7 used).

4.3 Virtual Blade Model - VBM

The Virtual Blade Model simulates the effect of the rotating blades on the fluid through a body force in the x, y and z directions, which acts inside a disk of fluid with an area equal to the swept area of the turbine. The value of the body force is time-averaged over a cycle from the forces calculated by the Blade Element method. The blade is divided into small sections from root to tip. The lift and drag forces on each section are computed from 2D aerodynamics based on the angle of attack, chord length and lift and drag coefficient of each segment. The free stream velocity at the inlet boundary is used as an initial value to calculate the local angle of attack (AOA) and, Mach and Reynolds number (Re) for each segment along the blade. Then, based on the calculated values of AOA, lift and drag coefficients are interpolated from a look-up table, which contains values of these variables as a function of AOA, Re and Mach (Mozafari, 2010). The VBM method adopts both momentum theory and the blade element method.

4.3.1 Momentum Theory

The Momentum Theory is also referred as the Actuator disk theory which simply uses a porous disk to express the pressure jump across the volume.

4.3.2 Blade Element Theory

The performance of a blade turbine can be simplified by considering the performance on a thin disk that will act to convert the kinetic energy of a current into rotational motion. Theoretically this disk contains an infinite number of rotating blades which function as an

energy extractor, and cause a sharp change in pressure (hydraulic jump) compared to the rest of the pressure along the stream line. This disk can be analysed in different ways. One way is to look at it in terms of the work done to convert axial momentum into rotational momentum. The shape and orientation of the blade area determines this momentum conversion. The blade is divided into strips at a fixed radius. The effective onset flow containing the axial free stream and rotational flow determine the effective angle of attack (Figure 4-2). The blade element analysis, which uses the 2D section performance, including the influence of stall and/or cavitation, requires knowledge of the deceleration of the free stream and the imposed reverse spin (circumferential/tangential component of velocity).

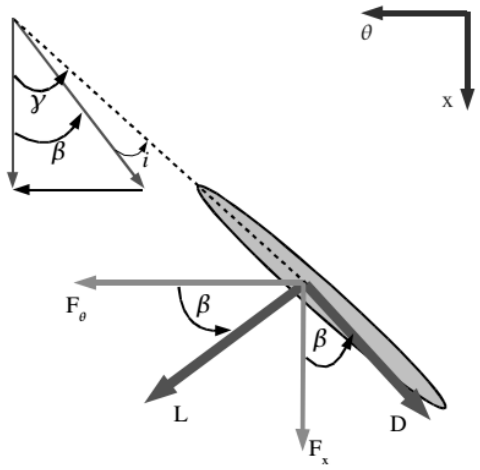

Figure 4-2 - Angles of lift and drag forces on blade section.

Bernoulli's equation is applied assuming the flow is frictionless; therefore, the axial(a), angular(a') induction factors and relative velocity (w) can be defined as:

$$a = \frac{v_1 - v_2}{v_1} \tag{4.12}$$

$$a' = \frac{\Omega_w}{2\Omega} \tag{4.13}$$

$$w = \frac{V(1-a)}{cos\beta} \tag{4.14}$$

where Ω is the blade rotational speed, Ω_w is the wake rotational speed and β relative flow angle onto blades. The momentum theory accounts for the rotor as a disk without dealing with the details of the flow and therefore will integrate with the blade element model.

The effective onset flow containing the axial free stream and rotational flow determine the effective angle of attack β.

$$\tan\beta = \frac{\lambda(1 + a')}{(1 - a)} \tag{4.15}$$

where λ is the tip speed ratio. The blade is divided into sections at a fixed radius. The effect of drag and torque (tangential) forces are calculated on each section of the blade as follows:

$$dF_x = B0.5\rho w^2(C_L sin\beta + C_D cos\beta)cdr \tag{4.16}$$

$$dF_{\theta=}dT = B0.5\rho w^2(C_L cos\beta + C_D sin\beta)crdr \tag{4.17}$$

$$B = \frac{2\sigma'\pi r}{c} \tag{4.18}$$

where B is the number of blades, σ' is the local solidity and c is the chord length. C_L and C_D are lift and drag coefficients respectively and their values are provided as part of the blade specification.

4.3.3 Blade Element Momentum Theory

Substituting equations (4.12), (4.13), (4.14), (4.15) and (4.18) in to (4.16) and (4.17):

$$S_x = dF_x = \sigma'\pi\rho\frac{V^2(1-a)^2}{\cos^2\beta}(C_L sin\beta + C_D cos\beta)rdr \tag{4.19}$$

$$S_\theta = dF_\theta = \sigma' \pi \rho \frac{V^2(1-a)^2}{\cos^2 \beta}(C_L cos\beta - C_D sin\beta) r^2 dr \quad (4.20)$$

where S_x and S_θ are the source terms in axial and tangential directions respectively. These source terms are added in the RANS equation 3.11 in the form S_i.

4.3.4 Virtual Blades

Blade specifications are accounted for without being physically present in the computational mesh. The blade is divided into multiple cross-sections along the span (Figure 4-3). The maximum number of sections allowed is 20. Each cross-section is provided with geometrical data such as chord length and angle twist (Figure 4-4). The same specifications were used in both the laboratory and CFD model.

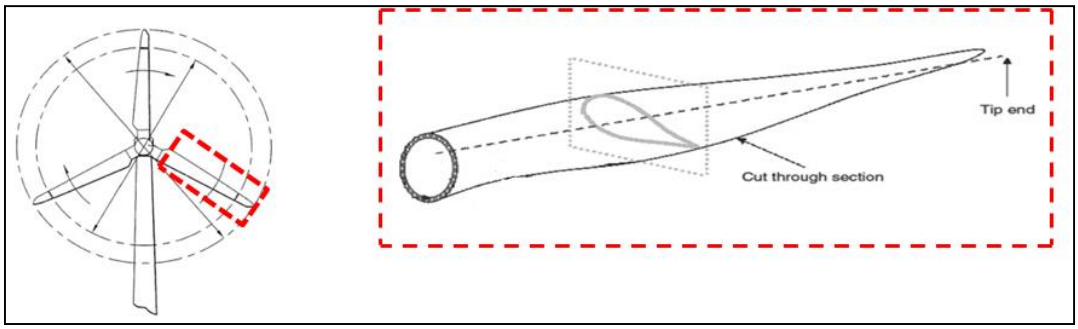

Figure 4-3 – HATT blade division.

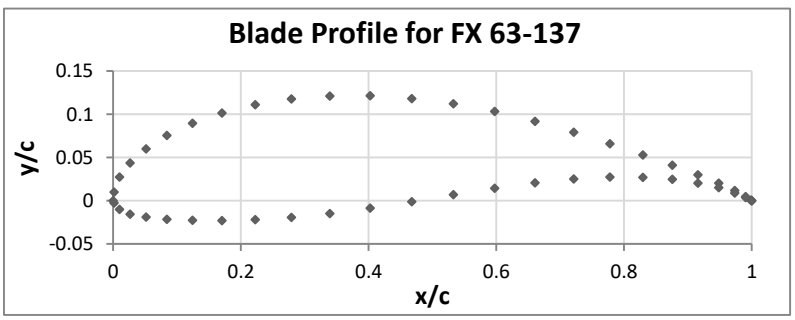

Figure 4-4 - Example of one cross-section profile of FX 63-137 blade.

4.3.4.1 Lift and Drag Coefficients

In order to work out the lift and drag forces induced by the flow passing blades, the coefficients of lift and drag should be obtained for each section along the span of the blade. Such data is obtained from experimental tests, where available. However, in many cases, they are limited between angles of attack of -15˚ to +20˚. Therefore, an interactive program (XFOIL) for the design and analysis of subsonic isolated aerofoils created by Mark Drela (Clark, 2006) is required to produce the entire coefficients for 360˚ angles of attack for each section.

4.3.4.2 Rotor Tip Effect

In a realistic condition, a secondary flow at the tip of the blade will be generated when a turbine is operating, i.e., tip vortices and radial flow (Nho et al., 2012). This secondary flow will violate the assumption of the local lift and drag forces being computed in 2D in the blade element theory, called the rotor tip effect. To avoid the lift force at the tip being neglected, this is represented by 96% of the span of the blade experiencing lift and drag and the remaining 4% drag only.

The tip speed ratio of the turbine operation will maintain maximum output of 5.5, where λ_r is found from:

$$\lambda_r = \frac{\Omega R}{\bar{u}} \tag{4.21}$$

where Ω is the rotor rotation speed radian per second and R is the rotor radius.

4.4 Limitations

ADM is a simple approach that operates on a static disk volume of fluid. This approach does not include the flow dynamics in the vertical and lateral direction due to the absence of rotation; hence, swirling in the downstream flow is missed out. Many researchers have used this method due to the flow being dominant in the longitudinal direction and therefore often acceptable to ignore the flow dynamic in other dimensions. This method is also used for near and far wakes characterisation where arrays are employed (Batten and Bahaj, 2006). However, the accuracy of computed shear stresses at the bed would be affected due to the omission of swirling effects that will exaggerate further downstream.

Although the VBM resolves the issue of vertical and lateral motion in ADM regarding the disk being stationary, it still encompasses a few limitations. Firstly, in the blade-element theory, the blade induced forces from incoming flow are averaged over the entire annular ring (cycle routine) and each ring is independent of one another. Hence it assumes a uniform symmetrical flow velocity in the wake. Secondly, the rotor tip effect is minimised to avoid the formation of secondary flows, which misses out the flow separation and subsequent swirling from the tip in the wake. Thirdly, the coefficients of lift and drag for all different cross-sections of the blade span also are difficult to accurately value. Fourthly, VBM is designed to operate in a single phase flow. When the free surface flow is involved as in the present study, the calculation will lose its accuracy once the blade rotates into a mixture fluid with very different density. Regarding the last point, the turbine is submerged entirely under water in the following study to avoid any integration with air. Overall, VBM remains a compromise method that is capable of representing turbines by interpreting the flow through and around them.

4.5 Model Implementation

This section will illustrate an overview of the models implementation in FLUENT 14.5. This will include the procedures and boundary conditions adapted for each methodology. Details of mesh generation developed in ICEM are also described in the following section.

4.5.1 Model setup

4.5.1.1 ADM Setup

The turbine zone is defined as a porous zone, with a porosity of 0.7. The boundary condition on the disk is defined as a porous jump. The parameters of the porous jump zone are assigned with the aid of equations 4.10 and 4.11 for face permeability and inertia resistance factor respectively. The porous medium thickness is also specified as the thickness of the turbine blade (1mm).

4.5.1.2 VBM Setup

The VBM approach is implemented into FLUENT through source terms in the momentum equation 3.2. To enable these source terms, a series of user defined functions (UDF) are coded and linked with FLUENT. In particular, a rotor model is used to compute all necessary variables involved in VBM, i.e., equation (4.19) (4.20). In addition, a memory management function, which is needed to pass the variable values, is also implemented along with the rotor model. A user interface function is used to enable the models' integration with the FLUENT graphic user interface.

The rotor related parameters, i.e., C_L and C_D, are stored in a text file which can be read into the memory when they are needed. The number of blades, radius and rotor speed are all assigned depending on the replicated turbine. The rotor disk origin and the pitch angle which describes the angle of attack of the entire blade with respect to the rotor disk plane are set accordingly. The rotor bank angle and the blade collective pitch are assigned based on the turbine configuration. No blade flapping is considered in the present work. The rotor tip effect percentage is set as 96 as discussed in section 4.3.4.2. The blade is divided into multiple sections. The specifications of each blade cross-section located along the length of span are specified in terms of chord length, twist and coefficients of lift and drag, described in chapter 5 for each model. The lift and drag coefficient are defined for each section. The trim option is enabled to run the model with a thrust trimming routine. This automatic

numerical trim routine has been recommended by Zori and Amer (1995) using a Newton-Raphson iterative method.

FLUENT starts the simulation using initial values of velocity, turbulent kinetic energy and dissipation rate defined at inlet. Local angle of attack (α), Mach (Ma) and Reynolds number (Re) are solved for each section of the virtual blade. These values are then used for computing the forces of lift and drag from following equation:

$$f_{L,D} = C_{L,D}(\alpha, Ma, Re) * c\left(\frac{r}{R}\right)\frac{\rho V_{tot}^2}{2} \tag{4.22}$$

where V_{tot} is the velocity relative to the blade and $c\left(\frac{r}{R}\right)$ is the section chord length. The coefficient of lift and drag are looked up from tables that provide complete values for 360 degrees of attack. Subsequently, the forces obtained are averaged over a full turbine revolution (annular ring). At a distance r, the width of the annular ring is dr which is defined manually. The area found as follows:

$$dA = 2\pi r dr \tag{4.23}$$

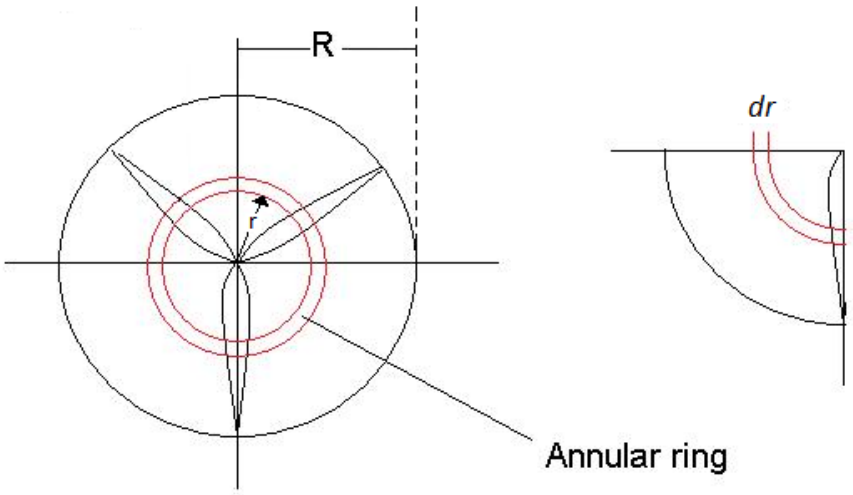

Figure 4-5 – Description of rotor disk.

The averaged forced over the annular ring is found by:

$$F_{L,D_{cell}} = N_b \frac{drd\theta}{2\pi} f_{L,D} \tag{4.24}$$

where N_b is the number of blades, r is the blade radius and θ is the azimuthal angle. The θ is expressed as:

$$\theta(r) = \alpha' + \frac{\lambda}{r} \tag{4.25}$$

where α' is the blade twist angle defined manually in the VBM input panel.

Finally, the source term is calculated at each cell in the numerical discretization by

$$\overrightarrow{S_{cell}} = \frac{F_{cell}}{U_{cell}} \tag{4.26}$$

where U_{cell} is the volume mesh cell. The source term ($\overrightarrow{S_{cell}}$) is inserted in the RANS equation to calculate the velocity in the x, y and z direction u, v and w respectively.

$$\frac{\partial}{\partial t}(\rho u_i) - \frac{\partial}{\partial x_i}(\rho u_i u_j) = -\frac{\partial p}{\partial x_i} + \frac{\partial}{\partial x_j}\left[\mu\left(\frac{\partial u_i}{\partial x_j} + \frac{\partial u_j}{\partial x_i} - \frac{2}{3}\delta_{ij}\frac{\partial u_k}{\partial x_k}\right)\right] + \frac{\partial}{\partial x_j(-\rho\overline{u'_\iota u'_j})} + \overrightarrow{S_{cell}} \tag{4.27}$$

As stated previously VBM is applied the water phase alone, avoiding any cavitation issue. The spatial discretization pressure scheme will apply pressure corrections and update the mass flux, velocity and pressure. The details of this interaction between FLUENT 14.5 main modules and VBM are presented as in the following schematic diagram (Figure 4-6).

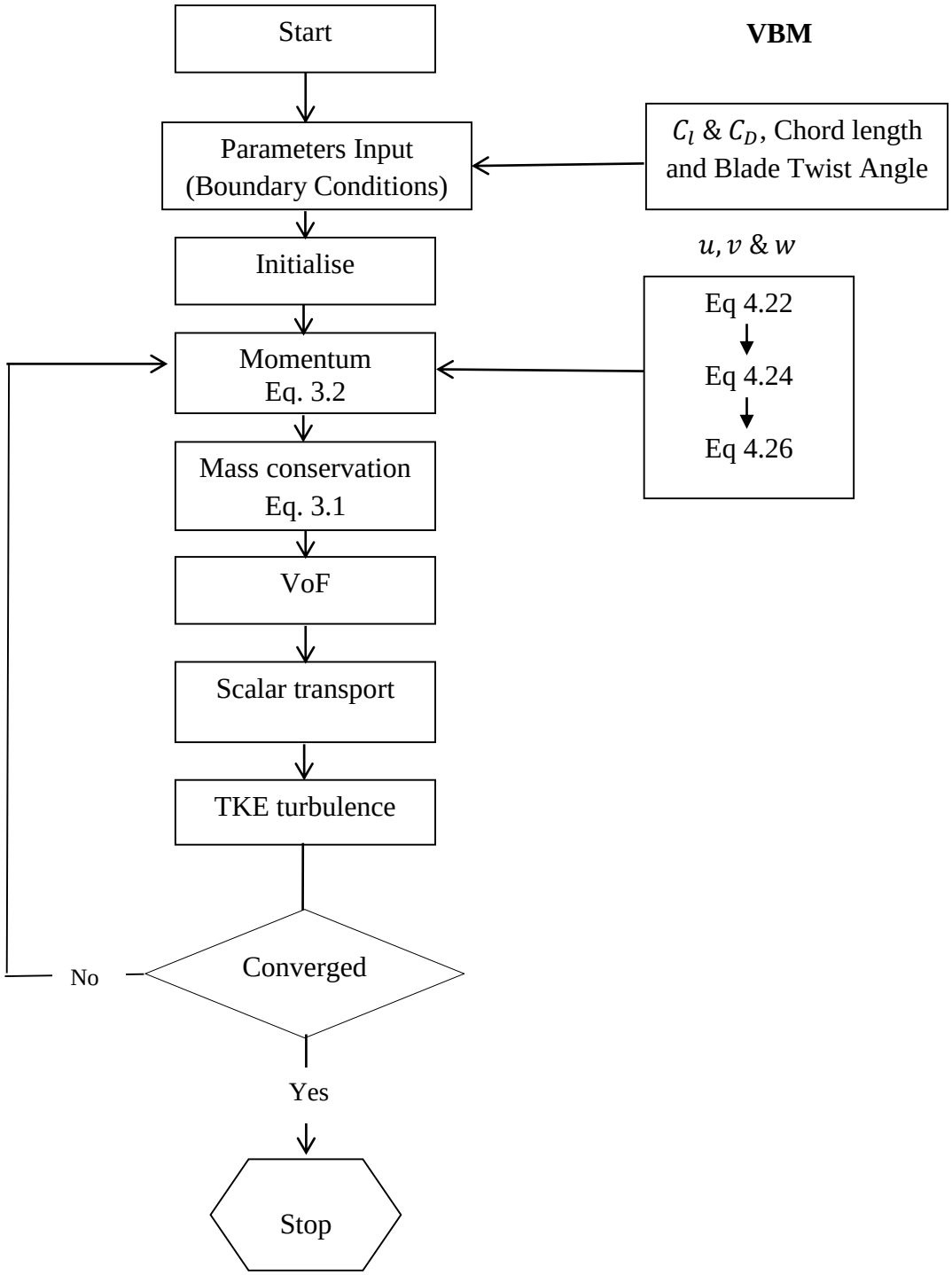

Figure 4-6 - Flow chart of FLUENT and VBM interaction.

4.5.2 Turbulence Model

The Large Eddy Simulation (LES) approach is able to capture the entire turbulence eddy with different length scales. However, it requires a sufficiently fine mesh to catch the stream field at the turbine, i.e., the blades. It was suggested by Mccombes et al. (2011) that for an effective application of LES, around 200 mesh nodes are required for a blade profile. This would mean that several millions of meshing cells will be created and in return will be computationally expensive. O'Doherty et al. (2009) proposed that the blade tip impact on the flow requires catching and therefore additional mesh should be created at the tips. However, the VBM method lacks the ability to induce these tip effects, i.e., vortex shedding and secondary flows. A comparative study between the two approaches RANS ($k-\varepsilon$) and LES was conducted by Chenga et al. (2003) when simulating a flow over a matrix of cubes. Results suggested that that RANS approach was able to capture the main flow features, including separation and recirculation. For these reasons, the RANS approach is selected in this study, particularly SST $k-\omega$ where SST accounts for the transport of the turbulent shear stress and $k-\omega$ is more robust in flows that exhibit stronger curvature and separation.

4.5.3 Mesh Generation

The open channel is created using explicit points to form the boundary geometry, and then the body of material (fluid) is assigned. The turbine area is treated as a porous disk. A gap in the centre of the disk is used to represent the hub section of the turbine. The volume of the porous medium was assigned to bodies of both ADM and VBM. The diameters of the disk and their thicknesses change depending on turbine blade swept area and its thickness.

.

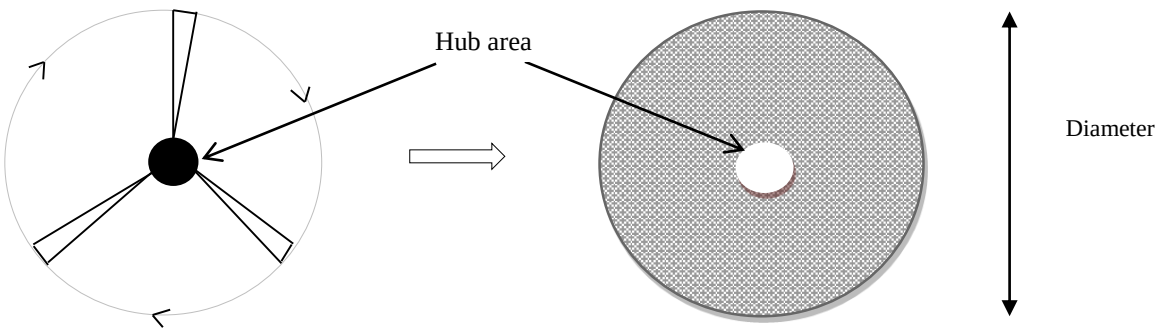

Figure 4-7 - Disk Geometry.

In the case of ADM, the mesh file is imported into FLUENT with no further amendments. However, when the VBM is employed, the disk zone undergoes a face separation with an angle of 80 degrees creating a total number of 4 faces. This was required for the VBM setup in order to construct a 2D platform for accommodating rotor specifications to allow computing lift and drag forces.

In order to achieve good accuracy in the model results, careful consideration on mesh generation has to be given at turbine location as well as the near the bed. In the near bed region, the mesh size can be determined using the dimensionless value y^+, where the logarithmic law for mean velocity is identified to be effective for $30 < y^+ < 300$:

$$y^+ = \frac{yu^*}{v} \tag{4.28}$$

where y is the distance from the wall to the centroid of the first cell and u^* is the shear velocity. The shear velocity can be calculated from wall shear stress (τ_w) or from the skin-friction coefficient c_f as follows.

$$u^* = \sqrt{\frac{\tau_w}{\rho}} = \bar{u}\sqrt{c_f} \tag{4.29}$$

The skin-friction coefficient c_f is:

$$c_f \approx 0.037 \frac{1}{\sqrt[5]{Re}} \tag{4.30}$$

For the models in this study, the Reynold numbers differ for the majority of the cases and therefore the shear velocity and the values of y. Table 4-1 below presents the calculated values of Re, u^*, c_f and y for all cases used in the present study.

Table 4-1 - Range of distances from the wall to the centroid of the first cell for 30 < y^+ < 300.

Models	Re	c_f	u^* (m/s)	y (when $y^+ = 30$) (mm)	y (when $y^+ = 300$) (mm)
UoL-1	765000	0.00246	0.04466	0.87	8.78
UoH	168000	0.00333	0.01617	2.41	24.25
Uol-2	702000	0.00250	0.04505	0.87	8.70
UoM	207000	0.00319	0.02545	1.53	15.41
FBM	1.2E+08	0.00089	0.05980	0.65	6.55

*UoL-1 (University of Liverpool - steady case) *UoH (University of Hull) *UoL-2 (University of Liverpool – unsteady case) *UoM (University of Manchester) 'FBM (Field Bench Mark).

For each model in the present study, the range of y shows different values. Therefore, different mesh cell sizes at the bed were chosen for each model. The y cell size in agreement to y^+ = 300 was selected for all of the models accordingly in order to keep the number of mesh cells as low as possible. Furthermore, the bed was divided into two sections, i.e., in front and behind the turbine. The area behind the turbine section was further divided into two more sections, i.e., beneath the wake region (2D wide) and along the sides until the channel walls. The beneath wake region is the section where y_{max} was applied. Figure 4-8 demonstrates the mesh arrangement across the channel bed.

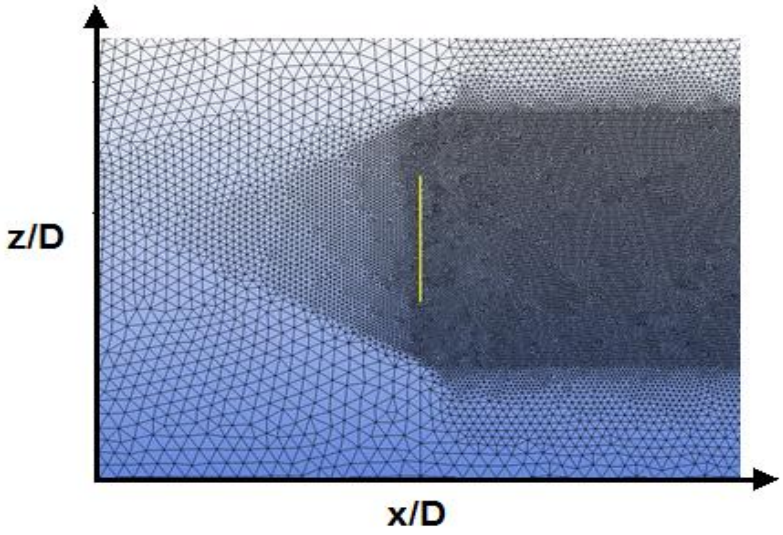

Figure 4-8 – Mesh across the channel bed.

A number of sensitivity tests were carried out to evaluate the accuracy of flow velocity behind the turbine for different mesh densities at the turbine face and consequently the wake region. Table 4-2 shows the simulations carried out on UoL-1 model setup to assess the accuracy of the averaged flow velocity at 2D downstream when compared with experimental data (Tedds et al., 2014). It can be seen from the table that the total mesh cells increased with increasing the number of nodes across the disk diameter. Consequently, the computational time increased considerably. The accuracy of the models improved with increasing the mesh. However, this improvement was not significant beyond 0.7 million mesh cells.

Table 4-2 – Description of model (UoL-1) convergence time and accuracy at different mesh sizes.

Tests	**Total Mesh Cells (million)**	**Computational Time (hour)**	**Streamwise velocity Accuracy (%)**
1	0.3	4	60
2	0.5	6	71
3	0.7	9	89
4	0.9	14	91
5	1.1	21	92

Figure 4-9 shows the streamwise velocity across the channel centre at 2D behind the turbine. It is clear that for all of the above tests the models were able to capture the velocity distributions. However, the accuracy particularly at the flow peaks, varied to show better correlation when number of cells was higher.

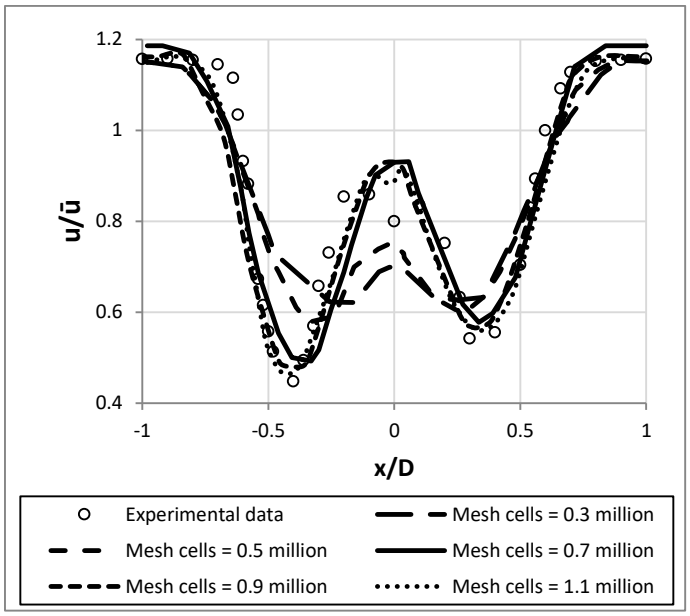

Figure 4-9 – Streamwise velocities across the centre of turbine at 2D behind the turbine for different mesh sizes.

Compromising between computational costs and levels of accuracy, the number of mesh nodes used across the blades was 20 and an overall element scale factor of 1.25 was used.

At the free surface region, the mesh resolution was improved in order to capture the surface fluctuations due to the turbine accurately. A similar study (Adamaski, 2013) showed that the cell size had to be smaller than 0.1m in order to predict the decay in surface height due to the friction on the channel floor. In this study, the cell size used was 0.07m. When waves are generated, the number of nodes across the vertical length of the wave height had to be selected. A number of waves with current tests were carried in an empty channel of water depth 0.78m and wave height 0.086m, to measure the surface elevation over one wave cycle. Figure 4-10 show the wave-cycle averaged surface elevation, adopting four different node sums across the wave height. Results show a remarkable improvement in the surface elevation accuracy when increasing the number of nodes across the wave height. Beyond 30

nodes however, the surface elevation shape more or less does not change. Therefore, 30 nodes were used across the vertical length of wave height to capture the surface elevation accurately

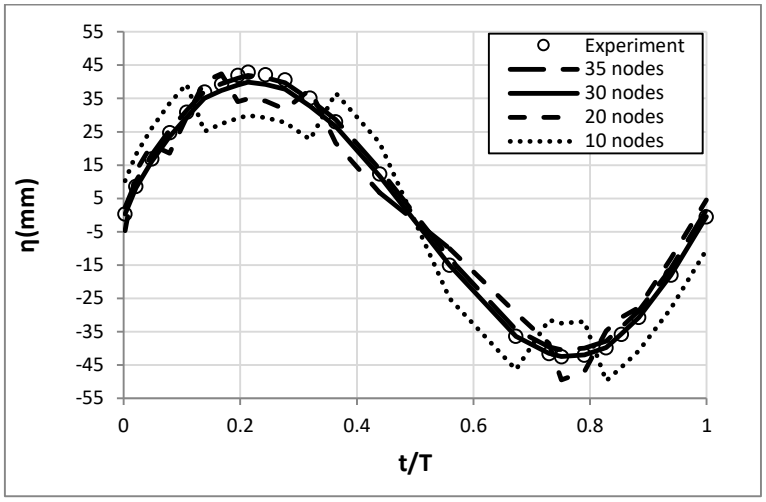

Figure 4-10 – Comparison of surface elevation between experimental data and computed results when adapted 4 different node counts across the wave length.

ANSYS ICEM is used as the meshing tool in the present study. The mesh generated for the model contains a hybrid mesh. The hexahedron cells are used on the disk by applying a 3D blocking system in order to have consistent (uniform) node distribution around the disk for VBM to be able to work. The block was created around the disk body. The edges of the block are associated to the outer curves of the disk. The front and back faces of the block are selected and divided into smaller blocks. The edges of the inner (centre) block are further associated to the inner curves of disk forming an O-grid. Remaining unwanted blocks are permanently deleted. The meshing parameters are then set and the blocks are checked and fixed if necessary. The mesh skewness is then checked to ensure the quality of the grid.

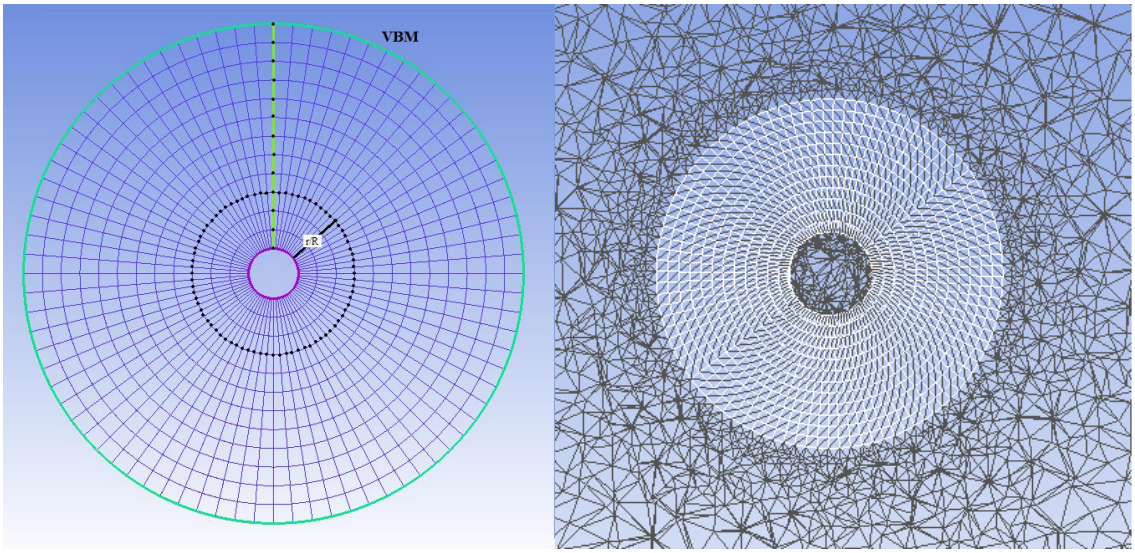

Figure 4-11 – Mesh across the turbine for experimental scale (UoL-1).

ICEM is able to adjust and connect with all the mesh nodes existing on faces allowing for denser mesh around the turbine region. The channel boundaries undergo surface meshing. The free surface region is meshed by introducing a mesh density box. The channel is created from tetra/mixed cells that were generated from existing surfaces (faces) meshes. Overall, the total numbers of mesh cells used were approximately 1.4 million for field scales and approximately 1 million for experimental scales.

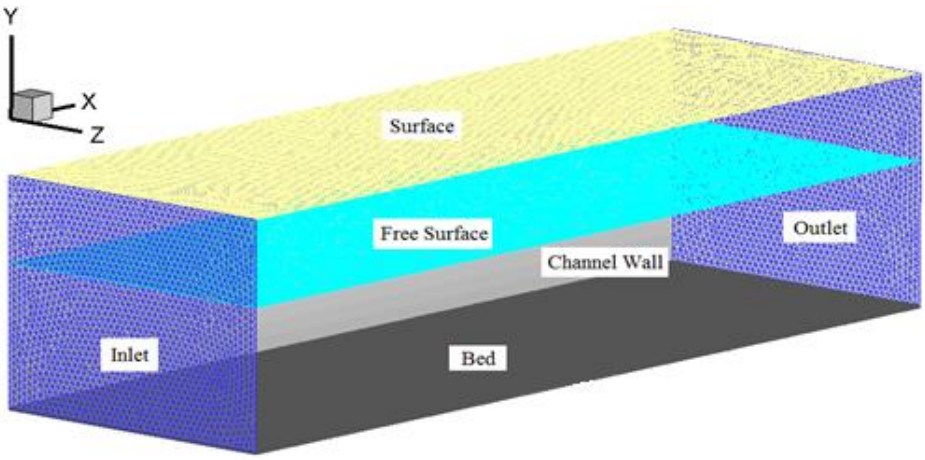

[a]

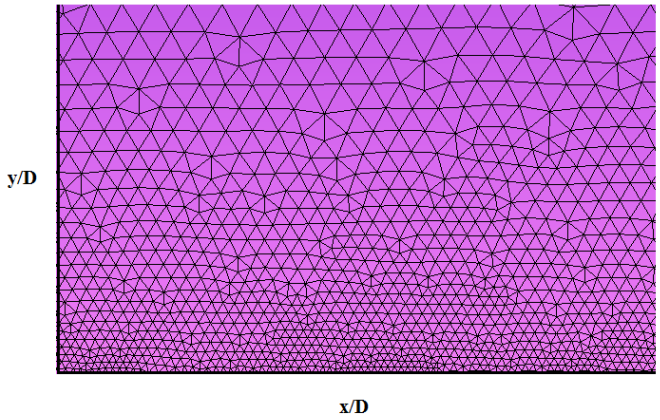

[b]

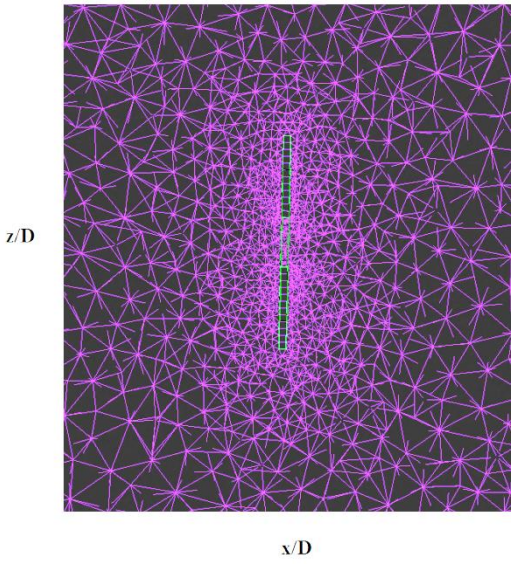

[c]

Figure 4-12 – [a] 3D overview of channel mesh, [b] side view of bed boundary layer mesh and [c] plan view of turbine inside channel.

The qualities of poor mesh cells are improved by using a quality based method that dramatically smoothes the mesh and increases the orthogonal quality. This avoids sudden jumps in cell size that will cause interpolation error and unacceptable magnitudes. Furthermore, the mesh is checked for connectivity of cells, face handedness, face node order and element type consistency.

4.6 References

Batten, W. M. J. and Bahaj, A. S. (2006) CFD simulation of a small farm of horizontal axis marine current turbines. In, Sayigh, A.A.M. (eds.), *World Renewable Energy Congress 2006. World Renewable Energy Congress (WREC-IX),* Elsevier Science.

Chenga, Y., Liena, F. S. and Yeeb, E. (2003) A comparison of large Eddy simulations with a standard k–e Reynolds-averaged Navier–Stokes model for the prediction of a fully developed turbulent flow over a matrix of cubes. *Journal of Wind Engineering and Industrial Aerodynamics,* Elsevier Science. vol. (91), pp.1301-1328.

CLARK, L., 2006. Mark Drela's research - and his teaching - offer beauty and functionality. (of AeroAstro, the annual report/magazine of the MIT Aeronautics and Astronautics Department).

Mccombes, T., Johnstone, C. and Grant, A. (2011) Unsteady wake modelling for tidal current turbines. *Renewable Power Generation, IET,* vol. (5), Issue: 4. pp.299-310.

Mikkelsen, R. (2003) *Actuator Disc Methods Applied to Wind Turbines*, PhD, Thesis, Department of Mechanical Engineering Technical University of Denmark.

Mozafari, A. T. J. (2010) *Numerical modelling of tidal turbines: Methodology Development and Potential Physical Environmental Effects*, MSc. Thesis, University of Washington.

O'Doherty, T., Jones, A., O'Doherty, D. M. and Byrne, C. B. (2009) Experimental and Computational Analysis of a Model Horizontal Axis Tidal Turbine. *Proceedings of the 8th European Wave and Tidal Energy Conference.* Uppsala, Sweden.

Von Kármán, T. (1930) Mechanische Ähnlichkeit und Turbulenz. Nachrichten von der Gesellschaft der Wissenschaften zu Göttingen, Fachgruppen. vol. (1), Issue, 5. pp.58-76.

Zori, L. A. J. and Amer, J. (1995) Navier-Stokes Calculation of Rotor-Airframe Interaction in Forward Flight. *Journal of the American Helicopter Society,* USA: vol. (40), Issue: 2.

Chapter 5 – Model Validations

5.1 Introduction

This chapter provides a description of model validations against several experimental data sets. Discussions include comparisons between measured and computed results of velocities in the x, y and z directions as well as Turbulence Kinetic Energy (TKE). There are four different validation cases described in this chapter as shown in Table 5-1. All four case have high Reynolds number (Re > $2x10^5$) and are defined as high turbulent regimes. In the case UoL-1 (experiment carried out at the University of Liverpool), the turbine representation methods ADM and VBM are both compared with the experimental data conducted by Tedds et al. (2014). The flow velocity in the recirculating flume is 0.9m/s, operating under current only condition (no waves) under high blockage ratio of 16.5%. This case was used as part of the mesh sensitivity test explained in section 4.5.3. The VBM method is then selected for further validation in the UoH case (experiment carried out at the University of Hull). The experiment is conducted by Jordan et al. (2015) in a flume with low blockage ratio of 3.2%. No waves are considered in this investigation and only a current with a flow velocity of 0.25m/s. In this experiment, the bed is placed with plywood boards covered with sand providing surface roughness. In the case UoL-2 (experiment carried out at the University of Liverpool), the experiment is divided into two part, firstly, the flume with current and following waves without a turbine, investigating the impact of waves on the flow. In this particular case, the ability of FLUENT 14.5 to generate surface waves with the correct wave-induced flow behaviours are examined. This case also was used as part of the mesh sensitivity test explained in section 4.5.3. Secondly, a turbine is placed in the flume with the same flow conditions introduced in part one of the test. The turbine and flume specifications are the same as those used in UoL-1 case. In these tests (UoL-2), the VBM method is assessed against experimental data given by Henriques et al. (2014), including surface elevations, velocity and TKE profiles. The ability and the accuracy of VBM method to perform under constantly varying velocity are evaluated specifically. In the UoM case (experiment conduced at the University of Manchester), the experiment is divided into two parts, current alone and current with opposing waves where the turbine is present in both

cases. The experiment is conducted by Olczak et al. (2013) to represent a full scale tidal stream (1:70) of 30m water depth. The VBM method is tested against measured data for both parts of the experimental investigation.

Table 5-1 – Description of validation tests.

Case Study	**Numerical Method**	**Flow Condition**	**Reynolds Number (10^6)**	**Validation**
UoL-1	ADM and VBM	Current alone	0.765	Tedds et al (2014)
UoH	VBM	Current alone	0.168	Jordan et al (2015)
UoL-2	VBM	Current + Waves	0.702	Henrique et al (2014)
UoM	VBM	Current - Waves	0.207	Olczak et al (2013)

*UoL-1 (University of Liverpool - steady case) *UoH (University of Hull) *UoL-2 (University of Liverpool – unsteady case) *UoM (University of Manchester).

5.2 UoL-1 (University of Liverpool)

5.2.1 Experiment Conditions

The experiment conducted by Tedds et al. (2014) took place at a high speed flume with dimensions of 3.7m length, 1.4m width and a depth of 0.85m. A 0.5m diameter three bladed turbine was centred at mid-depth (Figure 5-1) with blockage ratio 16.5%.

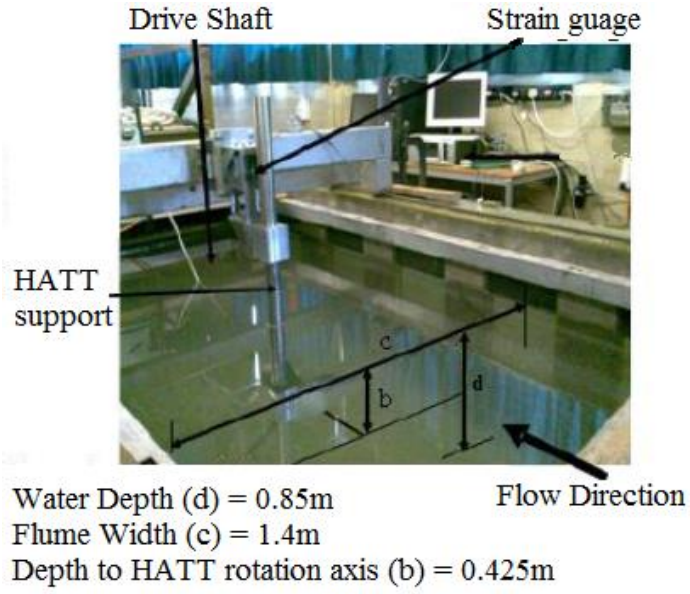

Figure 5-1 – High speed Flume discribtion (after Tedds et al., 2014).

The turbine hydrofoil profile was designed to operate at low Reynolds number flows. The inlet flow mean velocity was 0.9m/s with a turbulence intensity of 3%. An Acoustic Doppler Velocimeter was used to measure velocities and turbulences at five different locations behind the turbine. A servomotor was used to generate torque that was proportional to the drive rated current (10.1A max). The rotational speed of the motor was measured as a percentage of the rated velocity for the motor (TSR=5.5). Following O'Doherty et al. (2009), a blade pitch angle of 6 degrees was adopted. Precision machine angle blocks and a marking table were used to set the pitch angles. Optimal angled blocks were aligned with the chord at the tip of the blade. Subsequent to blade assembly a coned shape geometry cover is reattached on to the hub.

5.2.2 Numerical Model Setup

The model is set up according to the experiment conditions. A total of ≈ 0.9 million tetra/mixed cells were used. The velocities in the x, y and z directions and the TKE are measured at five locations, 2D and 3D, 4D, 5D and 6D downstream (Figure 5-2).

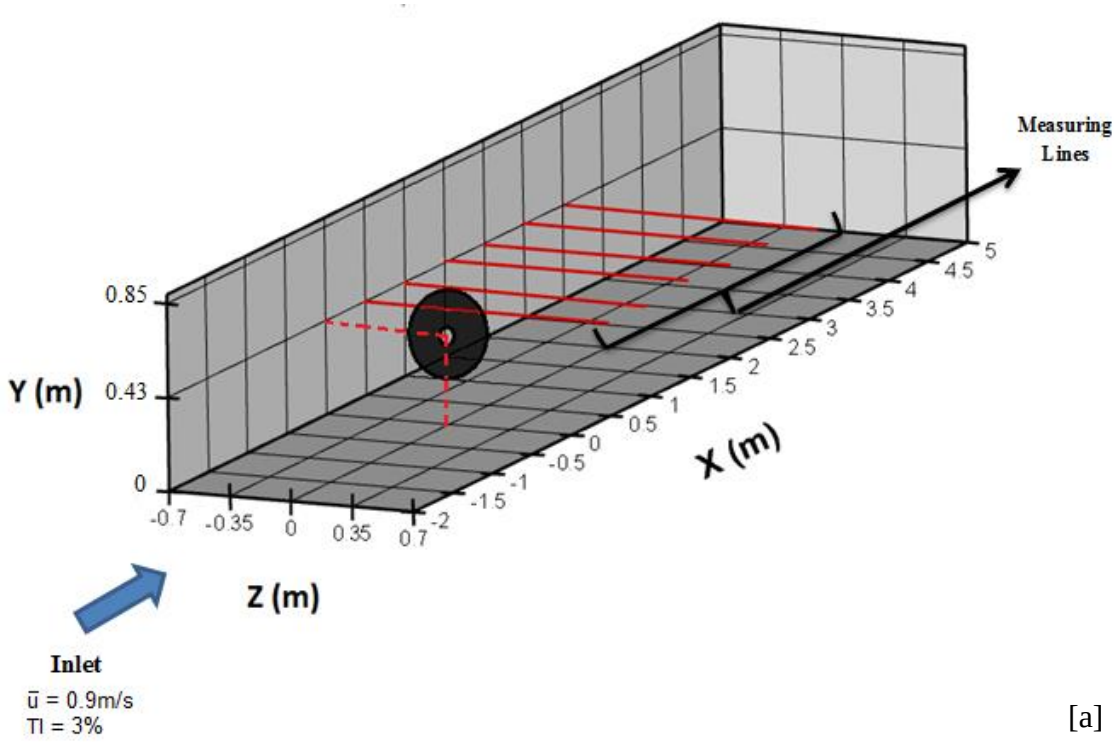

Figure 5-2 – Model description of measuring positions [a] deafult (3D) veiw, [b] plan veiw.

When the ADM method is adopted, the disk zone is defined as a porous medium of thickness 0.01m. The porous-jump condition is assigned to the disk face with viscous resistance of

$6.99x10^7$ m^2 calculated from Equation 4.10. The inertial resistance is found to be 4080/m, calculated from Equation 4.11.

When the VBM method is applied, the disk geometry is modified as described in section 4.5.1. The disk is defined as an interior boudary and is assigned with the relevent momentum source terms as described in section 4.5.3.2. The VBM model is activated and all the functional and geometrical specifications of the rotor are then defined (Table 5-2 and Table 5-3).

The simulation started as time-dependent and the calculation integrated forward until the solution converged to steady state (stability in velocity). The time step size is set as 0.001 seconds. After 30 seconds of run, results are then collected at intervals of 0.07s for a period of 4s to achieve mean-time flow model-data comparison.

Table 5-2 – General rotor setup.

Number of rotor zones	1
Number of blades	3
Rotor radius	0.25m
TSR	5.5
Disk pitch angle	90
Blade pitch	-6
Blade flapping	0

Table 5-3 – Geometrical rotor setup.

Radius (r/R)	**Chord (m)**	**Twist (deg)**
0.24	0.075	90
0.31	0.075	82
0.38	0.075	73
0.45	0.07	64
0.54	0.064	54
0.61	0.056	45
0.69	0.045	36
0.77	0.039	27
0.85	0.035	18
0.92	0.032	9
1	0.029	0

5.2.3 Results and Discussion

Figure 5-3 shows the contours of computed streamwise velocity along the horizontal plane at turbine centre. It is clear that the flow velocity undergoes many changes when a turbine is in place. The flow starts to slow down in front of the turbine at approximately 1.5D upstream. At the hub section, the flow diffracts at the blade root to show strong flow acceleration. Part of the flow goes through the turbine centre in the hub-blade connection but quickly dissolves in the wake region at 2D downstream. Behind the blades, the flow immediately decelerates due to the strong lift and drag forces experienced and shows reverse flow (eddies). At the blade tips, the flow swirls around the turbine and accelerates up to 1.5 times the ambient flow speed. The turbine in this case clearly influences the flow behaviour across the entire channel width.

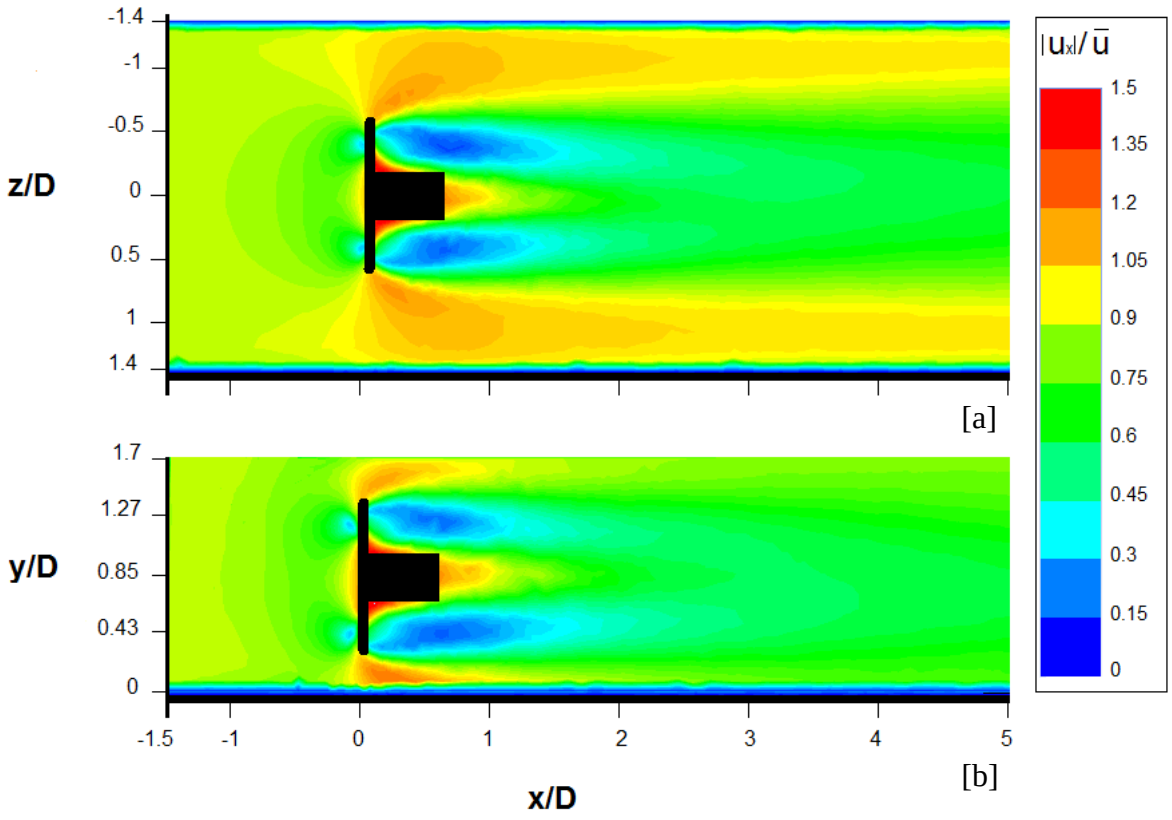

Figure 5-3 - Contours of streamwise velocity along the turbine centre plane [a] plan, and [b] side view.

In this case, two CFD models are tested with identical geometry for the comparison, i.e., the ADM and VBM methods separately. The mean velocity at the inlets of flume and the models are ū= 0.9m/s. Figure 5-4 shows the normalised streamwise velocity at upstream where measured and computed results show very similar values. Near the bed, the velocity tends to reduce and becomes zero at bed surface in the models due to roughness (no slip condition).

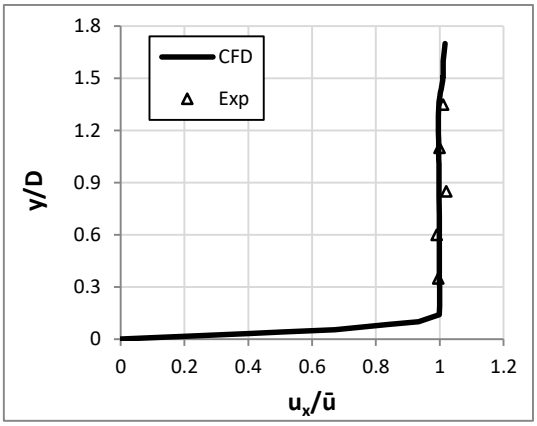

Figure 5-4 – Comparison of vertical profiles of normalised streamwise velocity at inlet between measured and computed (ADM and VBM).

Figure 5-5 compares the computed and measured streamwise velocities across the channel width at 2D, 3D, 4D, 5D and 6D downstream of the turbine. The solid lines denote the VBM results and the broken line represents the ADM results. The experimental data are shown as symbols.

In several previous studies where porous mediums (ADM) are employed, results did not show a "W" shaped velocity distribution immediately behind the turbine (Sun et al., 2008). This is simply because the disks are uniformly porous and there is no hub feature. Mozafari (2010) concluded that ADM lacks the ability to simulate accurately the flow behaviour immediately behind the turbine, hence poor data accuracy in near wake regions. When the modified disk is adopted as in the current study, the streamwise flow velocity profiles are captured better in comparison with the experimental data. On the other hand, results from VBM show similar accuracy with minor improvements in comparison with the ADM.

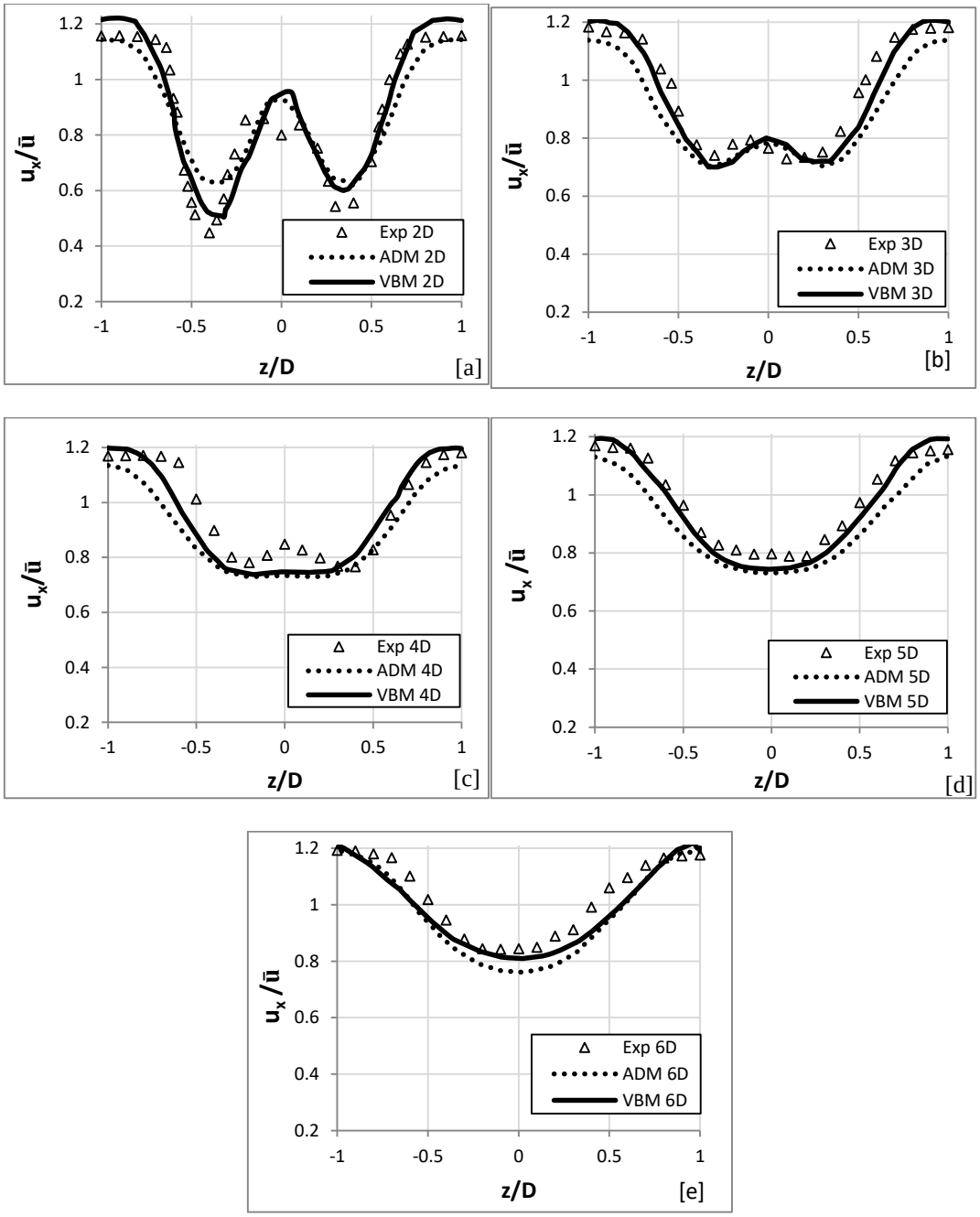

Figure 5-5 – Comparison of horizontal profiles between measured, ADM and VBM normalised streamwise velocities at [a] 2D, [b] 3D, [c] 4D, [d] 5D and [e] 6D downstream along the centreline.

Overall, both ADM and VBM results follow the experimental data reasonably well at all positions. At 2D and 3D downstream, both measurement and computed results clearly show a "W" profile distribution in the z direction (lateral). The increasing flow velocity near the channel sides is due to the blockage at the blades, which reduces the velocity in the centre of the channel and hence pushes the flow to the sides. At the centre (z = 0), however, the flow

speed recovers to the inlet flow speed quicker. Due to the rotational motion induced by the turbine, this "W" shaped profile has an asymmetrical character showing higher velocity deficit of around 25% on the left-hand side than the right-hand side (looking from upstream). This asymmetry is clearly captured by the VBM results.

However, the ADM approach gives a symmetrical distribution, which indicates the importance of the cross-flow in y and z directions to represent the flow behind the turbine. As the wake travels further downstream, it spreads and mixes with the primary flow to dissipate and recover gradually as shown at 4D, 5D and 6D.

At 2D the flow accelerates to 1.3ū on both sides around the turbine (+/- 0.7D from centreline), drops to a minimum of 0.6ū behind the blades and then recovers almost ū behind the hub (x=0). Both results from ADM and VBM follow the "W" shape of velocity distribution immediately after turbine (2D, 3D).

A noticeable difference can be seen at 4D position where the computed flow velocity drops at the centreline and forms a single "U" shape, whereas the measured data maintains a "W" shape at this location. The computed flow velocity is also slightly lower than the measured value at the centre line at 5D, particularly using the ADM method, which suggests a stronger flow reduction in the computed wake region than that in the lab. At 6D, the computed flow speed at the two sides is lower than the experimental values, probably due to the side wall effect. The ADM results in almost all positions show a wider spread of the wake. The error is estimated as 12% overall at the five sites. However, VBM results produce an error of 8% overall at the five sites.

Figure 5-6 compares vertical velocity across the width of the channel at different locations behind the turbine. The VBM results follow the experimental data reasonably well at all locations. The errors are within 11% of experimental measurements. The rotation (clockwise) of turbine-induced vertical flow in both positive and negative directions is captured by VBM reasonably well at all locations, especially the peak values. Both model results and measured data suggest that the flow behaves in an asymmetrical manner where the velocity in the downward direction (-) is stronger. This is due to the rotation motion induced by the turbine being influenced by the gravitational force. On the left-hand side of the hub (facing downstream), the blades are moving upwards, opposite to the direction of gravitational force,

which causes the flow speed reduction. However, on the right-hand side of hub, the flow moves downwards following gravity, which increases the speed of flow.

Furthermore, it is found that the negative peak positions tend to shift slightly towards the left-hand side of the hub by about 0.2D at 6D. This means the wake is changing its trajectory and slightly shifts towards the left-hand side from the hub. This is due to the asymmetrical flow behaviour of the streamwise velocity, where the flow is faster on one side (right-hand side of the hub) and as a result the flow guides itself towards the slower side (left-hand side of the hub).

In the VBM results, the model captured the wake shift with slight underestimation at 2D and 6D. The velocity distributions became out of position laterally (wider) when moving downstream, especially at 6D. In the ADM results, the computed values mismatch with the measured data entirely behind the turbine due to the absences of the rotating motion. Results show almost zero vertical velocity at 4D and 6D whereas at 2D the flow shows a pattern in which the flow converges back towards the centre after swirling around the turbine.

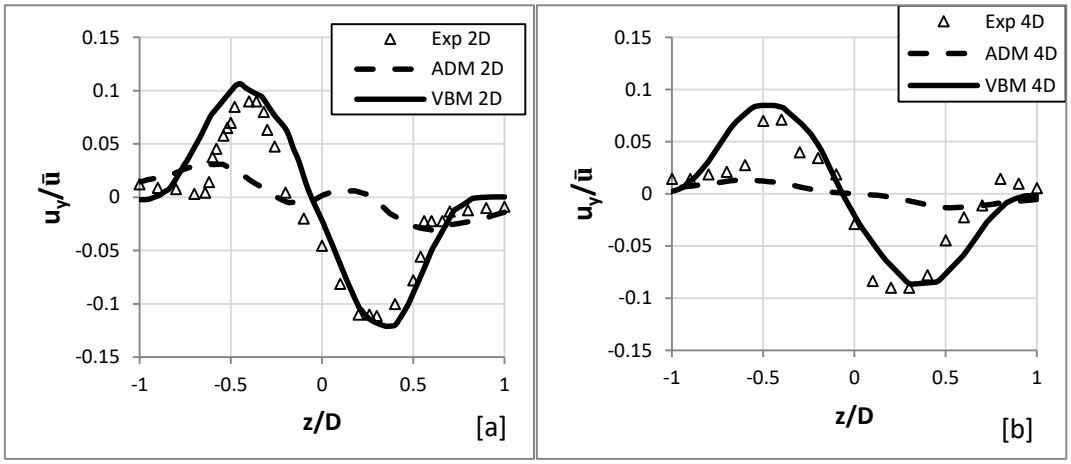

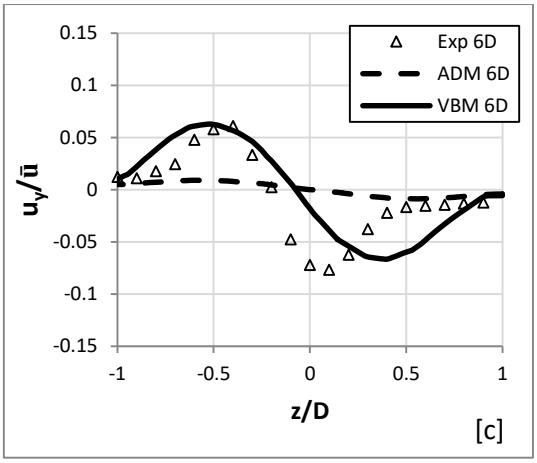

Figure 5-6 - Comparison of horizontal profiles between measured, ADM and VBM normalised vertical velocities at [a] 2D, [b] 4D and [c] 6D downstream along the centreline.

Figure 5-7 compares the computed cross-stream velocities from ADM, VBM and the measured data across the width of the channel. Positive velocities indicate that the flow is travelling to the right-hand side of the turbine and negative velocities to the left-hand side. In the VBM results, the computed values follow similar inward motion of flow towards the centreline of hub. Comparing with the lab data, results show that VBM under-estimates the average mean velocity by 20% at 2D. This difference reduces to 15% and 10% at 4D and 6D downstream respectively. Results show that the peak of negative flow moves towards the hub from 0.25D at 2D to zero at 6D. This is due to two processes taking place; firstly, the flow undergoes separation at the turbine where it diverges around the sideways and then converges back to meet behind the turbine.

Secondly, when the flow arrives onto the revolving blades, angular velocities are formed that rotate around the wake centreline to form a vortex which pulls the flow inwards towards its centre. Modelled and measured results show an asymmetric behaviour where the mean speed in the negative direction is around 45% faster than that on the positive direction at 2D downstream. This flow velocity variation persists downstream with different percentages.

Evaluating the velocities at positive and negative directions, it is found that there is a net drift towards the left-hand side of the hub. The computed velocity peaks are slightly out of position when compared with experimental data. This inconsistency occurs because the blade span area is only represented by 11 segments. This limited number of segments certainly affects the level of accuracy, where more segments will improve accuracy (Ingram, 2005). In

terms of ADM results, the method failed to imply any significant impact on the flow cross-stream velocity.

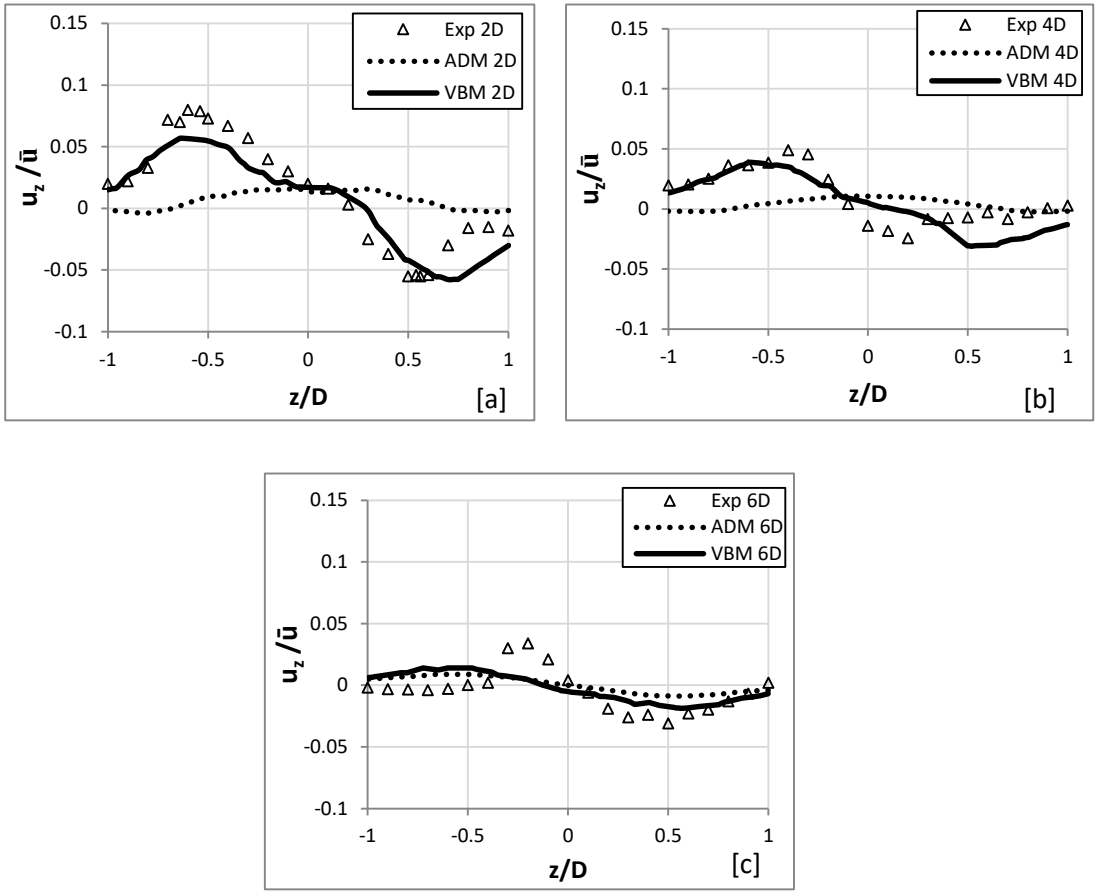

Figure 5-7 - Comparison of horizontal profiles between measured, ADM and VBM normalised cross-stream velocities at [a] 2D, [b] 4D and [c] 6D downstream along the centreline.

From Figures 5.5, 5.6 and 5.7, it can be seen that both experimental data and computed results clearly show the streamwise flow dominant at various sections downstream of the turbine. This dominance is consistent with previous results (see Chapter 2). However, this does not mean that vertical and cross stream velocities should be neglected.

Figure 5-8 presents the flow vorticity magnitude across the x plane immediately behind the turbine. It is clear that the flow highest vorticity magnitude is found around the blade tip and root. Further downstream, we can see the pattern changes as the wake starts to develop freely and interact with the ambient flow.

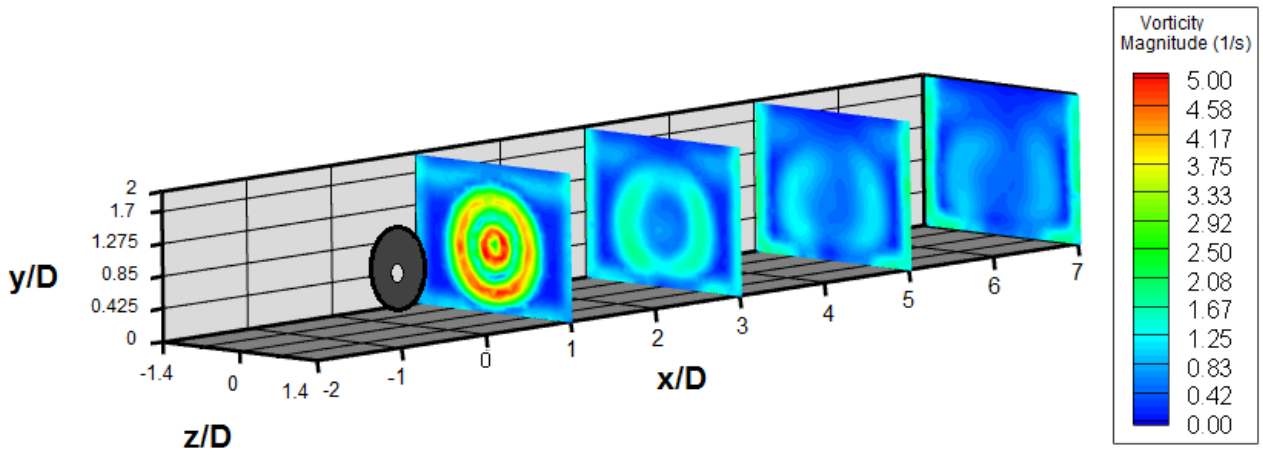

Figure 5-8 - Shows the vectors of turbine-induced vortex at 1D.

Figure 5-9 show the path lines released from the centre of the turbine, at 1D distance prior to the turbine, across the channel width. It is clear that the flow undergoes a complex swirling motion after crossing the turbine. Near the edge of the blade, e.g., y/D, z/D > 0.9 and y/D, z/D < -0.9, the flow is pushed to the side of the turbine and maintains straight lines. This is due to the fact that the drag/lift forces are not applied in the VBM at the tip of blade. But within the region of -0.9D < y, z < 0.9D, the flow starts to converge towards the hub and revolve clockwise once meeting the blade. The flow on the left-hand side of the turbine moves upwards while the right-hand side moves downwards.

Further downstream (x > 0D), the flow clearly diverges from the centre of the turbine and leaves the flow speed in the area immediately adjacent to the hub very low, as shown in previous figures. The magnitude of the swirling flow reduces gradually as the particle travels downstream. At the hub, the accelerated flow experiences rapid speed loss; this immediate change happens due to the flow clashing with the vortex at the rotating axis and diverging sideways from the turbine.

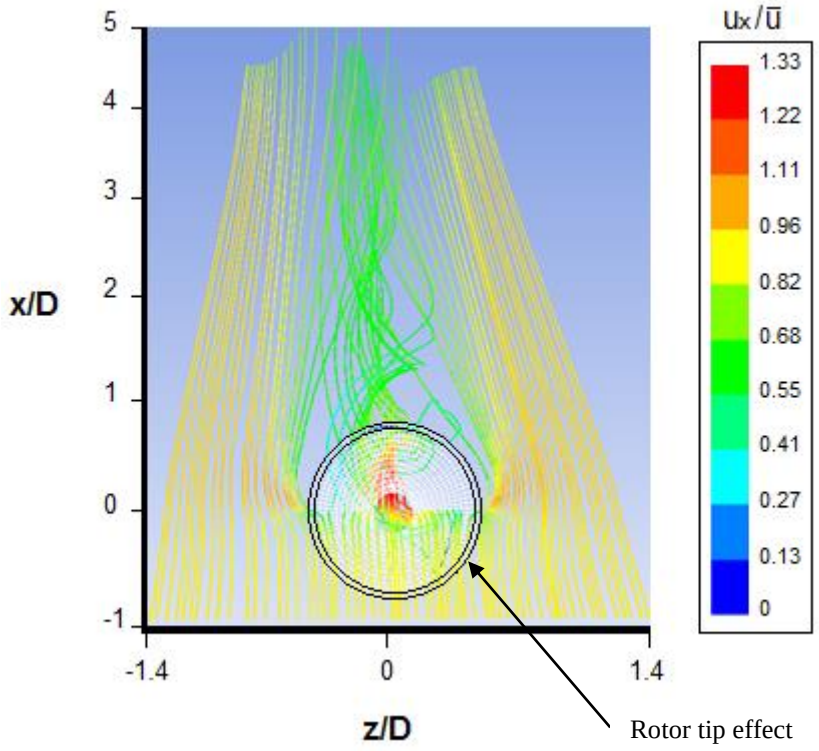

Figure 5-9 - Path lines of flow particles starting 1D in front of the turbine during operation (facing downstream).

Figure 5-10 compares VBM and ADM TKE values with measured data at 2D, 4D and 6D downstream. Overall, computed results from both models follow the measured data reasonably well. In VBM results, TKE values are under-estimated at blade tip at 4D and 6D because the rotor effect of both lift and drag are only presented for 96% of the blade span, as stated in the previous section. The model results underestimated, within 10% on average, that of the experimental data at those three sites. This is due to the fact that the rotation of the blade is not fairly resolved by VBM. The underestimated v and w clearly affect the TKE prediction as shown in previous figures. In ADM results, TKE values are also under-estimated at blade tip and this is simply because of the absence of blade rotation motion in the model. On average, the TKE is underestimated within 17% of that of the experimental data.

Results show that TKE values are highest around the blade tips region in both z/D = -0.5D and +0.5D, illustrating two peaks. This additional TKE appears as a result of stronger angular velocities induced at blade tip. The flow at the turbine undergoes complex physical processes, e.g., vortex shedding and secondary flow instabilities. Downstream, these peaks drop

gradually from $0.04\bar{u}^2$ at 2D to just $0.02\bar{u}^2$ at 6D. It is clear that the TKE also shows an asymmetric behaviour, being stronger at the right-hand side of hub at 6D. This occurs due to the asymmetric nature of flow velocity when passing through the turbine.

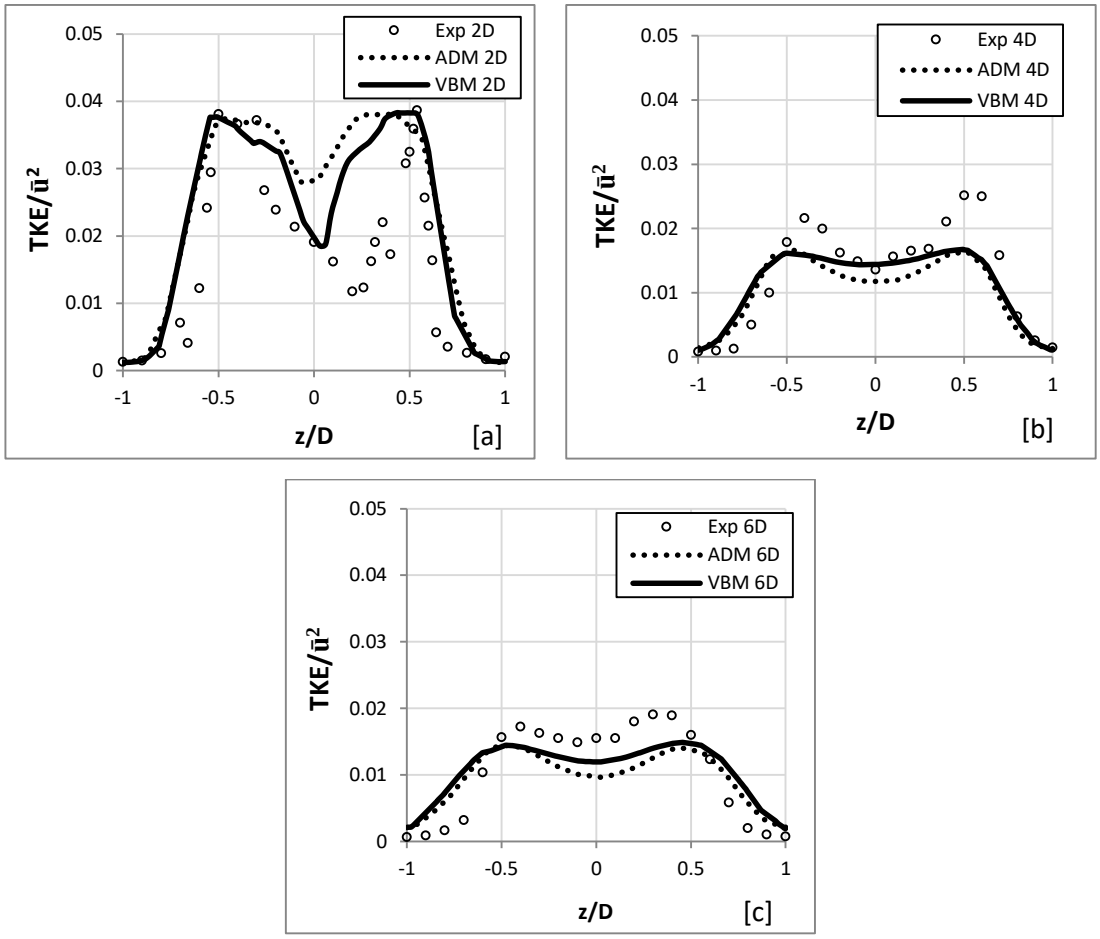

Figure 5-10 - Comparison of horizontal profiles between measured, ADM and VBM normalised Turbulent Kinetic Energy (TKE) at [a] 2D, [b] 4D and [c] 6D downstream along the centreline.

In some cases, computed velocity and TKE peaks were slightly under-estimated, especially right behind the turbine (x = 2D). This underestimation occurs due to the limited capability of representing the actual blades. Consequently, some wake details were not captured. Overall however, VBM results correlated reasonably well with measured data following similar distribution patterns.

On average, the error in streamwise velocity is within 12% and 8% for ADM and VBM results respectively. VBM results produce an error within 11% in the vertical flow velocity

and 20% in the cross-flow velocity. Results from ADM, however, show that the vertical and cross-stream velocities were not captured at all due to the absences of rotation. Similarly, the error in TKE for the VBM results are within 10% on average and 17% for ADM results at those measured positions.

Figure 5-11 presents the contour maps of bed shear stresses for both ADM and VBM applications. Overall, it is clear that the turbines have a significant impact on the bed surface where shear stresses are imposed immediately behind the turbine ($0D \leq x \leq 4D$). Both models impose more or less similar shear stress features, two peak regions as shown in the figure (A/A' and B/B'). For VBM [a] however, a more comprehensive detail of the bed shear stress is seen when compared with [b], showing more character near the turbine (A). [a] predicts stronger shear stresses on the bed behind the turbine and this is due to the generation of vortex. It is found that the velocity gradient near the bed is higher.

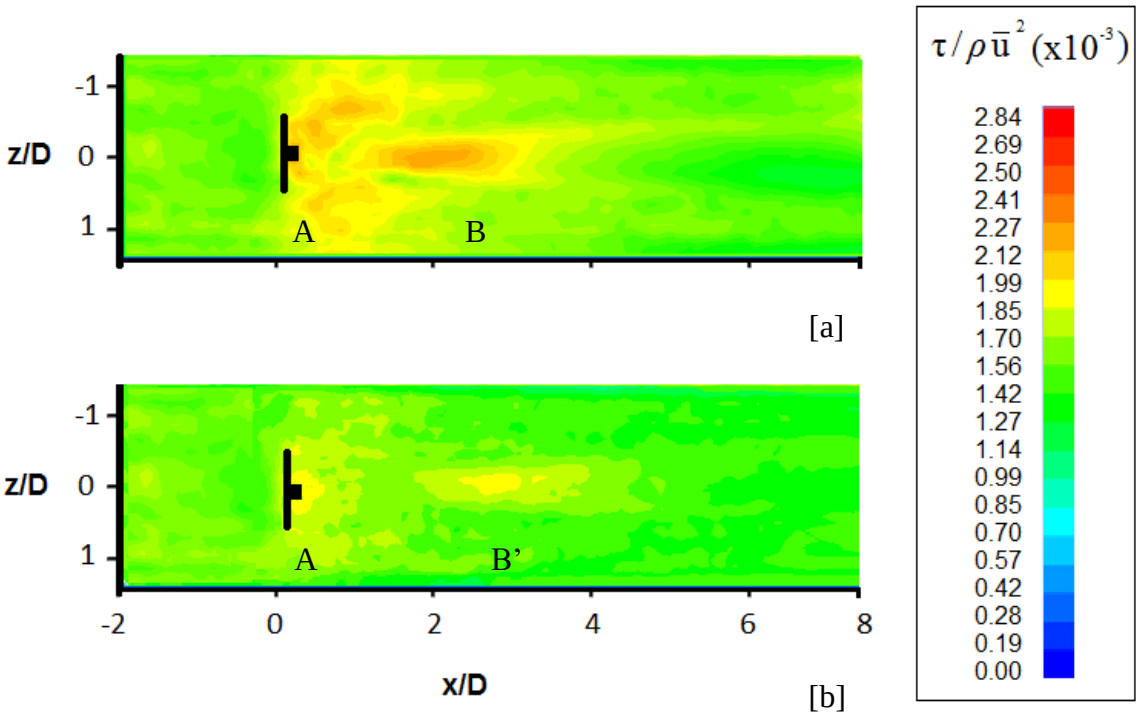

Figure 5-11 – Contour maps of bed shear stresses [a] VBM and [b] ADM.

5.3 UoH (University of Hull)

The data gathered from Jordan et al. (2015) is used for validating the CFD model in steady flow condition. One of the main reasons for considering this experiment is to further validate VBM at lower blockage ratio condition.

5.3.1 Experiment Conditions

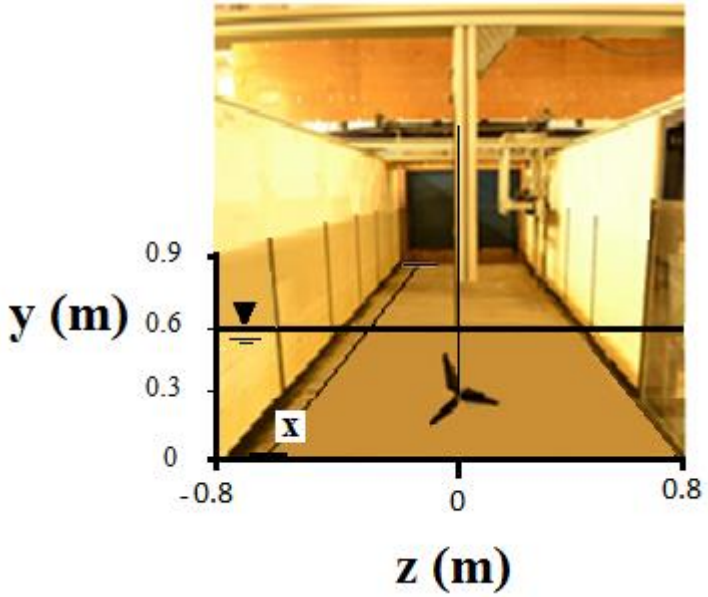

Figure 5-12 – Flume description (upstream view).

This experiment took place at the Total Environment Simulator at the University of Hull. The recirculated flume has dimensions of 1.6m wide, 0.6m deep and 10m long. The diameter of the turbine is 0.2m, producing a blockage effect of 3.2%.

Comparing this with Tedds et al. (2014) experiment, the turbine in this case is smaller in size and of different design. The vertical profiles of velocity and TKE are measured by an ADVP mounted on a moveable frame beneath support. The turbine is fixed on a thin, rigid support at centreline that can be vertically re-positioned. The turbine is positioned at 300mm above bed with TSR of 5.5. The bed is placed with plywood boards covered with sand of D_{50} = 425µm. The mean flow velocity at channel inlet is 0.25m/s.

5.3.2 Numerical Model Setup

The model is setup with a total sum of ≈ 0.9 million tetra/mixed cells under steady state conditions described in Chapter 3. VBM is set as described in sections 4.5.1 and 4.5.3.2 and the rotor specification is defined as shown in Table 5-4 and Table 5-5. The ADM method is not employed in this investigation. The flow vertical profiles are measured along the channel depth at 2, 3, 4 and 5 diameters behind the turbine (see Figure 5-13).

Table 5-4 – General rotor setup.

Number of rotor zones	1
Number of blades	3
Rotor radius	0.1m
TSR	5.5
Tip effect	96%
Disk pitch angle	90
Blade pitch	4
Blade flapping	0

Table 5-5 – Geometrical rotor setup.

Radius (r/R)	**Chord (m)**	**Twist (deg)**
0.2	0.025	19
0.3	0.022	10
0.4	0.02	6
0.5	0.018	4
0.6	0.015	2
0.7	0.015	1.5
0.8	0.01	0.8
0.9	0.008	0.4
1	0.008	0

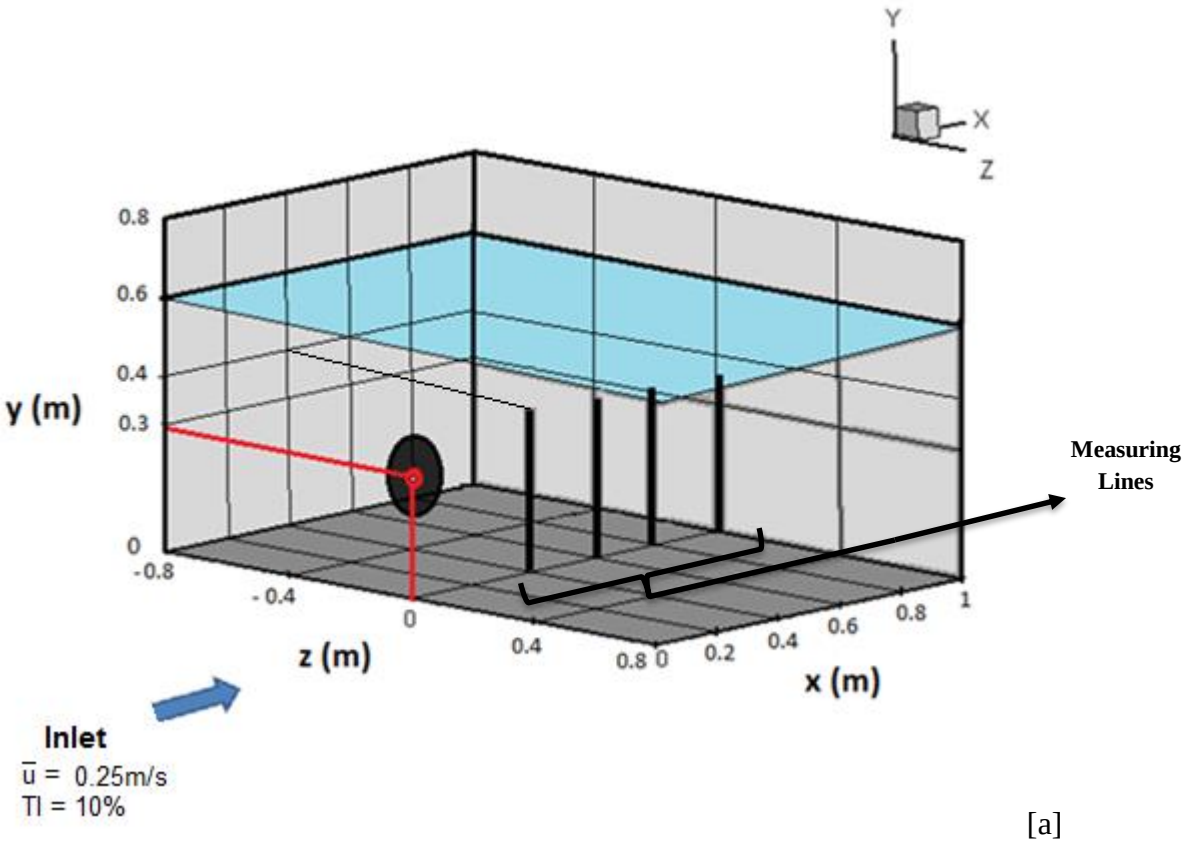

[a]

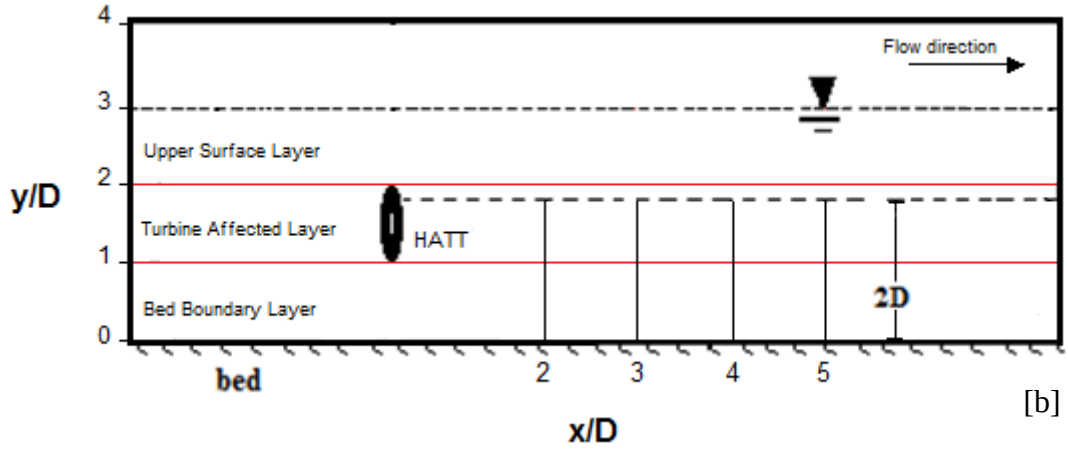

[b]

Figure 5-13 –Model description for vertical measuring positions [a] 3-dimensional view, [b] side view.

5.3.3 Results and Discussion

It is important to highlight that the blockage effect in this experiment is 5.2 times smaller (3.2%) than the previous case (16.5%) which is more physically realistic, and the mean velocity is 3.6 times slower, which means the turbine impact on flow is expected to be smaller. To assist the discussion, the water column is divided into three regions, where y/D <1 is the bottom boundary layer, 1 < y/D < 2 is the turbine-affected layer (turbine region) and y/D > 2 is the upper surface layer, as shown Figure 5-13[b].

Figure 5-14 presents the vertical profiles of normalised velocity at inlet. It is clear that the velocity is slightly underestimated at the turbine-affect layer, however, closer to the bed (y/D < 0.5) the velocity is well predicted. The channel bed is introduced with a constant shear stress condition of 0.02Pa. At the upper surface layer, the open channel (free surface) is subjected to atmospheric pressure (101,325Pa) and the air being stationary (air velocity is 0m/s). The velocity of water flow near the surface tends to reduce (velocity dip) due to the frictional resistance between the water and air at interface. This behaviour is not seen in the experimental results.

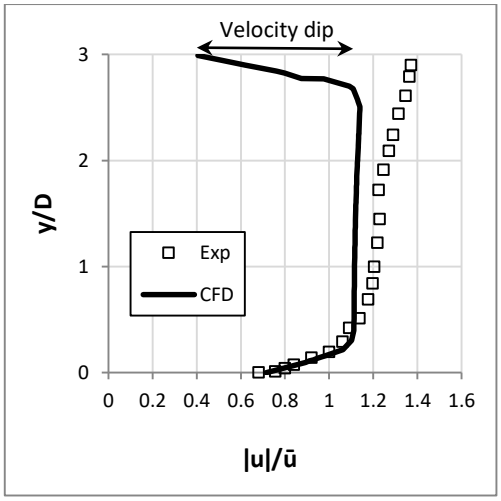

Figure 5-14 – Vertical profile of normalised velocity at the inlet.

Figure 5-15 presents the vertical profiles of normalised streamwise velocity at the centre line of the channel for both experimental and computed data at 2D, 3D, 4D and 5D downstream. Overall, the computed velocities compare reasonably well with experimental data. At 2D

however, the computed velocity deficit is seen at a higher level than that in the experiment. The deficit accounts for a larger proportion of water depth than in the lab data. This error reduces at the other downstream sites. The "W" shape in streamwise flow velocity distribution in the previous case cannot be found in this case at the turbine region. This is because the flow velocity in this experiment is much weaker (0.25m/s); in addition to the smaller-sized turbine e.g., low blockage.

Consequently, the pressure drop behind the turbine is not strong enough at the turbine face to force the flow to squeeze through the hub section. The reduction in the velocity at 2D is shown as a large deficit between y/D = 1D and y/D = 2D. At bed, it is clear that the flow speed reduces due to the roughness introduced by the sand layer.

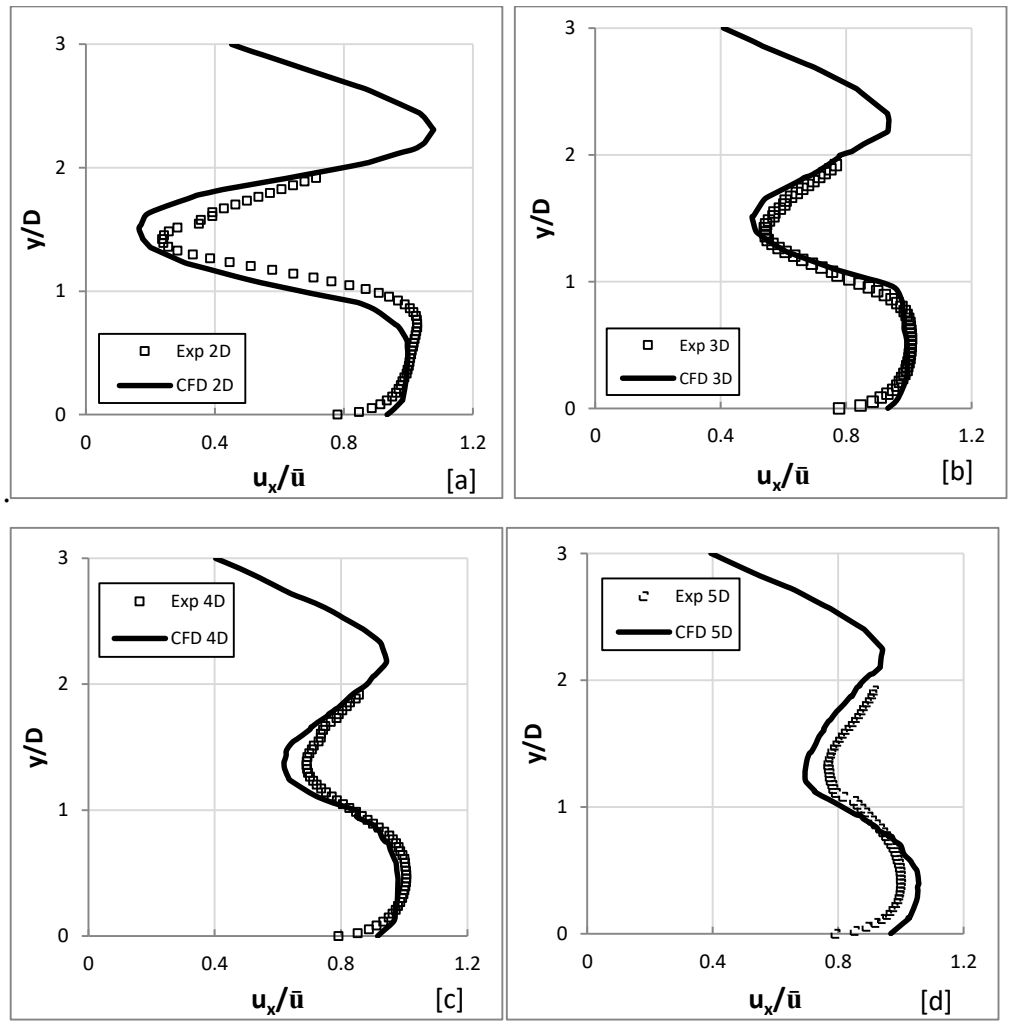

Figure 5-15 - Comparison of vertical profiles between measured and computed normalised streamwise velocities at 2D [a], 3D [b], 4D [c] and 5D [d] downstream along the centreline.

At x = 2D and 3D, the bottom boundary layer is affected by the deficit above. The flow is accelerated due to presence of the turbine but tends to be fairly uniform. At x > 3D, the bottom boundary layer appears to be less affected as the acceleration becomes less obvious. The flow velocity at the upper surface layer tends to reduce closer to the surface due to the influence of the interface explained above.

Figure 5-16 shows the positions of maximum velocity deficit values across the water depth along the channel length. It is found that the maximum velocity deficit tends to drop in height towards the channel bed as the flow moves downstream away from the turbine. The presence of the free surface allows more water to pass over the turbine by adjusting its elevation to create more passage space and therefore the higher water head tends to push the wake down. This behaviour was also observed in the experimental investigation conducted by Tedds et al. (2014). The computed results agree very well with the experimental data.

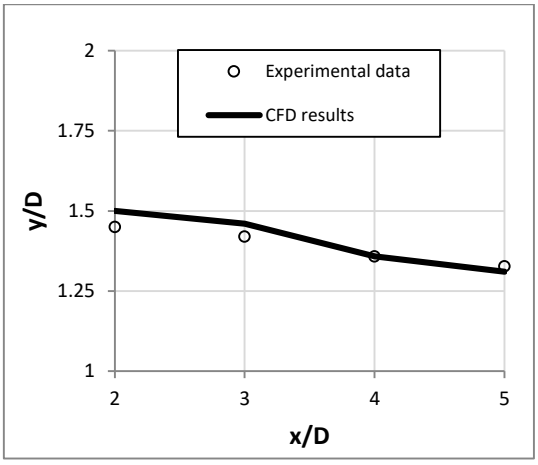

Figure 5-16 - Vertical locations of maximum velocity deficit at 2D, 3D, 4D and 5D downstream.

Figure 5-17 shows the contour of streamwise velocity along the vertical centre plane. It is clear that the wake undergoes a downward shift moving further downstream. In addition, the free surface shows a slight rise in front of the turbine followed by an immediate drop behind it due to the pressure change imposed by the turbine. This induced pressure creates a velocity change that influences the free surface elevation. In front of the turbine, the velocity reduces creating a surface rise; however, above the turbine the accelerated flow forces a surface drop.

This surface behaviour is previously seen in an experimental investigation conducted by Sun et al. (2008).

It is also clear that the "W" shape in streamwise velocity distribution occurs much closer to the turbine at x/D < 1.6. The highest flow deficits are found behind the turbine blades where maximum pressure occurs, especially below the hub. The accelerated flow is found to dissipate quicker in the bed boundary layer. This happens due to the different boundary conditions found below and above the turbine. The channel bed induces turbulences that enhance the mixing process of flow and therefore speeds up recovery, whereas above the turbine, the free surface does not contribute to the mixing of flow by being shear stress free.

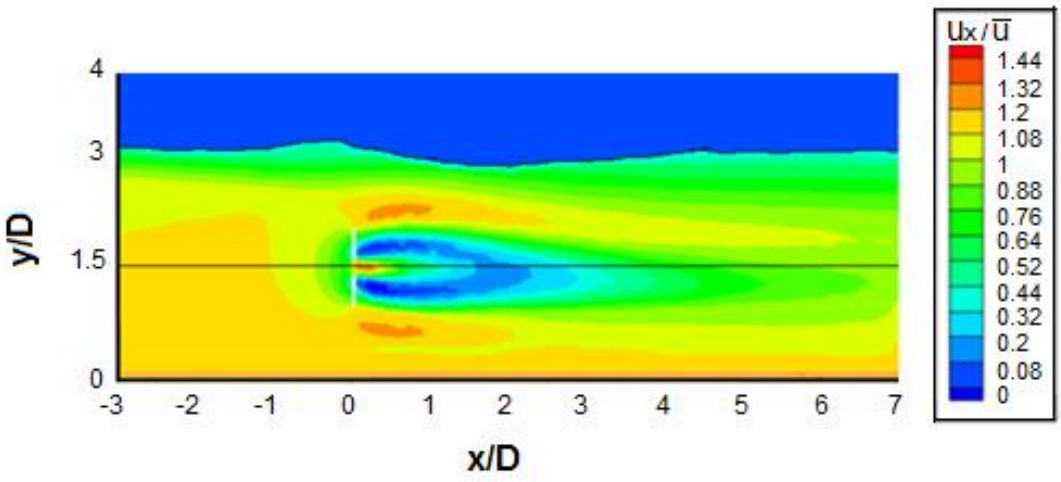

Figure 5-17 - Contours of streamwise velocity along the vertical centre plane.

From the model, Figure 5-18 shows the contours of streamwise velocity across the channel at turbine centre plane top-down view. The contours confirm that the wake undergoes a slight shift towards the left side of turbine centreline when looking from upstream. This occurs due to the asymmetric flow speed deficit behind the turbine that is higher at the left side, causing the flow to slant towards it. This was not seen in Figure 5-5 (case 5.2) due to the lateral space restriction.

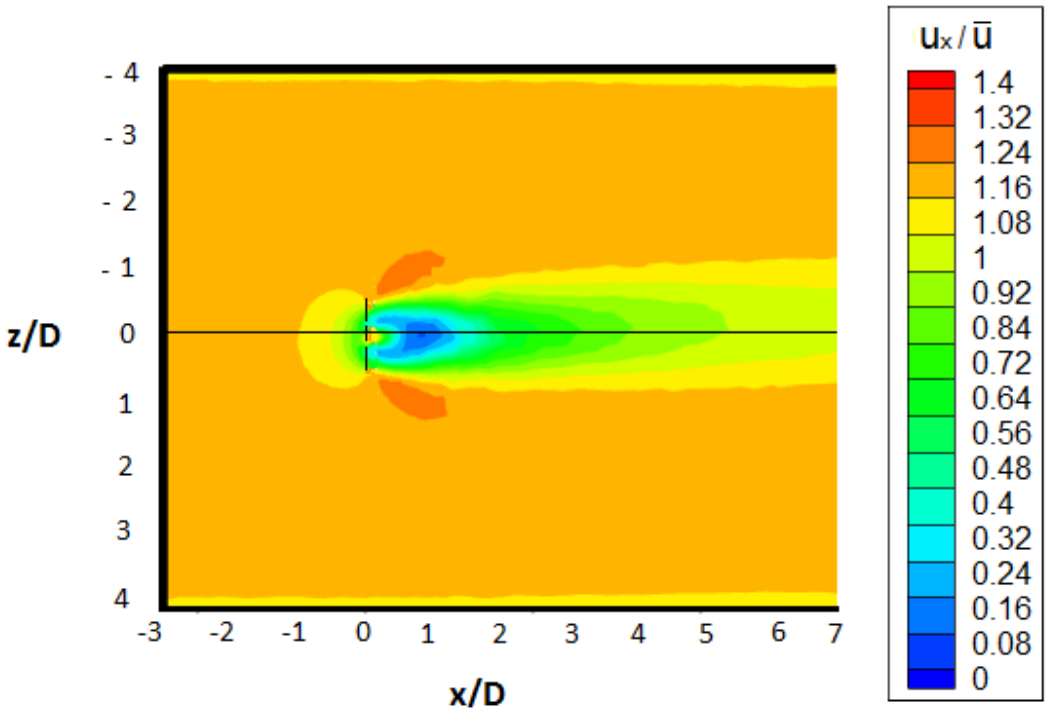

Figure 5-18 - Plan view of contours of streamwise velocity along the centre plane.

Figure 5-19 shows the vertical profiles of vertical velocity across water depth along the centreline of the channel, where negative values specify that the flow is moving downwards and vice versa. Overall, the computed results follow very well with the measured data with slight disagreement above the turbine hub region.

It is clear that the flow velocity predominantly shows a downward motion at 2D, 3D, 4D and 5D, which suggests that the wake may possibly have shifted towards the left-hand side to place the measuring line eccentric to the centreline and therefore capturing the downward velocity alone. At 2D, the flow undergoes multiple changes in terms of direction, especially at the turbine-affected region. The velocity shows strong variation that gradually recovers to negative flow.

The minimum velocity peaks drop in height at the first two locations (2D-3D) from 1.5D to 1D and then rise back to 2D at x = 4D, 5D. At bed boundary layer, the flow is affected by the turbine rotation and produces vertical flow velocity in the region that is underestimated by the model at 2D. At x > 2D, the measured flow velocity shows largely negative values due to the shift of the wake. At 3D however, the flow becomes zero over a considerable length above the bed.

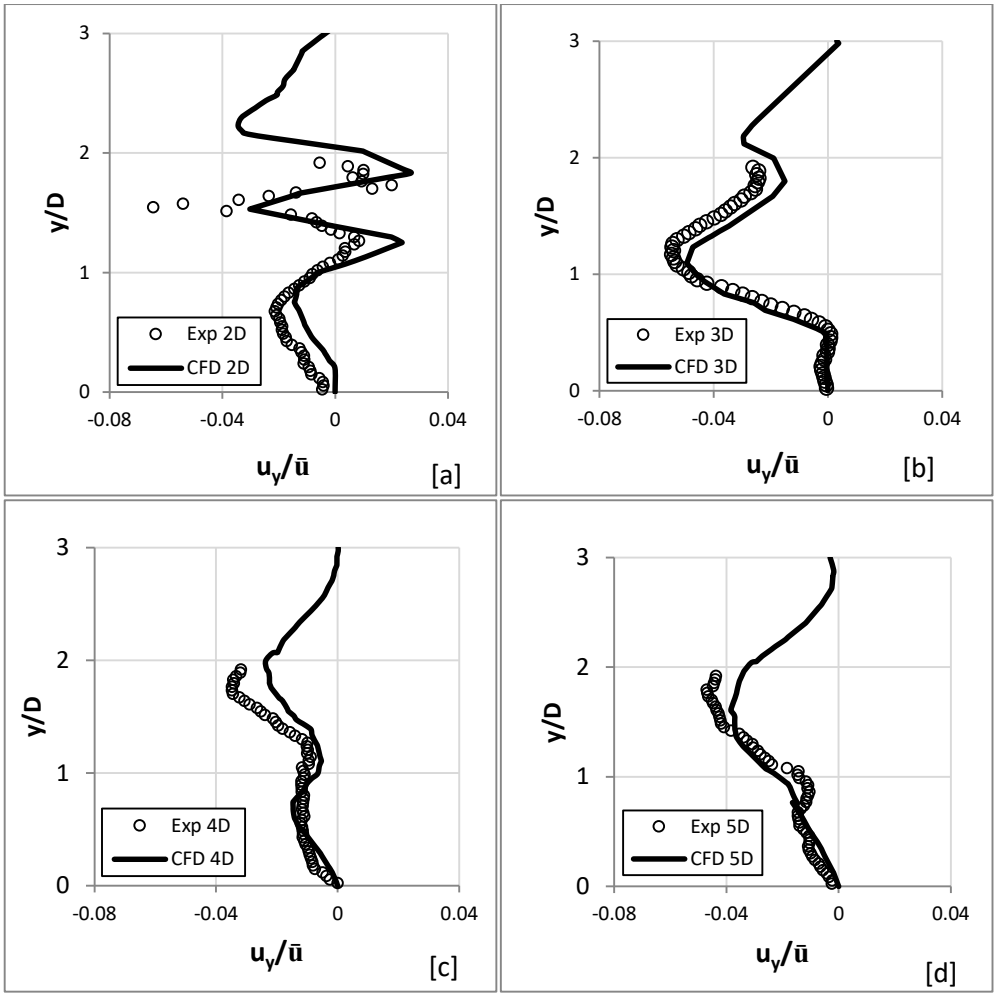

Figure 5-19 - Comparison of vertical profiles between measured and computed normalised vertical velocities at 2D [a], 3D [b], 4D [c] and 5D [d] downstream along the centreline.

Figure 5-20 shows the vertical profiles of cross-stream velocity along the centreline at several measuring sites where positive values specify from left to the right of the flow and vice versa. Overall, the computed results show good agreement with measured data, being able to capture the velocity changes. It is clear from results that the velocity is dominant in the positive direction (left to right).

Furthermore, near the bed, this velocity is found to increase going further downstream, i.e., gradually increasing in cross-flow from left to right. This occurs due to the wake path deviation seen in Figure 5-18. In contrast, at the surface, the cross velocity decreases gradually to become zero. At the turbine region (x = 2D), the flow undergoes stronger variations due to turbine rotation. Moving further downstream (3D, 4D and 5D), the wake shifts downwards and left, resulting in a gradual reduction in flow speed.

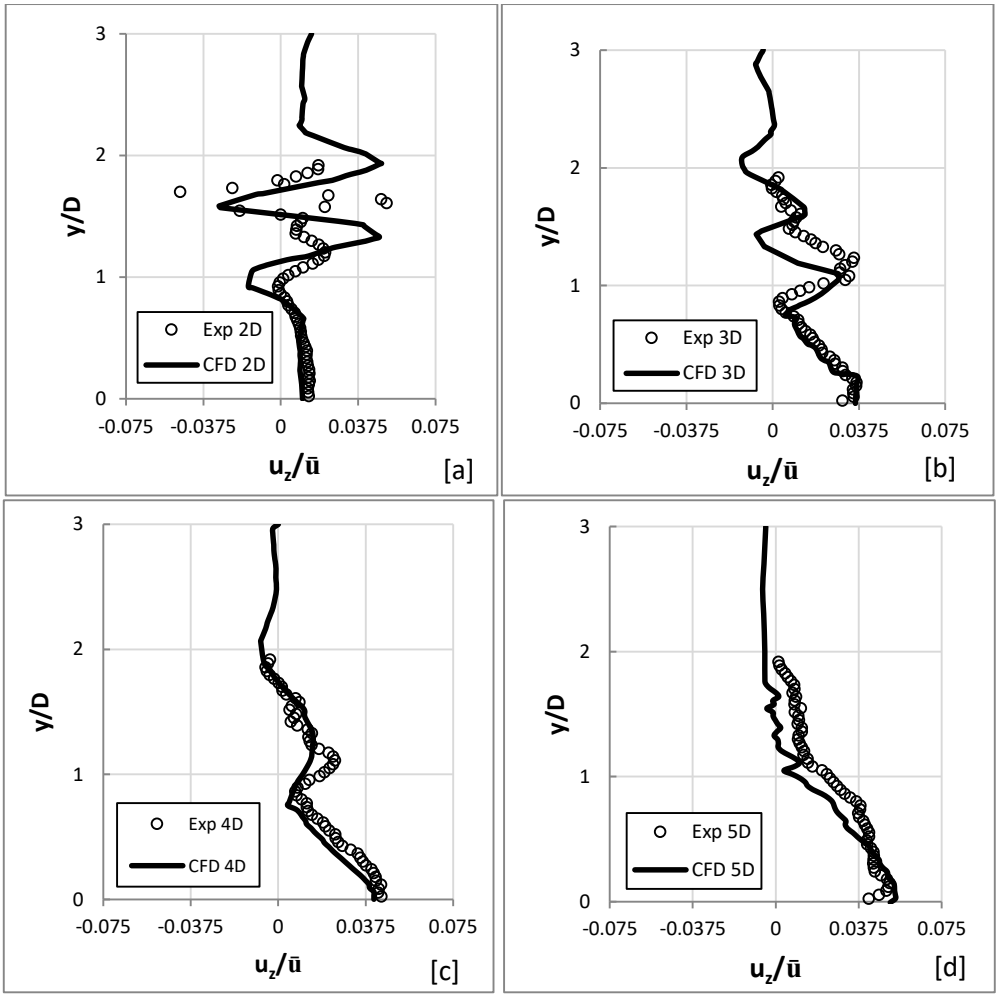

Figure 5-20 - Comparison of vertical profiles between measured and computed normalised cross-stream velocities at 2D [a], 3D [b], 4D [c] and 5D [d] downstream along the centreline.

Vertical profiles of TKE along the centre line at 2D, 3D, 4D and 5D are shown with measured data in Figure 5-21. The computed predictions follow very well the experimental data. However, the TKE values are slightly under-estimated, by less than 10%. High TKE values are generated at the turbine-affected region peaking around 1D-1.5D. Subsequently, the TKE generated from the turbine diffused/transported down into the bed boundary layer affect the top of the bed boundary layer (0.7D-1D) as it flowed downstream. TKE is also found at the bed due to the flow bed interaction. At the top surface layer, no TKE is visible.

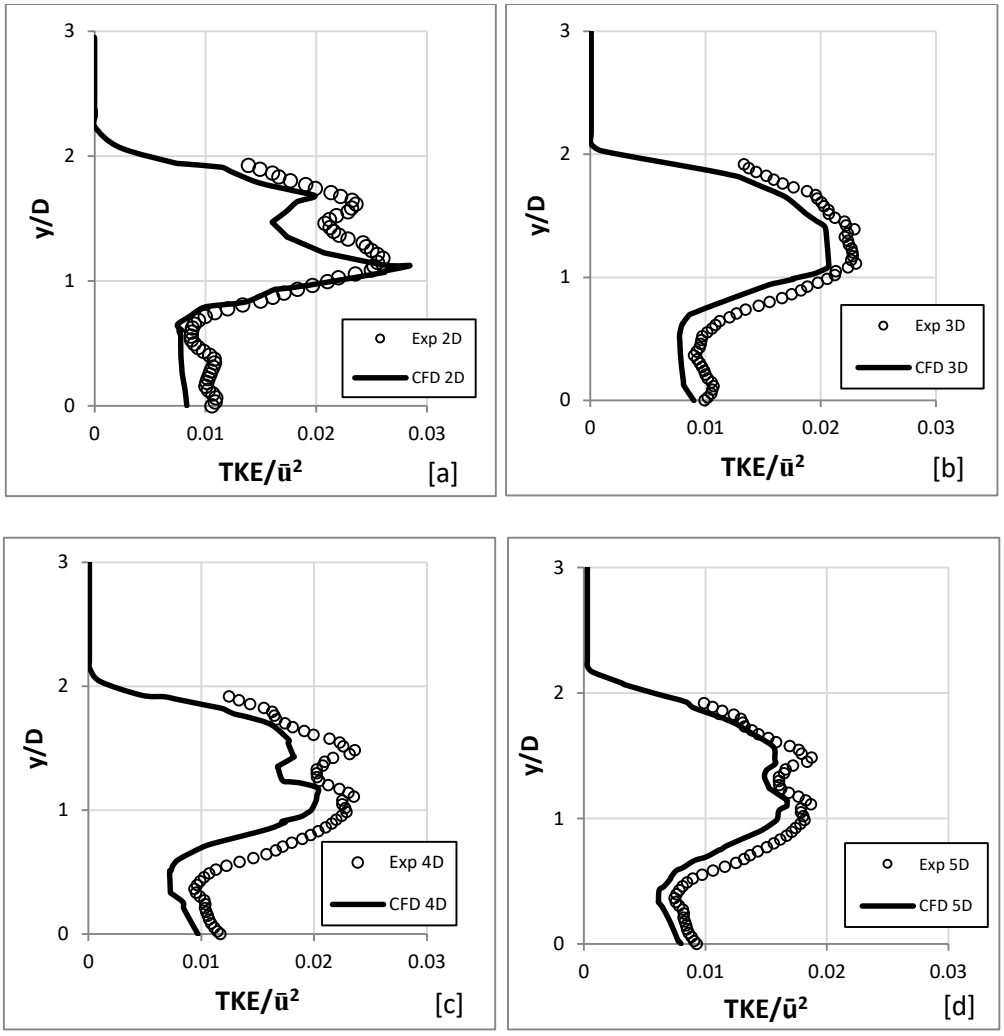

Figure 5-21 - Comparison of vertical profiles between measured and computed normalised turbulent kinetic energy at 2D [a], 3D [b], 4D [c] and 5D [d] downstream along the centreline.

On average, the error in streamwise velocity is within 9%, the vertical flow velocity 13% and the cross-flow velocity 12% at all sites. Similarly, the average error in TKE values is within 15%.

5.4 UoL-2

The experimental data of Henriques et al. (2014) is used to validate the model's prediction when the current is combined with streamwise waves. Firstly, the prediction is validated for wave only when the turbine is not present. Then the model's prediction is validated when a turbine is present.

5.4.1 Experiment Conditions

The experiment carried out by Henriques et al. (2014) took place in the same high speed flume used by Tedds et al (2014). In both parts of the experiment the flume dimensions are 0.78m deep, 7m long and 1.4m wide. Waves are generated via a paddle wave maker at the inlet where a current with mean velocity of 0.9m/s is also imposed in the same direction. For both cases, the waves have the parameters as shown in Table 5-6.

The orbital velocity (U_δ) at the edge of the wave boundary layer is defined as:

$$U_\delta = \frac{\pi H}{T \sinh(Kh)} = 0.0621 m/s \tag{5.1}$$

where H is the wave height, T is the wave period, h is the water depth and K is the number of waves. The wave number is defined as:

$$K = \frac{2\pi}{L} = 3.142 \tag{5.2}$$

where L is the wavelength.

Table 5-6- Waveform characteristics.

Wave Height H(mm)	Frequency f(Hz)	Period T(s)	Wavelength L(m)	d/L	Re	$\frac{U_\delta}{\bar{u}}$
86	1.33	0.75	2	0.39	702000	0.069

5.4.2 Numerical Model Setup (University of Liverpool)

Part 1 (No turbine)

The model is setup with a total of ≈ 0.6 million tetra/mixed cells. The models' inlet and outlet condition is set as described in Chapter 3. The wave parameters and current conditions are defined at the channel inlet. The waves are defined as 2nd order Stokes waves. The surface elevations as well as vertical profiles of velocity in horizontal and vertical directions are monitored at two meters from inlet, where the turbine will be placed (Figure 5-22).

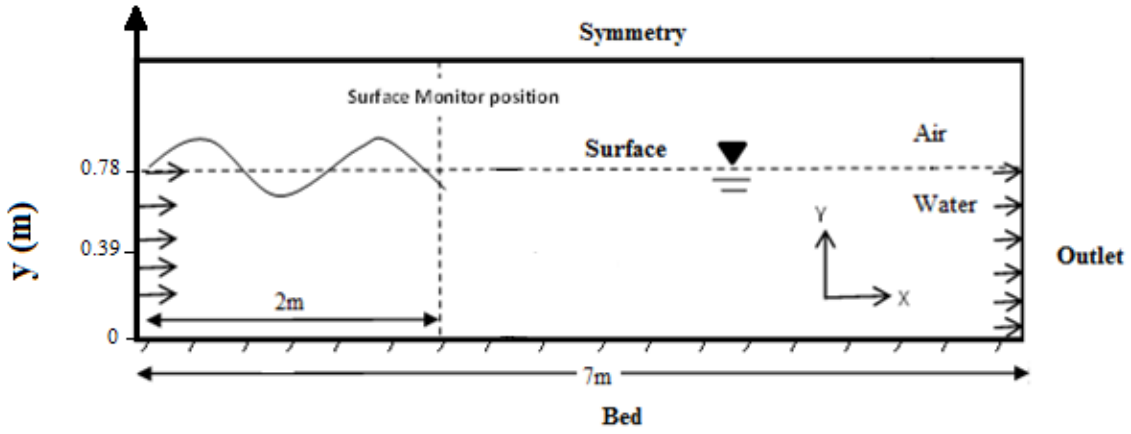

Figure 5-22 - Side view model description (no turbine).

Part 2 (Turbine)

A three bladed 0.5m diameter turbine is employed at 2m from inlet. The operating parameters are the same as those set in Tedds (2014) experiment. The model is developed with a total of

≈ 1 million tetra/mixed cells. The same model setup in part 1 is defined here in part 2. In this part of the test, the horizontal profiles of the three velocity components are measured (Figure 5-23). In addition, the surface elevation at 1.5D behind the turbine is measured to investigate the impact of turbine on the wave parameters.

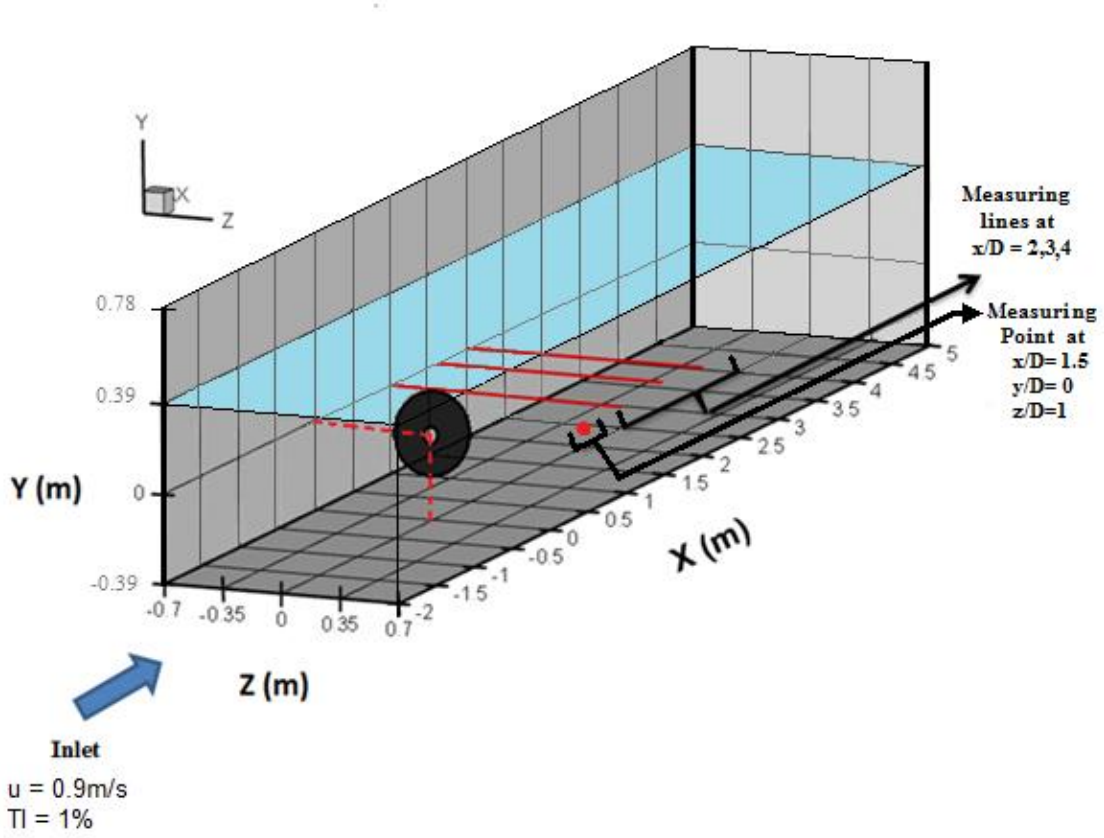

Figure 5-23 - Plan view of the horizontal measuring locations at 2D, 3D and 4D downstream along centreline.

In both cases, the model is run over 100 wave cycles before any data is collected to ensure the wave has converged. The last three wave cycles are averaged to achieve the averaged values that can compare with the measured data.

5.4.3 Results and Discussion

Part 1

Computed free surface elevation over a wave cycle is compared with the measured data in Figure 5-24, where t is time and T is the wave period. The computed surface elevation followed the measured data very well. However, the surface elevation at crest was slightly underestimated.

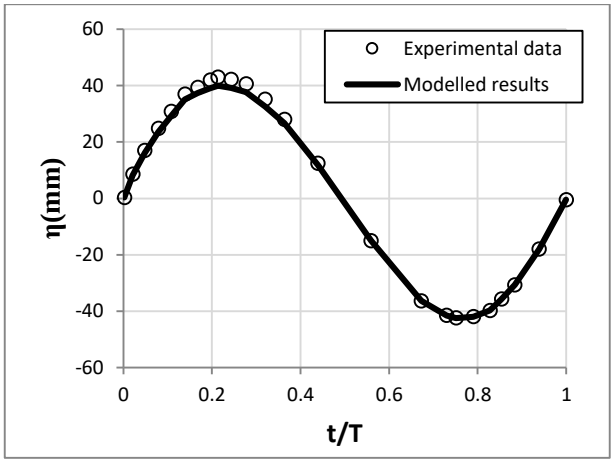

Figure 5-24 – Comparison of surface elevation between measured and computed results for one wave cycle.

Figure 5-25 presents the vertical profile of streamwise velocity under wave crest and trough from the model results and measured data. Computed results show excellent agreement with experimental data. Closer to the surface however, the model slightly under-predicts the flow velocity under wave crest. This is due to the fact that the surface elevation under the wave crests (on shore) is slightly underestimated, affecting the wave-induced velocity beneath it (Figure 5-24).

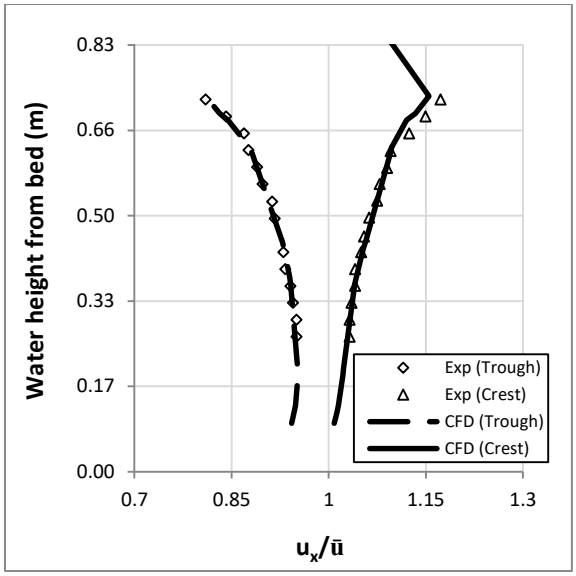

Figure 5-25 – Vertical profiles of horizontal velocity for one wave cycle at crest and trough. The water depth is defined from the mean water level (MWL) to the bed.

Figure 5-26 compares the vertical profile of vertical velocities under wave angles 0˚ and 180˚ respectively. Model results follow the experimental data very well; however, the vertical flow velocity under wave angle 180˚ is slightly under-predicted.

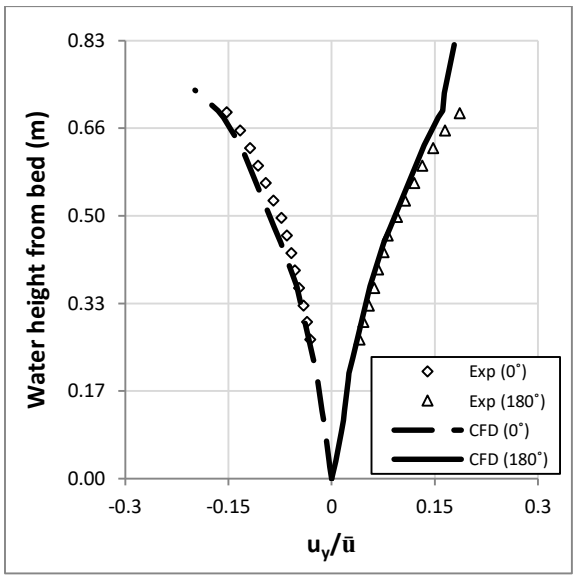

Figure 5-26 – Vertical profiles of vertical velocity for one wave cycle at maximum and minimum wave-induced velocities.

Part 2

Figure 5-27 shows the comparison of computed and measured wave-cycle averaged streamwise velocity across the width of the channel at the different stations downstream of the turbine. The computed results show reasonable agreement with experimental data. At x = 2D however, the computed flow velocity is slightly out of position leaning more towards the right-hand side in comparison with the measured data.

Furthermore, the velocity at turbine edges is overestimated, which is due to the blade tip effects not being fully captured. At 3D, computed results slightly underestimate the velocity results but show better agreement as the flow travels further downstream (4D).

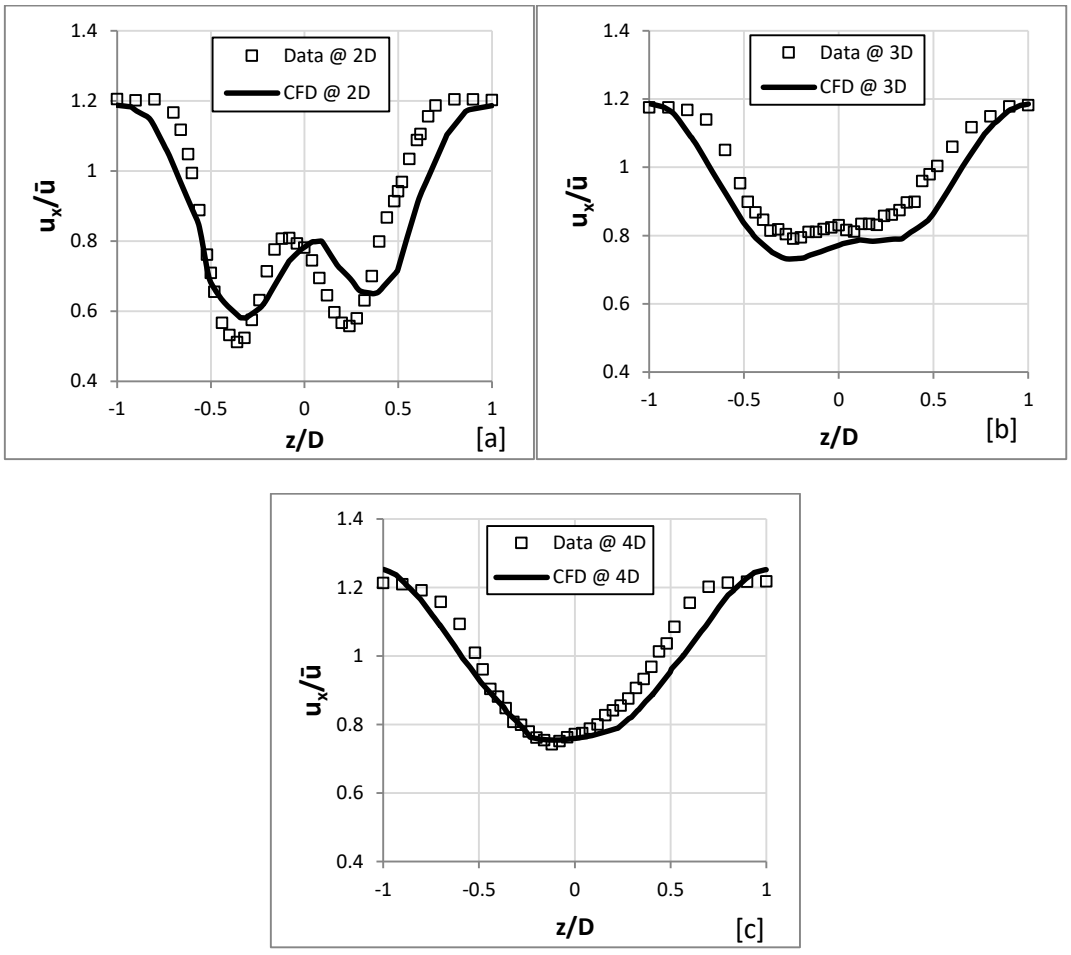

Figure 5-27 - Comparison of horizontal profiles between measured and computed wave-cycle averaged normalised streamwise velocities at 2D [a], 3D [b] and 4D [c] downstream along the centreline.

Measured data and computed results show a “W” distribution with an asymmetric behaviour across the width of the channel, leaning more towards the negative (left-hand side) in all three positions due to the operating nature of the turbine. This feature agrees well with the previous steady flow only condition as in Figure 5-5.

Further downstream, the wake gradually recovers and the “W” pattern starts to disappear. At 4D, it is clear that the velocity distribution changes to a “U” shape while at 3D it is undergoing transition. It is found that when waves are present the distribution transformation takes place completely at 4D, whereas for steady flow only it is delayed up to 6D. This indicates that the presence of waves is enhancing turbulent mixing and therefore shortening the length of the wake behind the turbine.

Figure 5-28 presents the computed and measured wave-cycle averaged vertical velocity distribution across the channel at 2D, 3D and 4D downstream. Computed results follow similar patterns as in previous steady flow cases (Tedds et al., 2014) with slight discrepancies. A strong asymmetry of velocity distribution is found across all the sites, especially at 2D where the maximum velocity in the negative direction (off shore) is about 15% of ū, whereas that in the positive direction (on shore) is less than 11%.

The VBM results underestimated the velocity peaks slightly at turbine tips (z = +/-0.25D) at all sites. In addition, the VBM results show zero velocity at +/- 1D, whereas in the experimental measurements, it shows positive flow velocity. The complex flow behaviour at z ≈ 0.4D - 0.6D in the experimental measurements is not seen in the computed results; instead, it shows a smooth velocity rise.

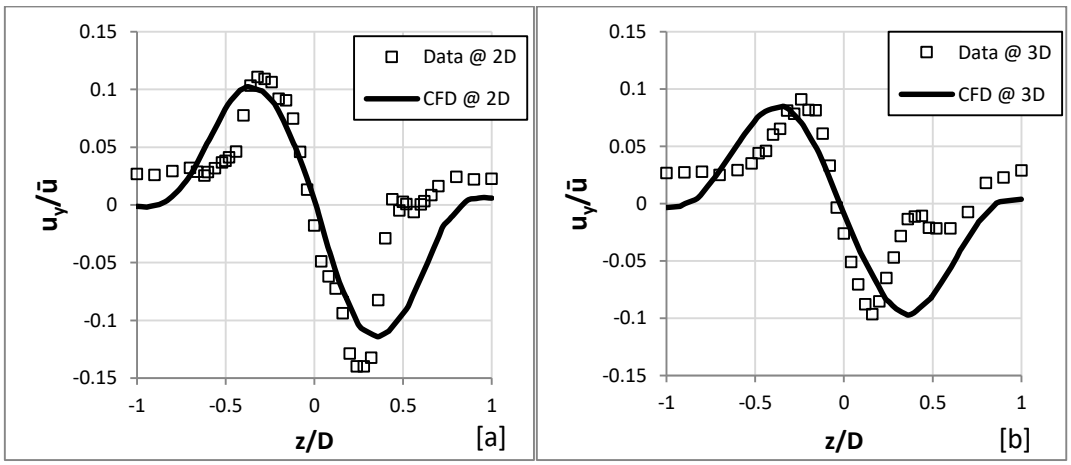

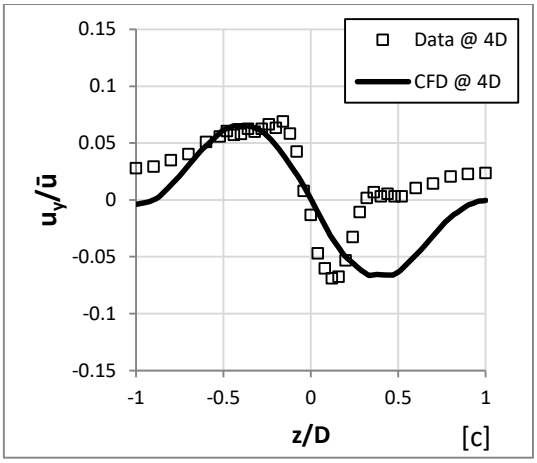

Figure 5-28 - Comparison of horizontal profiles between measured and computed wave-cycle averaged normalised vertical velocities at [a] 2D, [b] 3D and [c] 4D downstream along the centreline.

Figure 5-29 presents the measured cross-stream velocity distribution across the channel width at 2D, 3D and 4D downstream. In comparison with the model results, it can be seen that the velocity remains positive at the left-hand side of the hub and mostly negative in the right-hand side, which suggests flow is moving towards the wake centre, as shown for steady flow.

At z = -0.5D and -0.125D at x = 2D, there are two velocity peaks in the positive direction. In contrast, there is only one peak at z = 0.65D at the opposite side of the channel (z > 0D), but much larger magnitude ($u/\bar{u} \approx 0.7$). This velocity asymmetric behaviour is also noticeable at x = 3D. However, at x = 4D this pattern cannot be found at all. This is due to the unsymmetrical behaviour of flow when passing through a turbine as seen in Figure 5-27.

To further illustrate this point, Figure 5-30 sketches out the velocity vectors on the XZ plane before and after the turbine. The small (red) circles denote the area between the peaks x = -0.25D and -0.125D. The big (blue) circles denote the outer peaks at x = -0.5D and 0.6D. In the cross-stream velocity when flow arrives at the turbine, part of the flow converges through the small gap between the hub and blade root and then it diverges immediately once it passes. This behaviour produces the first set of opposing peaks near the centre (e.g. x = -0.125D and 0.25D) which quickly dissipates beyond this point.

Moving further away from the centre, the blade operation induces an inward movement of flow in the form of a vortex, resulting into the second set of opposing peaks (x = -0.5D and 0.6D).

Overall, the model tends to under-predict the flow velocity magnitude at all locations. However, the double positive peaks and the single negative peak are well captured by the model.

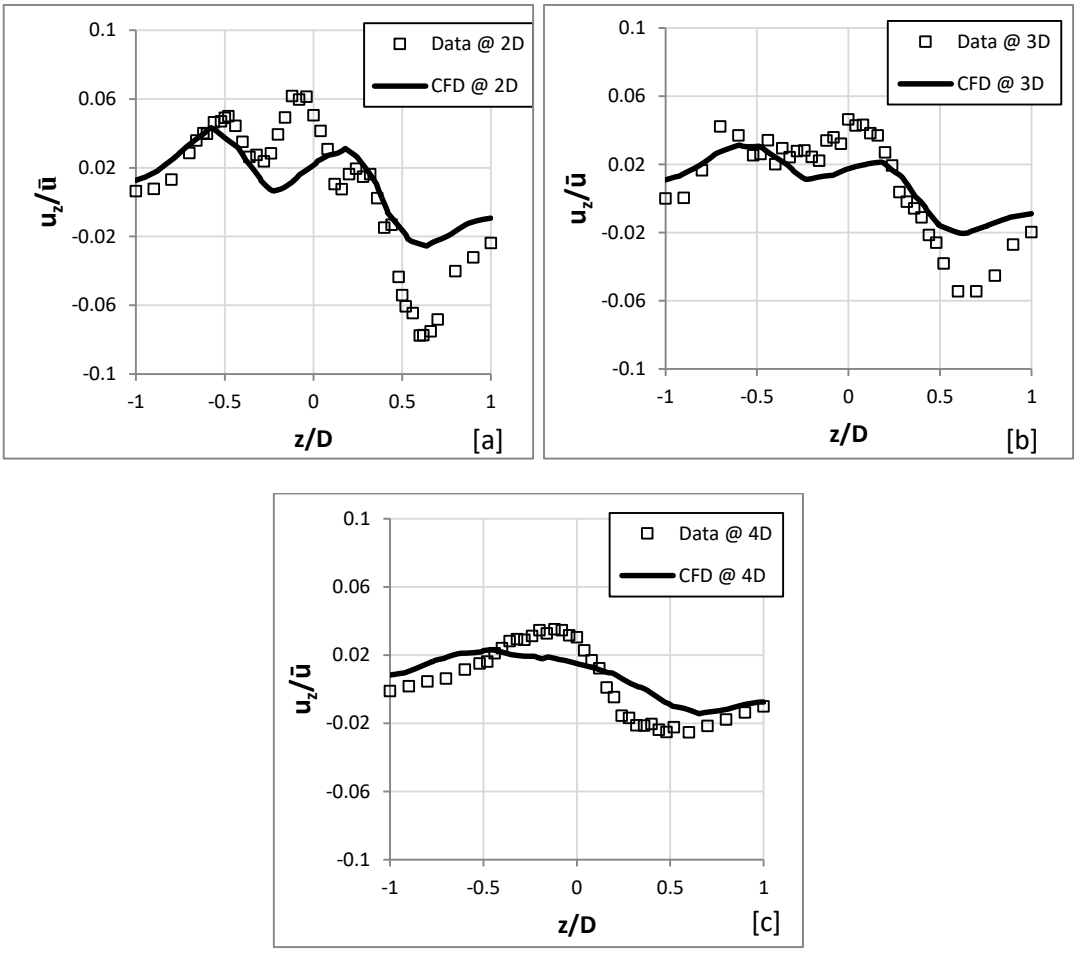

Figure 5-29 - Comparison of horizontal profiles between measured and computed wave-cycle averaged normalised cross-stream velocities at [a] 2D, [b] 3D and [c] 4D downstream along the centreline.

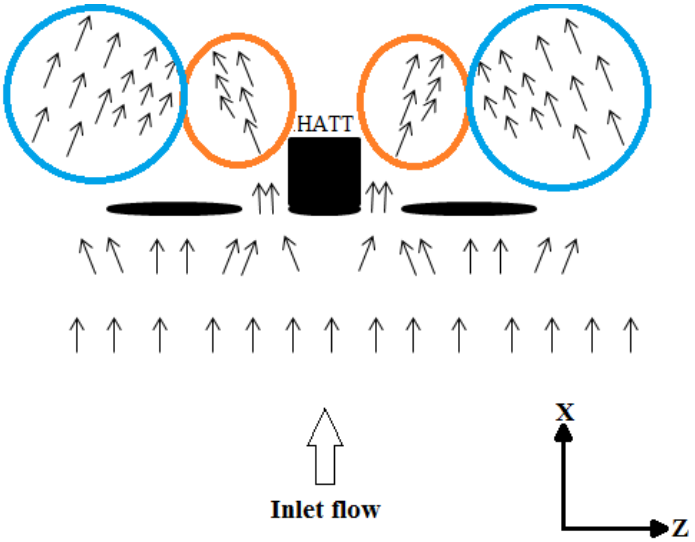

Figure 5-30 - Vectors of current when crossing the turbine.

With the presence of surface waves, the flow undergoes various changes within one wave cycle, involving forward and backward oscillating motion. This complex motion is further affected by the presence of the turbine and its rotation. The resultant flow structure therefore can be fairly complicated and dynamic.

The overall errors for the computed velocities on average are 5%, 8% and 28% for streamwise, vertical and cross-stream respectively.

Similarly, the presence of the turbine and its operation can influence the hydrodynamics and hence change the way the surface wave propagates. Figure 5-31 compares the computed and measured free surface variations during one wave-cycle for with and without turbine in Henriques et al. (2014) experiment. Comparing with the measured value, it is found that the model underestimates the surface elevation slightly; however, the wave follows the measured data very well.

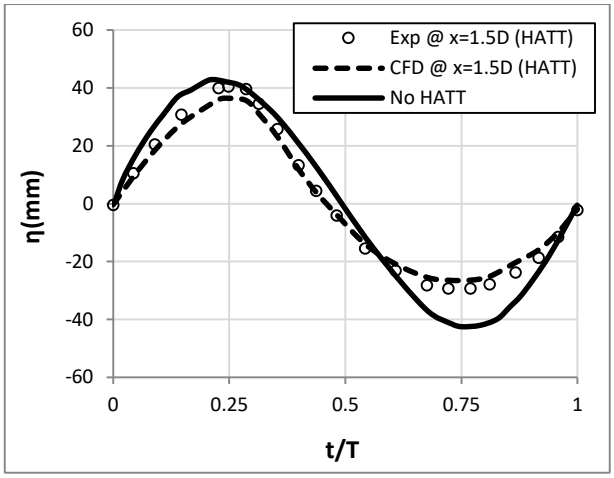

Figure 5-31 - Comparison of surface elevation between measured and computed results at 1.5D downstream.

Computed results provide additional evidence to that of experimental data where the wave shape is directly affected by the turbine operation. Firstly, it is found that the overall wave height reduces by almost 17% when propagating over the turbine. This reduction appears on both onshore and offshore sides, especially at the wave trough (offshore side). The wave-induced flow when trough ($t/T > 0.5$) tries to moves in the opposite direction of current (upstream) and the flow speed slight reduces. In addition, the presence of turbine causes further slowdown of the flow. Consequently, the pressure in the wake region rises and hence leads to the increase in water level. Looking at the onshore amplitude ($t/T < 0.5$), the accelerated flow induced by the turbine causes the current beneath the waves to flow faster and hence leads to the slight decrease in water level.

Secondly, the phase shift behind the turbine in the wake area becomes clear and the wave form deviates from its original shape. In particular, the onshore peak occurs slightly later and the offshore peak takes place slightly earlier. Combined with the rise in the water level during the offshore period, the wave shape becomes non-linear, closer to a Stokes 3rd order wave.

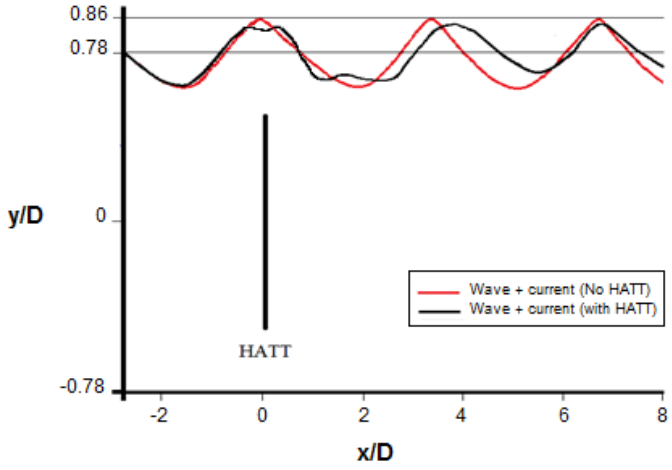

Figure 5-32 - Comparison of surface elevation for with and without turbine at turbine centreline.

Thirdly, Figure 5-32 shows the computed free surface elevation snapshot at t= 151s for with and without turbine along the length of the channel. The results suggest that the wave length has slightly increased by 19%.

Figure 5-33 shows the top view of the free surface; [a] shows the contours of vertical-displacement, where the yellow denotes the surface is offshore (below MWL) and the orange denote onshore (above MWL). It is found in this study that the wave alignment undergoes transformation when passing over the turbine area. Initially, the wave shows a straight alignment upstream. Downstream however, the wave tends to curve around the turbine region to form a crescent shape. It is also found that the turbine causes the wave length to temporarily increase for the first few diameters.

Figure 5-33 [b] shows the contours of streamwise velocity along the free surface. The wave speed is at maximum onshore and minimum offshore. At the turbine region, it is found that the turbine accelerates the flow speed at the surface, creating a hot spot of speed immediately behind the turbine site, which causes the wave crest line curvature as in [a].

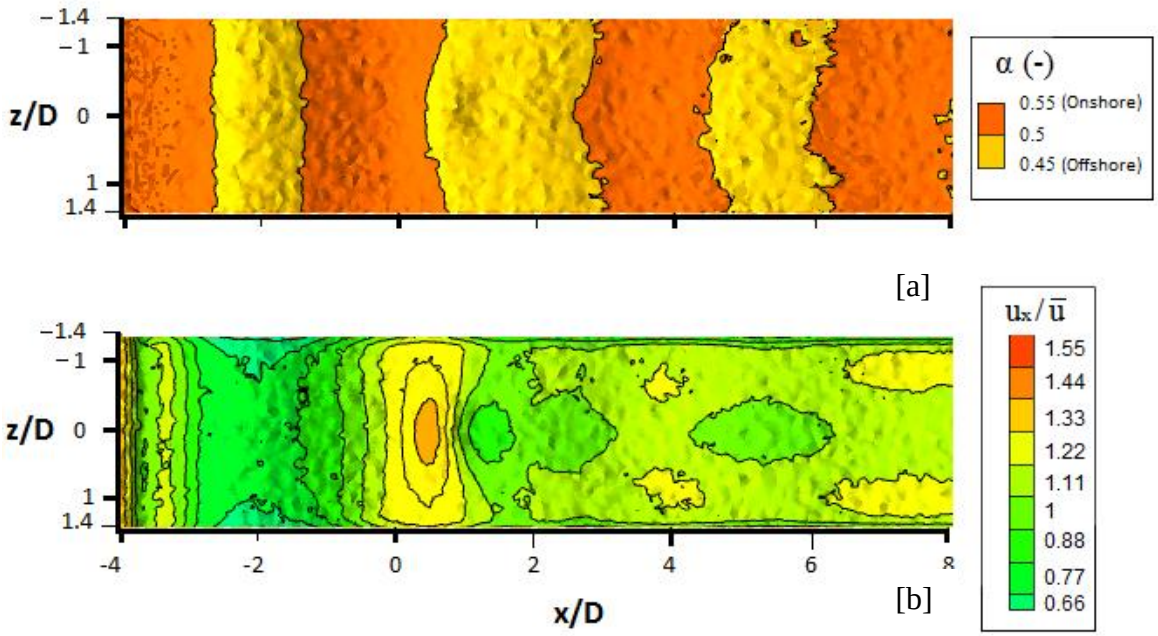

Figure 5-33 - Plan view: show the Iso-Surface at 0.5 volume of fluid, [a] contours of y-displacement where Mean Water Level (MWL) is at 0.39m, [b] contours of streamwise velocity.

Figure 5-34 shows the contours of streamwise velocity across the vertical centre planes under wave crest and trough at turbine position. Under the wave crest, the flow speed increases to 1.4ū above the turbine, this is similar to that under steady current condition. The flow also maintains its turbine operation causing features as in steady flow, e.g., the deceleration at the blades of the turbine and the acceleration at the hub section. This is largely due to the strong current in this particular case in comparison with wave-induced flows. Such increase near the bed surface (under turbine) is lower than that at the surface. The flow speed shows less reduction beyond x/D > 2 in the wake region, but it is noticeable that the flow structure under surface waves has been altered in the wake region, compared with that in front of the turbine (upstream).

Under wave the trough, however, the accelerated flow is not as strong when compared to that under wave crest, only reaching 1.03ū near the surface. The wake length is clearly stretched over approximately 2D downstream.

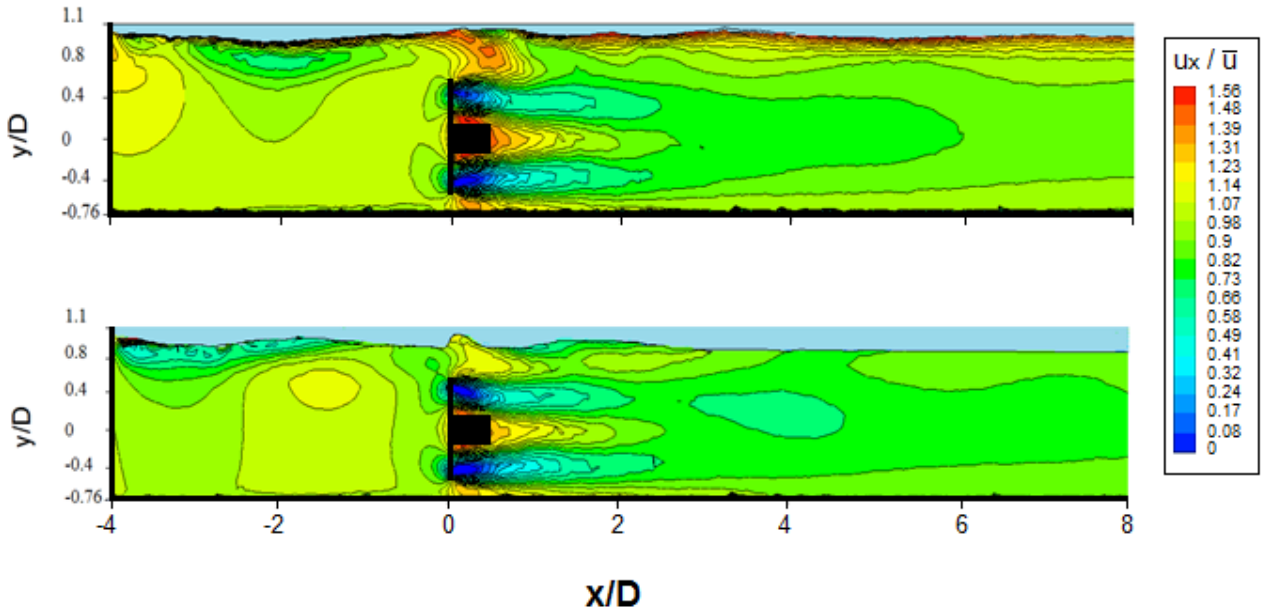

Figure 5-34 - Contours of streamwise velocity along the vertical plane at centre when the wave is at the turbine position [a] Crest and [b] Trough.

Figure 5-35 compares the streamwise, vertical and cross stream velocities at x/D = 1.5, y/D = 0 and z/D = 1 with the measured data across one wave-cycle. All three plots show that the velocities undergo variation during a wave cycle showing similar patterns to those without turbine influences, which suggests that the turbine effects on the flow are clearly less significant than the waves at this particular location in this case. Overall, computed results follow measured data reasonably well. However, results show underestimation of velocity at all three components possibly due to the underestimated wave height found in this region as shown in Figure 5-31.

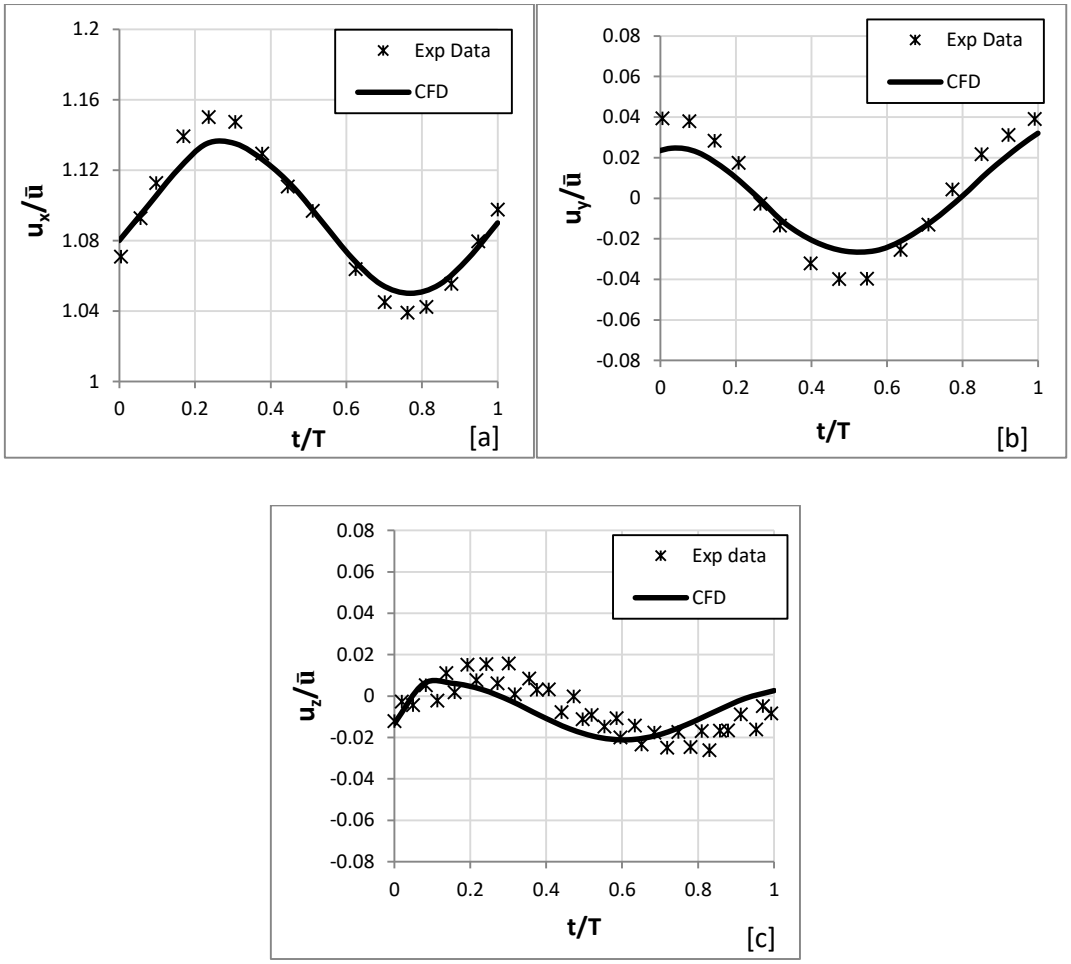

Figure 5-35 - Normalised wave-cycle averaged velocity profiles at x/D = 1.5, y/D = 0 and z/D = 1 for [a] streamwise, [b] vertical, [c] cross-stream, components.

Figure 5-36 presents the computed and measured wave-cycle averaged TKE across the width of channel at 2D, 3D and 4D behind turbine. The computed TKE under steady current is also shown in the figure as broken lines. Computed results follow the measured data very well. However, there are minor discrepancies along the edge of wake at z/D = -0.8 –1 and z/D = 0.8 – 1, where computed results hardly shows any TKE at that area. Overall, the error in the prediction is within 13%.

Comparing with the steady flow case, it is clear that the TKE magnitude is higher when the waves are present, due to the additional oscillatory motion from waves. The wave-induced turbulence at the upstream of channel is almost negligible. At downstream however, the results illustrate that the impact of turbine on the flow dynamics interferes strongly with the wave kinematics in that region and as a result initiates additional turbulence. This clearly

shows that there is a genuine interaction between turbine-affected region and the upper surface layer that enhances the generation of turbulence in a flow.

This influence is majorly seen across the turbine width (0.5D < z < 0.5D) but tends to reduce towards the sides of the wake region. Overall, the TKE distribution for the current + wave condition follows a similar pattern as that found in steady condition.

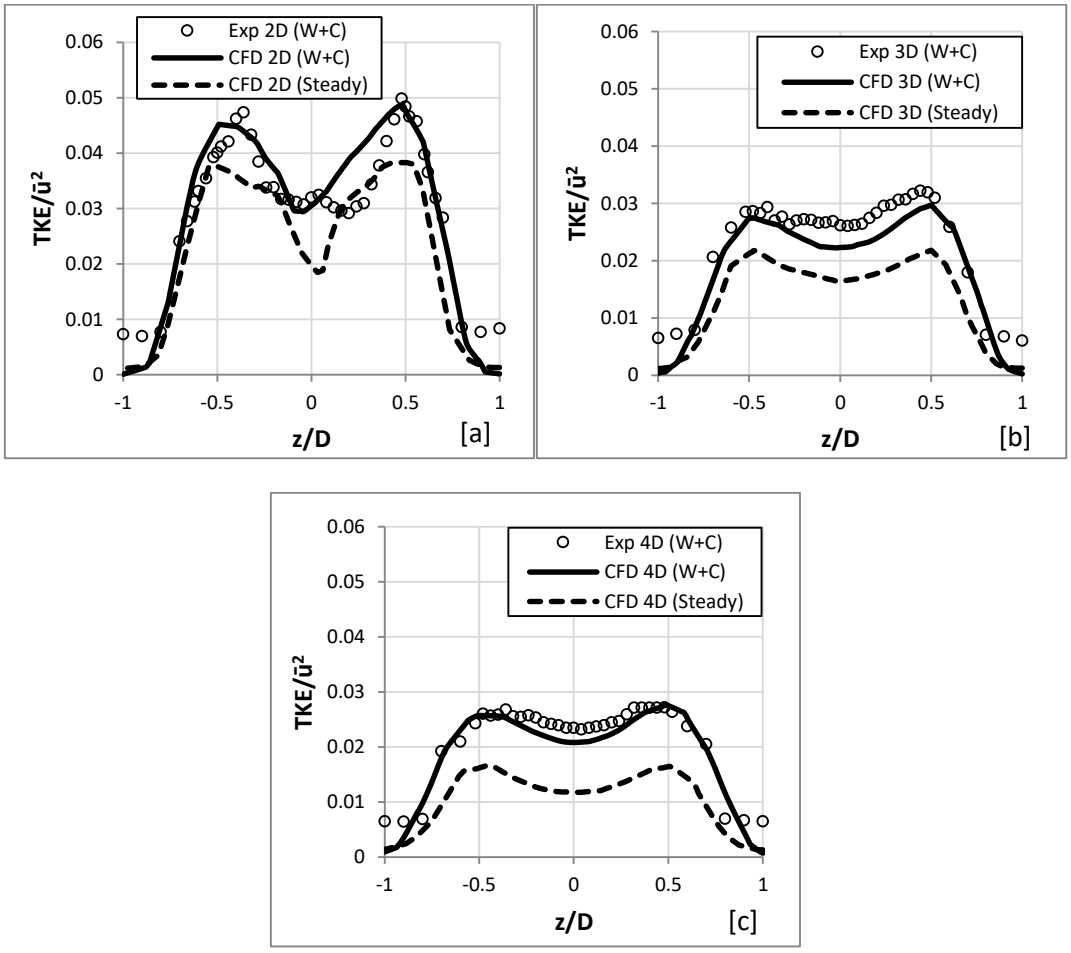

Figure 5-36 - Comparison of horizontal profiles between measured and computed normalised wave-cycle averaged TKE at 2D [a], 3D [b] and 4D [c] downstream across the centreline. Also, the TKE from the steady flow condition is added.

5.5 UoM (University of Manchester)

To test the model's prediction for turbine effects under wave propagating against current condition, the Olczak et al. (2013) experiment data is used for validation. The following is divided into two parts; Part 1, model validation against steady current alone and Part 2, the model is validated against current and opposing waves combined.

5.5.1 Experiment Conditions

The experiment took place to investigate the impacts of opposing waves on turbine wake recovery (Olczak et al., 2013). The waves are generated by an eight piston wave paddle located downstream. The wave parameters considered for this validation test are presented in Table 5-7. A three bladed rotor with a diameter of 0.27m is operated at TSR of 5.5. The motor speed control, optical encoder and the strain gauge are all placed above water level. The turbine is positioned at mid-depth inside a flume 12m long, 0.45m deep and 5m wide (Figure 5-37). The flume represents a full scale tidal stream (1:70) of 30m water depth. The mean velocity inlet is 0.46m/s with inlet turbulent intensity of 10%.

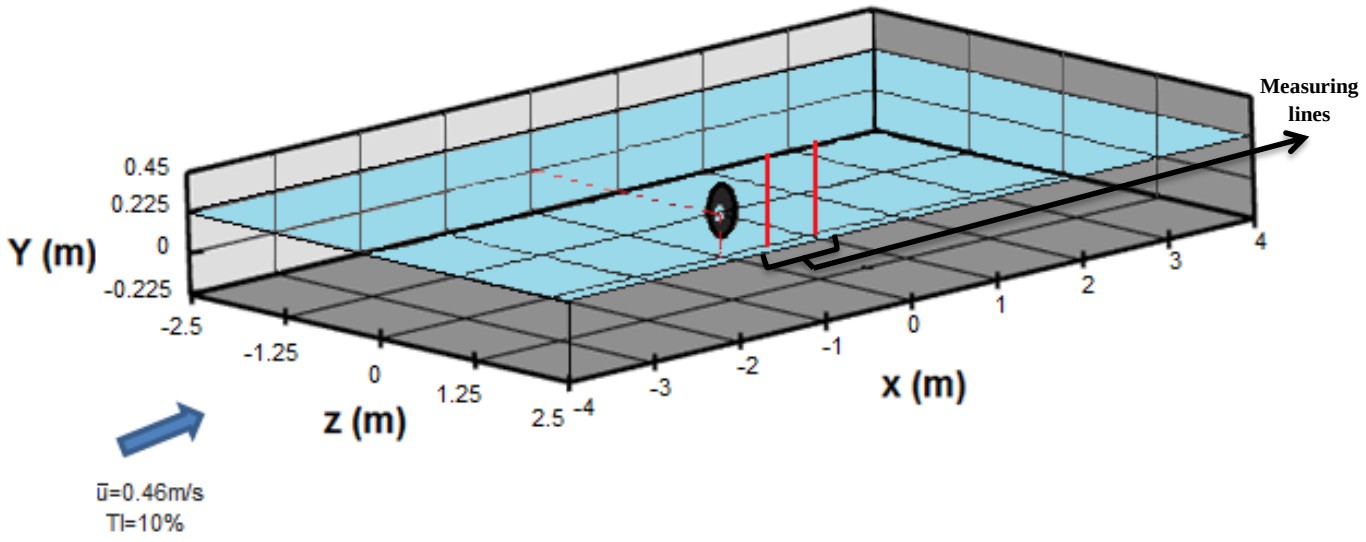

Figure 5-37 – Flume description.

The specification of waves was generated as periodic continuous motion and was classified as intermediate depth.

Table 5-7 – Wave parameters.

Wave Height (mm)	**Frequency (Hz)**	**Wave Length (m)**	**Wave Period (s)**	**d/L**	**Re**	$\frac{U_\delta}{\bar{u}}$
44.4	0.5	2.7	1.69	0.16	207000	0.14

5.5.2 Numerical Model Setup

The model is built with a total of ≈ 1 million tetra/mixed cells. At inlet, the channel flow is reversed (negative x direction) while the waves are generated in the positive x direction. This model setup produces similar opposing wave conditions as conducted in Olczak et al. (2013) experiment. The wave is set to intermediate (depth), adopting the third order Stokes theory. The wave height and length are defined as 0.044m and 2.7m respectively. The pressure is specified from free surface level and the density is interpolated from neighbouring cell volume fraction. The vertical profiles of velocity are measured at 2 and 4 diameters behind the turbine (Figure 5-38). The rotor is defined to match the specification of the experimental turbine that is set in the VBM model panel (Table 5-8 and Table 5-9).

Table 5-8 – General rotor setup.

Number of rotor zones	1
Number of blades	3
Rotor radius	0.135m
TSR	5.5
Tip effect	96%
Disk pitch angle	90
Blade pitch	15
Blade flapping	0

Table 5-9 – Geometrical rotor setup.

Radius (r/R)	Chord (m)	Twist (deg)
0.2	0.15	19
0.3	0.15	9.7
0.4	0.15	6.4
0.5	0.15	3.6
0.6	0.15	2.1
0.7	0.15	1.5
0.8	0.15	0.8
0.9	0.15	0.4
1	0.15	0

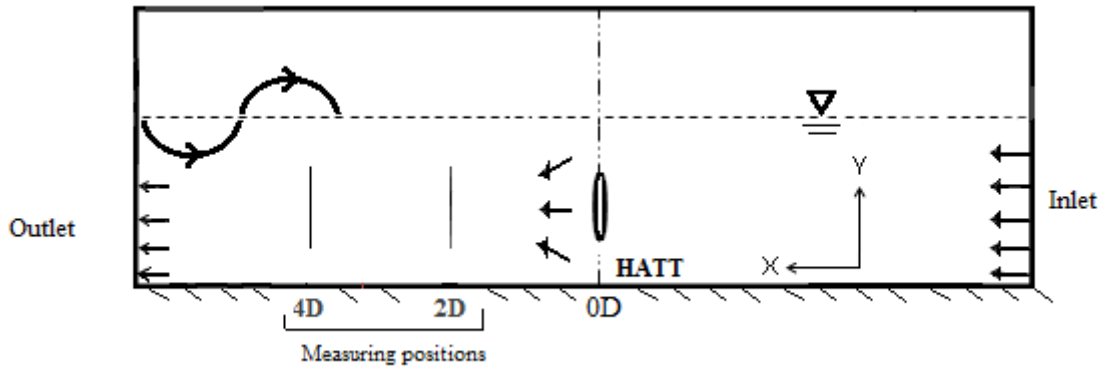

Figure 5-38 - Side view, measuring locations.

5.5.3 Results and Discussion

The results are divided into two parts including the steady and unsteady simulation. The model was calibrated in terms of velocity magnitude ($|u| = \sqrt{u_x^2 + u_y^2 + u_z^2}$) for 1D above and below the turbine centre.

Condition 1: Steady Current

Initially, a steady flow is simulated in a flume to measure the vertical profile at two different locations. Figure 5-39 presents computed and measured vertical profiles of normalised velocity magnitude at 2D and 4D behind the turbine along the centreline of channel. It is clear that the flow velocity shows a "U" distribution behind the turbine, unlike in Tedds et al.

(2014) experiment. This occurs because both flow velocity (0.46m/s) and turbine diameter (0.27m) are small.

As a result, flow separation at the hub is not created. The computed results display very good agreement with experimental data at 2 and 4 diameters behind turbine. However, the flow velocity is slightly over-estimated above the turbine centreline at 2D. This is due to the absence of a stanchion, which reduces the flow velocity (Jones et al., 2013). The flow interacts with the stanchion to create vortex shedding and as a result the velocity reduces. Maximum reduction appears behind the blade where stanchions exist. However, this stanchion impact does not persist for long and disappears at 4D downstream. The computed velocity follows the experiment data very well. At 4D, the flow velocity shows higher accuracy as stanchion impact withdraws.

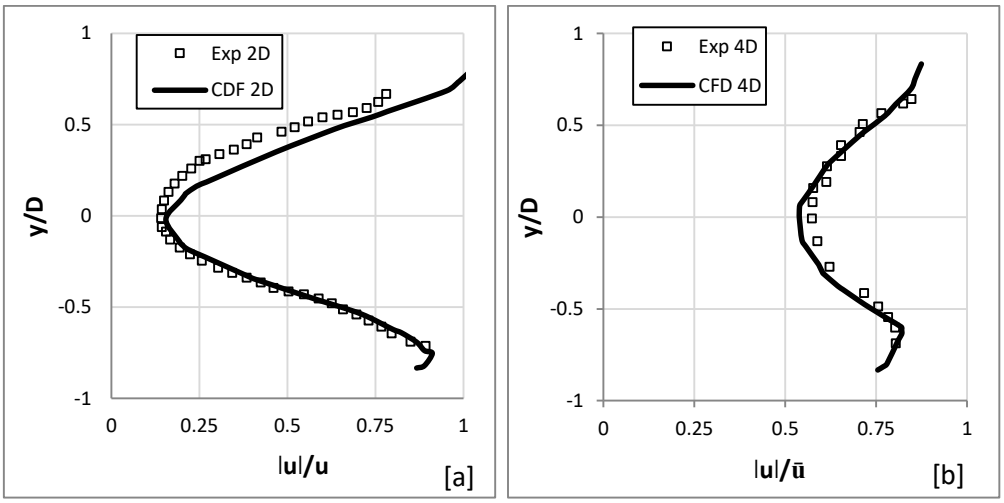

Figure 5-39 – Vertical profiles of normalised velocity magnitude for current alone at [a] 2D and [b] 4D downstream along centreline.

Condition 2: Wave against current

In this case, the steady current is combined with opposing waves. The velocity measurements are taken at intervals of 0.03s for five wave cycles. Figure 5-40 presents the wave-cycle averaged flow velocity magnitude at 2D and 4D behind the turbine. It is clear that the flow velocity distribution follows a similar pattern as in the current alone test and the wave +current condition. The computed results are reasonably accurate with minor discrepancies above the turbine centreline at 2D, similar to that in Figure 5-39. This happens for the reasons

explained earlier. At 4D, the computed results show better correlation. The flow velocity is slightly under-estimated at the turbine region.

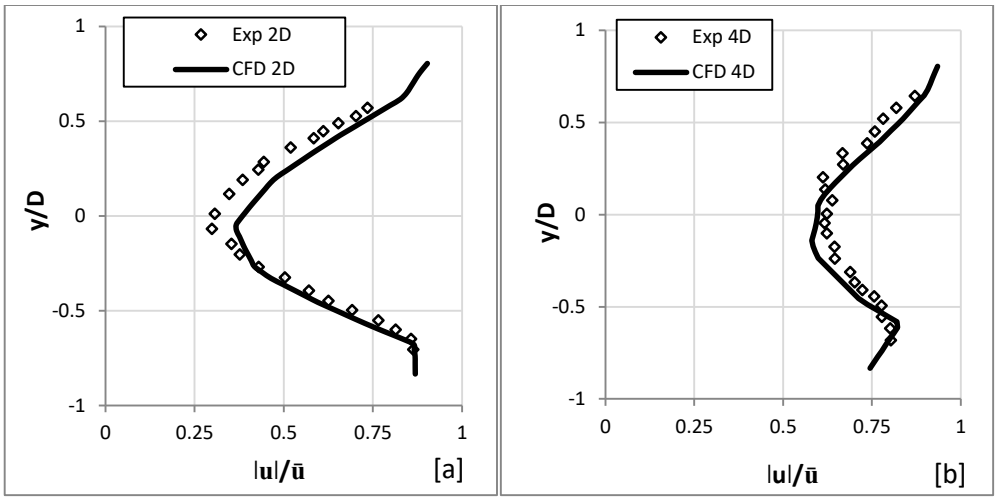

Figure 5-40 – Vertical profiles of normalised wave-cycle averaged velocity magnitudes at [a] 2D and [b] 4D downstream along centreline.

Overall, the wake appears to recover faster when waves are introduced to the current (Figure 5-41). At 2D, the whole water column is affected by the presence of opposing waves. Results illustrate higher velocity increase at mid-depth and minor increases near boundaries. At mid-depth, high turbulences are induced by turbines alongside waves causing better mixing of wake. At 4D, the velocity difference is much smaller.

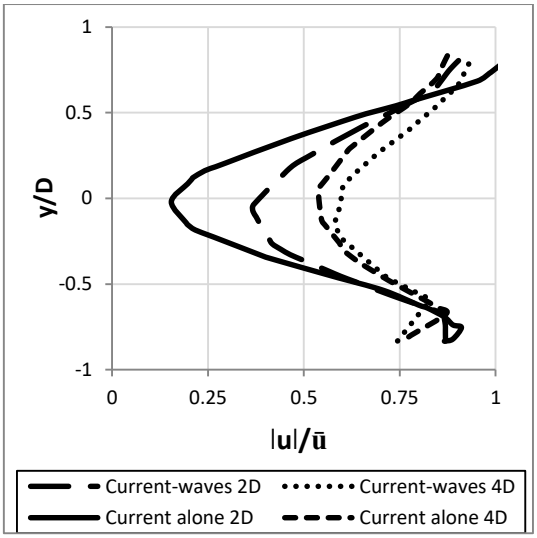

Figure 5-41 - Comparison between vertical profiles of average wave cycle normalised velocity magnituedes for current alone and current with opposing waves.

Figure 5-42 shows the computed and measured vertical profiles of wave-cycle averaged TKE in the presence of opposing wave and current alone at 2D and 4D at centreline. It is clear that the agreement between model predictions and the measured data is good and the error is less than 10%. At 2D, results show that the TKE increases almost three-fold on average when opposing waves are combined in comparison with current alone flow, especially in the turbine-affected and the bed boundary layers. At 4D, this increase drops down to double.

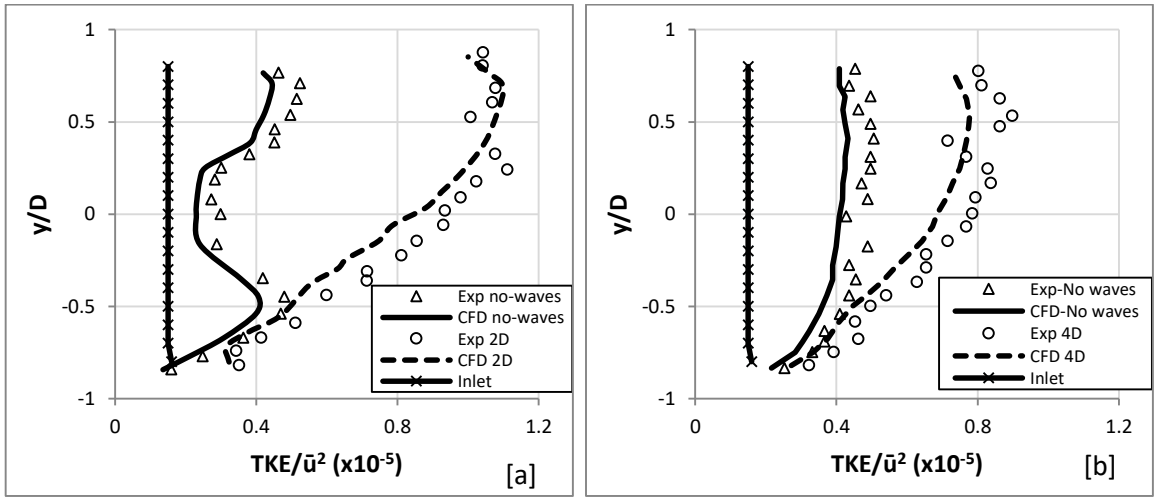

Figure 5-42 – Vertical profiles of normalised wave-cycle averaged TKE when with and without waves at [a] 2D and [b] 4D downstream along centreline.

5.6 Summery

Based on the above comparisons against available data for steady current and current with following and opposing waves, it is clear that VBM is able to simulate complex flows, with reasonable accuracy, in both hydrodynamics and turbulence quantities. In these validation tests, it is found that the choice of C_l and C_d are critical. On average, the error of the model is within 15% for both velocity and TKE results, which demonstrates the reliability of the model. The ADM approach is clearly unable to produce the vertical and cross-stream flows that are important to the turbine impact and turbulence generation. Therefore, in the following applications, VBM will be used to investigate turbine impacts to the surrounding environment for various flow conditions and turbine configurations.

Other conclusions are established from the above investigations:

- It is found that the wake tends to shift slightly towards the left hand side when looking from upstream due to the asymmetric nature of flow velocity behind the turbine. The turbine rotation in this case was clockwise.
- Additional evidence shows that the wake tends to shift downwards towards the bed due to the higher water head in the upper side of the wake.
- It is found that the waves show a straight alignment across the channel width before reaching the turbine. Downstream however, the wave tends to curve around the turbine region to form a crescent shape.
- It is also found that the turbine causes the wave length to increase for the first wave length behind turbine.
- Additional evidence showed that the height of a wave is slightly reduced when propagating over a turbine.
- It is found that there is a genuine interaction between turbine-affected region and the upper surface layer that enhances the generation of turbulence in a flow.
- It is found that VBM induces higher shear stresses on bed when compared with the ADM approach. The contours of shear stress showed more features on the bed which suggests that the rotational motion of flow (vortex) have a significant contribution to the generation of bed shear stresses.

5.7 References

Henriques, T. A., Tedds, S. C., Botsari, A., Najafian, G., Hedges, T. S., Sutcliffe, C. J., Owen, I. and Poole, R. J. (2014) The effects of wave-current interaction on the performance of a model horizontal axis tidal turbine. *International Journal of Marine Energy,* vol. (8), pp.17-35.

Ingram, G. (2005) Wind turbine blade analysis using the blade element momentum method. In Note on the BEM method*;* Durham University, USA.

Jones, A. M., O'Doherty, D. and Morris, C. E. (2013) Influence of a velocity profile & support structure on tidal stream turbine performance. *Journal of Renewable Energy,* vol. (52), pp.23-30.

Jordan, L. B., Simmons, S., McLelland, S., Murphy, B., Parsons, D. and Vybulkova, L. (2015) The Impact of Tidal Stream Turbines on 3D Flow and Bed Shear Stress Measured with Particle Image Velocimetry in a Laboratory Flume, *Proceedings of the 11th European Wave and Tidal Energy Conference (EWTEC),* Nantes, France.

Mozafari, A. T. J. (2010) *Numerical modelling of tidal turbines: Methodology Development and Potential Physical Environmental Effects,* MSc. Thesis, University of Washington.

O'Doherty, T., Jones, A., O'Doherty, D. M. and Byrne, C. B. (2009) Experimental and Computational Analysis of a Model Horizontal Axis Tidal Turbine. *Proceedings of the 8th European Wave and Tidal Energy Conference.* Uppsala, Sweden. http://orca.cf.ac.uk/id/eprint/16918.

Olczak, A., Stallard, T. and Stansby, P. (2013) The influence of waves on tidal stream turbine wake recovery, *In 10th European Wave and Tidal Energy Conference,* Aalborg, Denmark.

Sun, X., Chick, J. P. and Bryden. I. G. (2008) Laboratory-scale simulation of energy extraction from tidal currents. *Journal of Renewable Energy,* vol. (33), Issue: 6. pp.1267-1274.

Tedds, S. C., Owen, I. and Poole, R. J. (2014) Near-wake characteristics of a model horizontal axis tidal stream turbine. *Journal of Renewable Energy,* vol. (63), pp.222-235.

Chapter 6 – Model Applications

6.1 Introduction

There are many different marine conditions that will influence the characteristics of a wake behind a tidal turbine and possibly influence the surrounding environment. In this chapter, the model is applied to many different conditions of both experimental and field scales to investigate the impacts of a turbine within the near wake region. Table 6-1 describes different scenarios considered in this chapter. The results will be assessed in terms of flow velocity and Turbulent Kinetic Energy (TKE) profiles as well as the shear stresses imposed on the bed layer and in some cases surface elevation. Cases LBM and FBM are used as bench marks for experimental and field investigations respectively. In both cases the Reynold number are high ($Re > 7x10^5$) and are define as turbulent flow regimes. In the blockage ratio case study, comparisons between two different blockages, 16.5% and 5.3%, are carried out where the water depths remain the same (0.85m) but the width of the channels differ (HB = 1.7m and LB = 4.2m). The models are setup similarly to those found in LBM case (Tedds et al. 2014). In the yaw angle case study, the comparison between two different yawing turbines, 0˚ and 45˚, is carried out in two identical channels with similar flow conditions (LBM). For the turbulence intensity case study, the comparison between two different background turbulent flow intensities, 4% and 8%, are investigated, in a scaled up model under conditions found in a real site. The dimensions and conditions of the scaled up model (FBM) is explained below in this section. The amplification of turbulence induce by the turbine under different background turbulence will be explained. For the elevation case study, two different turbine elevations, h/3 and h/2 (above channel bed), are investigated under similar flow and channel conditions found in FBM. Finally, in the wave's case study, the impact of streamwise and opposing waves are assessed when combined with current in the presence of a turbine and without. The conditions adopted in this investigation are found in a storm where large waves are present. Waves are generated at inlet using the Stokes wave theory and the background flow turbulence is kept small to avoid interference with the wave-induced characteristics.

Table 6-1 – Model applications

Case Study	Geometry Size	Input	Turbine & Channel Dimensions	Note
LBM	Laboratory	UoL-1	UoL-1 BR=16.5%	Tedds et al. (2014) experiment is used as a bench mark for experimental scale cases.
Blockage Ratio	Laboratory	LBM	*LBM apart from: BR= 5.3% (W=4.2m)	
Yaw Angle	Laboratory	LBM	*LBM apart from Yaw=45˚	
FBM	Field	ū=2m/s, TI=4% OP= 101325	D_{ia}=15m, Yaw=0˚ TSR=5.5, BR=2.9% TE=2/3 Deep (40m) h=60m, W=100m, L=300m, RH=0.02mm	This model is used as a bench mark for field scale cases.
Turbulence Intensity	Field	*FBM apart from TI=8%	*FBM	FBM results are analysed in this case.
Elevation	Field	FBM	*FBM apart from: TE= Mid-depth (30m)	
Waves	Field	*FBM apart from TI=1% Current +/- Waves	*FBM	TI is kept small in order to avoid interference.

*LBM (Laboratory Bench Mark) *FBM (Field Bench Mark) *TSR (Tip Speed Ratio) *RH (Roughness Height *TE (Turbine Elevation) *BR (Blockage Ratio) *OP (Operation Pressure) *L (Channel Length) *W (Channel Width) *h (Water Depth) *

For the laboratory bench mark (LBM) model, the turbine and channel setups and configuration follow those in Tedds et al. (2014) experiment. For the field bench mark (FBM) model, the model is scaled up by approximately 1:65 from the experiment conducted by Jordan et al. (2015). The turbine is created to maintain similar geometrical and meshing techniques to avoid inconsistency. Likewise, the channel bed remains flat, and the boundary conditions are kept the same. The model is created from ≈ 1.4 million tetra/mixed elements. Conditions in Black & Veatch (2005) are cited to achieve realistic tidal parameters. Hence, in all field cases the channel water depth is kept as 60m and the turbine diameter remain as 15m. The turbine is positioned at 2/3rds of the depth from the mean water level (MWL) and 100m away from the flow inlet in order to avoid any boundary effects. The turbine operates at maximum output of tip speed ratio of 5.5 at all times, producing a blockage ratio effect of 2.9%. The mean flow velocity is set as 2m/s to give a Reynolds number 2.18×10^8. The channel is 100m wide and 300m long, featuring a free surface. Figure 6-1 describes the dimensions of field model.

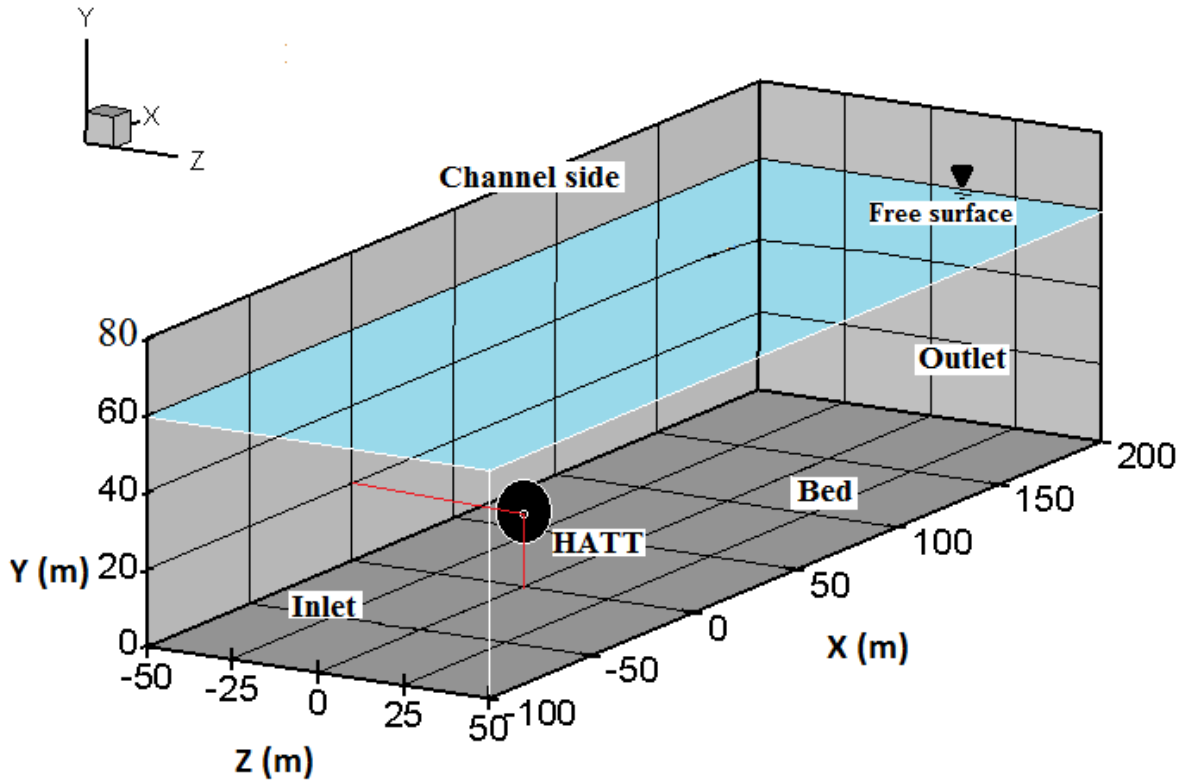

Figure 6-1 - Field model description (FBM).

6.2 Blockage Effect

In practice, tidal stream devices are often located at narrow straits where current speed is high. In the present study, two lateral scale tests were used with blockage ratios of 5.3% and 16%. Other researches such as Consul et al. (2013) compared between 10% - 25%, and Takafumi and Willden (2012) used 3% - 50%. However, it is expected that in the natural environment, such ratios can vary and it is therefore necessary to identify the potential difference in the impacts from turbines operating with different blockage ratios.

To test blockage effects, a model with low blockage ratio (5.3%) is created with similar turbine configuration and operating conditions as those found in the LBM model. Results from these two models can then be compared to identify the blockage effects on turbine wake and other physical processes. The channels have similar length and water depth; however, for one of the channels the width is 2.8m wider. The mean velocity at inlet is 0.9m/s with an ambient turbulence intensity of 3% (Table 6-1). This condition is set to investigate the impact of the turbine on the flow dynamic and surrounding environment when different channel widths are adopted. The blockage ratio percentage is defined by:

$$\mathrm{BR} = \frac{\pi r^2}{hw} \mathrm{x} 100\% \tag{6.1}$$

where πr^2 the turbine swept area and hw is the channel cross-section area. The model is built with a total of 0.95 ≈ million tetra/mixed cells. Both models are set under the steady flow condition. Measurements of horizontal and vertical profiles are taken at 1D, 3D and 5D behind the turbine as shown in Figure 6-2.

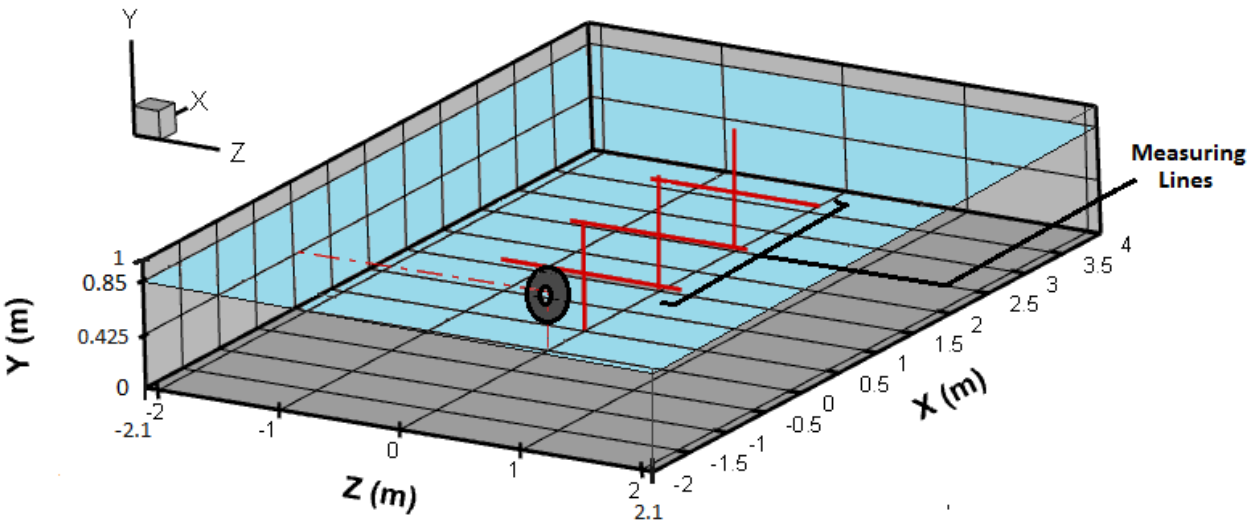

Figure 6-2 - Model description for low blockage condition (horizontal and vertical measuring lines are shown at 1D, 3D and 5D turbine centres).

Figure 6-3 compares the horizontal profiles of normalised streamwise velocity between high and low blockage ratios at 1D, 3D and 5D downstream, where HB = high blockage and LB = low blockage. It is clear that blockage ratio has a significant impact on flow velocity especially near the turbine (1D). In the high blockage ratio case, the flow velocity at 1D downstream shows strong variation within the turbine region ($-0.5 < z/D < 0.5$). This is due to the high resistance experienced at the face of a turbine exerting greater pressure drops and, hence, flow with higher velocities is pushed around the turbine. Similarly, at the hub, the flow velocity accelerates strongly from $0.25\bar{u}$ to nearly $\bar{u}$, suggest higher permeability. At 3D, results show that the flow speed in the high blockage channel is slightly higher than that found at low blockage conditions. This velocity difference is further reduced at 5D.

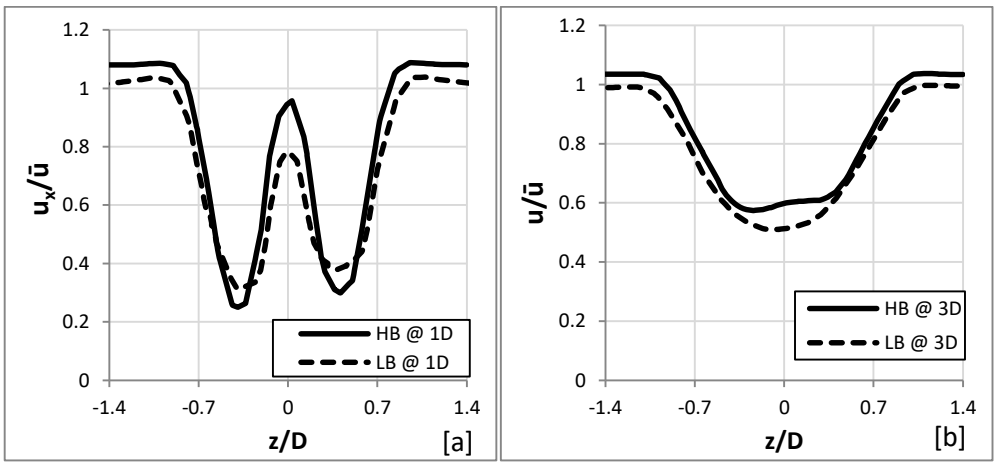

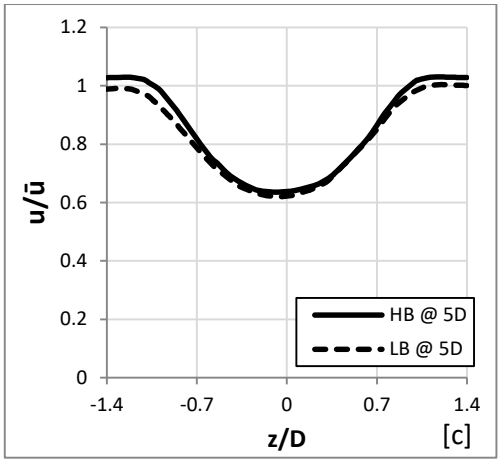

Figure 6-3 – Comparison between horizontal profiles of streamwise velocity for high and low blockage ratios at 1D [a], 3D [b] and 5D [c] downstream (centreline).

Figure 6-4 shows the top-down view of the contours of streamwise velocity for both cases across the channel width along the turbine centre plane (y = 0). Overall, the two cases share fairly similar patterns of flow velocity distribution, with flow deceleration in front of the turbine, acceleration on both sides of the turbine and along the wake behind the structure. The differences lie in many details of these distributions so to compare these two cases directly, the flow velocity at the same deficit levels is marked in the figures as well, i.e., A-A' is $u_x/\bar{u}$ = 1.25 and B-B' is for $u_x/\bar{u}$ = 0.5. It is found that in the high BR condition, the accelerated flow passing the turbine persists over a longer distance downstream (A) due to the constricted lateral space between the turbine and channel walls.

Consequently, the accelerated flow enhances the mixing process of the wake by accelerating the flow behind the turbine. At around 3.5D-4D the accelerated flow dissipates into background flows. In lower blockage ratio cases, the velocity deficit area is longer behind the turbine (B`). This is because the accelerated flow (A`) is unrestricted and tends to spread laterally across the channel causing it to dissipate quicker after 1D, which minimises the ambient flow speed beside the wake area.

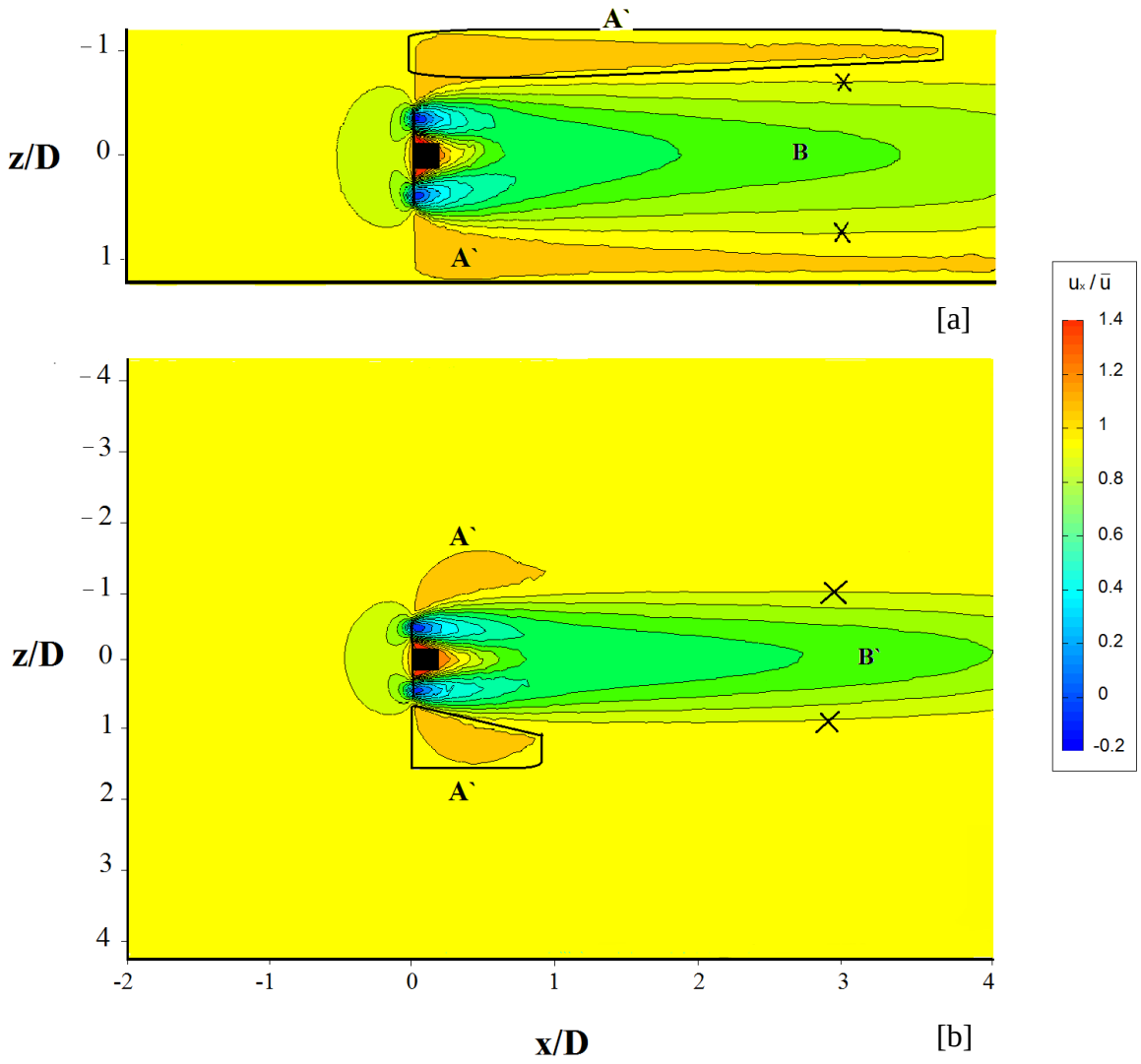

Figure 6-4 – Top view: contours of streamwise velocity illustrating wake structure for [a] High blockage (16%) and [b] Low blockage (5%).

Regarding the width of the wake, it is mainly controlled by the expansion range of the accelerated flow around the turbine. For the lower blocked channel, the primary flow alone forms the barrier that confines the lateral expansion of the wake. In the high blockage ratio case, the wake width is slightly shorter by 0.3D. This is because the flow is restricted by the small lateral space between turbine and channel walls.

Figure 6-5 shows the normalised vertical velocity across the channel width at 1D, 3D and 5D downstream. It is clear that in the flow with low blockage ratio, the vertical velocity is slightly smaller especially at 1D. This feature is also seen for cross-stream flow, however

overall these two cases share a fairly similar distribution of vertical velocity at this level above the bed.

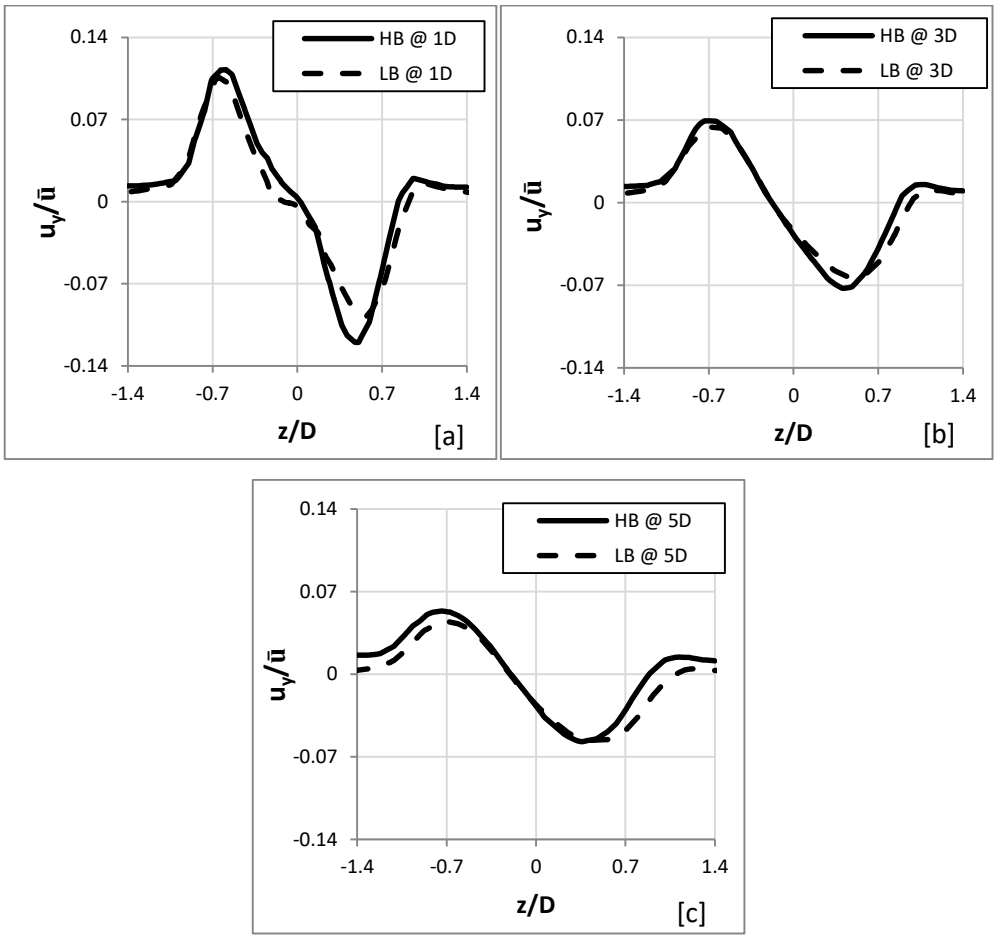

Figure 6-5 - Comparison between horizontal profiles of vertical velocity for high and low blockage ratios at 1D [a], 3D [b] and 5D [c] downstream (centreline).

Figure 6-6 compares the normalised cross-stream flow velocity across the channel width for both cases. At 1D, four velocity peaks in both positive and negative directions are seen among the left (-) and right (+) sides of hub. Such distribution is only seen close to the turbine due to the flow behaviour explained in Chapter 5. The outer peaks (A and A') are stronger in magnitude and remain apparent at 3D and 5D downstream.

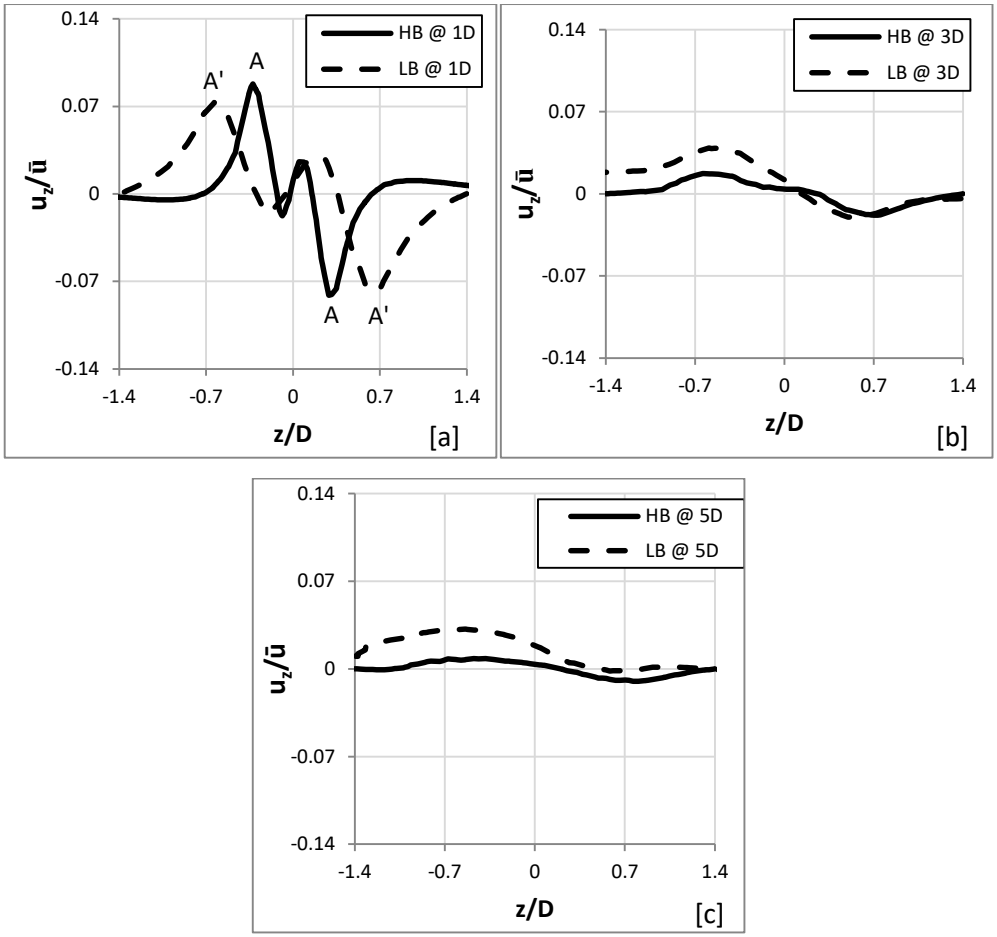

Figure 6-6 - Comparison between horizontal profiles of cross stream velocity for high and low blockage ratios at 1D [a], 3D [b] and 5D [c] downstream (centreline).

At 1D, the results show higher peaks in both positive and negative directions in high blockage condition but narrower width e.g. -0.7 < z/D < 0.7. In the low blockage channel however, the distribution takes a wider range (-1 < z/D < 1) with smaller peaks. It is clear that the wakes in both conditions are shifting towards the left-hand side of the hub (- direction). This occurs due to the clockwise rotation of the turbine that leads to unsymmetrical flow behaviour as discussed previously. At 3D and 5D, the results in low blockage conditions show higher peaks in the positive direction, this means that the flow converges towards the hub with higher speed.

Figure 6-7 shows the vertical profiles of velocity magnitude at 1D, 3D and 5D from bed to surface for these two cases. In general, the flow with low blockage ratio illustrates higher velocity deficit. Along the turbine-affected area (0.35 < y/D < 1.35), velocity differences between the two cases gradually decrease from upstream to downstream as flow tends to

return to ambient velocity downstream. However, the velocity difference close to bed layer and surface remains more or less constant.

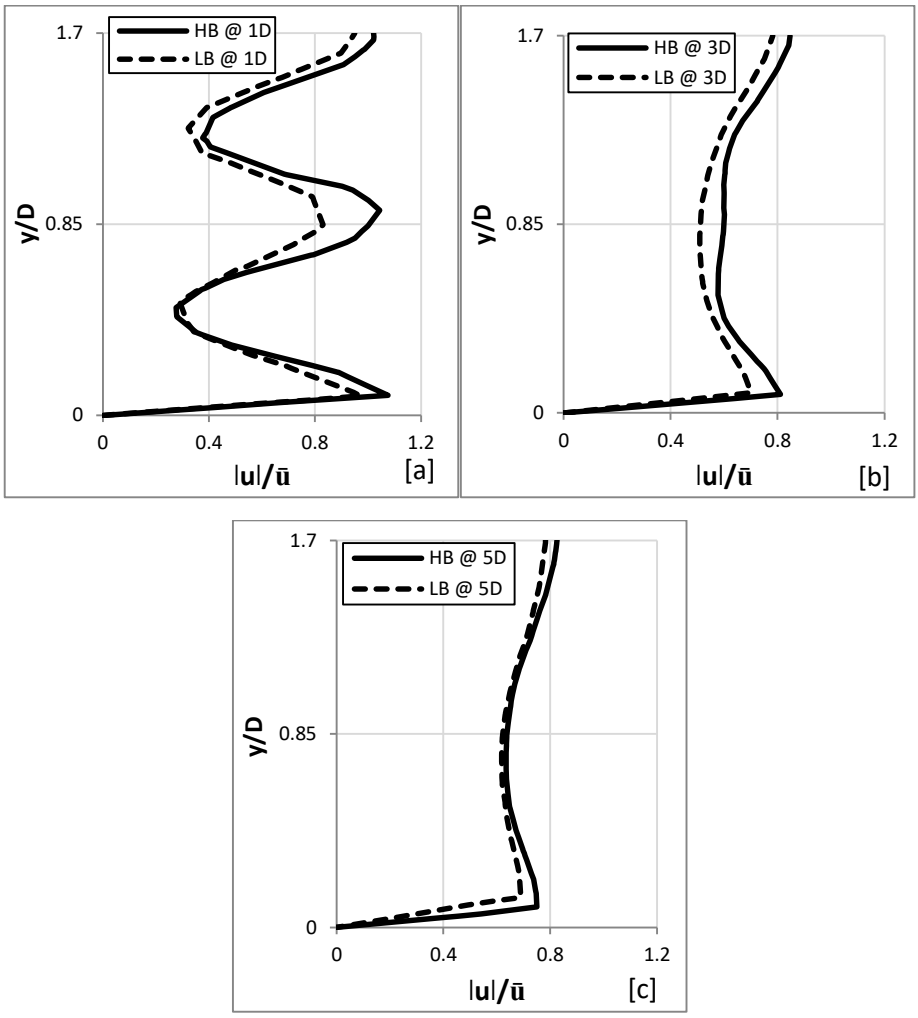

Figure 6-7 – Comparison of velocity magnitude vertical profiles between high and low blockage ratios at 1D [a], 3D [b] and 5D [c] downstream (centreline).

In comparison with high blockage cases, the flow with low blockage ratio has lower flow speed especially at 1D-3D because there is enough space to spread laterally. The sufficient lateral space also aids to absorb the pressure change at the turbine. Therefore, the accelerated region around the turbine covers more channel space with slightly lower magnitude, as shown in Figure 6-8. The figure shows the contours of streamwise velocity magnitude across the channel width at 1D.

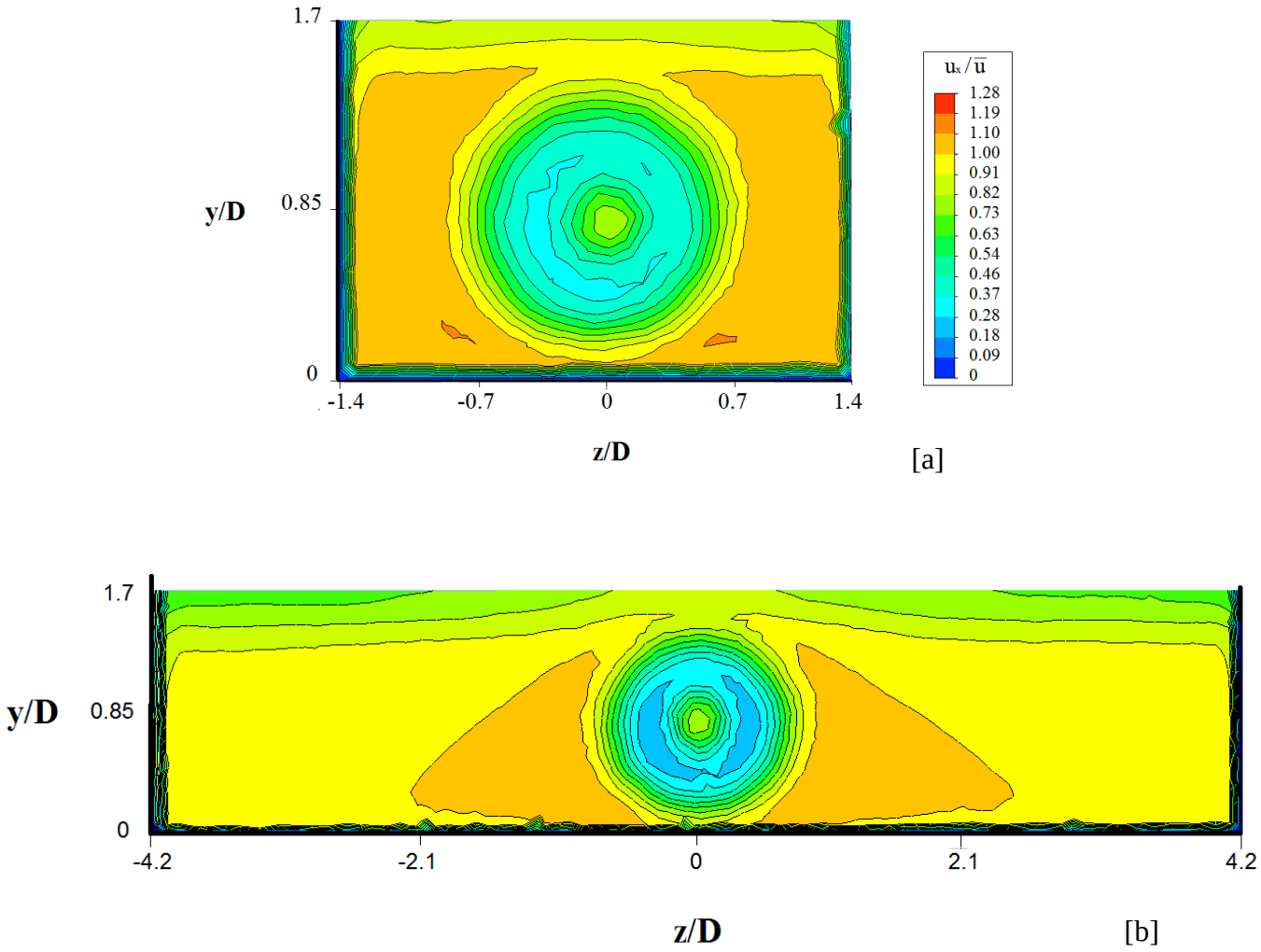

Figure 6-8 - Contours of streamwise velocity across the channel width at 1D for [a] High blockage and [b] Low blockage.

Figure 6-9 shows the contours of velocity magnitude across the vertical plane at turbine centre. In [a], it is clear that the accelerated flows above and below the turbine persist over a longer distance downstream for the flow with high blockage ratio. This behaviour contributes to the wake recovery downstream through velocity shear boundary. In [b], it shows that the accelerated flow dissipates faster and the wake undergoes vertical expansion downstream.

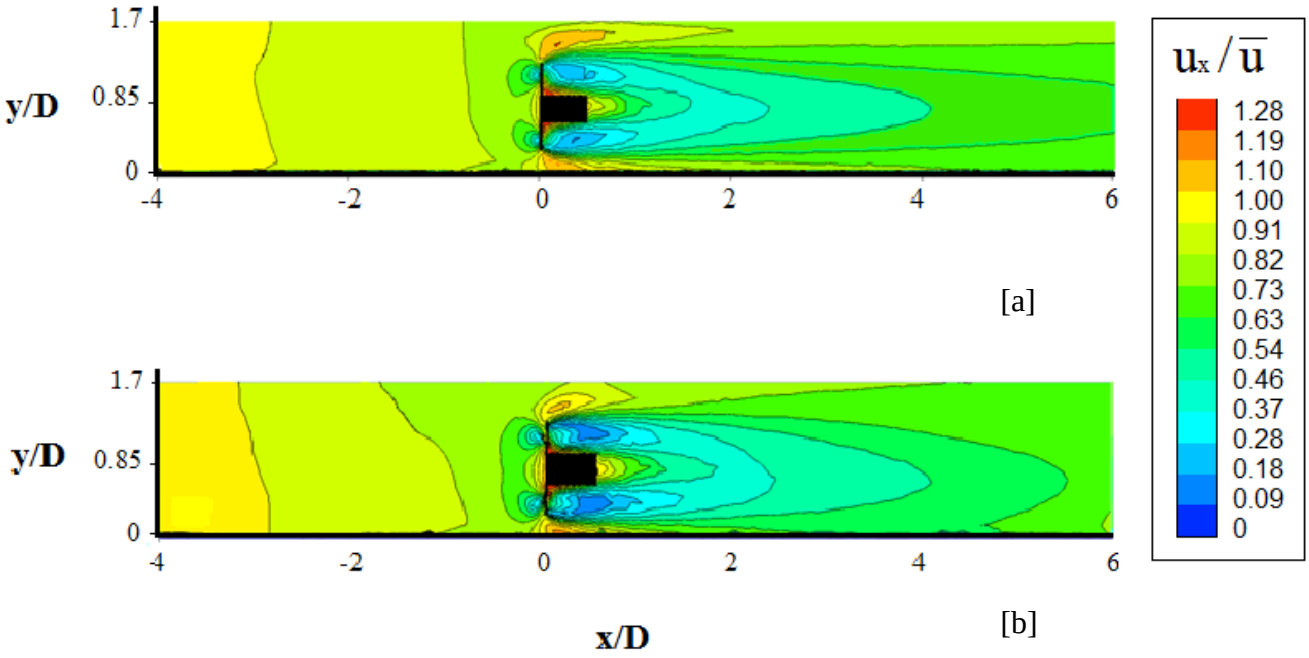

Figure 6-9 - Shows the contours of velocity magnitude across the vertical plane at turbine centre for [a] high blockage and [b] low blockage.

In general, the highest TKEs are found at the turbine region where strong pressure jumps occur. Figure 6-10 shows the horizontal profiles of normalised TKE at 1D, 3D and 5D downstream. For the flow with high blockage ratio, the additional blockage imposes stronger forces on the blade, which in return allows the passage of more water across the turbine and as a result higher turbulent kinetic energies are found. Further downstream the TKE gradually reduce as flow starts to recover and turbulences ease. This clearly indicates that the flow generates higher turbulences at narrow sites where blockage ratios are large.

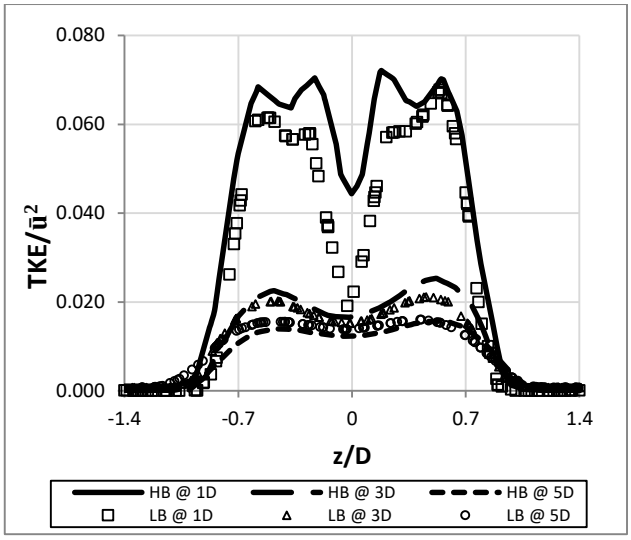

Figure 6-10 – Comparing horizontal profiles of TKE for both high and low blockage ratios at 1D, 3D and 5D downstream.

The TKE vertical profiles are presented in Figure 6-11. It is found in both cases that slightly higher TKEs are induced at the bottom half of the channel when compared to the top half. This is because the bed boundary layer contributes to the TKE induction, whereas the free surface does not enforce any resistance and hence does not have an influence on the TKE. Results show that the high blocked channel produces higher TKE, especially at the hub area. But overall, both cases share fairly similar patterns as we saw in the previous chapter, for turbine operation under steady flows.

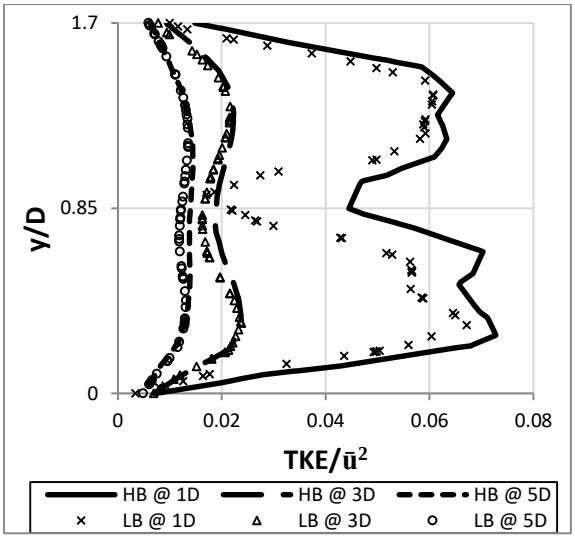

Figure 6-11 - Comparison of TKE vertical profiles between high and low blockage ratios at 1D, 3D and 5D downstream.

In addition to flow velocity and turbulence characteristics, the near bed shear stresses caused by the presence of tidal stream turbines is also an important physical property, especially in terms of its substantial influence on sediment transport. Figure 6-12 [a] presents the normalised bed shear stress along the centreline across the channel bed for high and low blockage ratio cases. In front of the turbine (-0.5D), shear stresses start to increase as the flow starts to change its trajectory. The obstruction of the turbine reduces the flow speed in front of the rotor and accelerates the flow above and beneath it. At turbine location (0D), the flow experiences maximum pressure change where part of the flow undergoes separation and the other part penetrates through the rotor. The diverted flow beneath the rotor increases the bed shear stress to its maximum as shown in [b]. With low blockage ratio, it is found that the first shear stress peak at the bed is weaker by almost 15% than that found for high blockage conditions.

Although the elevations of turbines for both blockage conditions are the same, the low blockage channel provides more space for the accelerated flow beneath the turbine to spread laterally and reduces flow acceleration. Behind the turbine, a common feature that can be found in both cases is that there are two stress peaks. In high blockage ratio cases, these peaks show no difference in magnitude but differ in terms of length. The first peak (A) affects the bed over a short distance (low angle peak) followed by another peak at 2.5D (B) to cover a longer distance of the bed (high angle peak). The high stresses persist over a distance of 3D before they start to ease at an average rate of 0.09 Pascal/D.

For the low-blocked channel, the behaviour of shear stress peaks is slightly different. The 2nd stress peak is found to be stronger and persists over a distance of 1.5D (B`). Subsequently, the stress starts to reduce at an average rate of 0.19 Pascal/D, which is faster than that found in the high blockage ratio. The overall shear stress on the bed is greater for the high-blocked channel by approximately 19% across the turbine centre.

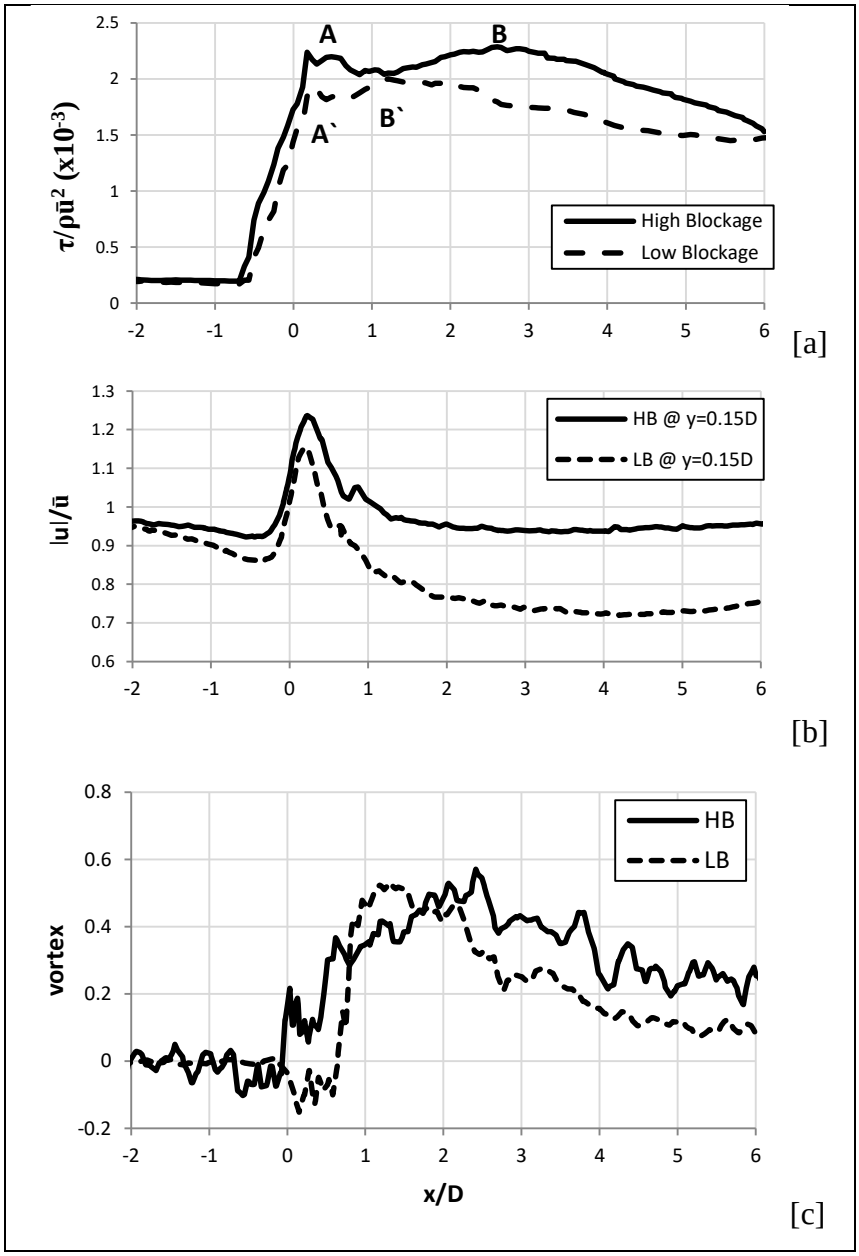

Figure 6-12 – Comparison between high and low blockage conditions, [a] Bed shear stress along the centreline of channel, [b] velocity magnitude along the channel length at 0.15D above bed and [c] vortex magnitude at 0.15D above bed.

The reason for the first stress peaks (A) and (A') is due to the immediate increase of flow velocity behind the turbine as shown in Figure 6-12 [b]. However, the second stress peaks (B) and (B`) take place due to vortex generation by the turbine that clearly increases in magnitude to impose an additional cross-stream flow motion [c]. Between the two peaks a slight drop in shear stress is seen at the bed. Figure 6-13 shows the Iso-surface of swirling flow across the

turbine for both conditions. It clearly demonstrates an interaction between the turbines generated flow swirls and the near bed boundary layer processes.

The interaction of flow with the bed starts at -0.5D in front of the turbine then increases immediately behind the turbine where the accelerated flow is generated. At 1D, the accelerated flow above and beneath the turbine weakens, which causes the drop in bed shear stress from this point downstream. The vortex in the flow starts to grow as the flow detaches from the turbine and free turbulence develops along with the bed boundary layer, which leads to the 2nd peak at B and B'. In the low blockage case, these processes take place within fairly short distances vis-à-vis the high blockage case.

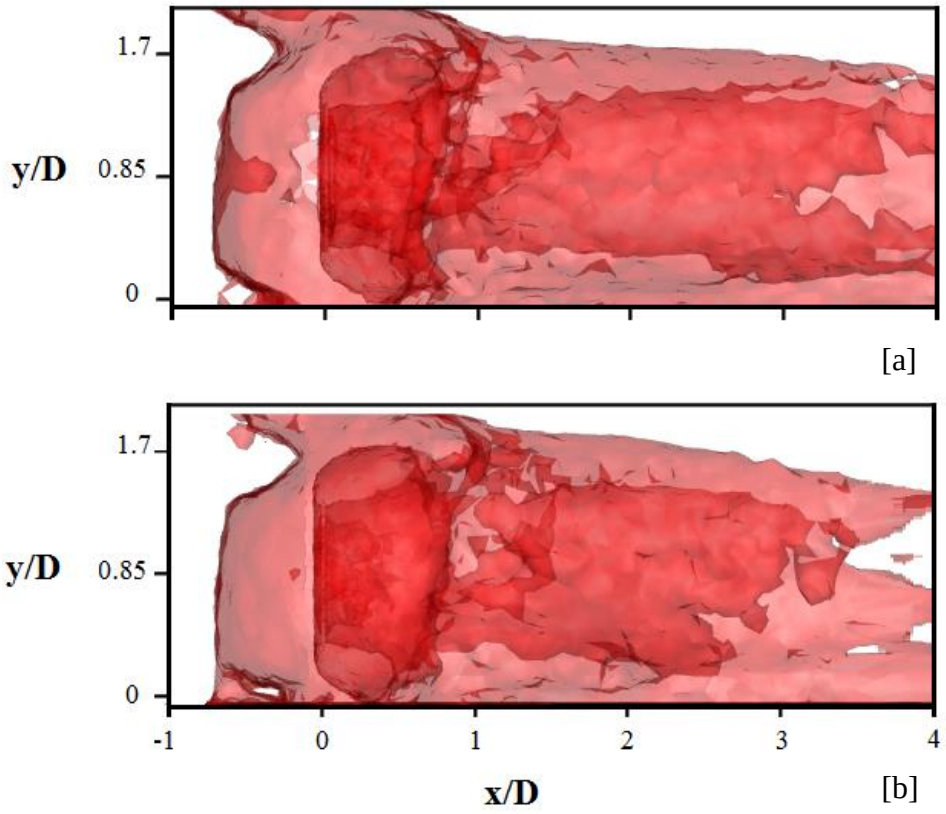

Figure 6-13 - Iso-surface of flow vortex strength at magnitude 0.035 (1/s) [a] high blockage [b] low blockage.

The above double-peak phenomena can also be explained by examining the flow trajectory. Figure 6-14 shows the contours of vertical velocity along the vertical central plane for the high blockage case. The arrows on the figure illustrate the vertical component of flow before

and after the turbine. These vertical vectors play a significant role in altering the flow trajectory as well as the turbulent generation. It is clear that the accelerated flow deviates towards the bed as it approaches the turbine and swirls around it to create the first stress peak. The flow then reflects back off the bed, as shown in the figure, to collide with the wake vortex. At this stage the shear stress on the bed reduces slightly because the reversed flow behind the blade holds back the acceleration of the swirling flow.

Subsequently, the flow beneath the turbine moves back towards the bed again but this time with an additional cross-stream component generated from the wake vortex to create a second peak. Beyond the second peak, this interaction moderates and shows no further peaks. The wake starts to recover and the stresses on the bed start a gradual reduction.

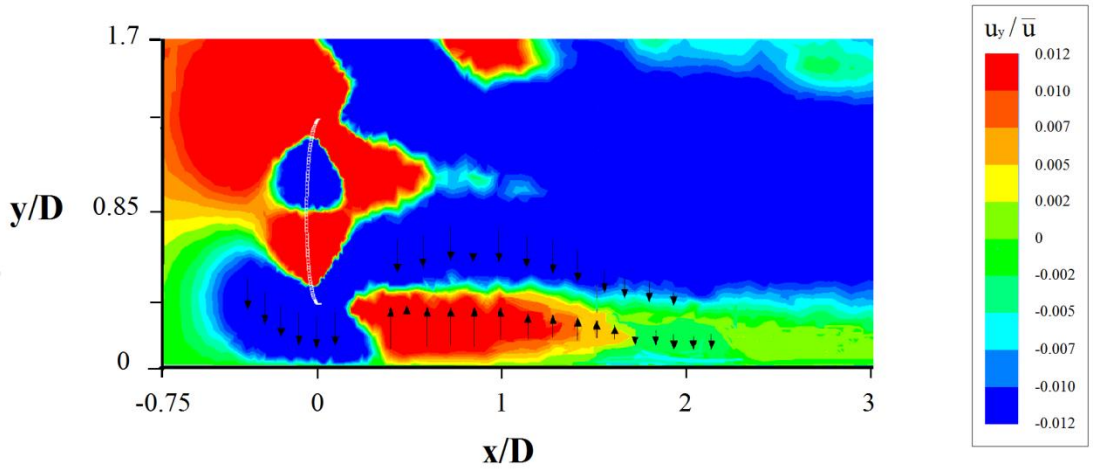

Figure 6-14 - Side view: contours of vertical velocity at centre plane.

Figure 6-15 shows the contours of shear stress on the bed surface for the two different blockage conditions. Overall, the high bed shear stresses are found along the central line where the wake is expected to dominate. It is clear that for the high blockage condition the turbine impact on the bed covers a wider area (almost the entire bed). For low blockage condition, the shear stresses are found to be limited within a small area behind the turbine. It is also clear that the shear stresses tend to move to the left-hand side of the turbine (-z/D) following the wake shift.

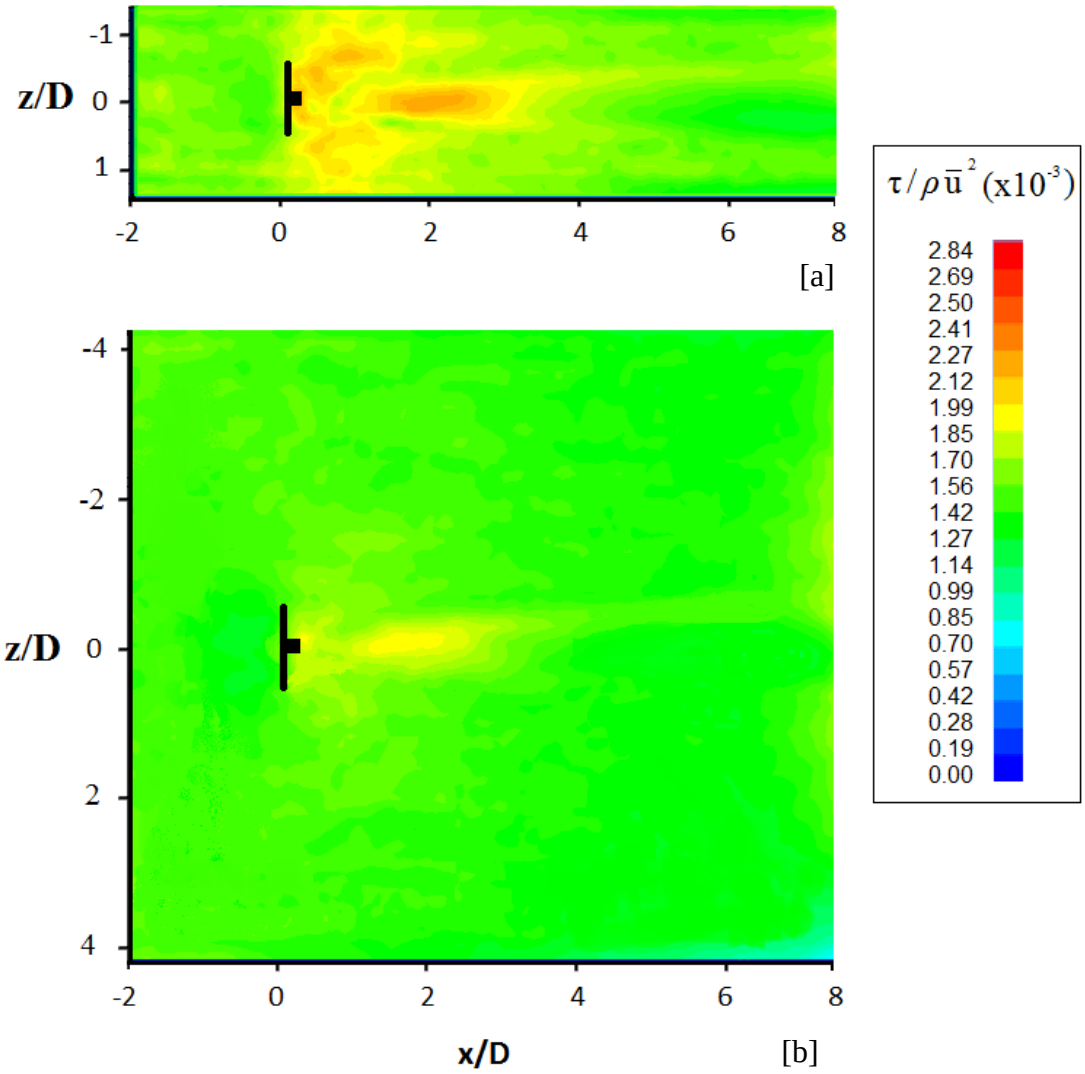

Figure 6-15 – Top view: contour of shear stresses along the bed surface for [a] High blockage and [b] Low blockage.

Figure 6-16 [a] compares the free surface elevations for both cases. It is found that high blockage has a stronger impact on both the magnitude of surface elevation changes and its length. This relates directly to the flow behaviour beneath the surface induced by the turbine operation, as seen in [b]. In front of the turbine, the flow near the surface experiences velocity reduction imposed by the turbine obstruction and therefore the discharge is compensated by area increase to cause a surface rise.

Conversely at the turbine the flow diverges and accelerates around it, inducing high flow velocity beneath the surface, which consequently causes the surface to drop. It is found with high blockage that the surface undergoes a stronger surface change, 34% greater than in low blockage case.

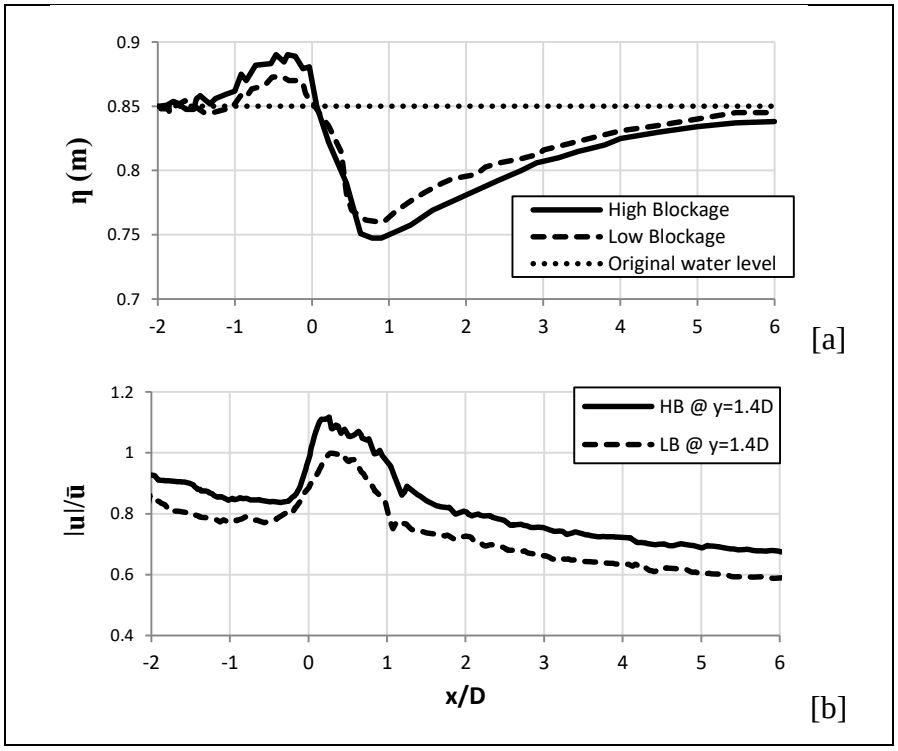

Figure 6-16 - Comparison of blockage conditions, [a] surface elevation, [b] velocity magnitude along the centreline at y = 1.4D.

6.3 Yaw Effect

In natural tidal flows, a tidal turbine is liable to be attacked from any angle. The angle of flow will vary depending on the tidal condition. It has always been a common practice to study flows perpendicular to turbines (yaw = 0˚). However, when yawed turbines are considered, usually the performance and loading on the rotor are investigated. It is as yet uncertain from literature how the impact of a yawed turbine would affect the flow dynamic and surrounding environment. In this study, a turbine with yaw angle of 45° is assessed to characterise the changes in wake, shear stress on the channel bed and variation on the free surface. The model is identical to LBM case, apart from the alignment of the turbine as shown in Figure 6-17.

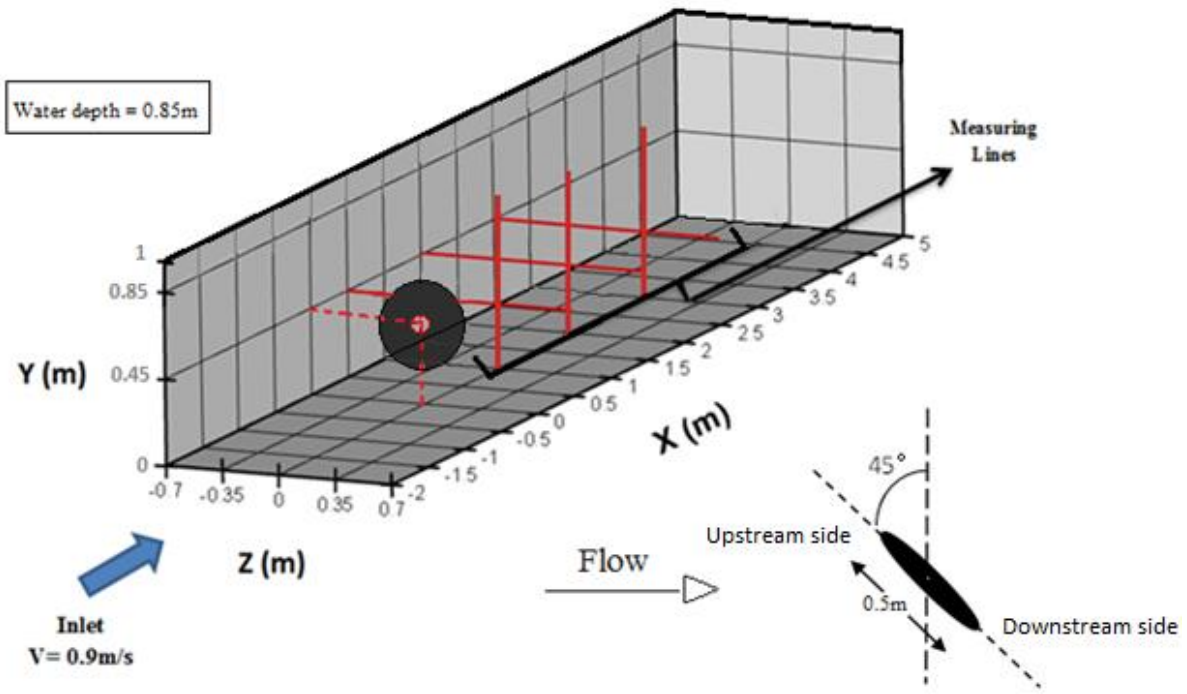

Figure 6-17 – Model description for turbine with 45° yaw.

The initial exercise is to look at the velocity profiles across the channel at 1, 3 and 5 diameters downstream. The model is set up with ≈ 0.95 million tetra/mixed cells. As shown previously in the LBM case, close to the turbine the horizontal profiles of streamwise

velocity show a “W” shape. However, when the turbine is at 45° yaw angle, such a distribution is deformed.

Figure 6-18 shows the comparison between the horizontal profile of velocity magnitude at 1D, 3D and 5D (centreline) for a turbine at 0° (solid lines) and 45° yaw (broken lines). It is found that when the turbine is at 45° towards the flow direction, the “W” distribution in the flow streamwise velocity totally disappears and instead a “U” shape becomes apparent. Consequently, low permeability at the turbine centre is seen where higher velocity reduction takes place of around 6% at 1D.

However, this strong reduction is not seen behind the blades and towards the channel walls, as shown in Figure 6-19, where top-down view of streamwise velocity distribution across the whole channel at y/D = 0.85 level is presented for both normal and yawed turbine cases. It is also found that the turbine yaw produces an unsymmetrical velocity deficit which imposes the flow with some curvature. At 3D and 5D, the flow velocity profiles show faster velocity recovery for the yawed turbine (45°).

Based on Figure 6-19 [b], the asymmetry is more likely because the reduction in flow speed behind the two sides of turbine is not the same. The up-water side has very small reduction area (shadow). But the down-water side has very large shadow which dominates the wake, and hence diminishes the leverage of flow in the centre.

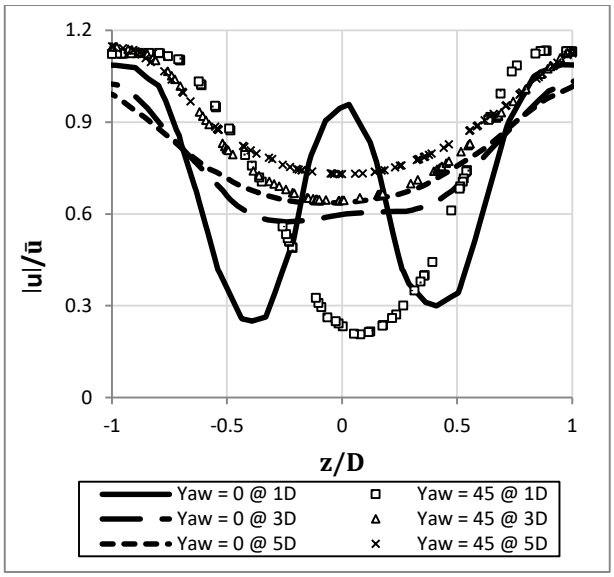

Figure 6-18 – Compares the horizontal profiles of velocity magnitude between straight (0°) and yawed (45°) turbines at 1, 3 and 5 diameters downstream.

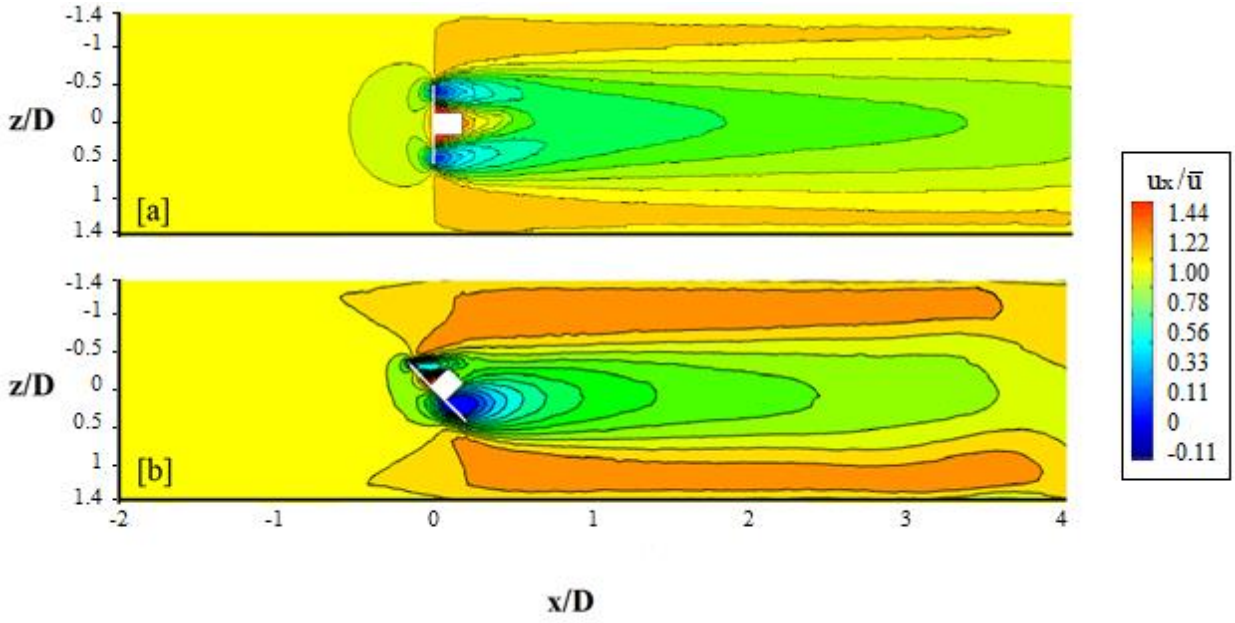

Figure 6-19 - Plan view: represents the streamwise velocity contour map across the channel width at [a] yaw = 0°, [b] yaw = 45°.

Figure 6-20 represents the vertical profiles of velocity magnitude for both 0° and 45° yawed turbines along the centre plane of the turbine at 1D, 3D and 5D downstream. It is clear that the distributions of flow velocity above and below the turbines are very different in the two cases. Similar to previous analysis, the water column is dived into three sections; the bed boundary layer (BBL) presented between 0D and 0.35D, the turbine-affected area (TAA) between 0.35D < y < 1.35D and the upper surface layer between y > 1.35D. For a 45° yaw turbine, the velocity in the bed boundary layer is clearly stronger than that at the other two layers by almost 35% on average at all three locations behind the turbine.

At the upper surface layer, however, apart from 1D, the velocity difference does not exceed 5%. The flow acceleration at the centre of the turbine is not seen for the 45° yaw condition due to low permeability, unlike the 0° yaw. The velocity distribution of the 45˚ yaw turbine follows a “U” shape with significant velocity reduction at the centre level of the turbine. The deceleration of flow behind the blades are stronger for the 0° yaw condition and occupies a wider area than that found for the 45° yaw turbine. However, at 5D, the flow distribution in both cases is very similar although close to the bed, the velocity from the 0˚ yaw turbine is low compared to that under the turbine with 45˚ yaw.

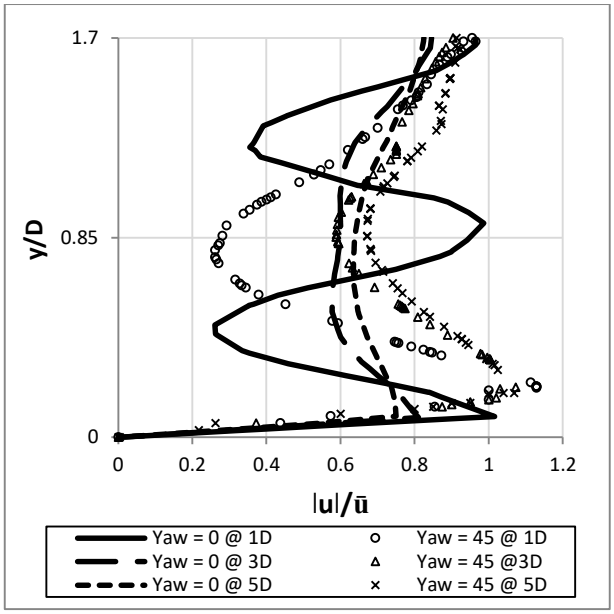

Figure 6-20 – Comparison between normalised velocity magnitude vertical profiles at 0° and 45° yaw for 1, 3 and 5 diameters downstream.

Figure 6-21 represents the contour maps of the streamwise velocity across the central vertical plane for both cases. It is found that when the turbine is at 0° yaw, the wake expands to a wider depth of the channel with a greater impact on the channel bed and free surface. The accelerated flow beneath the turbine collides with the channel bed and increases the bed shear stress. Near the surface, the accelerated flow above the turbine covers a longer range when compared with yaw 45˚, which as a result would increase and then decrease the surface elevation more. With 45˚ yaw, the asymmetrical feature of the flow above and beneath the turbine is fairly apparent, with the majority of the flow swirling underneath the turbine and dominating the wake behind.

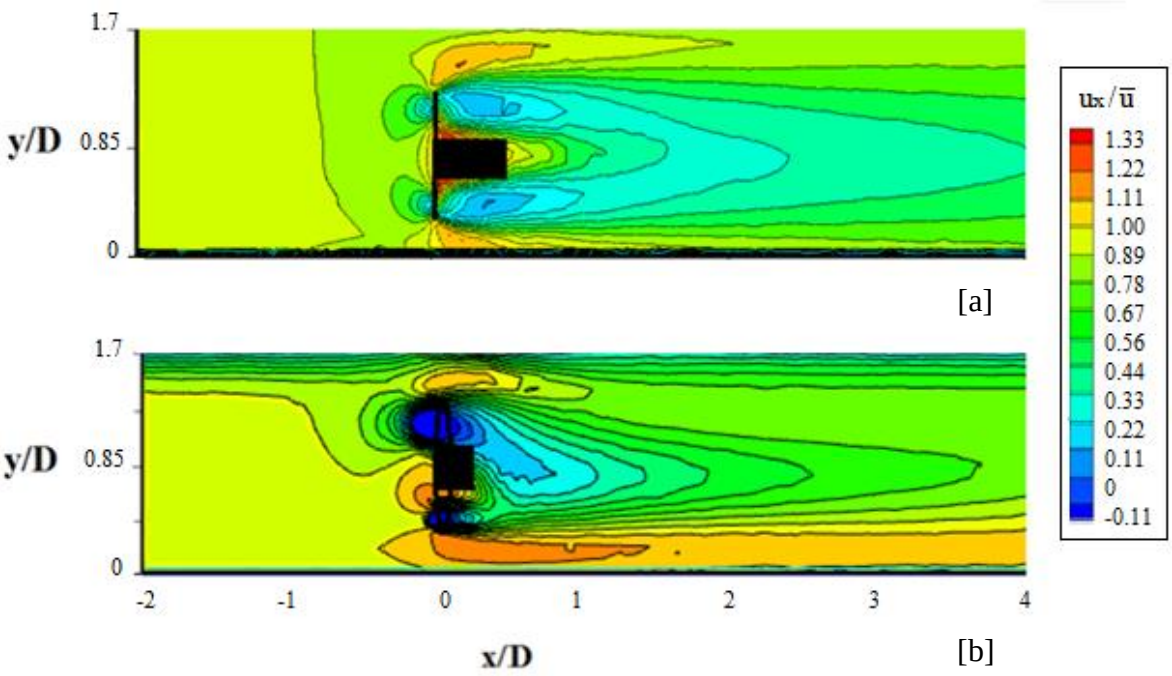

Figure 6-21 – Side view contour maps of streamwise velocity at channel centre [a] 0 yaw, [b] 45° yaw turbine.

Vortices are generated at both tip and tail of the blades. These vortices will induce frequencies which may cause resonance affecting the stanchion (Dahl, 2007). Figure 6-22 presents the plan view of the yawed turbine when tip vortices route the blade. Two coordinate systems are presented, the origin Cartesian x, y and z coordinate system and the aligned x_n, y_n and z_n coordinate system.

The vortex expansion is the distance between the blade tip and the vortex centre indicated as r. In general, vortices tend to expand on the outside of the blade tip [r > 0] (Haans, 2011). The vortex length is the distance from the blade tip to the point of vortex termination, indicated as ϒ. The vortex is calculated using $\frac{d\vec{w}}{dt} = (\vec{w}.\nabla)\vec{v} + \nu\nabla^2\vec{w}$ where $\vec{w}$ describes the evolution of vorticity, ∇ is the Laplace operator and ν is the kinematic viscosity (for more detail see ANSYS, 2010).

Figure 6-23 shows the contours of vorticity magnitude at the centre plane across the channel width. The 0° yaw turbine shows a symmetrical distribution of vorticity, however, the 45° yaw turbine clearly shows an asymmetric distribution. The asymmetric nature of the flow has a direct influence on the length and lateral expansion of the vortex. It is found that the vortex

length at the upstream side of the turbine is stretched more when compared to that of the downstream side.

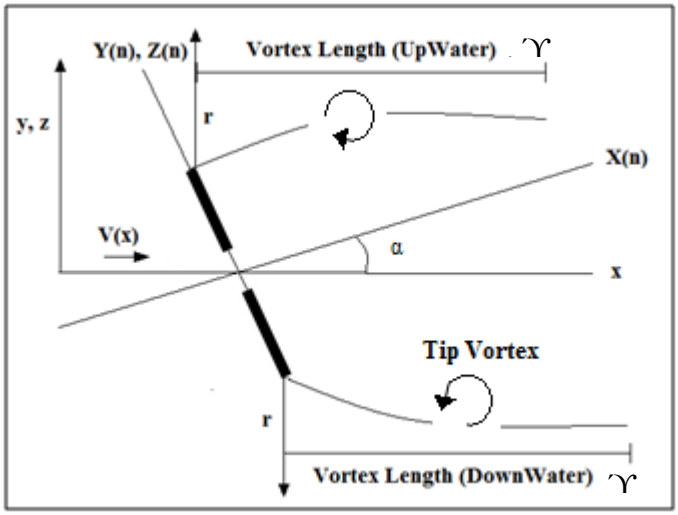

Figure 6-22 – Vortex description with reference to stream wise flow (after Haans, 2011).

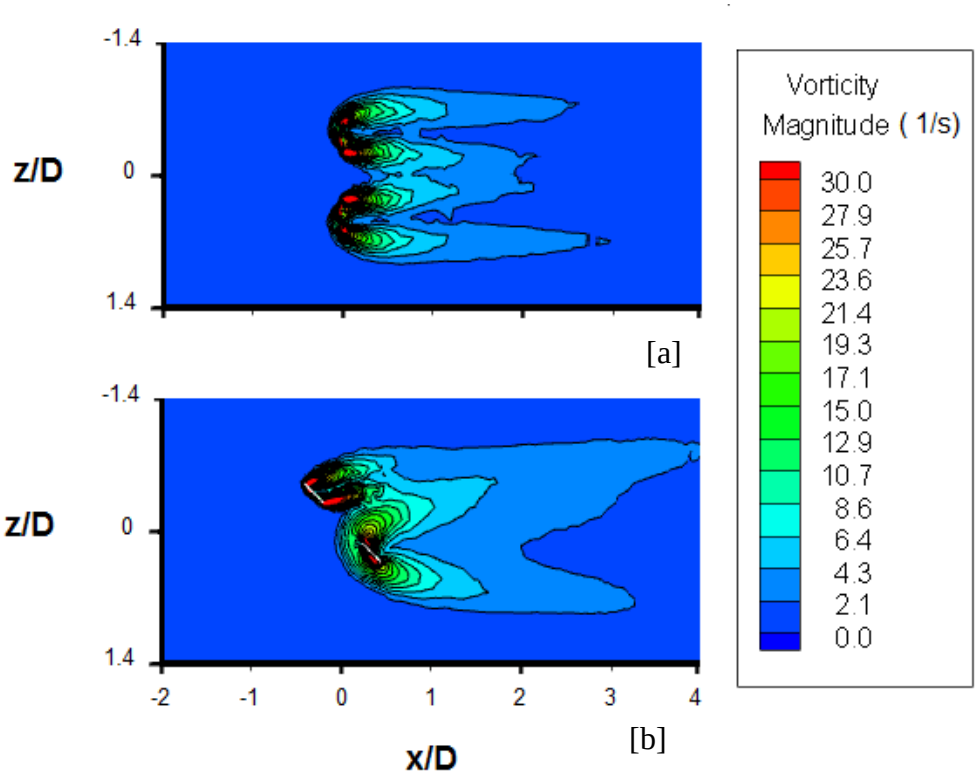

Figure 6-23 – Plan view: contours of vorticity magnitude in [a] 0˚ yaw and [b] 45˚ yaw.

Figure 6-24 compares the vortex expansion in the lateral (cross-field) direction between the two turbine conditions. The solid line denotes the straight turbine and the broken line the yawed turbine. It is found that maximum expansion occurs when the turbine is yawed, particularly at the downstream side. The figure indicates that the vortex obtains a wider radius (r) when the turbine is yawed. Thus this should be considered when arranging turbines in an array, to avoid wakes clashing with adjacent turbines or wakes causing higher turbulences (resonance). This also means that wake may have a wider impact on the aqua environment as the wake is covering a larger area.

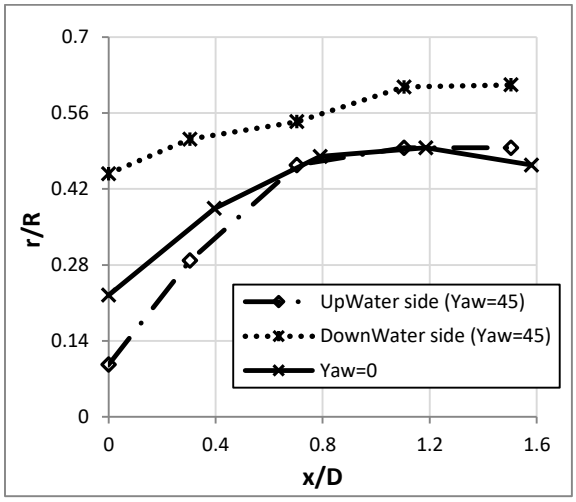

Figure 6-24 – Comparison of vortex lateral expansion between yaw=0˚ and yaw=45˚.

Figure 6-25 show the vertical view of vortices' magnitude for 0° and 45° yaw turbines across the channel depth at the centre. Similarly, the asymmetric nature of the vorticity distribution is apparent. It is clear that the vortex length is longer beneath the turbine for both cases; however, the expansion dominates the hub area.

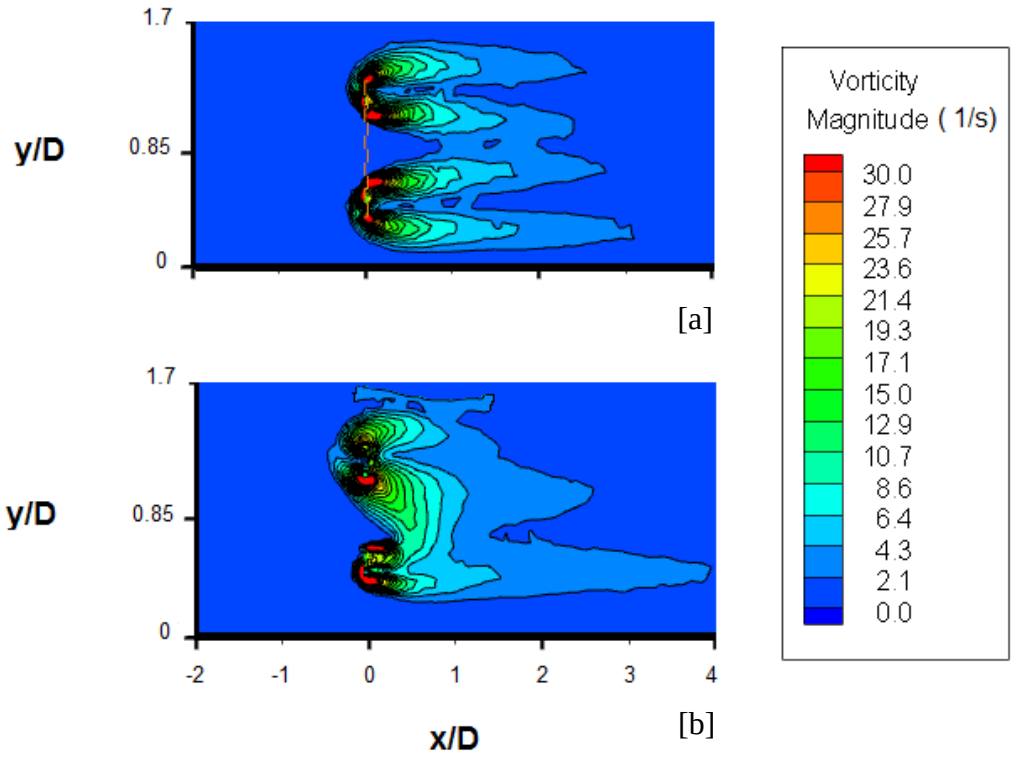

Figure 6-25- Side view: contours of vorticity strength across the channel depth at centre plane.

The asymmetry nature of flow directly influences the generation and dissipation of TKE behind the turbine (Figure 6-26). Comparing with 0˚ yaw, it is found that higher TKE is generated when the turbine is at 45˚ yaw at all sites. The maximum TKE increases by two times at 1D on the downstream side. This is because the surface area of the turbine that is in contact with flow at the instant of flow arrival is smaller for the yawed turbine, hence the flow can pass the turbine more smoothly. As well as this, the extra vortex expansion found at the downstream side leads to enhanced vertical and lateral motion that contributes to additional turbulence generation. Such a difference becomes less apparent further downstream as the wake starts to recover. Furthermore, it is clear that the TKE slightly shifts towards the downstream side due to the yaw effect.

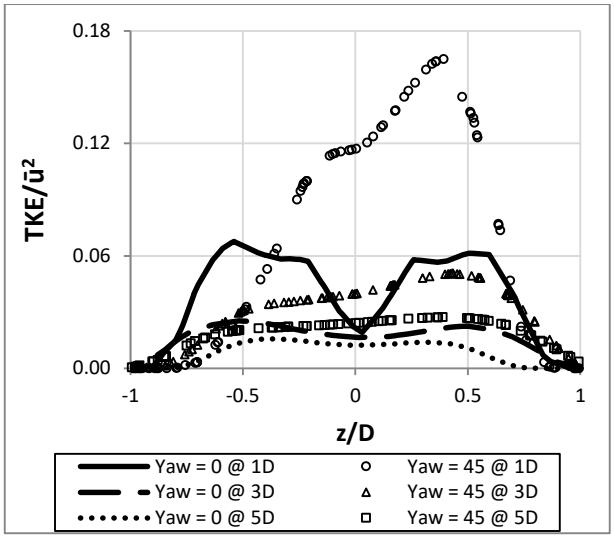

Figure 6-26 - Comparison of horizontal profiles of normalised TKE between straight and yawed turbine at 1D, 3D and 5D downstream.

Figure 6-27 shows the vertical profiles of TKE at 1D, 3D and 5D for both cases. It can be seen that at all three sites the 45˚ yaw turbine produces higher magnitudes of TKE across the water column. The largest differences can be found closer to the turbine at 1D, with 37% increases on average, which is smaller than that along the channel width as shown in Figure 6-26 (61%).

For 45° yaw turbine, it is found that the TKE is much higher at the lower half of the turbine-affected area (y/D < 0.85) when compared to the upper half (y/D > 0.85). However, such large TKE seems not to affect the bottom boundary layer as the value at the level below y/D < 0.2 is fairly small in comparison with the other part of fluid.

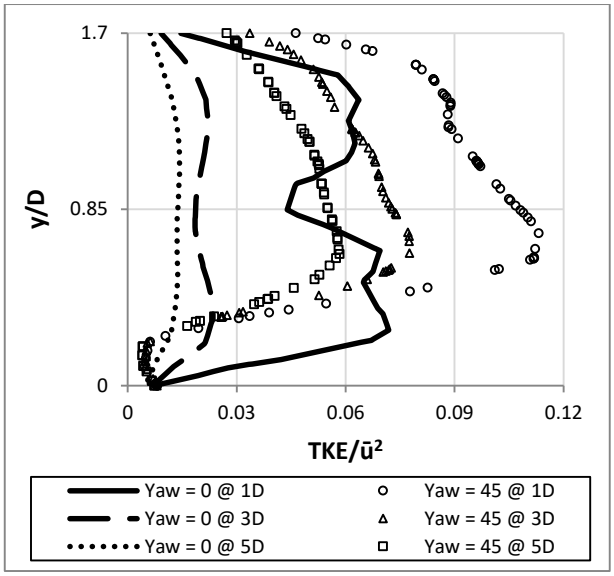

Figure 6-27 - Comparison between normalised TKE vertical profiles at 0° and 45° yaw for 1, 3 and 5 diameters downstream.

Figure 6-28 shows the contour of TKE distribution for both 0° and 45° yaw across the channel sections at 1D, 2D, 3D and 5D. It can be seen that for the 0° yaw, the turbine-induced TKE remains symmetrical. However, with 45° yaw, the TKE follows an asymmetrical shape with higher value at the downstream side until 5D downstream. The magnitudes of TKE at 1D, 2D, 3D and 5D for the 45° yaw turbine are also higher than that in the 0˚ case as shown in previous figures.

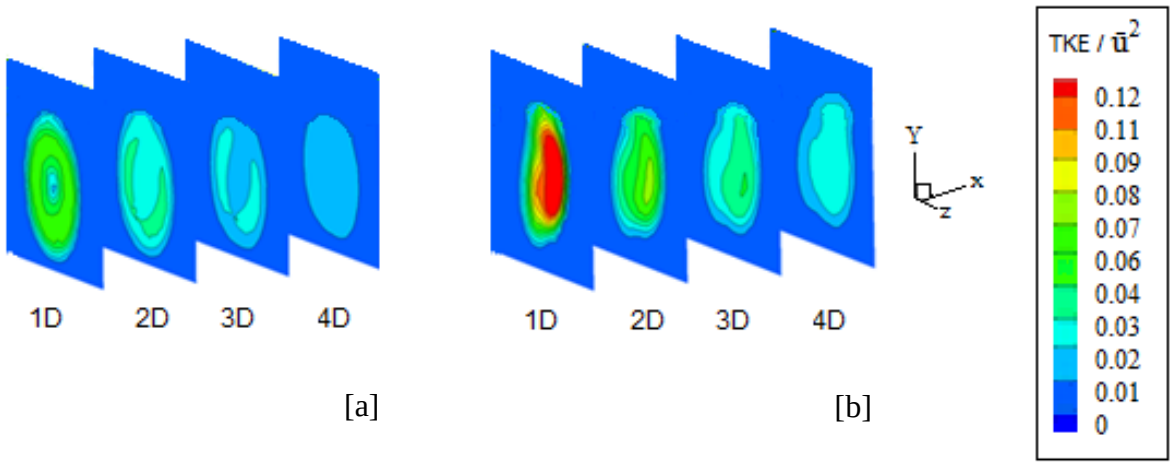

Figure 6-28 – TKE contour maps at 1, 2, 3 and 5 diameters downstream, [a] 0° yaw and [b] 45° yaw.

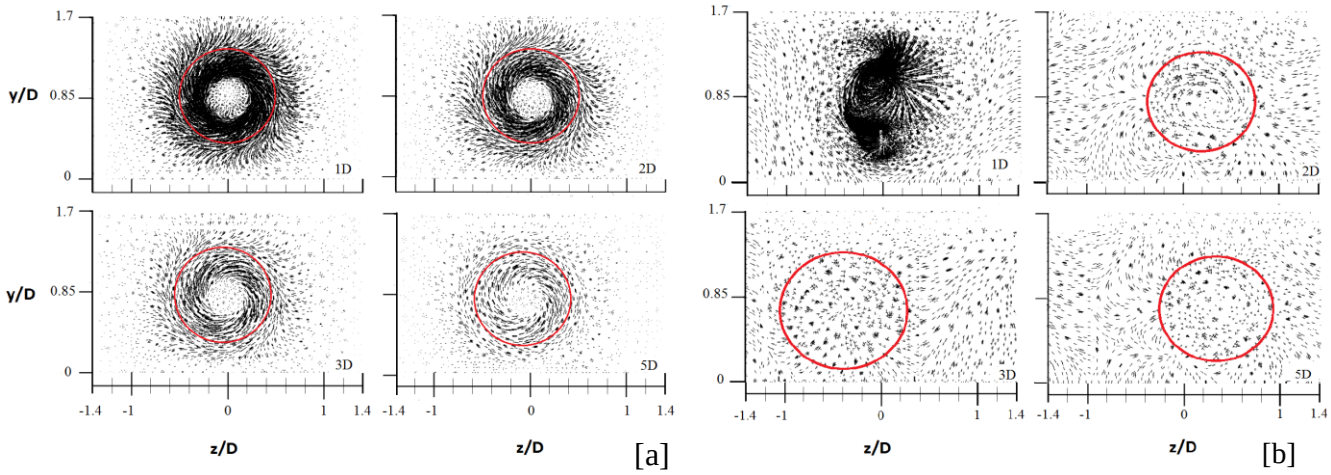

Figure 6-29 - Vectors of flow across the x-plane at 0D, 1D, 3D and 5D downstream [a] yaw = 0˚ and [b] yaw = 45˚.

Figure 6-29 present the vectors of flow across the x-plane at 1D, 2D, 3D and 5D for both turbine conditions, where the solid red circle marks the vortex. It is clear that the vortex more or less persists at a central location behind the 0˚ yaw turbine, not showing any significant oscillation or transformation [a]. For the 45˚ yaw turbine [b], it is clear that the vortex axis is not uniform and is shifting from right to left and vice versa as the flow travels downstream.

Figure 6-30 compares the distribution of shear stresses on the bed surface for the 0˚ and 45˚ yawed turbines along the centreline in the streamwise direction. In the 45° yawed turbine case, it is clear that the near bed shear stresses are on average lower by 7% than that for a 0˚ yaw turbine. This is due to the different blockage effects produced by the turbines. When the flow approaches the 45˚ yaw turbine, it experiences less blockage from the turbine and therefore the velocity deficit in front of the rotor is not as strong, which directly influences the shear stress.

As a result, at turbine location (0D), the flow beneath the turbine is not interacting with the bed floor as strong as that from the 0˚ yaw turbine. Behind the turbine, the shear stress for the 45˚ yaw turbine shows a reduction on average of around 20%. Comparing the distribution of shear stresses with the 0˚ yaw turbine, it is clear that the 2nd peak is not seen in this case.

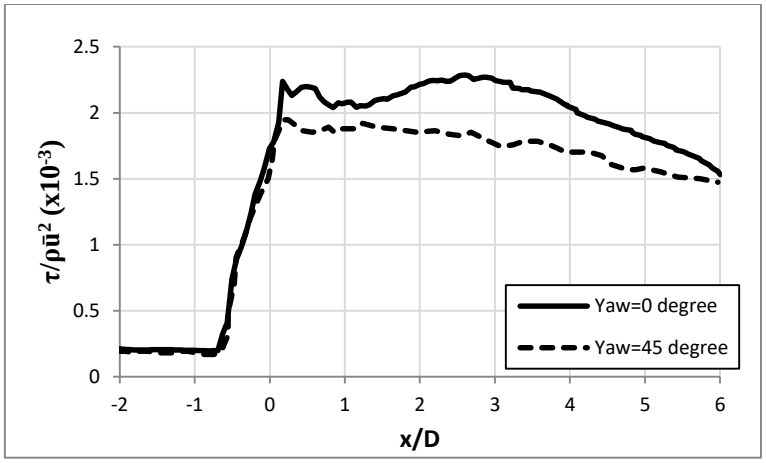

Figure 6-30 – Comparison of longitudinal profiles of bed shear stress between straight and yawed HATT at centreline and z = 1D.

Figure 6-31 shows the contour maps of shear stress across the channel bed for the two cases. Comparing with that in the 0˚ yaw case in [a], it is clear that the 45˚ yaw produces distribution along the channel in which two stress peaks appear at the upstream side (A and B) and two peak at the downstream side (C) immediately behind the turbine and (D) at 6D. This vortex movement in Figure 6-29 [b] correspond with the shear stress pattern seen here.

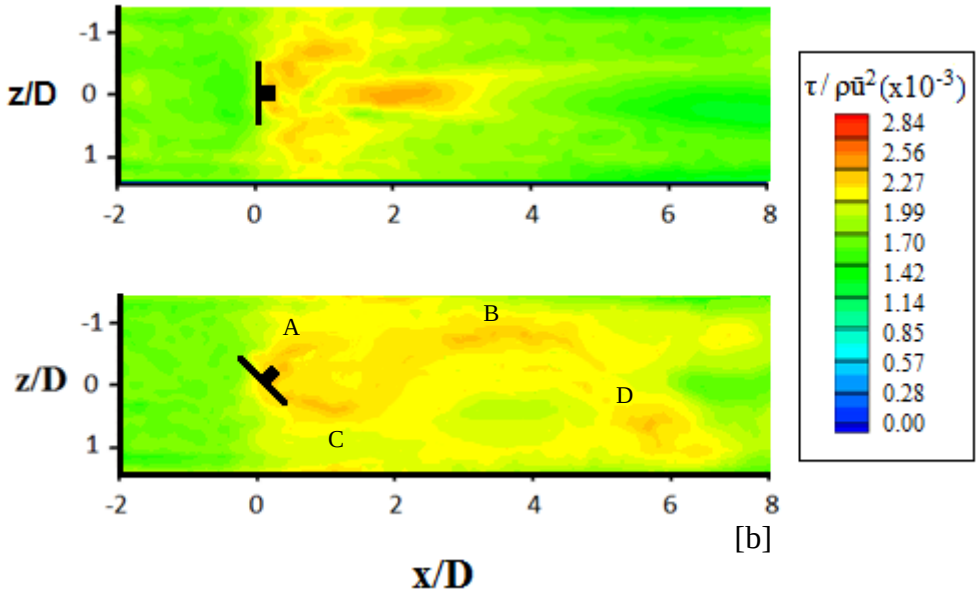

Figure 6-31 - Plan view: contours of shear stress on channel bed [a] 0° yaw and [b] 45° yaw.

[a]

These clear differences in near bed shear stress between a 0˚ yaw and 45˚ yaw turbine suggest that the angle of incoming current can have considerable impacts on the near bed process and, consequently, on the sediment transport on the seabed.

Figure 6-32 compares the free surface elevation across the central line of channel length. The comparison shows that the free surface variation is stronger for the 0˚ yaw turbine approximately 35% higher than that in the 45˚ yaw case.

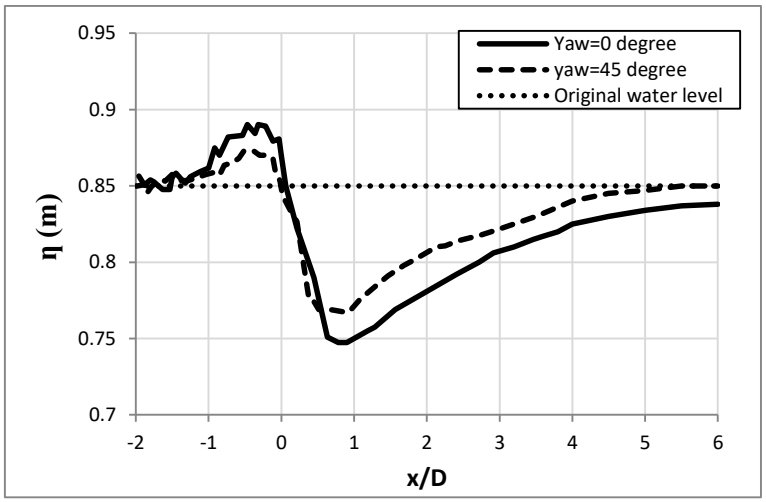

Figure 6-32 – Free surface elevation for straight and yawed turbine.

6.3 Turbulence Intensity

The aim of this test is to investigate and quantify the effects of background turbulence intensity (TI) on the turbine impacts on the wake characteristics and bed shear stress in realistic conditions. This is motivated by the fact that the natural condition in which the turbine works is highly complex and varies constantly. There are no exact values of background TI found in literature.

However, typical TI values used vary between 3%-15% for experimental and real tidal sites (Tedds et al., 2014, Milne et al., 2013, Batten et al., 2013 and Richmond et al., 2011). The tests in the present study involving laboratory experiments use typically 3% - 10%. Therefore, it is important to fully understand the coupling between turbine-generated turbulence and background turbulence. The model FBM (see Figure 6-1) is employed with an ambient turbulence intensity of 4% (see section 6.1 for setup conditions). The results are taken at three different positions, e.g., 1, 3 and 5 diameters downstream at turbine centre for comparison. The turbulence intensity is defined as:

$$TI = \frac{u'}{\bar{u}} \tag{6.2}$$

where u' is the turbulent velocity fluctuation and $\bar{u}$ is the mean velocity.

Figure 6-33 presents the contours of streamwise velocity across the channel centre plane (FBM). Similar wake characteristics are seen as those found in the experimental scale in Figure 5-18 (Jordan et al., 2015). This also includes the wakes slight alignment shift to the left-hand side of the hub of around 2˚.

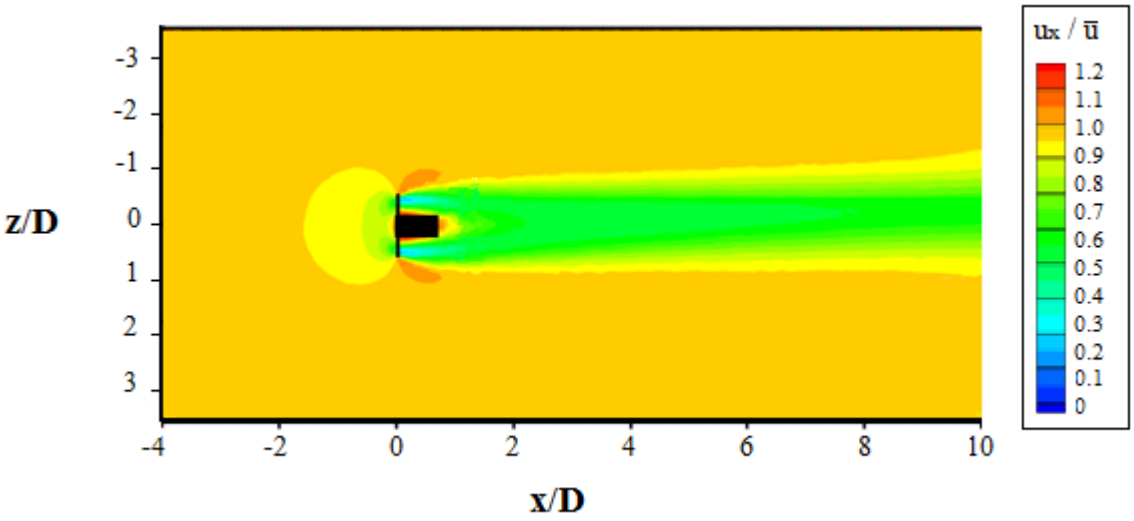

Figure 6-33 - Contours of streamwise velocity across the channel width centre plane with TI 4% (FBM).

To identify the TI effects on the turbine-induced wake and impacts to the surroundings, a test was conducted with 8% TI, keeping the other parameters as the above case. The results are then compared in the following section. Figure 6-34 presents the horizontal profile of streamwise velocity at 1D, 3D and 5D downstream from the TI= 4% and TI =8% cases.

It can be seen that the shape/distribution of velocity across the width of the channel is fairly similar between both cases. With higher turbulence intensity, the mix effect becomes stronger and hence it is seen that the velocity peak reduces its magnitude and smoothes out other areas of wake.

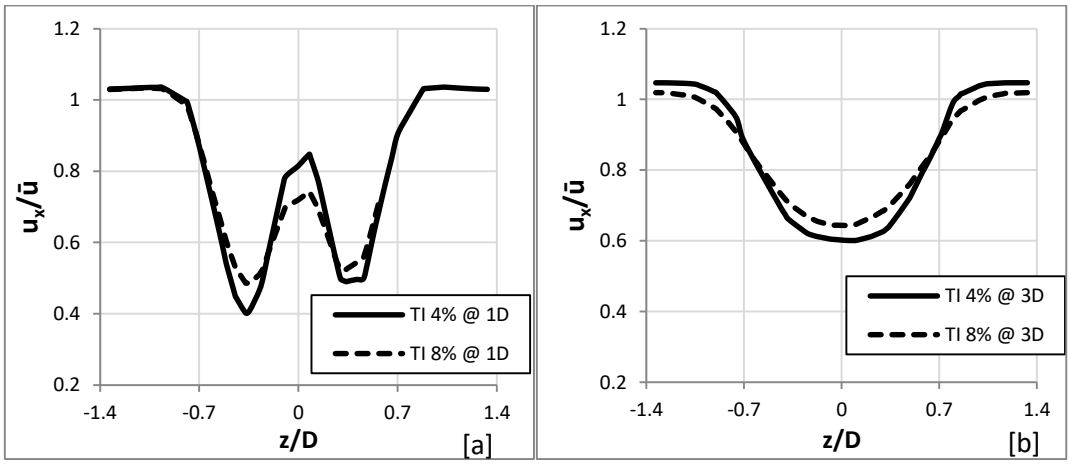

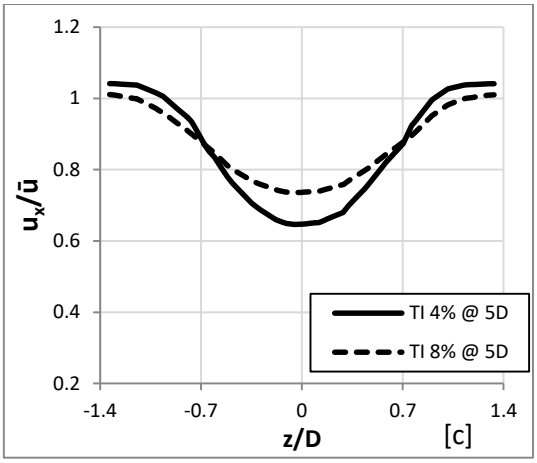

Figure 6-34 - Comparison of horizontal profiles of streamwise velocity between 4% and 8% inlet turbulence intensities at 1 [a], 3 [b] and 5 [c] diameters downstream (centreline).

Overall, it is clear that the velocity deficit is lower when the turbulence intensity is higher. The differences in maximum and minimum velocity between both cases increase further away from the turbine. At 3D and 5D, the velocity deficit is seen to reduce more apparently and the differences in velocity deficit peak increase to 7% and 14% respectively. It is also clear that this flow speed recovery takes place within the turbine area. This shows that TI has stronger influence in areas with high velocity reduction. Furthermore, at 1D, it is also found that the flow shows stronger velocity variation between maximum and minimum peaks when turbulence intensity is lower. This indicates that high background turbulence levels will reduce the flow asymmetric velocity behaviours.

Figure 6-35 compares the vertical velocity distribution across the width of the channel at 1D, 3D and 5D downstream for the 4% and 8% TI cases. Again, the velocity profiles at all locations follow very similar distributions as those found in the experiments (Chapter 5). The results indicate that the flow undergoes a clockwise rotation that forms a vortex. It is found that with higher turbulence intensity the vertical velocity reduces in magnitude that implies that wake recovery is enhanced with higher background turbulences as the vortex is dissipated within shorter distance in comparison with that from low TI.

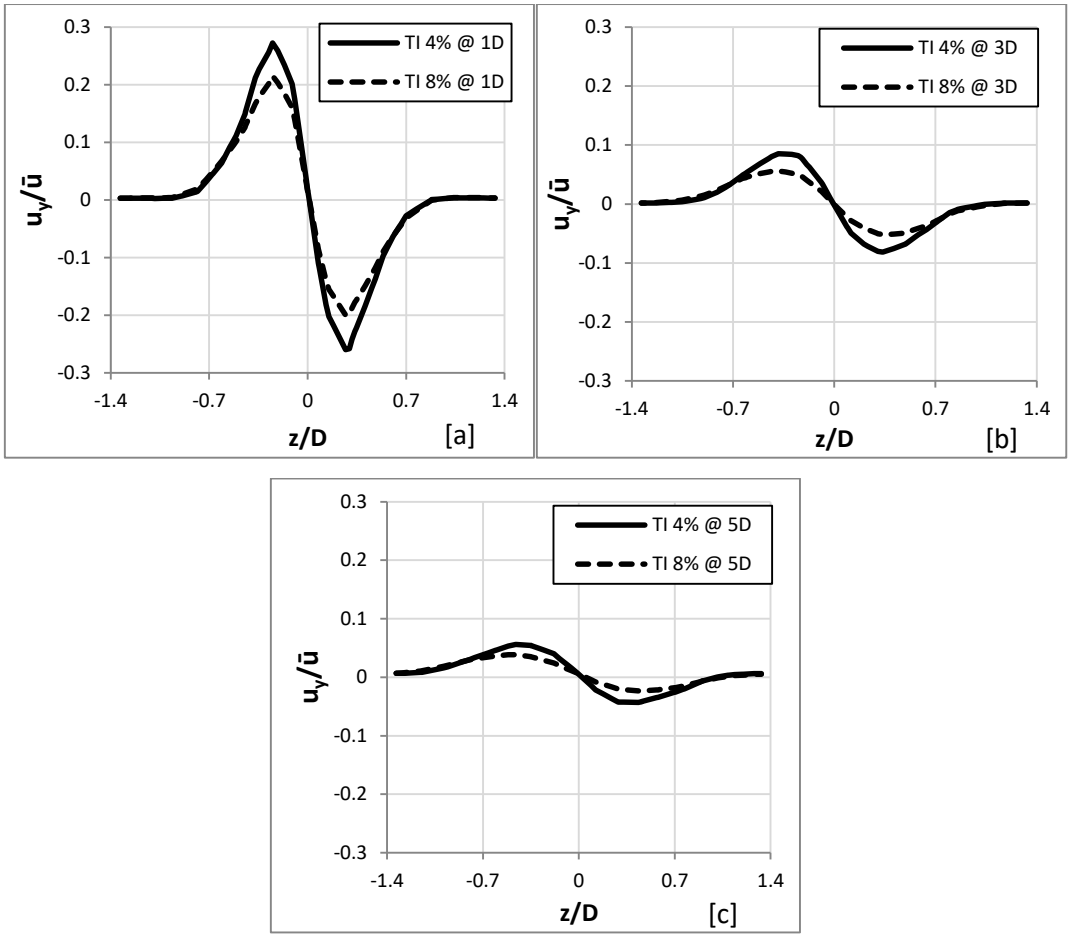

Figure 6-35 - Comparison of horizontal profiles of vertical velocity between 4% and 8% inlet turbulence intensities at 1D [a], 3D [b] and 5D [c] downstream (centreline).

Figure 6-36 compares the cross-stream velocity distribution across the channel width at 1D, 3D and 5D downstream for the 2 cases. Again, similar velocity behaviours are found to that of experimental condition at all locations (Figure 5-7). At 1D, it is found that the flow velocity is lower when the turbulence level is high. However, such a difference disappears at 3D and 5D. When the cross-stream velocity becomes zero, this means that the vortex is no longer present and the flow becomes straight again.

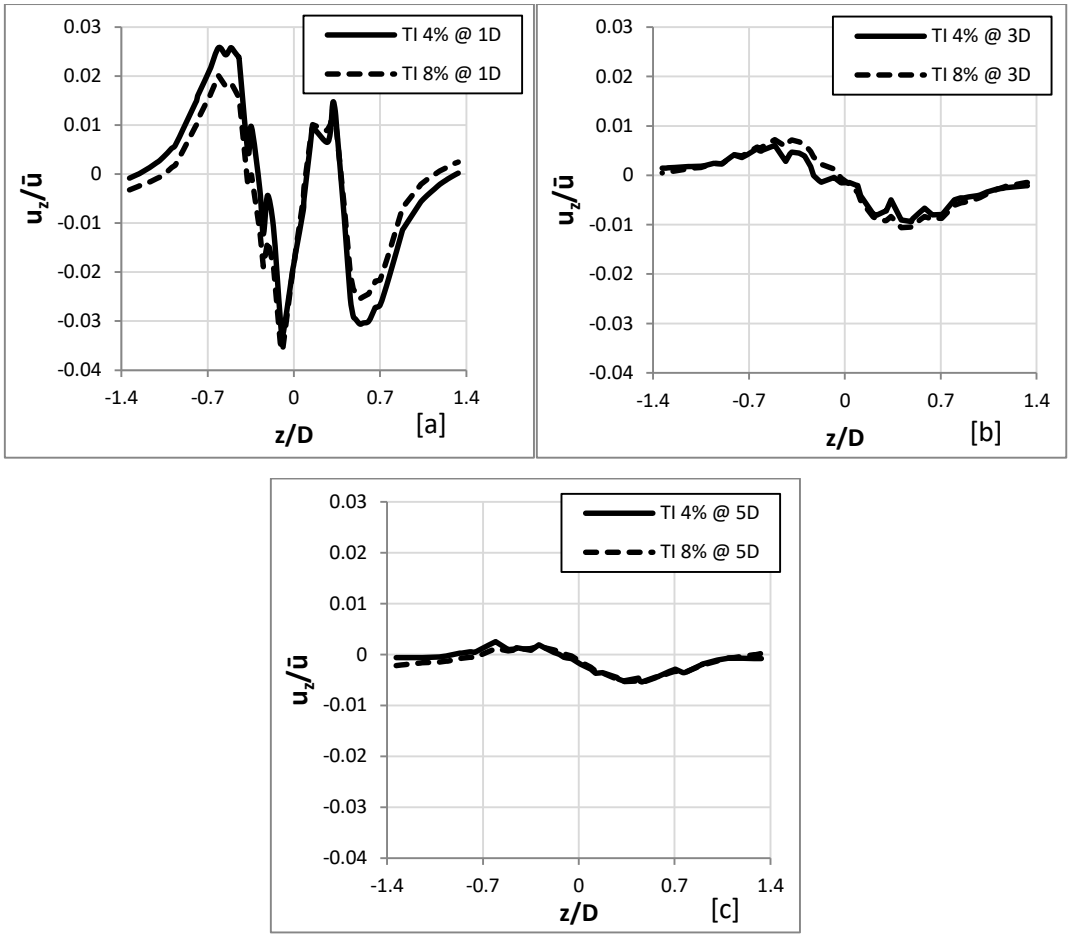

Figure 6-36 - Comparison of horizontal profiles of cross-stream velocity between 4% and 8% inlet turbulence intensities at 1D, 3D and 5D downstream (centreline).

Figure 6-37 shows the contours of streamwise velocity across the channel length along the centre plane (z = 0). Flow features similar to those seen in Jordan et al. (2015) experiment are found close to the turbine. However, we cannot see the position of the wake shifting towards the bed as that in previous chapter Figure 5-17

.

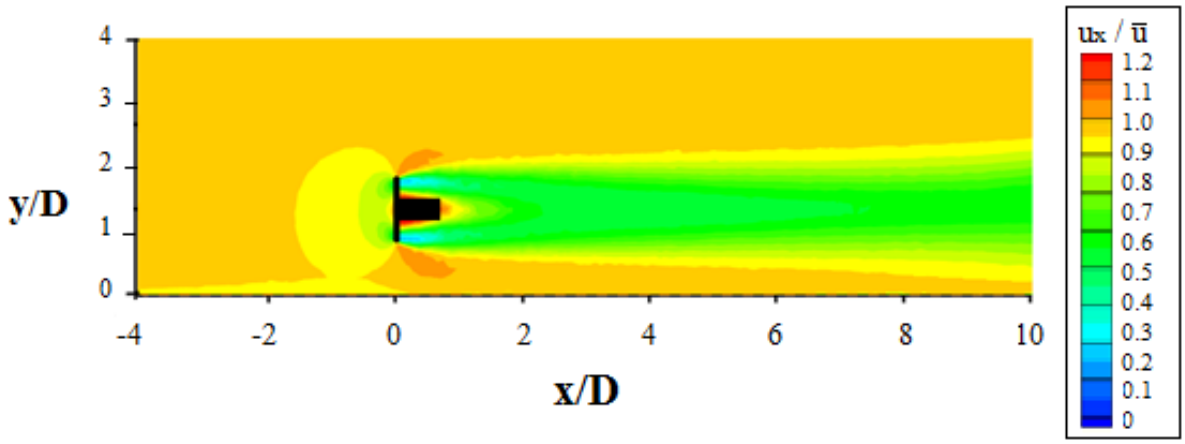

Figure 6-37 - Contours of streamwise velocity across the channel length along centre plane, z = 0 (FBM, TI = 4%).

Figure 6-38 shows the vertical profile of normalised velocity magnitude at 1D, 3D and 5D downstream for both cases. Initially, it is found that background turbulence intensity does not have any effects to the velocity both near bed and free surface. However, at turbine region (1 < y/D < 2) the velocity difference becomes smaller with higher inlet turbulent intensities. Maximum differences in velocity can be found at the centre of turbine.

At 1D downstream, it is found that the change in velocity across the turbine area is less significant when the background turbulence intensity is high. For example, when the TI is 4%, the difference in velocity is 7% higher, suggesting higher flow speeds at the hub area and lower speeds behind and around the turbine. At 3 and 5 diameters, it is clear that the velocity deficit becomes smaller when higher inlet TI is set, indicating differences in velocity reduction of 7% and 20% respectively. It is found that high TI smoothes out velocity, reducing the variations.

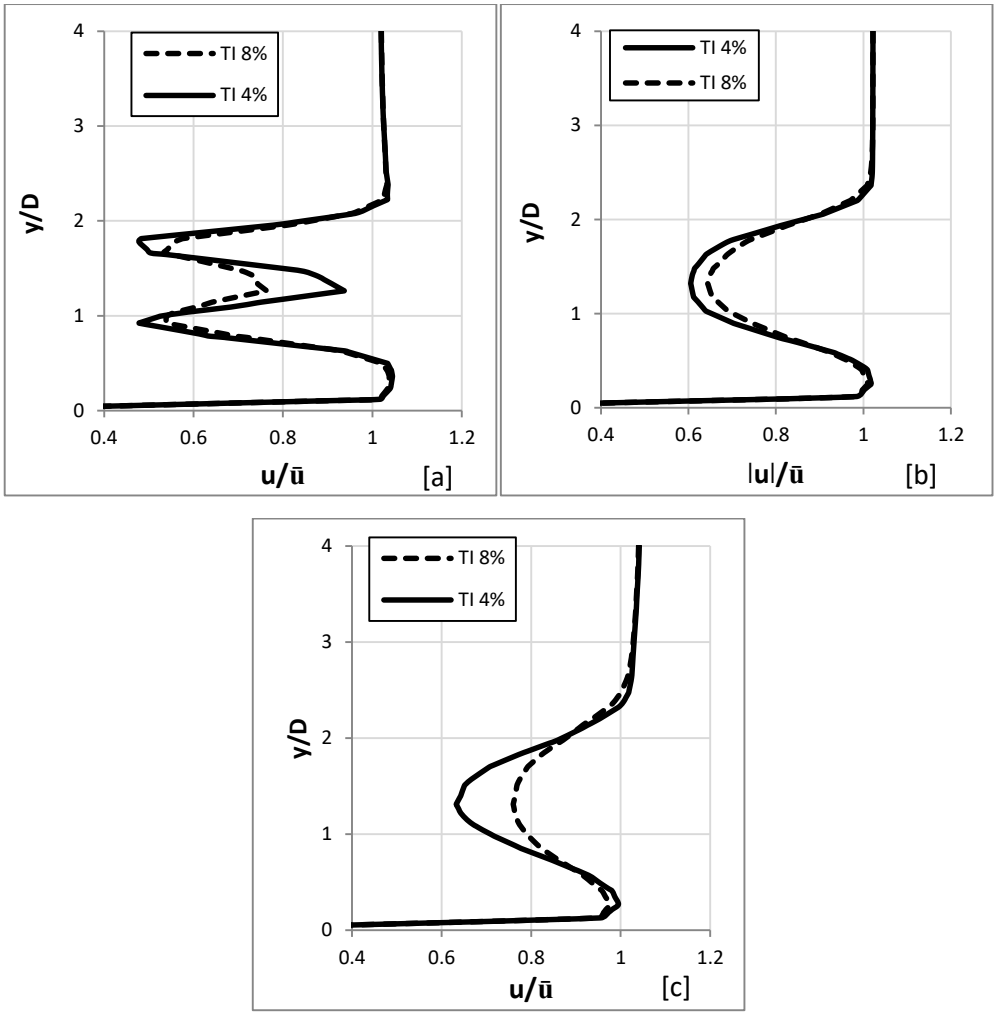

Figure 6-38 – Comparison of vertical profiles of velocity magnitude between 4% and 8% inlet turbulence intensities at 1D [a], 3D [b] and 5D [c] downstream (centreline).

Figure 6-39 shows the horizontal profiles of TKE at 1D, 3D and 5D for these 2 cases. It is clear that in both cases the maximum change in turbulence occurs behind the turbine blades and hub, where high TKE is are generated. For TI=8%, it is found that the TKE is almost twice higher than that found for TI=4% condition at 1D, 3D and 5D downstream.

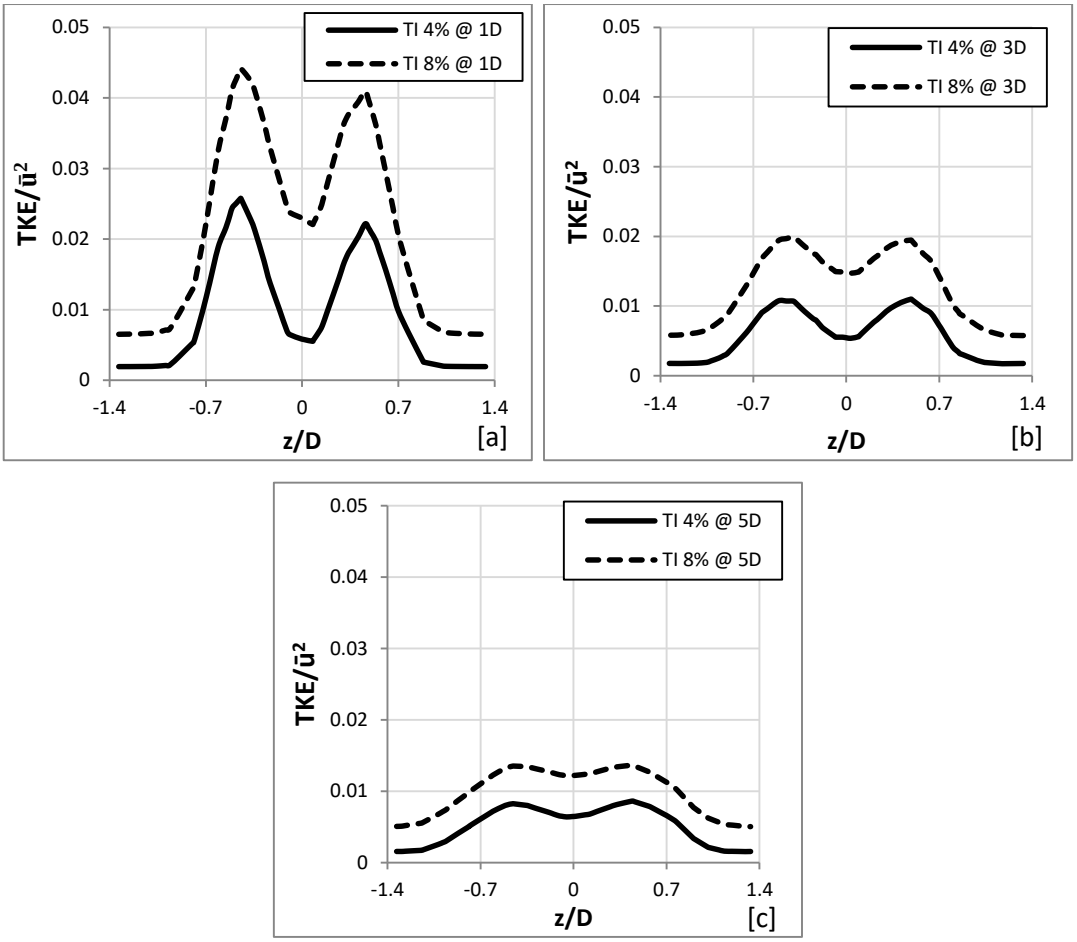

Figure 6-39 - Distribution of TKE across the width of channel at x = 1D [a], 3D [b] and 5D [c] behind the turbine with 4% and 8% TI respectively at turbine centre.

Similarly, Figure 6-40 compares the vertical profiles of normalised TKE at 1D, 3D and 5D with the two different TI backgrounds. The results show that the TKE values are influenced across the whole depth in both cases. Away from the turbine towards downstream however, the difference between the two conditions reduces. Comparing the two cases, the maximum difference is seen closer to the turbine.

At upper surface layer y/D > 2.5, the averaged TKE is higher for the TI 8% condition by about one times compared with TI the 4% case. In this particular region, influence on TKE generation is majorly affected by background TI rather than the turbine itself. At turbine region (0.5 < y/D < 2.5), the averaged TKE from 8% case is about 2 times, 1.65 times and 1 times when compared with the TI 4% case at 1D, 3D and 5D respectively. Such large difference actually is due to both background TI and turbine influence from these two cases.

It seems that the background TI enhances the turbine effects and turbulence generation in particular.

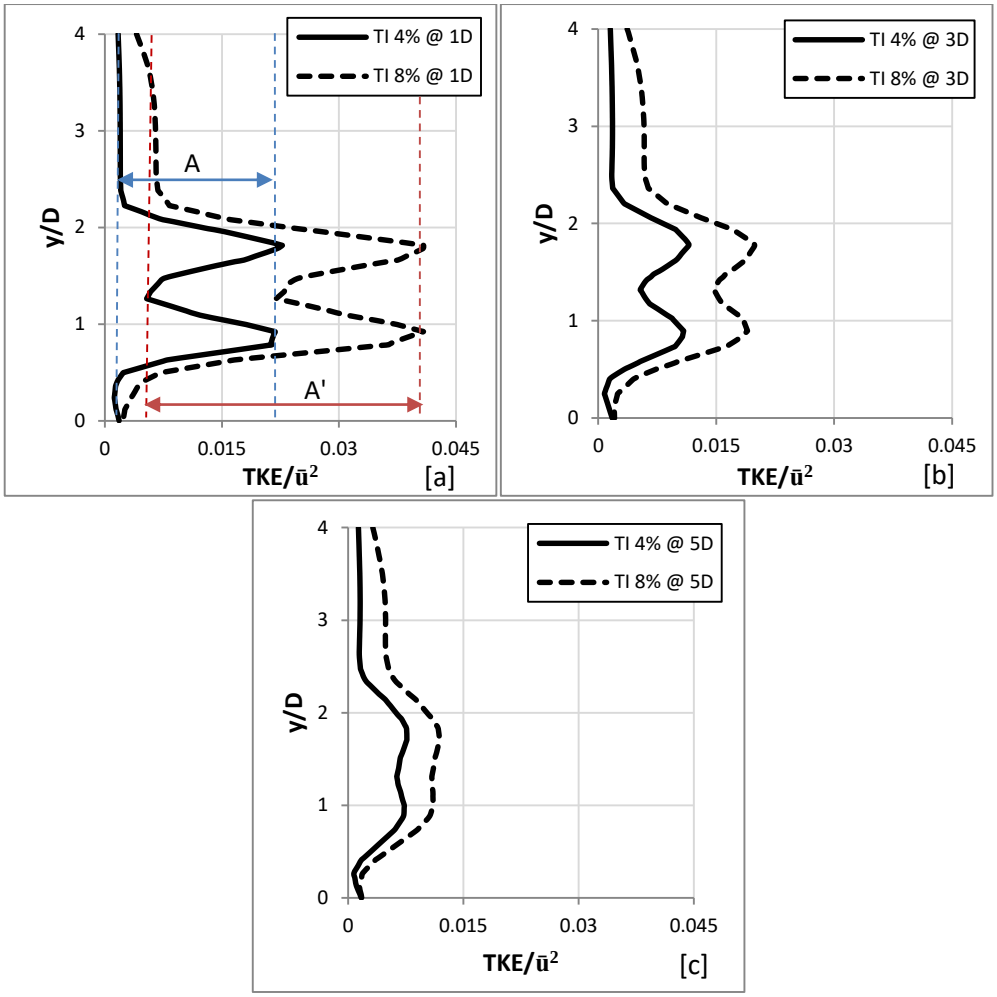

Figure 6-40 – Comparison of vertical profiles of TKE between turbulence intensities 4% and 8% at 1D [a], 3D [b] and 5D [c] downstream (centreline).

At bed boundary layer (y/D < 0.5), the averaged TKE in 8% case, is higher by 1.5 times, 1.43 times and 1.25 times when compared with the TI 4% case at 1D, 3D and 5D respectively. This indicates that there would be a potential impact on the channel bed due to this turbulence characteristics difference. Figure 6-41 presents the TKE across the channel width downstream. Due to the higher background TI in the 8% TI case, the turbulence level at all sites are higher than that in the 4% case. However, these two cases share fairly similar distribution of TI throughout the whole channel with circular pattern of high TKE at the level where turbine operates at these stations. At the last station, the difference between the cases in TKE is very small as shown in previous section.

Overall, it is found that the additional turbulence intensity did not only affect the background turbulence but also generated extra turbulence energy in the turbine region. In the TI = 8% case, it can be seen close to the turbine (x = 1D) that the turbine-induced TKE increases to a peak (A') that is approximately 2 times as that found in the 4% case (A). However, this added TKE is not found further downstream at 3D and 5D.

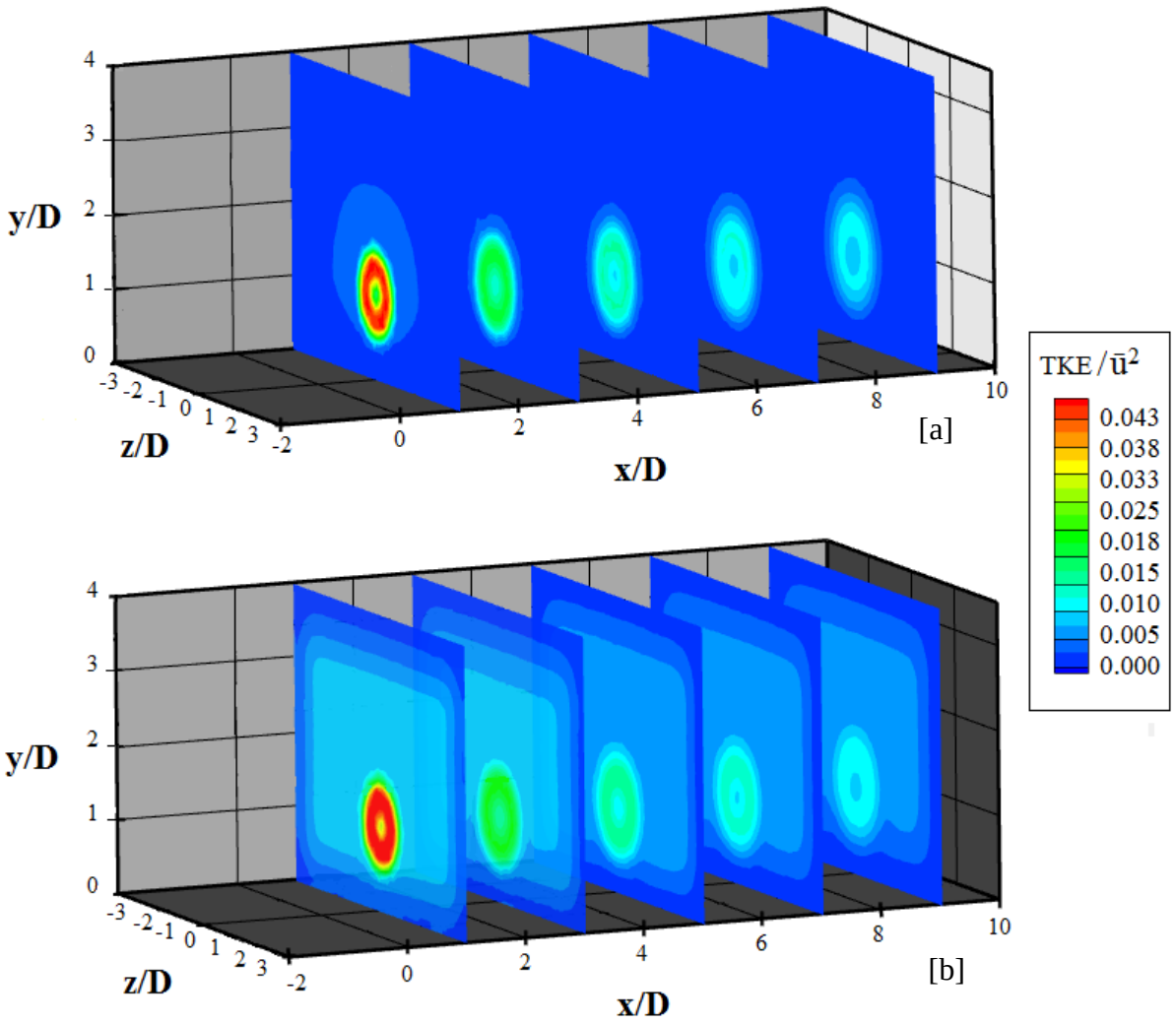

Figure 6-41 - Contours of TKE across the channel width at 1D, 3D, 5D, 7D and 9D [a] TI 4% (FBM) and [b] TI 8%.

Figure 6-42 illustrates the longitudinal profile of shear stress along the channel bed centreline under these two different TI conditions. It is clear that the shear stresses on the bed show an increase starting from the turbine position and maintain high shear stress in the downstream.

With higher background turbulence intensity, the shear stress on bed increase 23% in the wake region (x/D > 0). This means that background turbulence intensity variations can have stronger impact on bed shear stress in the wake region, which would certainly have an impact on sediment suspension and transport.

Figure 6-43 shows the contours of bed shear stress for both cases. It shows that with higher TI, the shear stress becomes narrower and distributed with longer tail. This is due to the changes in the near bed flow velocity as shown in Figure 6-38. The flow reduction at the turbine-affected area (y/D = 1.5) is reduced in the 8% TI case. Consequently, the near bed velocity in the boundary layer region (y/D < 0.5) reduces slightly and the velocity gradient increases, which leads to the slight increase in the bed shear stress.

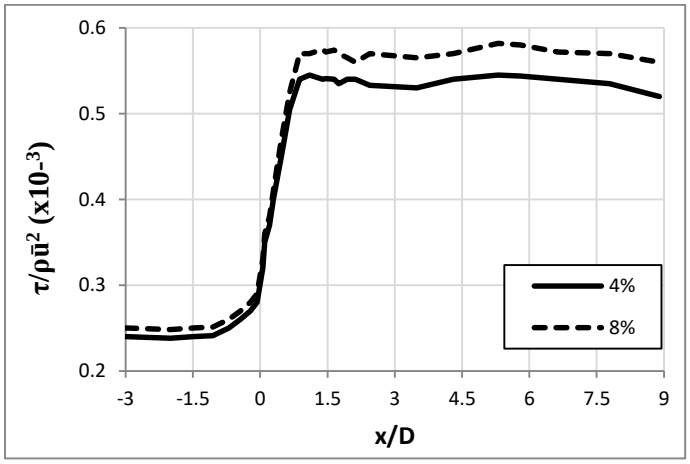

Figure 6-42 – Comparison of longitudinal profiles of shear stress between 4% and 8% inlet turbulence intensities at channel bed (centreline).

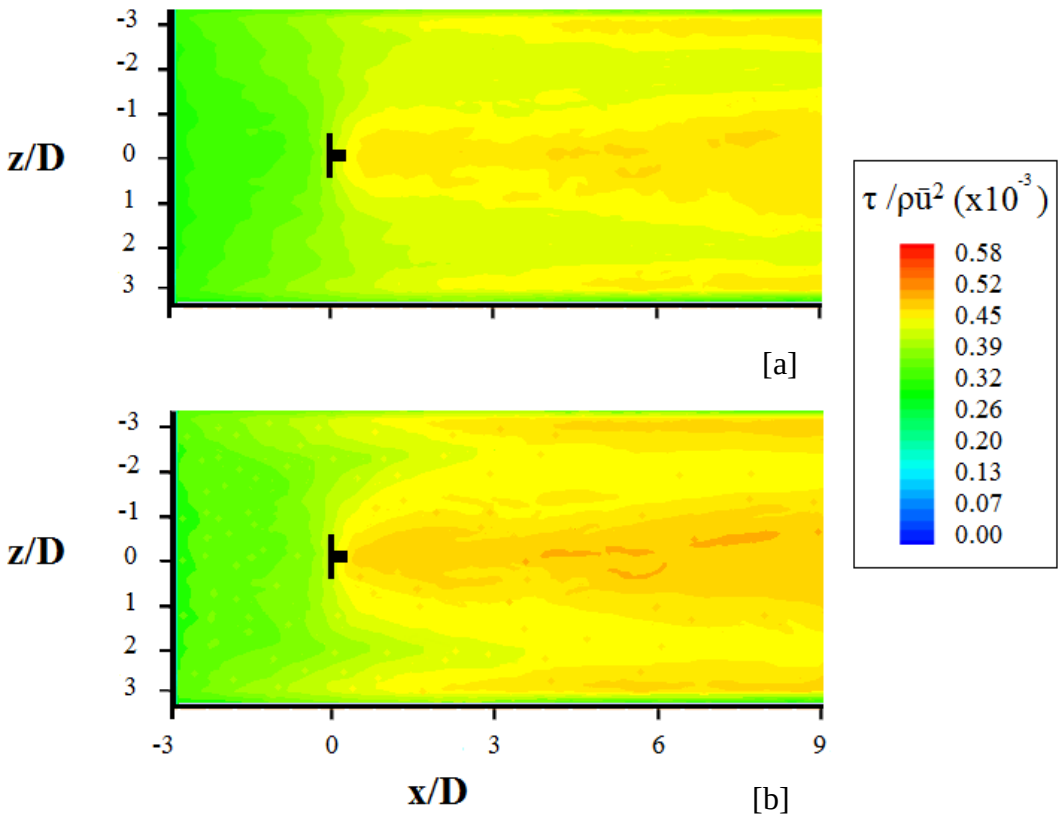

Figure 6-43 - Contours of shear stress on the channel bed. [a] FBM (TI=4%) and [b] TI=8%.

6.4 Elevation of HATT

The height of a turbine from a bed is an important parameter that has an influence on design of the turbine in terms of power generation and loading on the structure. At the same time, its environmental impact can be different with different elevations above the ground. A fully developed flow will trail an alternating distribution across the water column. This pattern is usually illustrated as a logarithmic profile which is best expressed by the logarithmic profile as:

$$u = u^* log\left[\frac{y}{z_0}\right] \tag{6.3}$$

where u_* is the near bed friction velocity value and z_0 is the elevation where velocity equals zero. It is not ideal to place a turbine very close to a stream bed, because the flow speed is low and would not produce maximum energies. However, placing a turbine at higher elevations will bring extra costs as loading on the structure will increase. Therefore, a compromise solution would be to place a turbine at 2/3 of the water depth.

It is important to identify the impact of turbines at different elevations above the bed, as it is still not clear what consequence to the near bed flow and outer flow would be with the increase of height above the bed from the turbine. In this case, two models are created with two different turbine elevations. The first model has a turbine located at 2/3 of the water depth and the second at mid-depth. Both models are set under the steady flow condition with average inlet velocity of 2m/s and turbulent intensity of 3%. A logarithmic profile is defined as in equation 6.3 with z_0=0.002mm and u^*=0.059m/s. Figure 6-44 presents the vertical distribution profile of velocity magnitude upstream as well as the turbine elevation positions in the water.

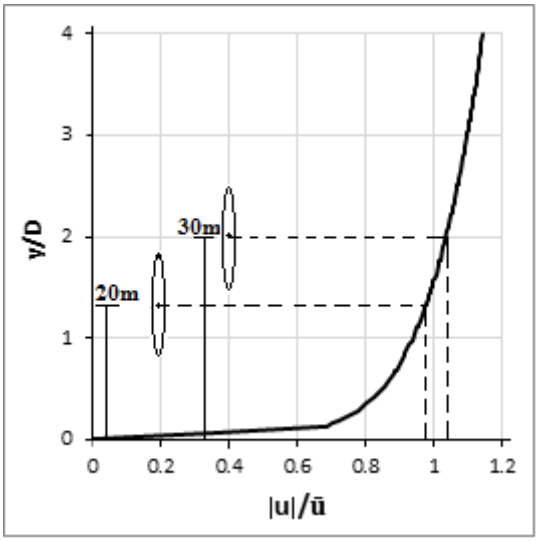

Figure 6-44 - Vertical profile of velocity magnitude at inlet. It also shows the turbine positions.

Figure 6-45 presents the horizontal profiles of velocity magnitude across the channel width at turbine centre level at 1D, 3D and 5D. The figures compare the velocity magnitude of both models, where the solid line denotes the turbine at mid-depth and the broken line denotes the turbine at 2/3 depth. At all locations, the turbine is experiencing stronger flow speeds when at mid-depth. This is reflected from the average velocity measured across the channel, showing an average increase of 8% at 1D, followed by 6% at both 3D and 5D.

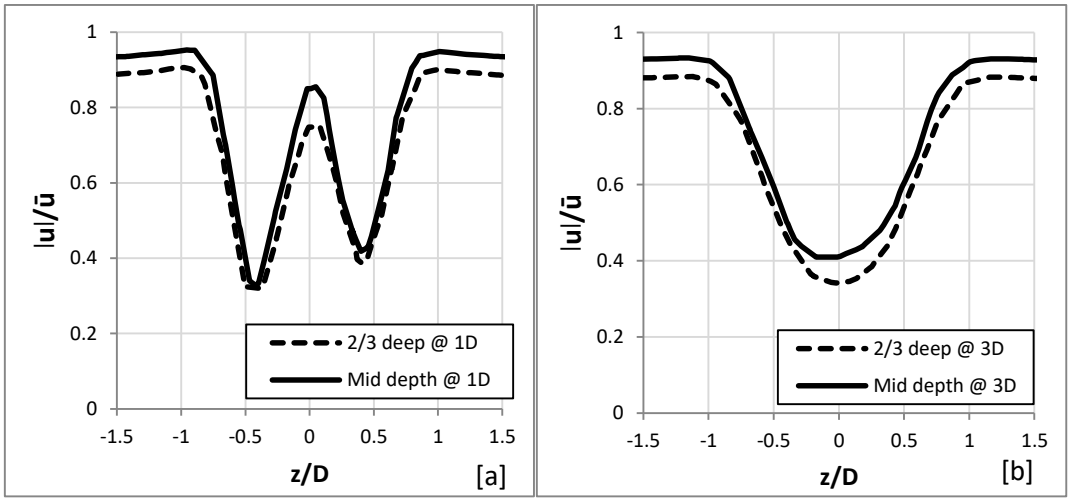

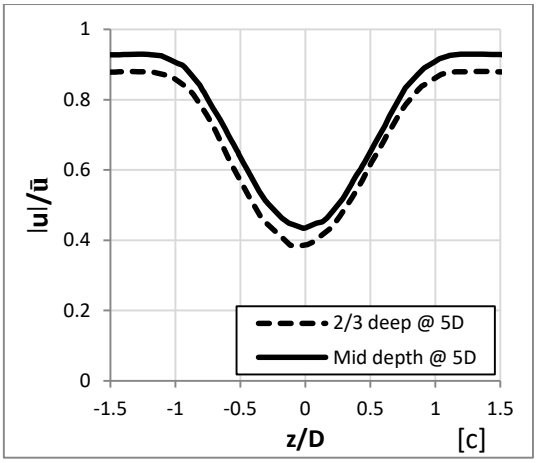

Figure 6-45 - Comparison of horizontal profiles of velocity magnitude between 2/3 deep and mid-depth turbine elevations at 1D [a], 3D [b] and 5D [c] downstream (centreline).

At 1D, it is found that when the turbine is at mid-depth, the level of velocity variation is higher in comparison with that for 2/3 depth case e.g. 9%. This is due to the turbine experiencing higher flow velocity and therefore producing stronger drag. Figure 6-46 compares the pressure change across the turbine centreline along the channel length. The change in pressure (Δp) across the turbine appears greater when the turbine is at mid-depth. As a result, higher velocity deficit is experienced.

At 3D and 5D, it is clear that the flow speed change is almost the same in both cases. In addition, in both cases, the velocity distribution of flow follows the same pattern as that found in the experiments.

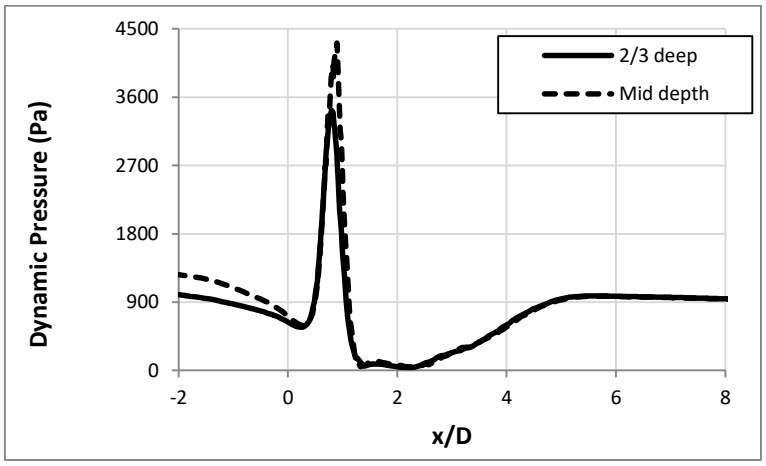

Figure 6-46 Comparison of longitudinal profiles of dynamic pressure across the turbine centreline between 2/3 deep and mid-depth turbine elevations.

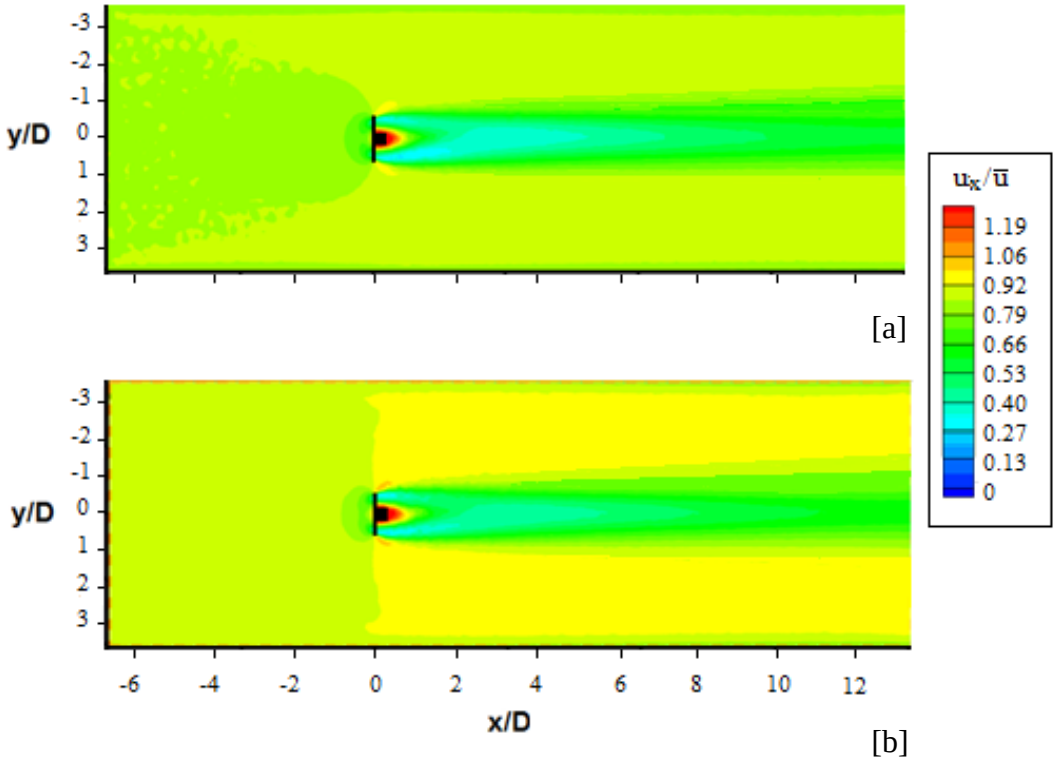

Figure 6-47 - Contour maps of velocity across the horizontal plane at turbine centre [a] turbine 2/3 deep [b] mid-depth.

Figure 6-47 shows the computed streamwise velocity distribution at turbine level across the channel. It can be seen that the reduction and acceleration are slightly different.

Vertical profiles of velocity magnitude are also compared at 1D, 3D and 5D downstream for both models (Figure 6-48). At 1D, the average flow velocity appears to be higher by approximately 4 % when the turbine is at mid-depth. Similarly, at 3D and 5D, the average velocity increase is approximately 2% at both locations. Again, highest velocity differences are seen at 1D due to the turbine effect. It is clear that velocity reduction peaks are not the same in both cases. The flow speed is lower behind the turbine when 2/3 deep, however the changes in velocity due to the turbine operation (velocity difference between maximum and minimum) are bigger when turbine is at mid-depth.

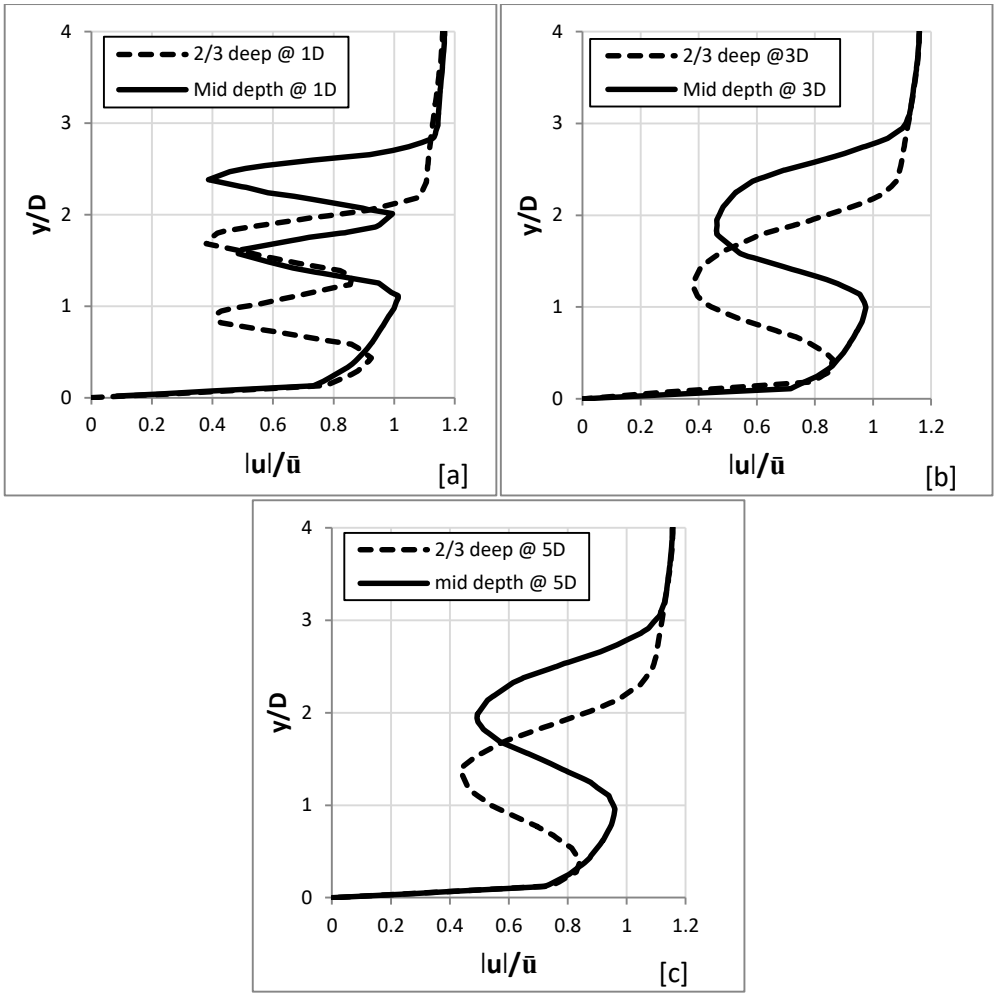

Figure 6-48 – Comparison of vertical profiles of velocity magnitude between 2/3 deep and mid-depth turbine elevations at 1D [a], 3D [b] and 5D [c] downstream (centreline).

When the turbine is at mid-depth, more space for the flow beneath the turbine is accessible. It is clearly seen from Figure 6-49 that the flow at the bed boundary layer is recovering faster than that in the turbine at 2/3 deep. Thus, the influence of bed-induced turbulence on flow mixing is almost negligible when compared to that due to turbine-induced turbulence higher above the bed. At the turbine-affected area ($1 < y/D < 3$), the flow distribution is almost the same in both cases However, the upper surface layer is experiencing higher velocities when the turbine is at mid-depth due to the fact that the accelerated flow above the turbine is stronger and closer in that region.

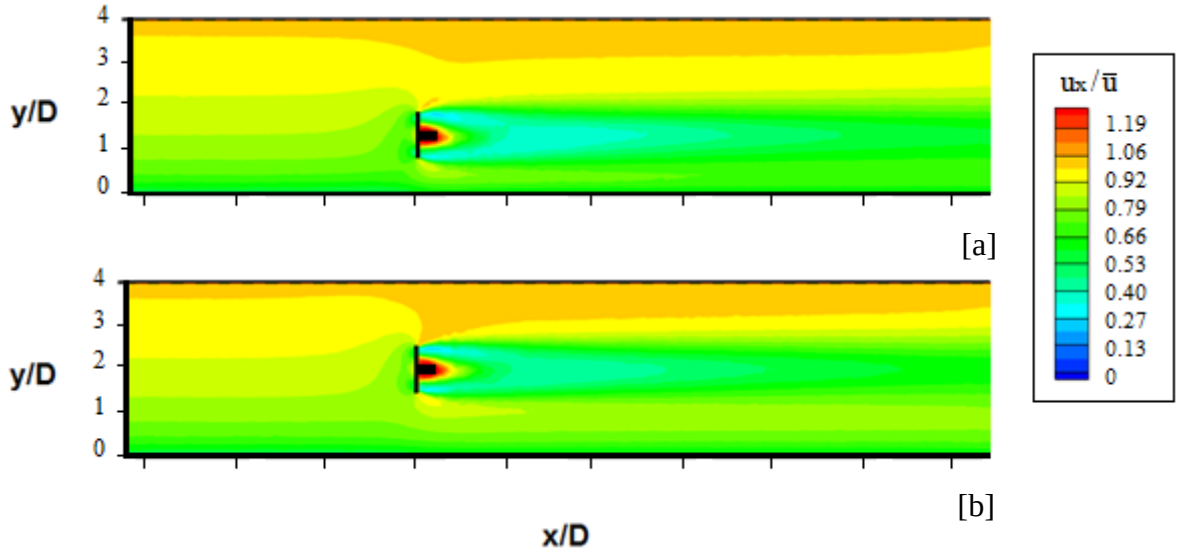

Figure 6-49 - Contour of velocity across the vertical plane at turbine centre [a] 2/3 deep and [b] mid-depth.

The velocity distribution of the flow in the channel reflects similarly on the TKE generated from the turbine. In the mid-depth case, the TKE levels are found to be higher. Figure 6-50 shows the horizontal profiles of TKE for the two turbine elevations at 1D, 3D and 5D downstream. It is found that the depth-averaged TKE generated by the mid-depth case is greater by approximately 14%, 4% and 1% at 1D, 3D and 5D respectively.

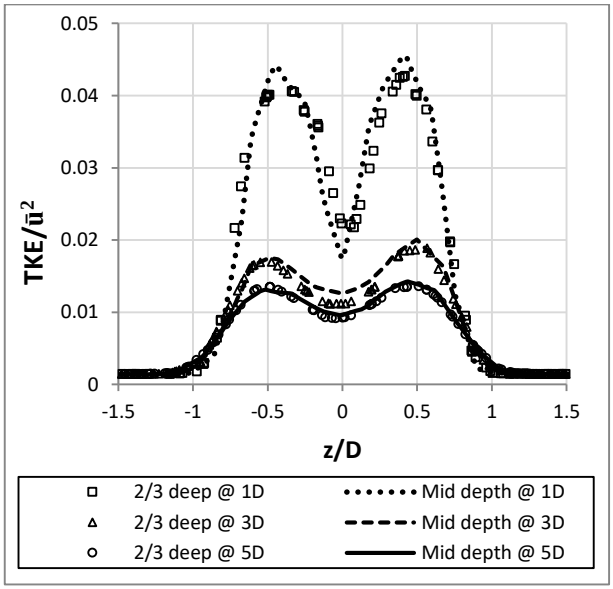

Figure 6-50 - Comparison of horizontal profiles of TKE between 2/3 deep and mid-depth turbine elevations at 1D, 3D and 5D downstream (centreline).

Figure 6-51 shows the vertical profiles of TKE across the water column along channel centre plane at 1D, 3D and 5D. Similarly, the TKE shows slightly higher values when the turbine is placed at mid-depth. However, the size of increase is found to be higher where the depth-averaged TKE generated is approximately 15%, 8% and 4% at 1D, 3D and 5D respectively. The TKE distributions show an asymmetric distribution with higher TKEs on the upper half of turbine as the flow speed is higher, in comparison with that at the lower part near the bed.

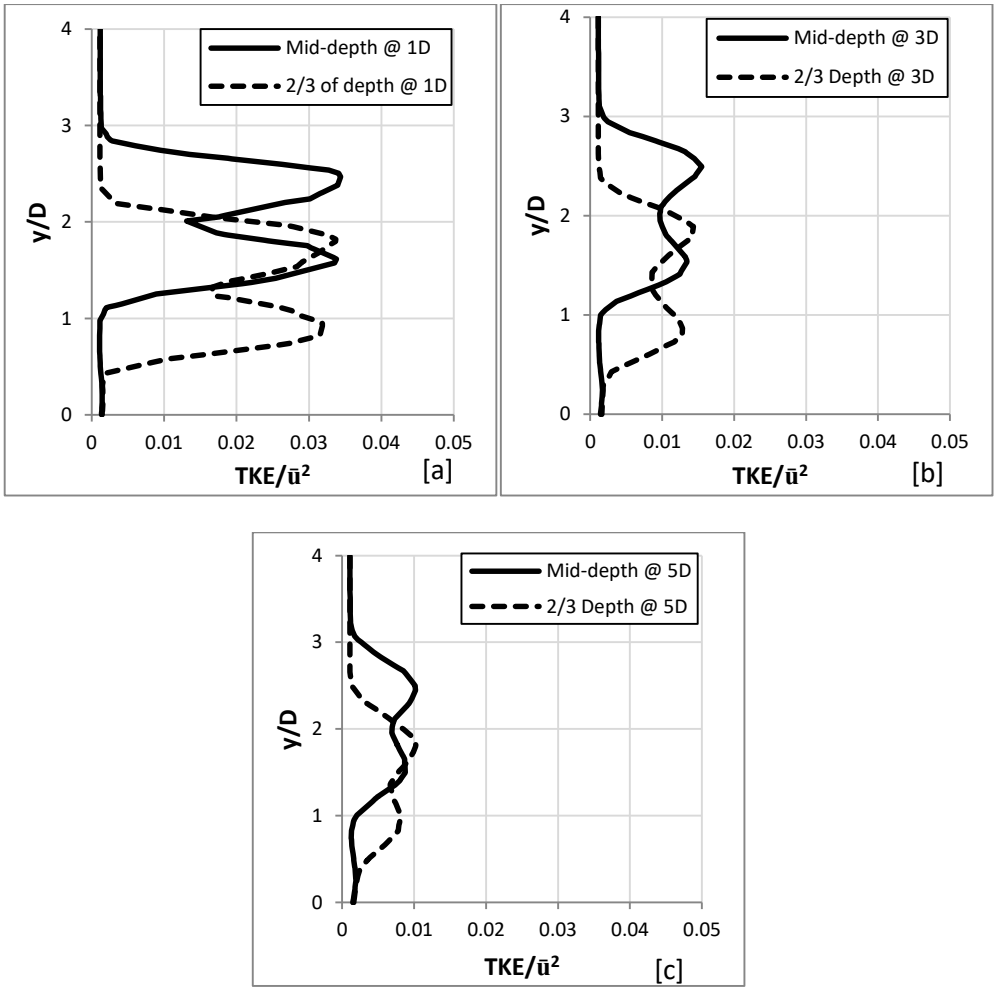

Figure 6-51 – Comparison of vertical profiles of TKE between 2/3 deep and mid-depth turbine elevations at 1D, 3D and 5D downstream (centreline).

Figure 6-52 presents the contour of TKE across the x-planes at 1D, 3D, 5D, 7D and 9D downstream for both cases. The TKE generated from the turbine shows similar shapes for both cases, however, TKE clearly interacts with the bed-induced TKE beginning at 5D when turbine is placed near bed surface.

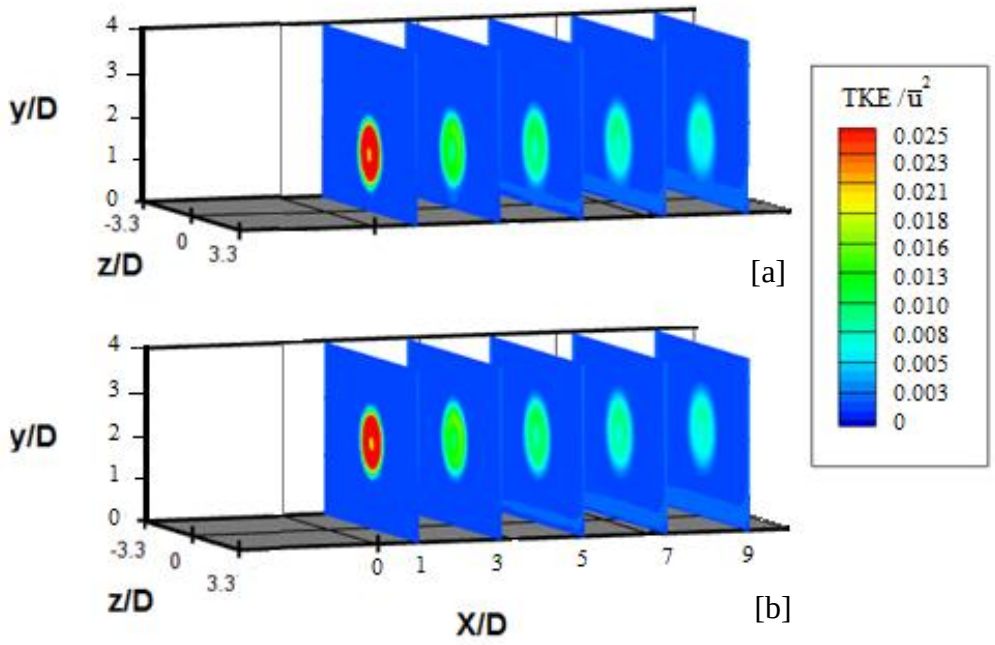

Figure 6-52 – Cross-section plane of TKE at 1D, 3D, 5D, 7D and 9D downstream at [a] 2/3 deep and [b] mid-depth.

It is expected that the shear stress on the bed surface is higher when the turbine is closer to the channel bed. In this case, the shear stress at the bed is investigated in the region between 3D in front and 9D behind the turbine, in order to avoid any implication from upstream and downstream boundaries. Figure 6-53 shows the normalised shear stress along the bed at centreline. It is found that in front of the turbine, the bed stresses start to build as the flow deviates from its trajectory when approaching the turbine. This rise is stronger when the turbine is 2/3rd of depth.

Behind the turbine, the shear stresses immediately reach peak values within 1D in the 2/3 depth case as the accelerated flow around the turbine interacts with the bottom bed layer. The shear stress remains strong along the channel length till 9D downstream.

It is clear that the shear stress distribution has a similar pattern as that found in the previous experimental scale tests but with smoother variation between the peaks. For the turbine at mid-depth case, the shear stresses start to increase within 1D in front of the turbine, similar to the 2/3 deep turbine. However, the rate of increase is much slower and reaches its maximum value at x/D > 3. Thereafter, the shear stresses remain more or less constant along the channel

length. It is found that the averaged shear stress along the centreline is higher by 65% when the turbine is 2/3 deep.

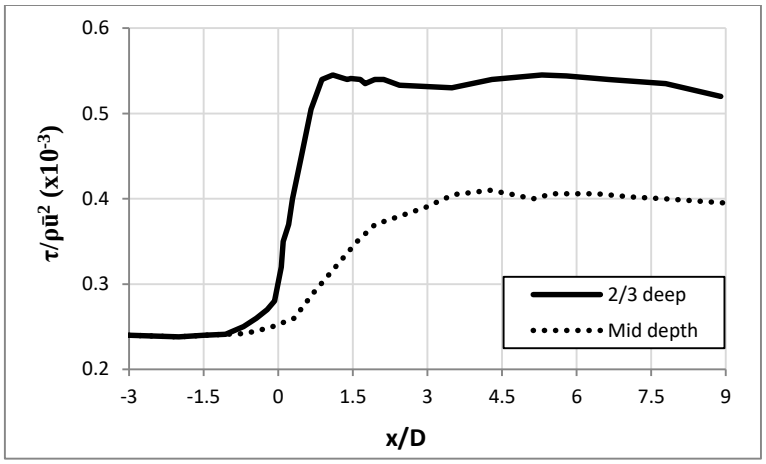

Figure 6-53 – Comparison of longitudinal profiles of shear stress along the centreline of channel bed between 1/2 and 2/3 deep turbines.

Figure 6-54 shows a plan view of the bed shear stress distribution across the bed surface for both conditions. As expected, the turbine closer to the bed has a wider influence on the stress at bed surface [a]. At downstream, the area of increase in shear stress gradually becomes wider.

When the turbine is at mid-depth [b], the influence of wake on bed shear stress is significantly smaller. The stress peak appears first on the right-hand side of the turbine where the blades are directing the flow towards the bed. Similarly, the affected area increases, as moving further downstream extra stress appears near the channel walls.

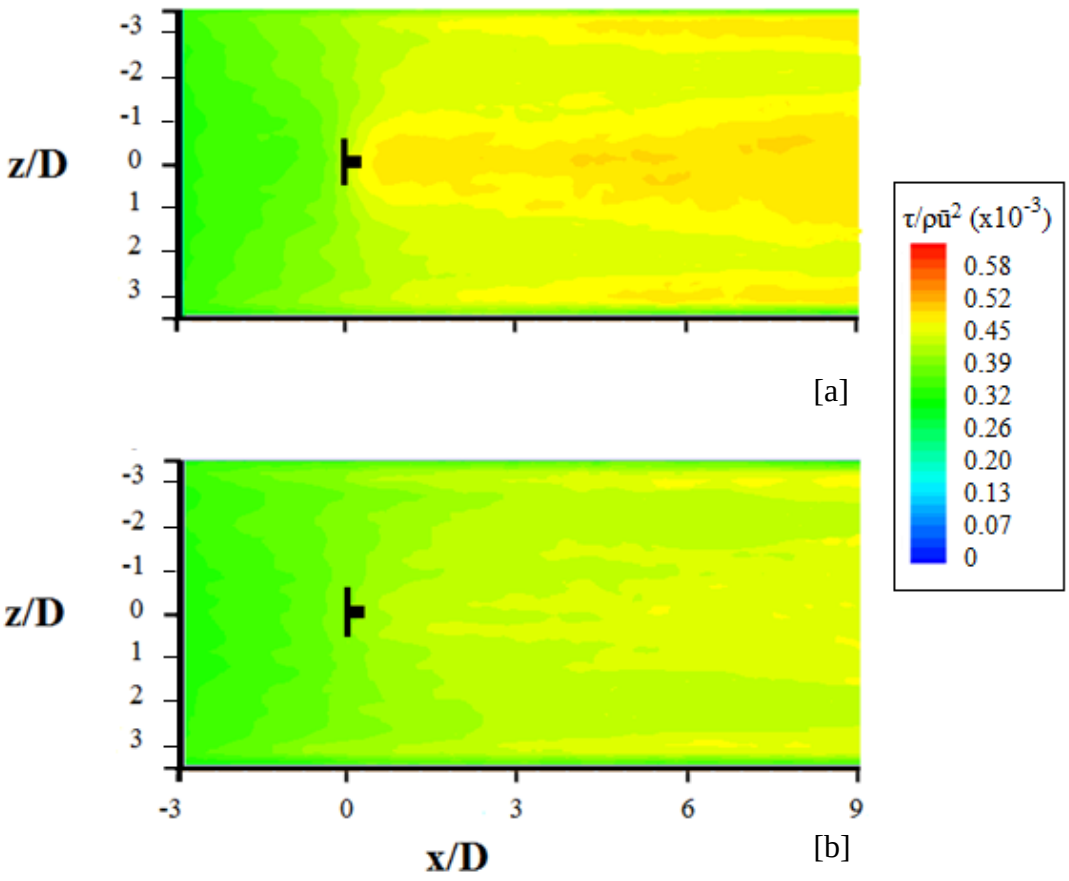

Figure 6-54 - Plan view: contours of shear stress on channel bed [a] turbine 2/3 deep and [b] turbine mid-depth.

6.5 Waves with Current

As highlighted in the literature review, waves are most common at the site where stream turbines are located. In addition to the tides, the oscillation due to waves is also expected to affect the dynamics of fluid flow around the turbine and hence needs to be identified. A series of tests were conducted, including waves and current without turbine and with turbine.

6.5.1 Waves with Current (no turbine)

Initially, an empty channel is employed to investigate the impact on the free surface and flow behaviour of waves alone, waves following the current and waves opposing the current. The model is set up with ≈ 1 million cells. The solution follows previous methods for wave with current condition (Chapter 5). Data are then taken after 100 wave cycles to ensure the wave converges. The defined wave at inlet is 6m in height, wavelength of 250m and wave period of 13.2s over a water depth of 60m (Table 6.2). These parameters are typically found in UK waters during storms (Black and Veatch, 2005). The flow velocities at inlet are 0m/s, 2m/s and –2m/s for wave alone, streamwise and opposing currents respectively. The background turbulence intensity is kept low to avoid its interference with the wave-current generated turbulence.

In general, waves undergo physical adjustments when combined with currents. Underneath the surface, waves produce a rotating orbital motion. With the presence of current, such a motion is often altered, e.g., when a wave is travelling in the same direction as that of the steady current. In the onshore (positive) half cycle, the streamwise flow velocity is accelerated and the maximum speed is found near the wave crest. In the offshore (negative) half-cycle, the streamwise flow velocity is reduced due to the steady flow, hence the minimum speed is found at the wave trough. When the wave is propagating against the current, the opposite effects are expected. Meanwhile, the surface level will change as a result of the velocity change, i.e., the crest level will drop and trough level rise in the case of a wave with following current and the opposite effect takes place when a wave propagates against the current.

In Figure 6-55, the streamwise velocity of flow is assessed over one wave cycle in the presence of following and opposing waves to the current, at different water depths. The wave inlet condition is described in Table 6-2. All three measuring points are taken at the turbine location x = 6.67D (100m) downstream from the water inlet. The first measuring point is taken in the upper surface layer at 2m depth (y/D = 2.6 from bed). The second point is in the turbine-affected layer at 40m depth (y/D = 1.3 from bed). The third point is in the bed boundary layer at 52.5m depth (y/D = 0.5 from bed). It is clear that the velocity variation within a wave cycle reduces when moving deeper into the water which shows that the wave impact is decaying.

Table 6-2 – Wave inlet parameters.

Wave Theory	**Period T(s)**	**Wavelength L(m)**	**Wave Height H (m)**	**Ursell number (HL^2/D^3) [Max limit=105]**	**D/L [Max-limit = 1000]**	**ū (m/s)**	$\frac{U_\delta}{\bar{u}}$
2nd order Stokes	13.2	250	6	1.74	0.24	2	0.33

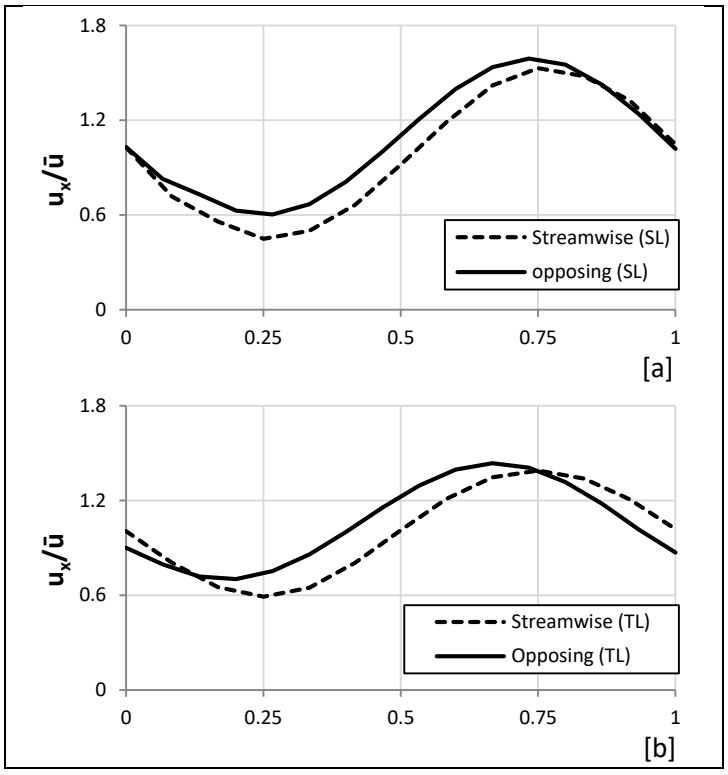

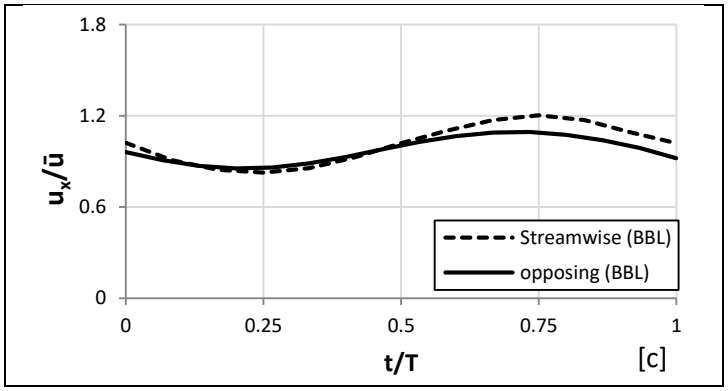

Figure 6-55 - Compares the streamwise velocity of flow during following and opposing waves propagation [a] Upper surface layer at 20m depth, [b] Turbine-affected layer at 40m depth and [c] Bed boundary layer at 52.5m depth.

Furthermore, Figure 6-56 compares the vertical profiles of wave-period averaged streamwise velocity for current with following and opposing waves, against current alone condition. It is clear that wave direction has an influence on the velocity distribution along the whole water column. For waves with following current, the wave-period averaged velocity in the bed boundary layer (BBL) increases, and reduces in the upper surface layer (USL). For waves with opposing current, the current experiences higher resistance near bed and therefore the velocity is slightly reduced.

However, away from the bed, the orbital motions result in an averaged velocity increase and are further increased near the surface due to surface effects. The computed results show similar velocity behaviours to those in the experiment conducted by Kemp and Simons (1983) for smooth beds, which indicates that the model is able to simulate wave-current interactions.

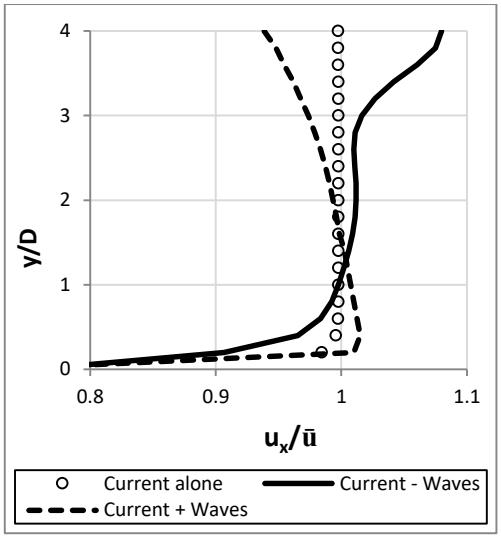

Figure 6-56 – Vertical profiles of wave-cycle averaged velocity for +/- waves and current alone.

Figure 6-57 presents the surface elevation variations for one and a half wave cycles for wave only condition (solid line), wave with following current (dashed line) and wave with opposing current (dotted line). Samples of computed results are taken at 100m away from the channel inlet where the turbine will be installed later.

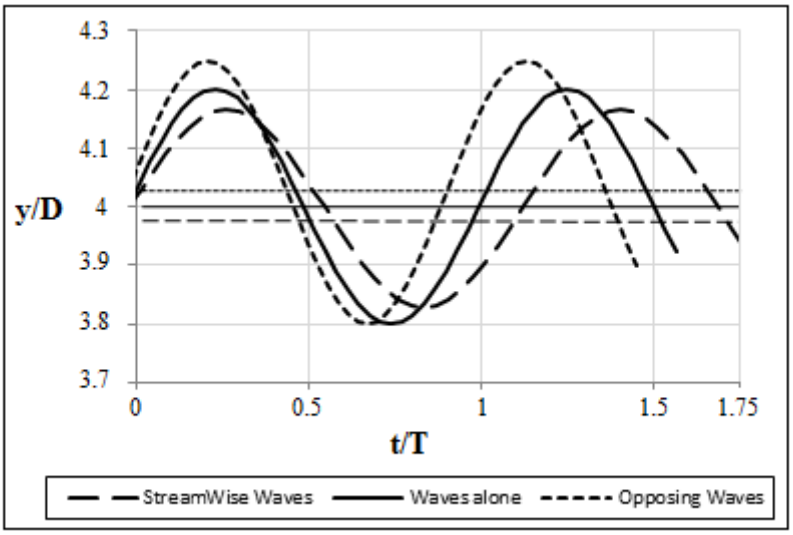

Figure 6-57 – Free surface elevation of 1.5 wave-cycles of standing, streamwise and opposing waves with no turbine.

For streamwise waves, the generated waves experience forward push whereas the opposing waves experience pull from the forthcoming current. As a result, the wave self-adjusts to the situation. For streamwise waves, the period becomes longer by 12% (14.8s) when compared with the wave alone condition. The amplitude becomes lower by 12% and the wavelength increases by 17%. For opposing waves, the period reduces by 9% (12s). The amplitude increases by 12% and the wavelengths decrease by around 15% (Table 6-3).

Table 6-3 - Wave output parameters

Case	**Waves Type**	**Period T(s)**	**Wavelength L(m)**	**Wave Height H (m)**	**Ursell number (HL^2/D^3) [Max limit=105]**	**D/L [Max-limit = 1000]**	**Velocity (m/s)**	$\frac{U_\delta}{\bar{u}}$
6.7.1	Opposing	12	212.3	6.72	1.40	0.28	-2	0.31
6.7.2	Wave only	13.2	250	6	1.74	0.24	0	-
6.7.3	Streamwise	14.8	293	5.34	2.12	0.20	2	0.34

The impact from currents is not limited to the wave shape alone; it also influences the average water level. In terms of the streamwise waves, the free water level illustrates a minor drop. In contrast, with opposing waves, the free water level presents a minor rise as shown in Figure 6-57.

Figure 6-58 shows the averaged normalised bed shear stress for one wave cycle at channel centre for waves with following and opposing currents. In general, waves affect the near bed boundary layer dynamics and hence would influence the bed. This contributes to the bed shear stresses and consequently to sediment transport. The total shear stress on the bed is measured from the shear stresses induced by current and waves. The presence of waves clearly increases the shear stresses on the bed in comparison with current alone flow. In addition, it is found that streamwise waves induce 23 % higher shear stresses on the channel compared to opposing waves. This is due to the higher velocities found near the bed explained earlier.

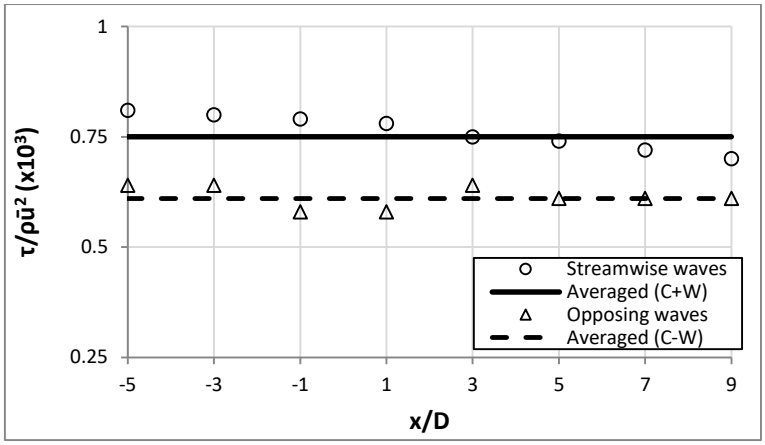

Figure 6-58 – Comparison of wave period averaged shear stress along channel bed centreline at turbine position between streamwise and opposing wave propagation when no turbine in operation.

6.5.2 Waves with Following Current (with turbine)

After the initial test of the method, the channel is installed with a turbine of 15m diameter to test its impacts to the combined currents and waves. The water column is divided into three regions where the velocity profiles illustrate different behaviours as previously explained. The model simulation involves a total of ≈ 1.4 million cells. The first condition is the current + waves, with parameters described in Table 6-3. The velocity is recorded at intervals of 1s over one wave cycle. However, the velocity profiles will be illustrated for wave angles of 0˚, 90˚, 135˚, 225˚ and 270˚ as shown in shown in Figure 6-59.

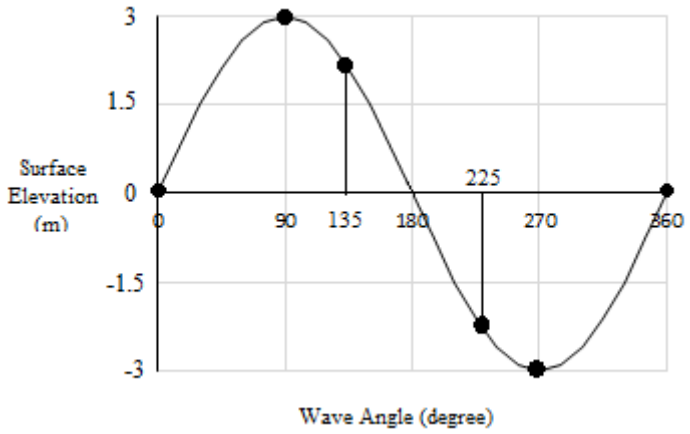

Figure 6-59 - The wave angle at which the measurements are taken.

Figure 6-60 presents the vertical profiles of streamwise velocity at 1D, 2D, 3D and 4D downstream along the centre plane at the five selected wave phases. It is found that the highest velocity speed is recorded under wave crest (90º) and the lowest velocity speed is under wave trough (270º). The largest velocity differences within one cycle are seen closer to the free surface, which is consistent with the depth decay of the wave and induced orbital motion**.**

Similar features as observed in experimental scales can be seen in these figures. At 1D, it is clear that the velocity profile follows a "W" distribution as in steady states unaffected by the waves. Effects on near bed boundary layer processes are not obvious, although different boundary layer thickness can be seen.

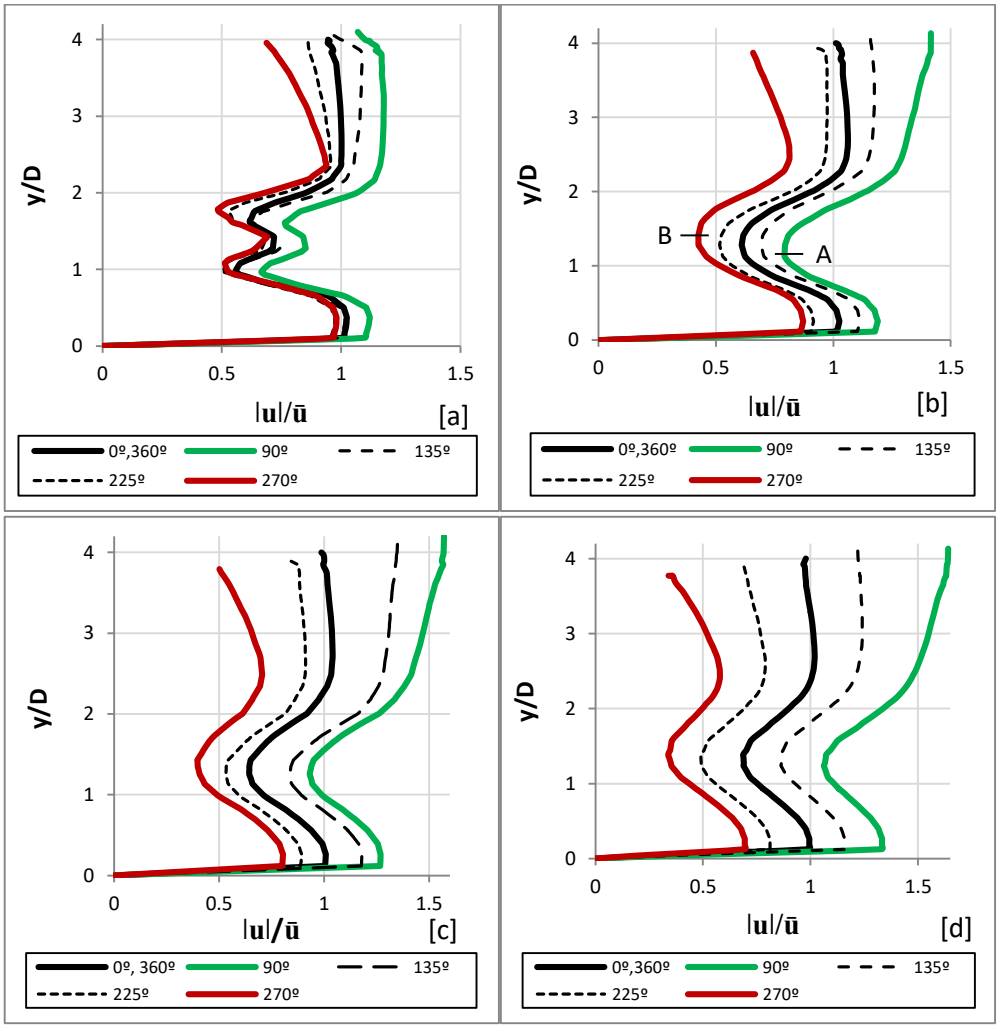

Figure 6-60 – Vertical profiles of velocity magnitude for 1 streamwise wave cycle at [a] 1D, [b] 2D, [c] 3D and [d] 4D downstream (centreline) when wave angle is 0˚, 90˚, 135˚, 270˚ and 360˚.

In the above figure, it can be seen that the elevation of the maximum velocity reduction changes at different phases of the wave at these locations. For example at 2D, wave crest, the elevation of the minimum velocity appears to slightly drop below y/D = 1.3 as marked by A, while at wave trough (270˚), the level of the minimum velocity is above y/D = 1.3, as marked by B. This is because the flow speed reaches its maximum at 90˚, with more water flowing over the turbine with higher water head. As a result, the wake is pushed downwards towards the bed.

At wave trough (270º), the opposite affect is seen where the velocity above the turbine reduces and causes the wake centre to rise up. This indicates that the wake centre is constantly rising and falling throughout the wave cycle. However, the turbine-affected region more or less remains the same region, e.g., $0.5 < y/D < 2.5$ at the different locations downstream.

Comparing the velocity distribution at the four sites, it is found that the velocity profiles 1D remains almost the same at every wave phase, especially close to the turbine-affected region and further below, e.g., $y/D < 2$. However, the flow speed variation becomes apparent at other sites. For example at 2D, the difference between maximum velocity and minimum is above 75% and such variation increases further at 3D and 4D. This indicates that the wave intensity influences changes at different locations away from the turbine.

Close to the turbine, the current undergoes strong transformation and the wave effect is less significant. Moving away from the turbine, wake recovery takes place and the wave effect grows again to cause more pronounced variation in velocity at different phases. It is concluded that the presence of turbines supresses the impact of streamwise waves by showing minimum velocity variation near the turbine.

Figure 6-61 compares the vertical profiles of wave-period averaged velocity magnitude at 1D, 2D, 3D and 4D behind the turbine and without turbine presence. It clearly shows that the period average flow velocity largely follows a similar distribution as in the steady current case, as shown previously, e.g. accelerated flow above and below the turbine and strong velocity reduction at turbine region. Comparing with the no turbine case, the most noticeable change can be found between 0.5D-2.5D at the turbine-affected layer. The bottom boundary layer is affected due to the flow reduction at all wave phases. But at the upper surface layer,

the flow tends to follow the non-turbine condition as the velocity reduces close to the surface, which is a typical feature in a wave with following current condition.

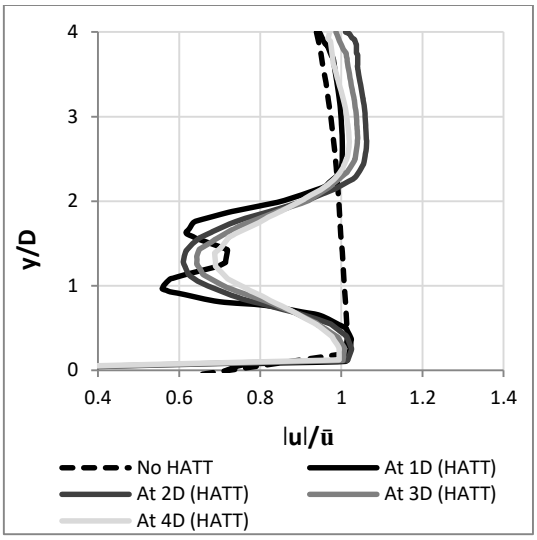

Figure 6-61 - Vertical profiles of wave-period averaged velocity magnitude at 1D, 2D, 3D and 4D downstream (centreline) when streamwise waves are present. It also shows the mean inlet velocity profile.

Figure 6-62 shows a snap-shot of velocity magnitude across the centre plane when the wave crest is at the turbine location (90˚) for no turbine, with turbine conditions, and the top-down view of the velocity magnitude across the channel at the turbine level. It is clear from [a] that the waves have a significant impact on the flow pattern, which extends down to the bed of the channel. When the turbine is in place [b], the wake behind the turbine is clearly visible, extending to the end of the channel and interfering with the wave-induced flow pattern. The accelerated flow induced by the turbine further increases the acceleration to the flow above, and especially beneath, the turbine.

But further downstream, the velocity reduction is also clearly noticeable (x/D =0-3). At the region 4D-8D, the wave-induced flow reduction is enhanced by the wake impact extending the range from 3D to 9D. Similar behaviours are seen in the horizontal plane [c] where the turbine interferes with the wave-induced oscillatory flows.

A new low velocity region in $3D < x < 10D$ in horizontal and $0.5D < y < 2D$ in vertical is clearly visible underneath the wave trough, which also extends its influence to the region

under the following wave crest in 9D < x < 13D. This is due to the interaction between turbine-induced wake and wave-induced oscillations in the water, i.e., in the wake region, the flow speed is reduced. When such reduction is superimposed onto the wave oscillating flow, the high velocity and wave crest is reduced, and the lower velocity under the trough is further reduced.

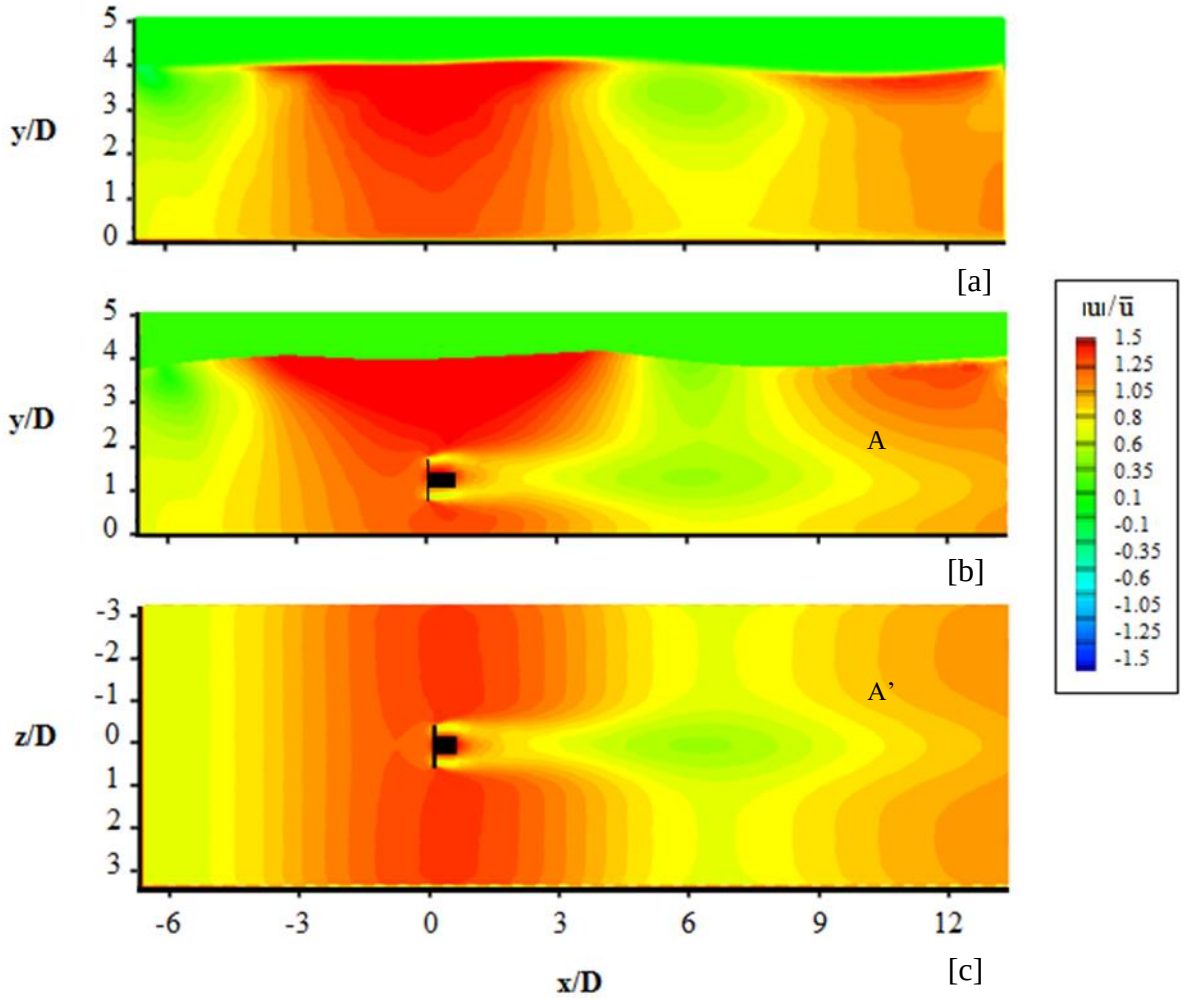

Figure 6-62 - Vertical plane at turbine centre showing the contours of velocity magnitude when the wave angle is equal to 90˚ at turbine location [a] side-view: no turbine, [b] side-view: with turbine and [c] top-down view: with turbine.

Similar to figure 6-62, figure 6-63 shows a snapshot of velocity magnitude when the wave trough is at the turbine location (270˚) across the centre plane for no turbine in [a], with turbine in [b] and top-down view of the horizontal plane at turbine level. At the turbine position, the flow speed is increased above and beneath the turbine, interfering with the

wave-induced flow reduction under the trough although the flow speed is lower under the wave trough.

The wake behind the turbine, however, still extends downstream until 12D. Immediately behind the turbine, the wave-induced flow reduction region is extended (b) until x = 5D. The flow speed in the region under the following wave current (5D < x < 10D) is also reduced and leads to the halving of the original high flow speed region in C and C'. The surface also drops in that area; this will be discussed in detail in the following section.

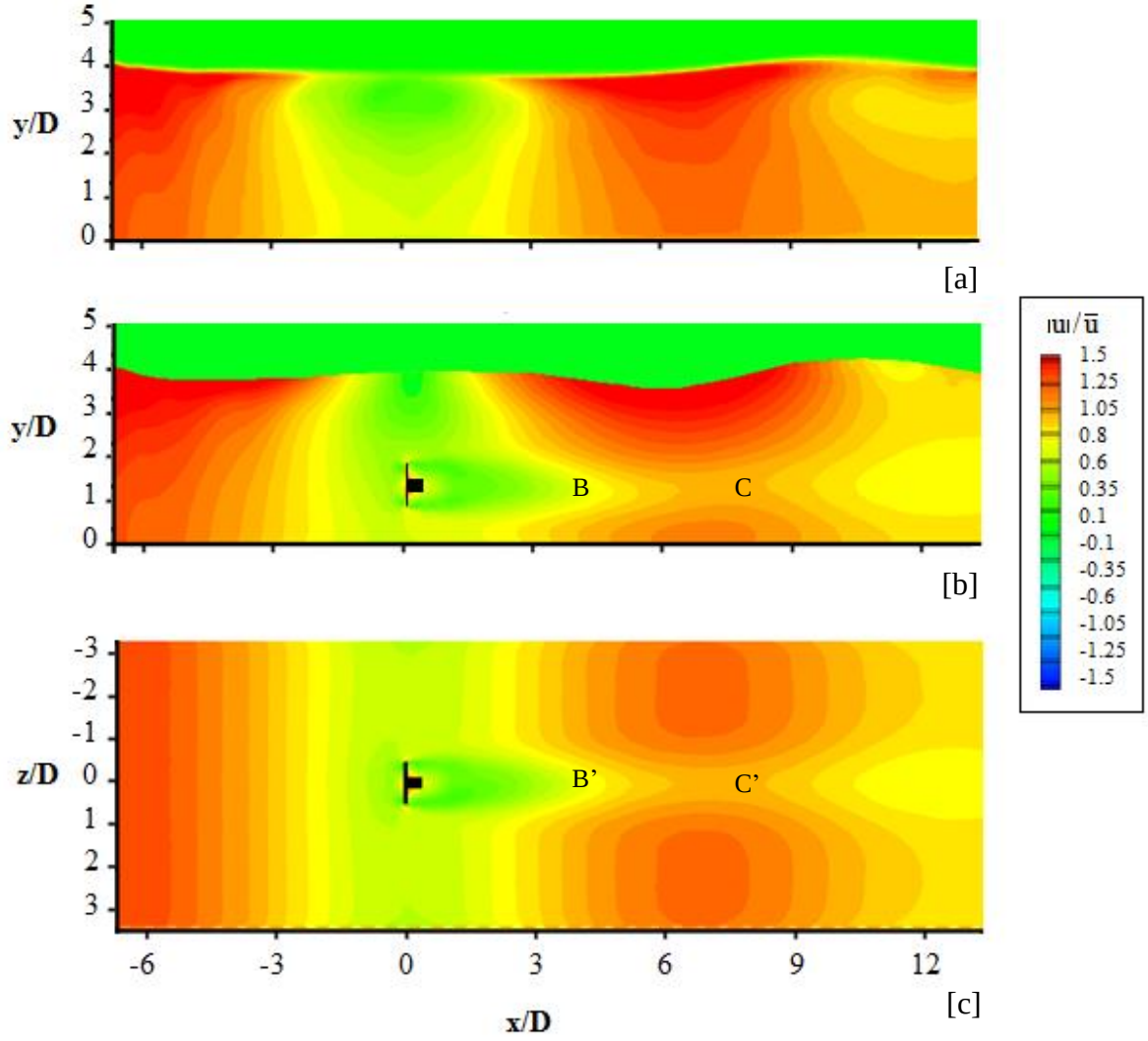

Figure 6-63 – Vertical and horizontal plane at turbine centre showing the contours of velocity magnitude when the wave angle is equal to 270˚ at turbine location [a] side-view: no turbine, [b] side-view: with turbine and [c] top-down view: with turbine.

Figure 6-64 shows a snapshot of TKE when the wave is at crest and trough at turbine location across the centre plane, with turbine, side-view, (90˚) [a], top-down view (90˚) [b], side-view (270˚) [c] and top-down view (270˚) [d]. It is clear that waves start to induce turbulent kinetic energy in the upper surface layer as they approach the turbine at x = -2D then gradually diffuse downstream towards the bed. Meanwhile, the turbine generated turbulence also propagates downstream within the water body. Stronger TKE is found during a wave crest, approximately twice that found during a wave trough. It is also seen that a high level of TKE is found on the right side of the hub, as the flow velocity is higher on that side as explained in the previous chapter. The TKE level is also stronger beneath the hub when compared to the above hub. The TKE contours show an oscillatory distribution pattern that can clearly be seen in the wake, especially close to the turbine.

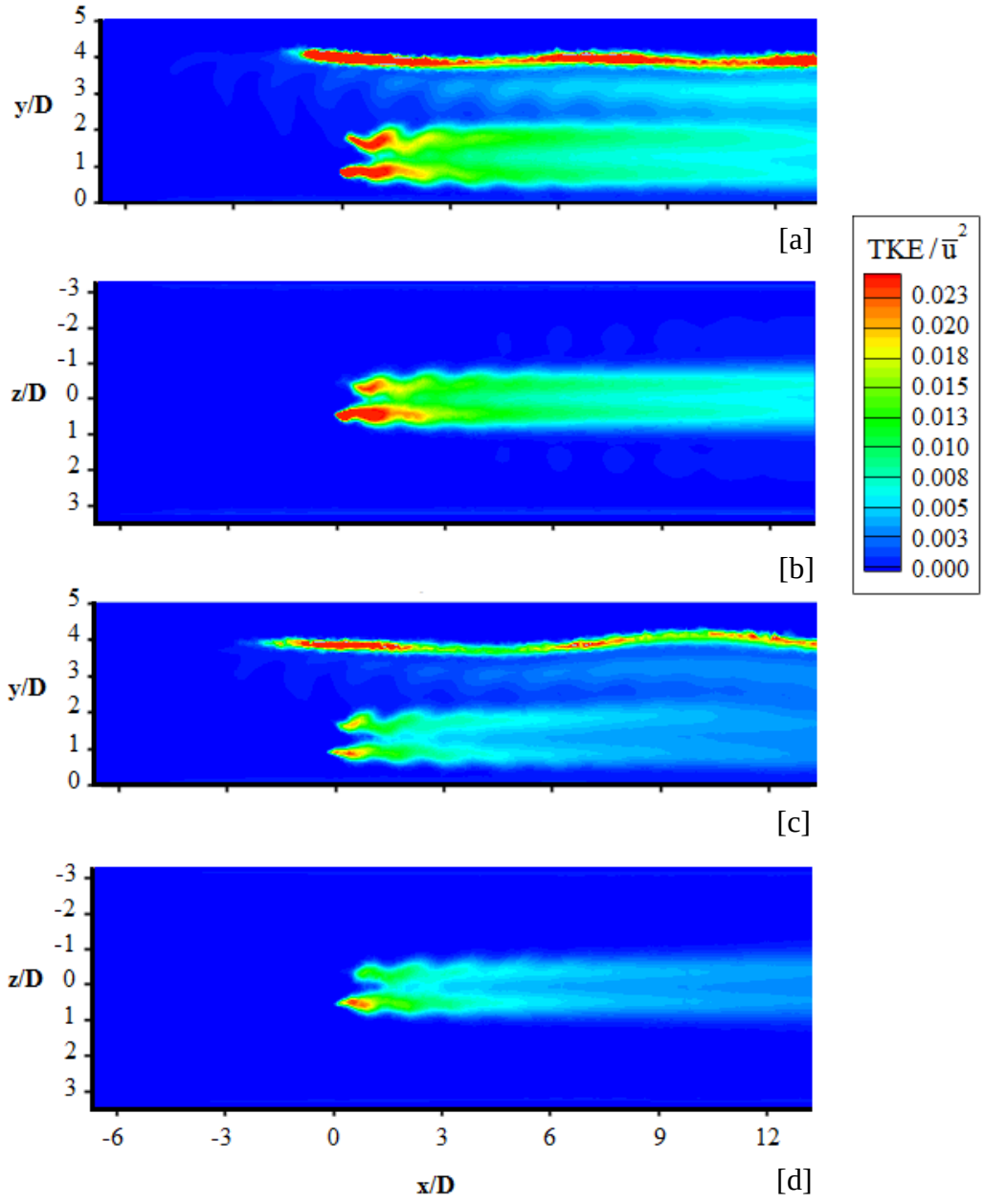

Figure 6-64 - Vertical and horizontal planes at turbine centre showing the contours of TKE when the wave angle is equal to 90˚ and 270˚ at turbine location [a] side-view: 90˚, [b] top-down view: 90˚, [c] side-view: 270˚ and [d] top-down view: 270˚.

Generally, at y = 2.5D level, there is noticeable interactions between these two turbulence sources, starting from x = 1D. This interaction clearly becomes stronger as it moves further downstream, as seen in Figure 6-65. But the wave-produced turbulence energy is generally lower than that in the turbine wake region and hence we see the turbine wake still dominates the turbulence characteristic in the water column.

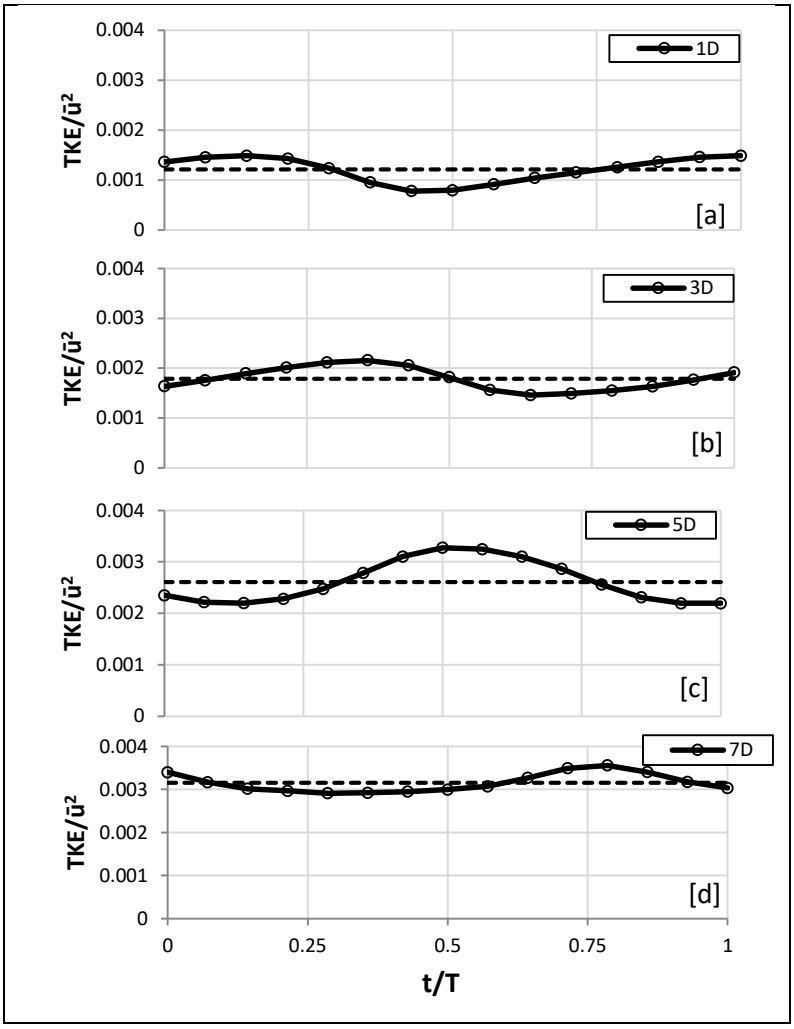

Figure 6-65 – Shows the TKE over one wave cycle at points z = 0D, y = 2.5D for x = [a] 1D, [b] 3D, [c] 5D and [d] 7D downstream.

Figure 6-66 shows the surface elevation along the channel length when the wave is 270º at the turbine position (0D). The black line denotes the surface elevation when the channel is empty; the red line denotes the surface elevation when the turbine is installed.

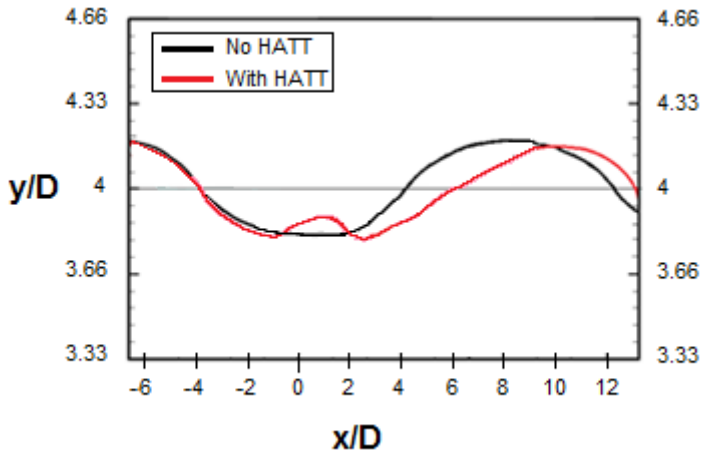

Figure 6-66 - Comparison of surface elevation along the channel length between turbine and no turbine cases. The wave is propagating in the direction of current and is in trough (270º) at turbine position.

It is found that the wave shape deforms when the turbine is installed in the channel. Such impact is expected, as Sun et al. (2008) had previously found that the free surface experiences a slight rise in front of a turbine followed by an immediate drop when a turbine is employed in a steady flow.

In the present study, it is clear that the wave surface in front of turbine is interrupted from descending by the turbine-induced flow acceleration near the surface. This velocity increase delays the surface drop (trough) at the turbine location to show a surface rise between -1d < x < 2D.

Apart from the water level rise around x = 0D, it is also clear that there is a water level drop further downstream at approximately 3D which subsequently rises fairly quickly, cresting at approximately 10D. As a result of these physical processes, the overall wavelength is extended by 12% of the original wavelength. It is also found that the wave height is reduced by almost 0.053D (13%) due to the surface uplift above the turbine area.

Figure 6-67 shows the surface elevation along the channel length when the wave crest (90˚) is at turbine location (x = 0D). The flow slows down in front of the turbine and leads to a surface rise between -2D < y < -1D. The accelerated flow above the turbine increases the flow speed beneath the wave and causes a surface drop that interferes with the ascending motion of the wave at x = 0. Further downstream, the accelerated flow dissipates and the

wave crest is created ≈ 2D away from its original position. Similarly to Figure 6-55, the wavelength is found to increase by 12% in comparison with the original wave.

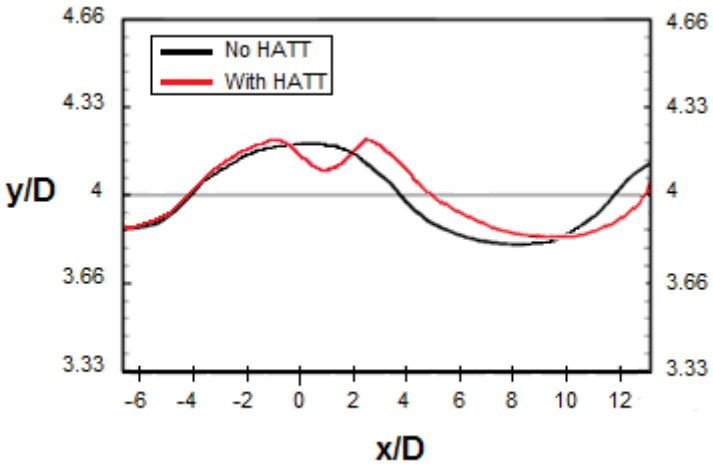

Figure 6-67 - Comparison of surface elevation along the channel length, with and without a turbine. The wave is propagating in the direction of current when the crest (90°) is at turbine position.

Figure 6-68 shows the computed surface elevation over one wave period at x= -2D, 0D, 2D, 4D, 8D and 12D downstream in comparison with the no turbine case. It is found that the presence of the turbine leads to wave asymmetry, e.g., the shape becomes more close to a second order Stokes wave, with a shorter onshore period but large peak and prolonged but flatter offshore peak. As seen in the previous figure, the wave height is also reduced as a result of the turbine effects. The turbine influences the surface elevation and changes the wave shape towards a non-linear wave.

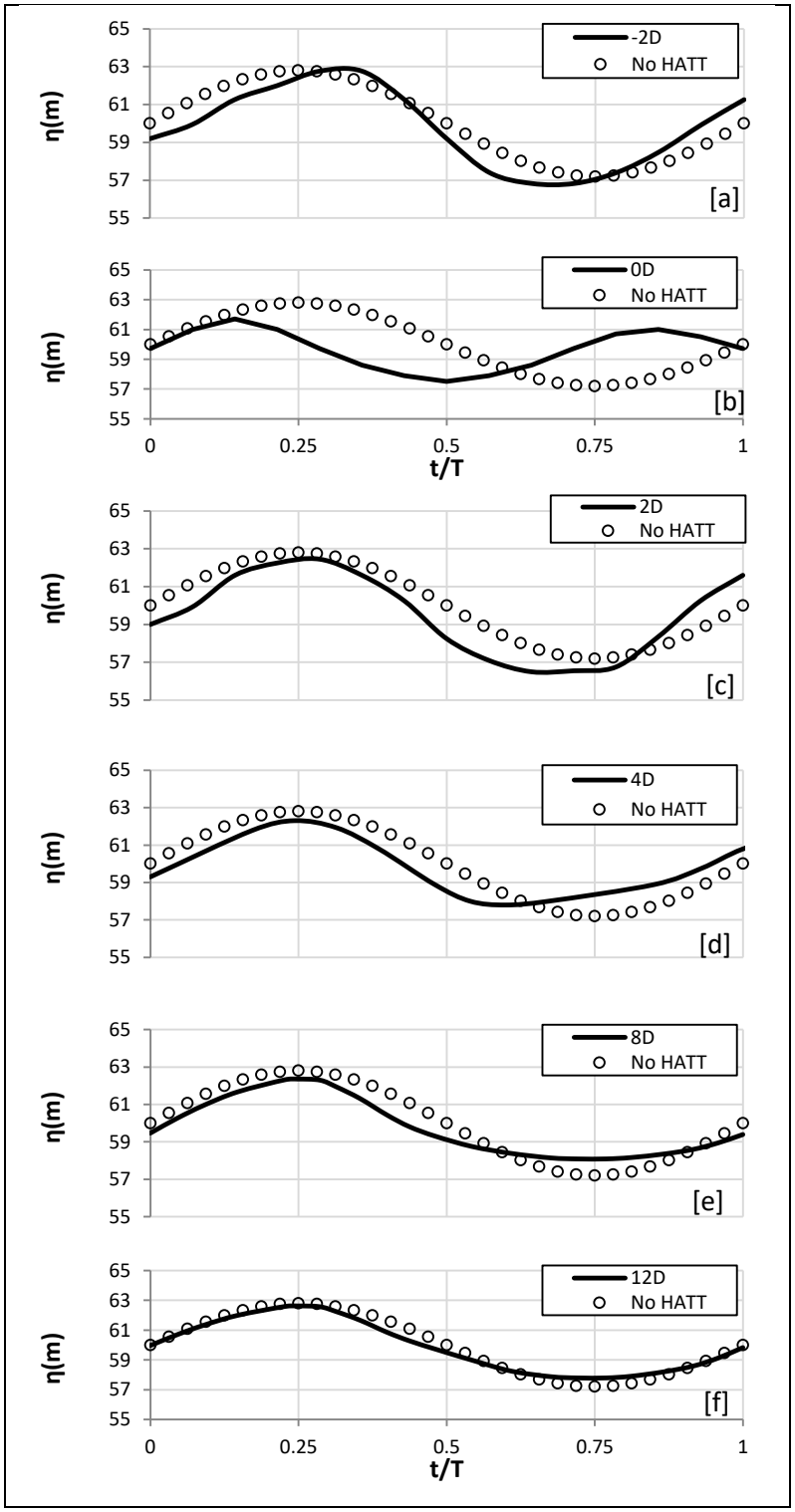

Figure 6-68 - Comparison of surface elevation one wave cycle at x = [a] -2D, [b] 0D, [c] 2D, [d] 4D, [e] 8D and [f] 12D downstream when with and without a turbine for streamwise waves.

Figure 6-69 presents the amplitude wave height distribution along the centreline of the channel in the streamwise direction. It can be seen that the turbine operation affects the wave propagation by increasing the wave height in front of the turbine at x = -2D and behind the turbine at x= 2D. The average increase in wave height in these two positions is approximately 6%. However, at the turbine (x ≈ 1D), the wave height undergoes maximum drop of 30%.

This wave shape distortion can also be seen in Figure 5-33 [a]. The velocity at the surface undergoes rapid velocity change, i.e., drop-rise-drop at x = -2D, 0~1D and 2D respectively (Figure 5-33 [b]). On average, in the presence of the turbine, the wave height undergoes a reduction of approximately 10% compared to the original wave height.

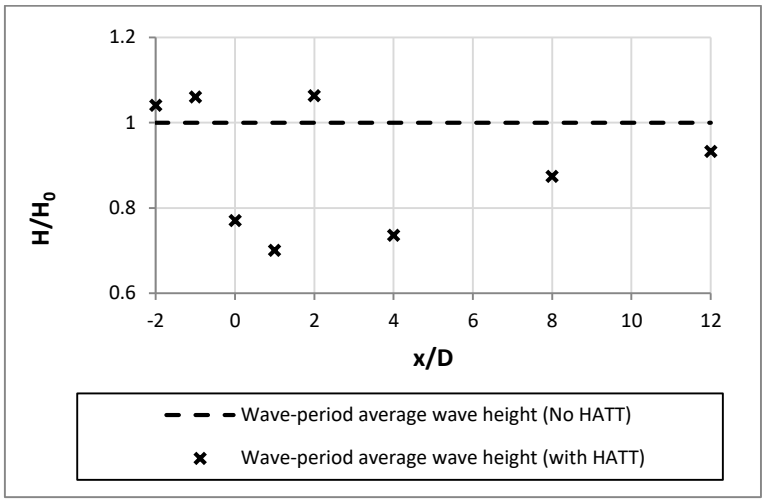

Figure 6-69 – Amplitude wave heights along the centreline of channel at different positions downstream.

Figure 6-70 compares the instant shear stresses along the channel bed centreline both in the presence of a turbine and without at wave crest above turbine in [a] and trough above turbine in [b]. As expected, the turbine presence increases the shear stress on the bed in both cases. It is clear that the turbine increases the shear stress on the bed to its maximum when the wave crest is above the turbine. As in the steady current case, the flow accelerates underneath the turbine, which leads to higher shear stresses. Under wave crest, the maximum increase in shear stress on bed (at x ≈ 1D) is found to be approximately 36% in comparison with no turbine cases. However, under the wave trough, the shear stress increases by 32% when compared to the no turbine case. It is also recognised that the double-peak feature behind the

turbine in steady current, is found when waves are present. The increase in shear stress persists under the wake until x ≈ 8D [a] and x = 5D [b], at which point the shear stress becomes lower than that of no turbine due to the flow velocity deficit seen in Figures 6.62 and 6.63 respectively.

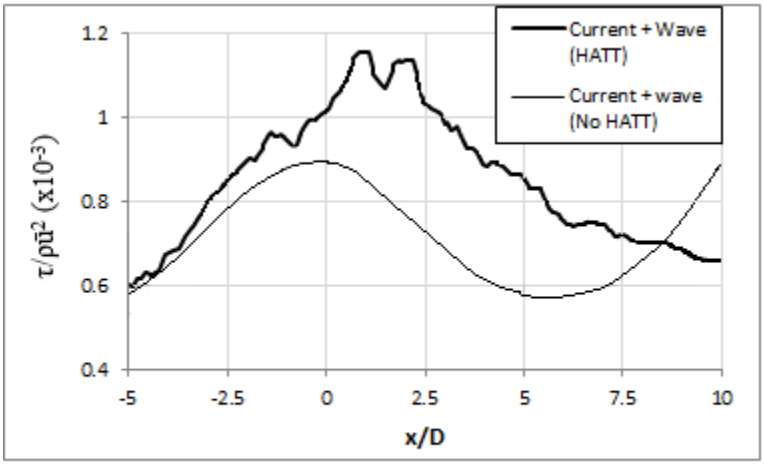

[a]

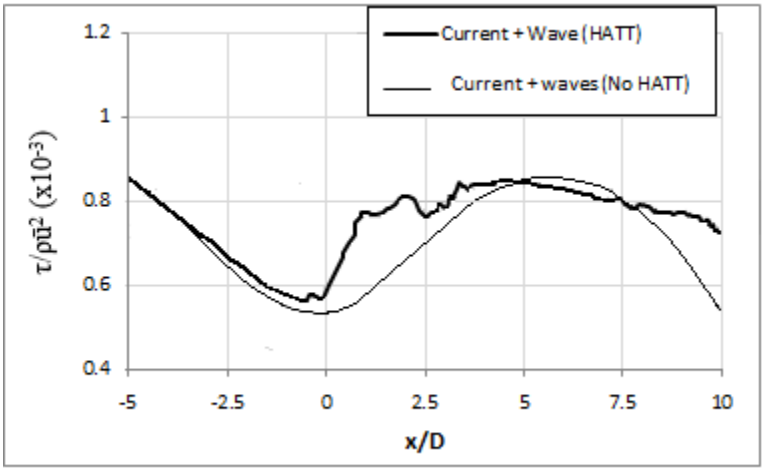

[b]

Figure 6-70 - Comparison of instant shear stress on channel bed along the centreline between turbine and no turbine in channel during streamwise wave propagation [a] wave crest at turbine location and [b] wave trough at turbine location.

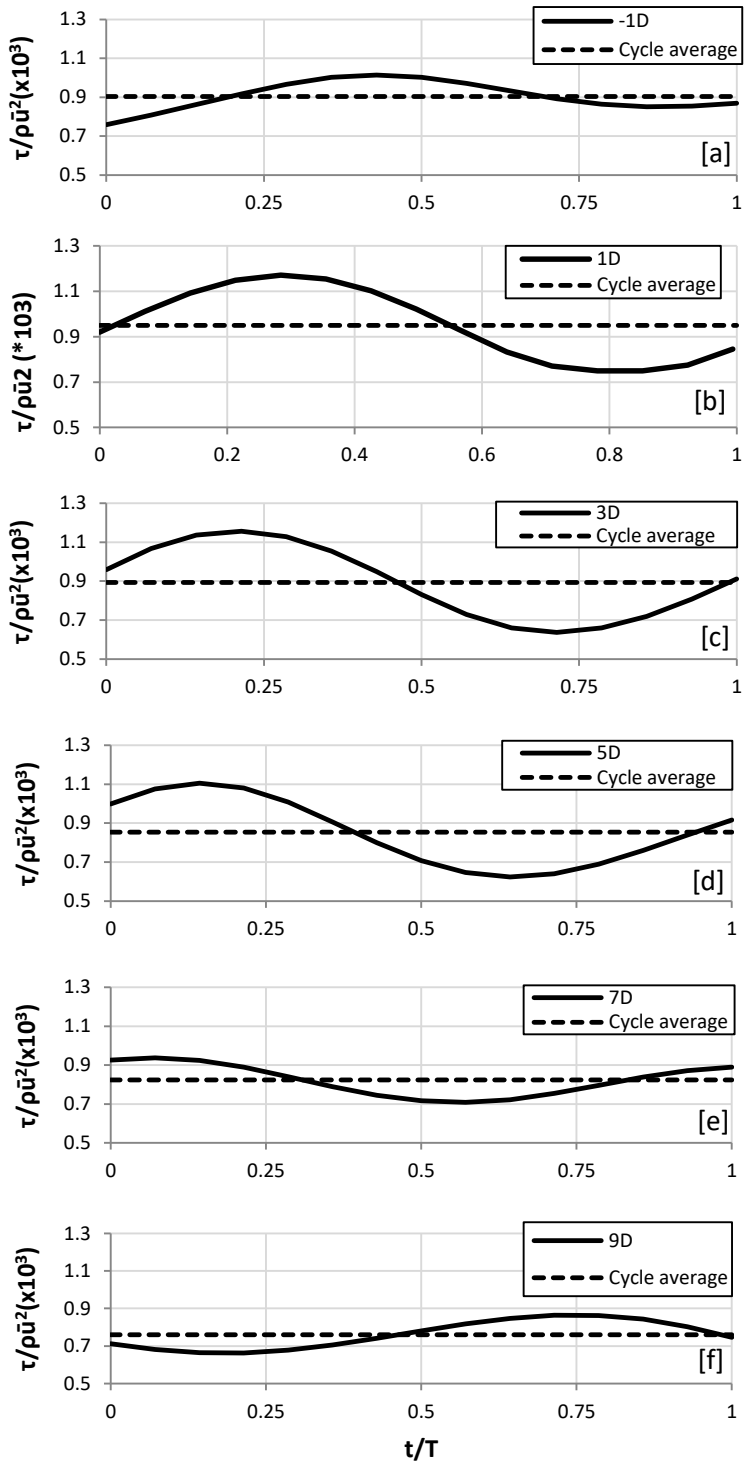

Figure 6-71 – Shows the shear stress for one wave-cycle at [a] -1D, [b] 1D, [c] 3D, [d] 5D, [e] 7D and [f] 9D downstream at bed centreline.

Figure 6-71 shows the shear stress on a point for one wave-cycle at -1D, 1D, 3D, 5D, 7D and 9D downstream at the bed centreline. Results show a continuous variation in the shear stress values during a wave-cycle. At -1D (1D in front of the turbine), this variation between maximum and minimum stresses is suppressed. Further downstream at x = 7D - 9D, this suppression is seen again due to the flow velocity deficit seen in that region. It is clear that the highest shear stress variations are experienced between 1D < x < 5D, which indicates that the turbine wake increases it.

Figure 6-72 shows the wave-period averaged shear stresses along the channel centre at x = -5D, -1D, 1D, 2D, 3D, 4D, 5D, 7D, 9D and 11D. It can be seen that the shear stresses increase significantly when the flow approaches the turbine. The highest shear stresses on the bed are found behind the turbine at x ≈ 1D (wave-period average shear stress increased by 24% compared to no turbine). Subsequently, these stresses reduce gradually, which indicates that the wake velocity is recovering and the turbine vortex is fading. The bed shear stress along the channel centreline increases by 14% on average compared to the no turbine case.

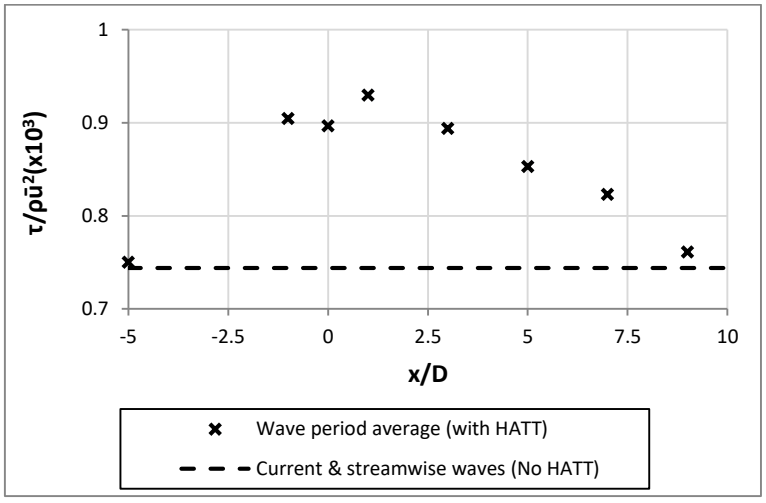

Figure 6-72 - Bed shear stress at x = -1D, 1D, 3D, 5D, 7D and 9D, and z = 0 for 1 wave-cycle

Figure 6-73 presents the contours of bed shear stress when the turbine is wave crest (90º) and wave trough (270º). It is clearly seen that the turbine increases the shear stress near the bed immediately behind the structure.

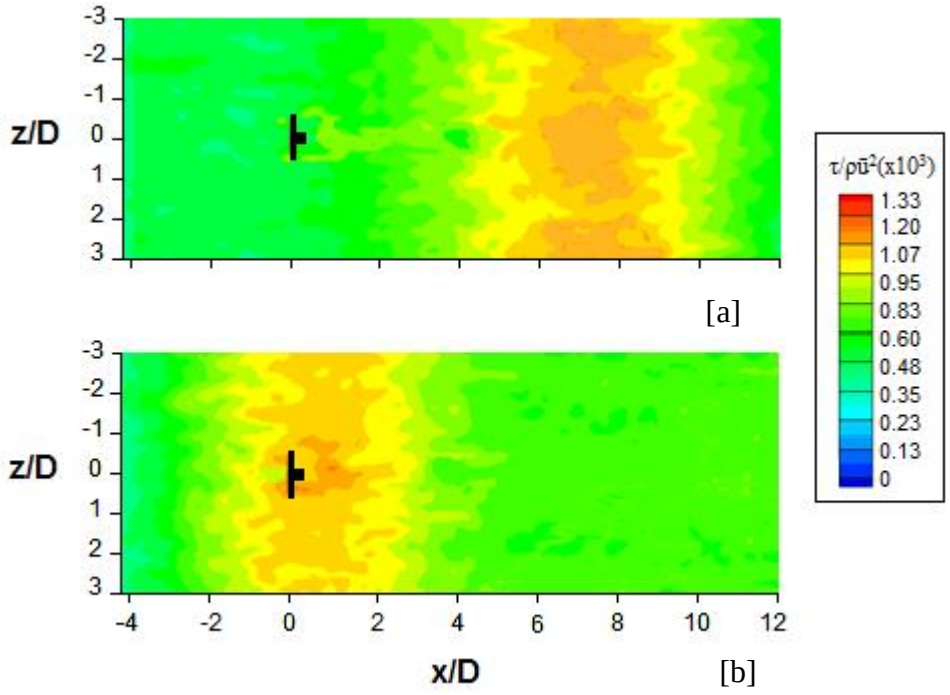

Figure 6-73 - Plan view: snap shot of instant shear stresses across the channel bed when wave at turbine location is [a] trough [b] crest

6.5.3 Waves with opposing current

Similar to the wave with following current, a model test was carried out for wave with an opposing current condition. Figure 6-74 shows the vertical profiles of streamwise velocity at different phases at 1D, 2D, 3D and 4D downstream. As in Figure 6-60, it is seen that the maximum velocity difference can be found closer to the surface. In this case however, an opposite behaviour is seen where the difference in velocity reduces with moving downstream. For example, the velocity variation between maximum and minimum is recorded as 230% 96%, 39% 32% of that at 1D, 2D, 3D and 4D downstream respectively. This is due to the fact that, behind the turbine in the wake region, the flow speed is reduced due to a higher velocity deficit which allows the wave to penetrate deeper inside the water and drive larger scale oscillatory motion between phases; hence the wave has more apparent effects.

Away from the turbine in the downstream, however, the steady current dominates the flow pattern and reduces the variation between phases due to wave effects. Unlike the previous case, for opposing waves, the highest velocity is recorded under a wave trough (270º). The lowest velocity is found under a wave crest (90º).

In Figure 6-75, it also can be seen that the elevation of the peak of velocity deficit changes between phases, which is similar to the previous case. However, this behaviour is much weaker. This is because the difference between flow speeds above and below the turbine during a wave-cycle is not as strong as in the case of streamwise waves. Away from the turbine (3D & 4D), the flow speed above the turbine even remains high at all phases due to the strong current component, in comparison with the wave-induced flows. Overall, the effects of the turbine on the bed boundary layer are less significant in this particular case.

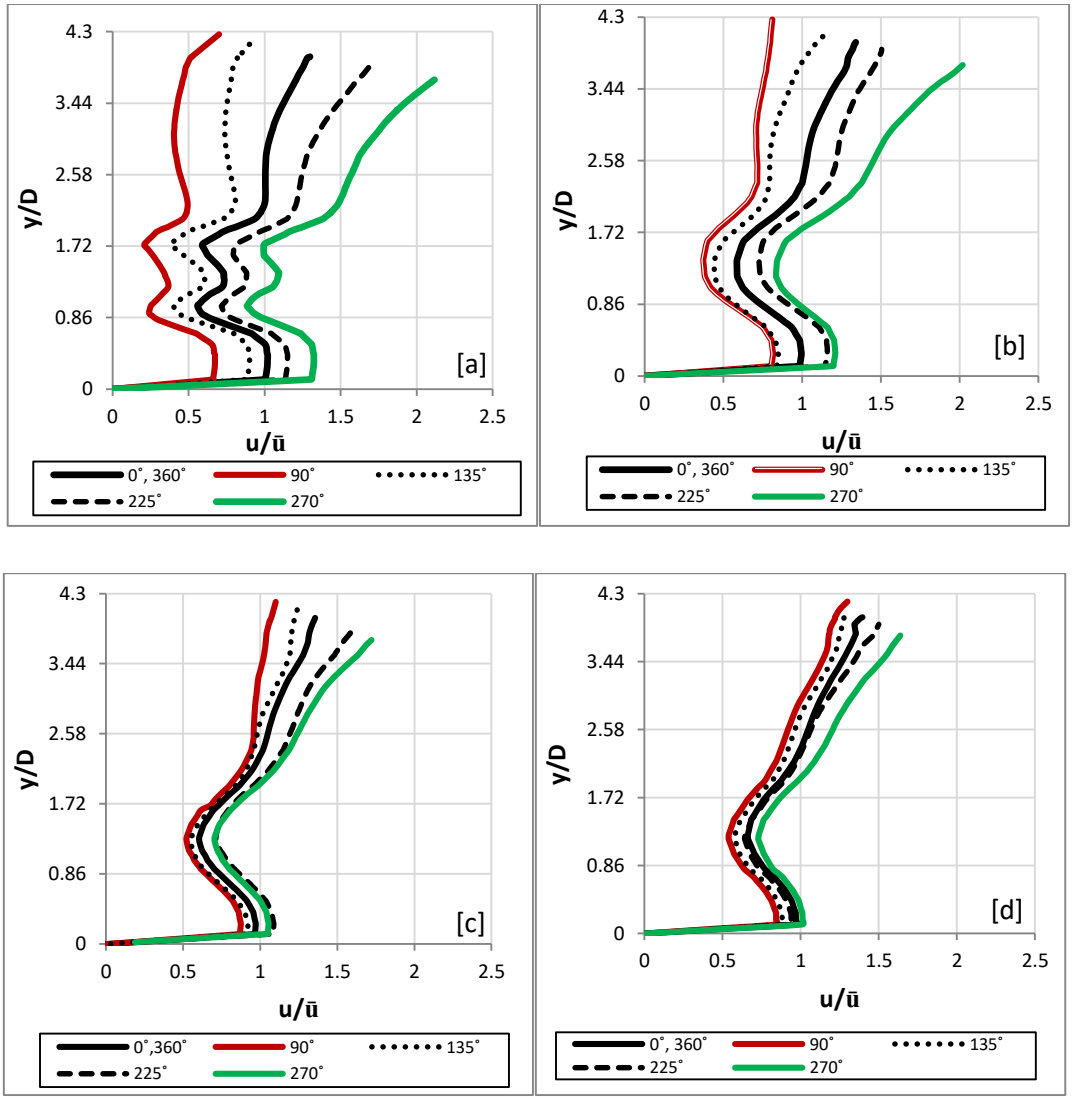

Figure 6-74 – Vertical profiles of velocity magnitude for one opposing wave cycle at [a] 1D, [b] 2D, [c] 3D and [d] 4D downstream (centreline) when wave angle is 0˚, 90˚, 135˚, 270˚ and 360˚.

Figure 6-75 shows the vertical profiles of wave-period averaged velocity magnitude for opposing wave conditions when the turbine is present and absent. The reduction in speed at the turbine effect region (0.5D < y < 2D) is clearly seen. In addition, the presence of the turbine causes higher velocities near the bed and surface regions as under a steady flow case. Higher up (y > 3D), the effects of wave-current interaction can be clearly seen, e.g., the enhanced flow near the surface. It is also interesting to note that the flow reduction behind the turbine is more or less the same as the streamwise wave case. This is largely due to the strong current in comparison with the waves, in these two particular cases.

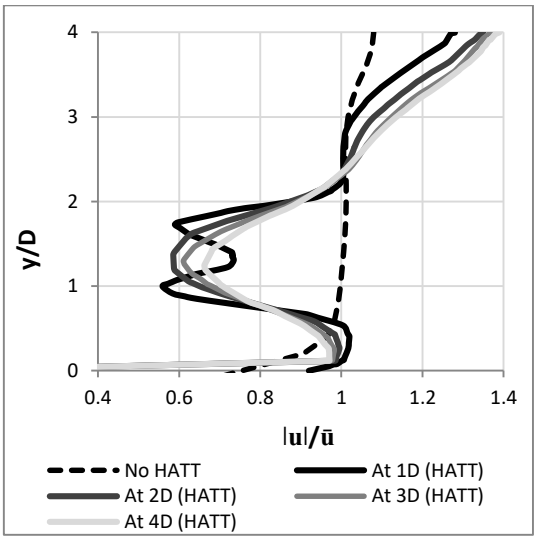

Figure 6-75 - Vertical profiles of wave period averaged velocity magnitude at 1D, 2D, 3D and 4D downstream (centreline) when opposing waves are present. It also shows the mean inlet velocity profile.

Figure 6-76 shows a snapshot of velocity magnitude when the wave crest is at turbine location at centreline across the centre plane for no turbine in [a] and with turbine in [b] and [c]. It is again shown that waves have a strong influence across the whole channel depth. This is different from the streamwise waves case, where high flow velocity is found under trough between 2D < x < 10D, especially near the free surface.

However, the reduction in flow speed behind the turbine is clearly seen, as in the streamwise wave case, extending from 0D to 4D downstream. Further downstream between 6D < x < 12D, a rise in flow speed is noticeable under the wave trough. This is due to the accelerated flow around the turbine being pushed towards the downstream under high pressure from the wave crest and shortening the wake region, leading to the increase in flow speed under the wave trough (A). It is also noted that the lengthening of wavelength shifts the trough area downstream to around 9D instead of 6D in the no turbine case. This is also clearly seen in the top-down view of the velocity distribution at the turbine level in [C] (A').

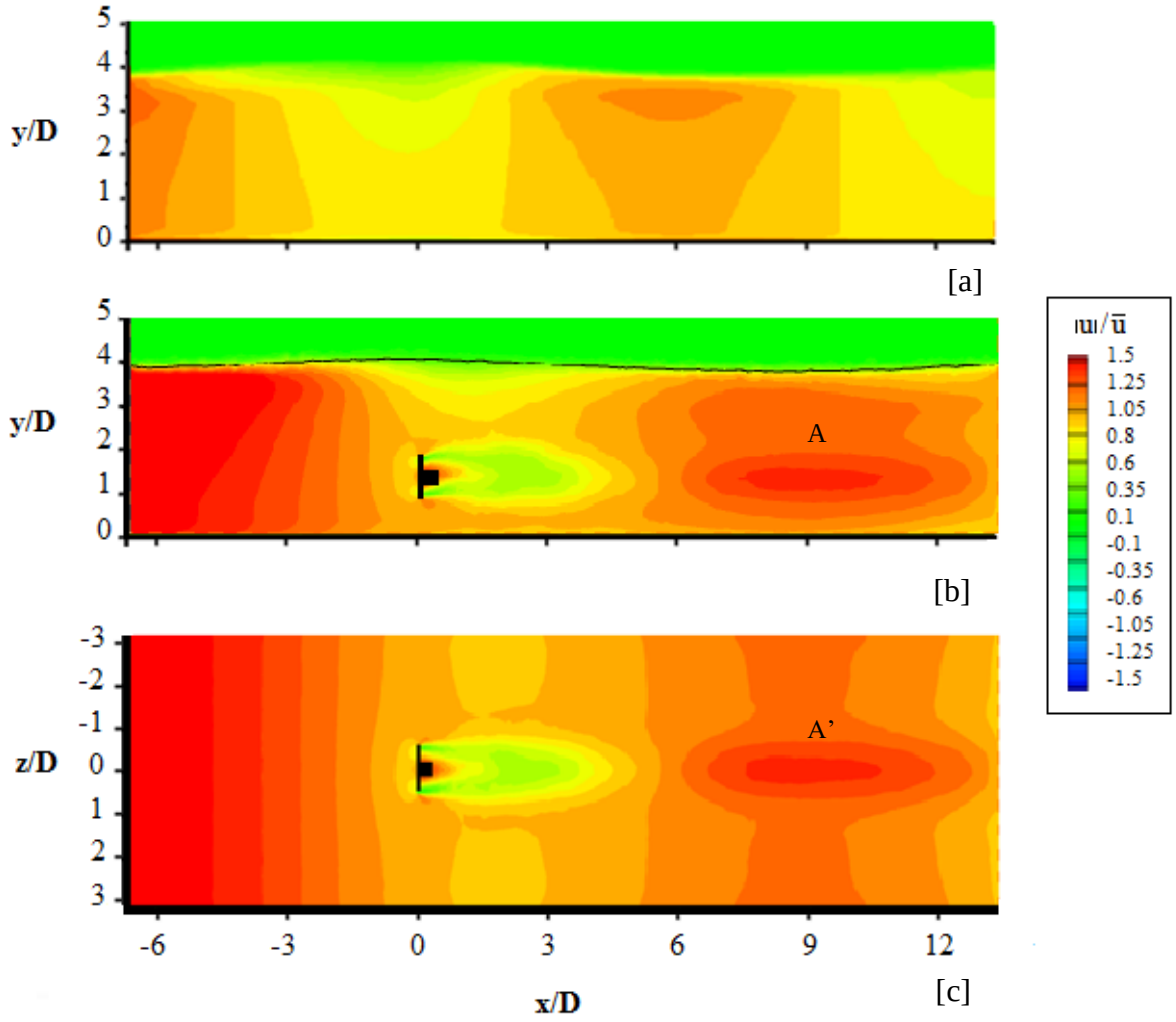

Figure 6-76 - Vertical and horizontal plane at turbine centre showing the contours of velocity magnitude when the wave angle is equal to 90˚ at turbine location: [a] side-view: no turbine, [b] side-view: with turbine, [c] top-down view: with turbine.

Figure 6-77 shows a snap-shot of velocity magnitude when the wave trough is at turbine location at centreline across the centre plane, for no turbine in [a], with turbine in [b] and [c] both showing velocity vectors. The maximum flow speeds are seen under the wave trough in [a]. The turbine-affected layer [b] shows reducing flow speed (0D < x < 3D). But following that, a region with increased flow speed can be seen between (4D < x < 13D), which also alters the wave-induced flow under the crest, which limits the low flow speed region to y/D > 3 (at 9D < x < 12D).

Such a feature can also be seen in the top-down view of the flow speed at the turbine level in [c]. As mentioned in Figure 6-76, in which we can see strong wave-wake interaction, the flow

vectors in Figure 6-77 [a] and [b] indicate that the flow is converging at x ≈ 4D due to the turbine, which leads to an increased velocity flow region (4D < x < 9D) away from its original position between -1D < x < 3D.

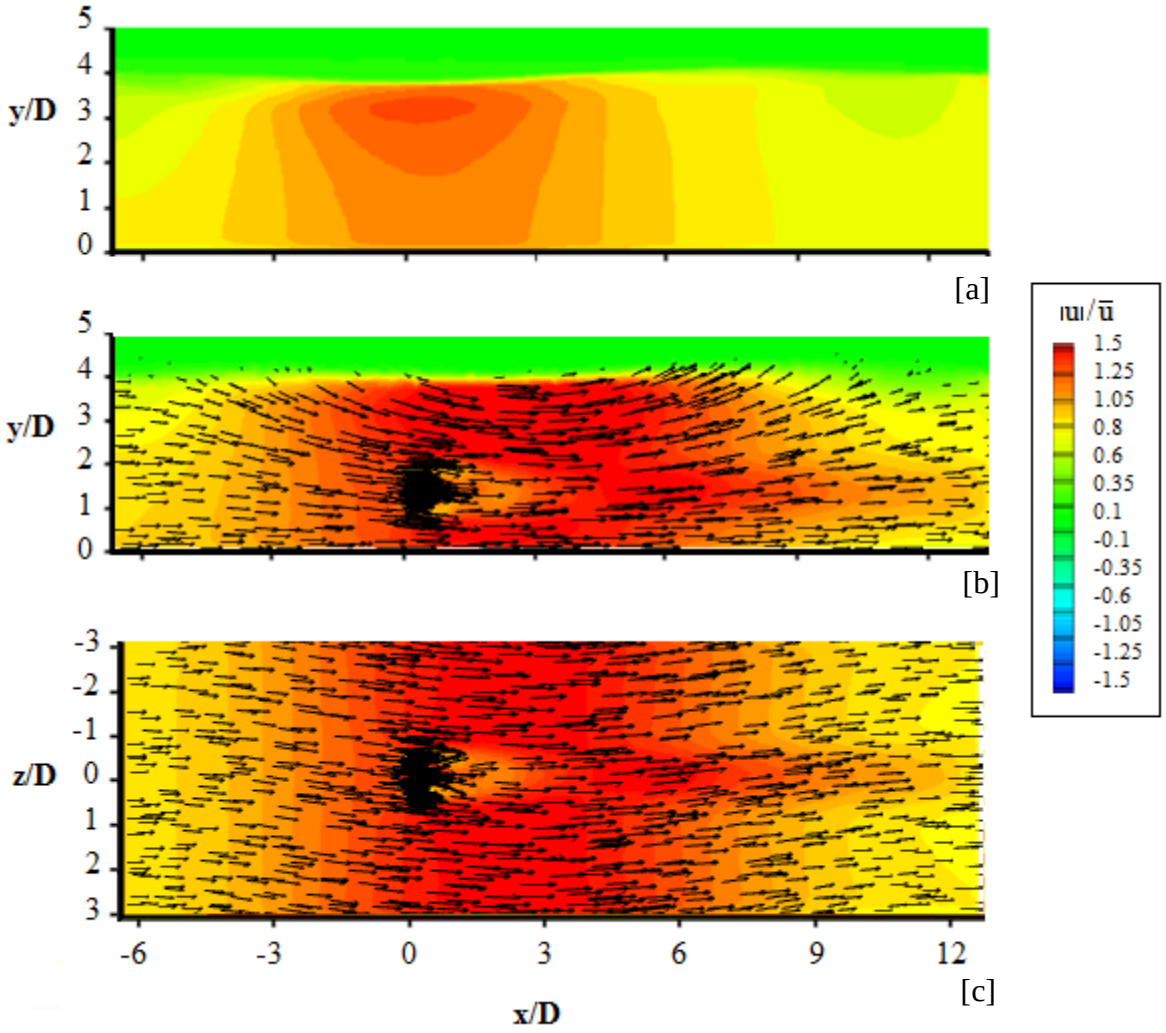

Figure 6-77 - Vertical and horizontal plane at turbine centre showing the contours of velocity magnitude when the wave angle is equal to 270˚ at turbine location [a] side-view: no turbine, [b] side-view: with turbine and [c] top-down view: with turbine.

Figure 6-78 shows a snap-shot of TKE when opposing waves are crest and trough at turbine location across the centre plane [a], side-view (90˚) [b], top-down view (90˚) [c], side-view (270˚) [d] and top-down view (270˚). It is clear that the TKE level behind the turbine is low due to waves.

Comparing with Figure 6-64, it is also clear that the streamwise waves produce higher TKE, as flow velocity in general is lower at the turbine-affected layer when compared to streamwise waves. The interaction between wave-induced turbulence and turbine-induced turbulence is less strong in this case. It is apparent that the waves induce turbulent kinetic energy in the upper surface layer along the entire channel. Similarly, the TKE level is higher on the right side of the hub as in streamwise case. However, the TKE level in higher above the hub in this case due to the wave effect.

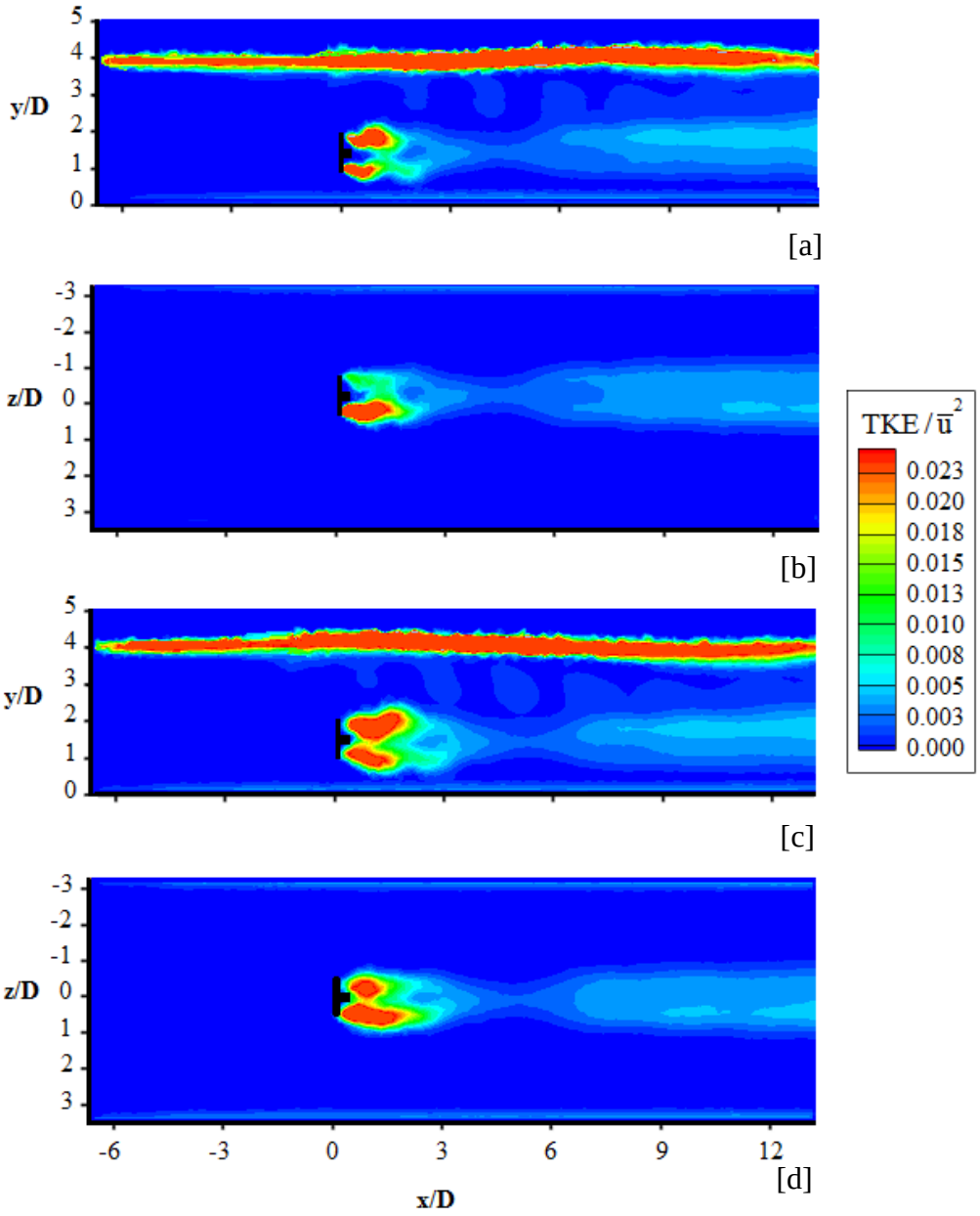

Figure 6-78 - Vertical and horizontal planes at turbine centre showing the contours of TKE when the wave angle is equal to 90˚ and 270˚ at turbine location [a] side-view: 90˚, [b] top-down view: 90˚, [c] side-view: 270˚ and [d] top-down view: 270˚.

Figure 6-79 shows the surface elevation along the channel centreline when the wave trough is at the turbine position (x = 0D). When the wave is propagating against the current, the accelerated flow in the upper surface layer causes the surface to rise, especially when approaching the turbine. But unlike the wave + current case, the shape of the wave undergoes less obvious deformation. This is partly due to the smaller Ursell number in this case compared with the wave + current case.

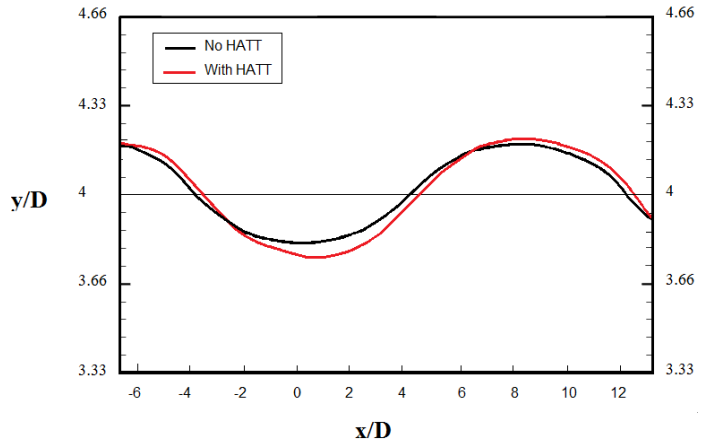

Figure 6-79 - Comparison of surface elevation along the channel length between a turbine in operation, and without a turbine, during opposing wave propagation when the wave is trough (270º) at turbine position.

Figure 6-80 presents the amplitude wave height distribution along the centreline of the channel. In this case the turbine has a different impact on the wave. It can be seen as the wave comes closer to the turbine, that the wave height increases due to the accelerated flow induced by the turbine. In front of the turbine at x = -2D, the wave height drops 3% compared to the upstream wave height (H= 6.72m). This behaviour is different than that found in the streamwise wave's condition. It can also be seen that the maximum change in wave height takes place at x ≈ 1D where it increases by almost 28% due to the accelerated flow beneath the wave. At around x= 8D, the wave height rises slightly due to the accelerated flow region found in Figure 6-76 and Figure 6-77. Overall, the wave height increases by about 11% on average in the channel compared to the original wave.

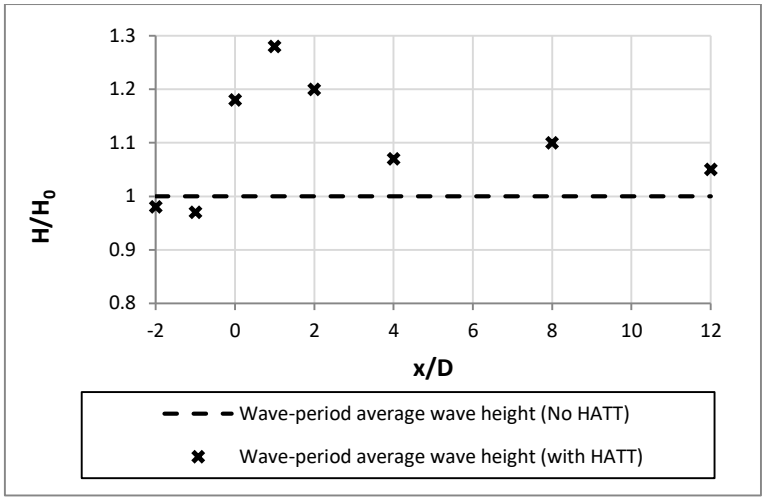

Figure 6-80 - Amplitude wave heights along the centreline of channel at different positions downstream.

Figure 6-81 compares the instant shear stresses along the channel bed centreline both in the presence of a turbine and without when the wave crest is above the turbine [a] and the wave trough above the turbine [b]. The maximum shear stress ($x \approx 1D$) on the bed (under wave trough at turbine position) increases by 41% when compared to no turbine. When the wave crest is above the turbine, the stress peak propagates downstream to 6D. This indicates that stress peaks on the channel bed alternate continuously during wave phases. Behind the turbine ($x \approx 1D$), the shear stress increases by 8% in comparison with no turbine.

It is also recognised that the double-peak feature is found in front and behind the turbine, which is different from the steady current case, in terms of position. The increase in shear stress persists under the wake downstream unlike streamwise waves, due to the accelerated flow region (which is consistent with the flow speed-up in Figure 6-76 and Figure 6-77).

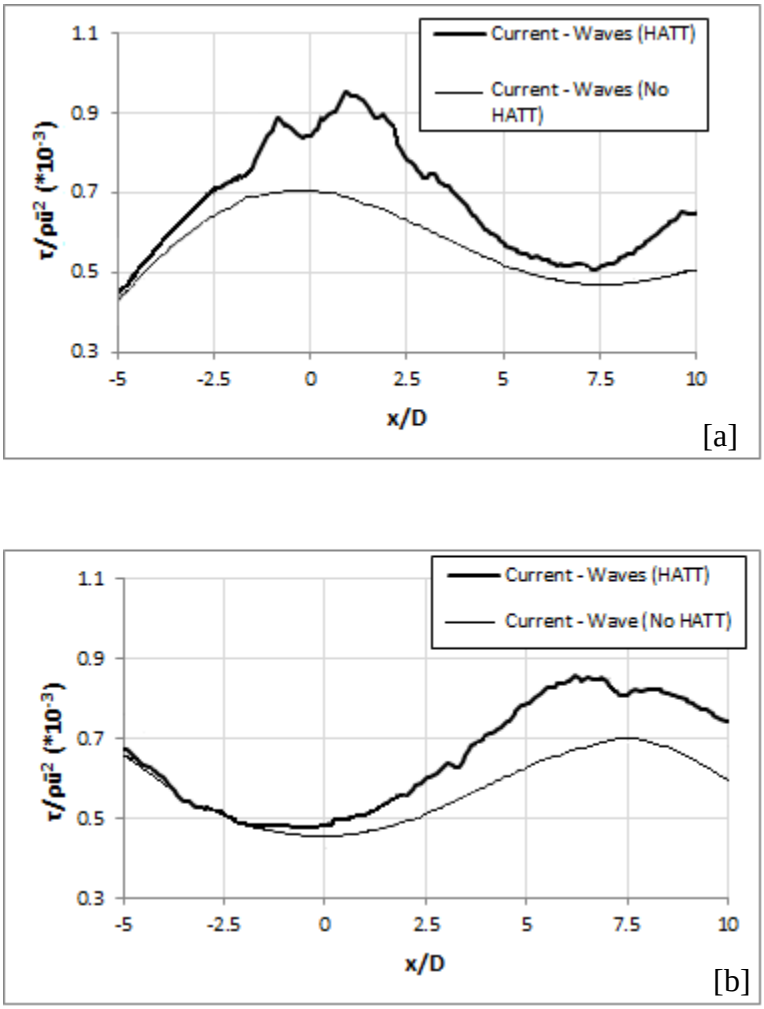

Figure 6-81 - Comparison of instant shear stress on channel bed along the centreline between turbine and no turbine in channel during streamwise wave propagation [a] wave crest at turbine location and [b] wave trough at turbine location.

Figure 6-82 shows the shear stress for one wave-cycle at -1D, 1D, 3D, 5D, 7D and 9D downstream at bed centreline. Similar to the streamwise wave's case, the variation between maximum and minimum stresses is suppressed in front of the turbine. It is clear that the strongest shear stress peaks are experienced at 1D-3D behind the turbine. At 3D behind the turbine, the average shear stress becomes 1.35τ of that at upstream. At x/D > 3, the shear stresses on the bed start to dissipate. At 7D - 9D, the shear stresses show a significant change between maximum and minimum values due to the wake interference with wave-induced flow seen in Figure 61 and 62. Further downstream, maximum values of shear gradually reduce.

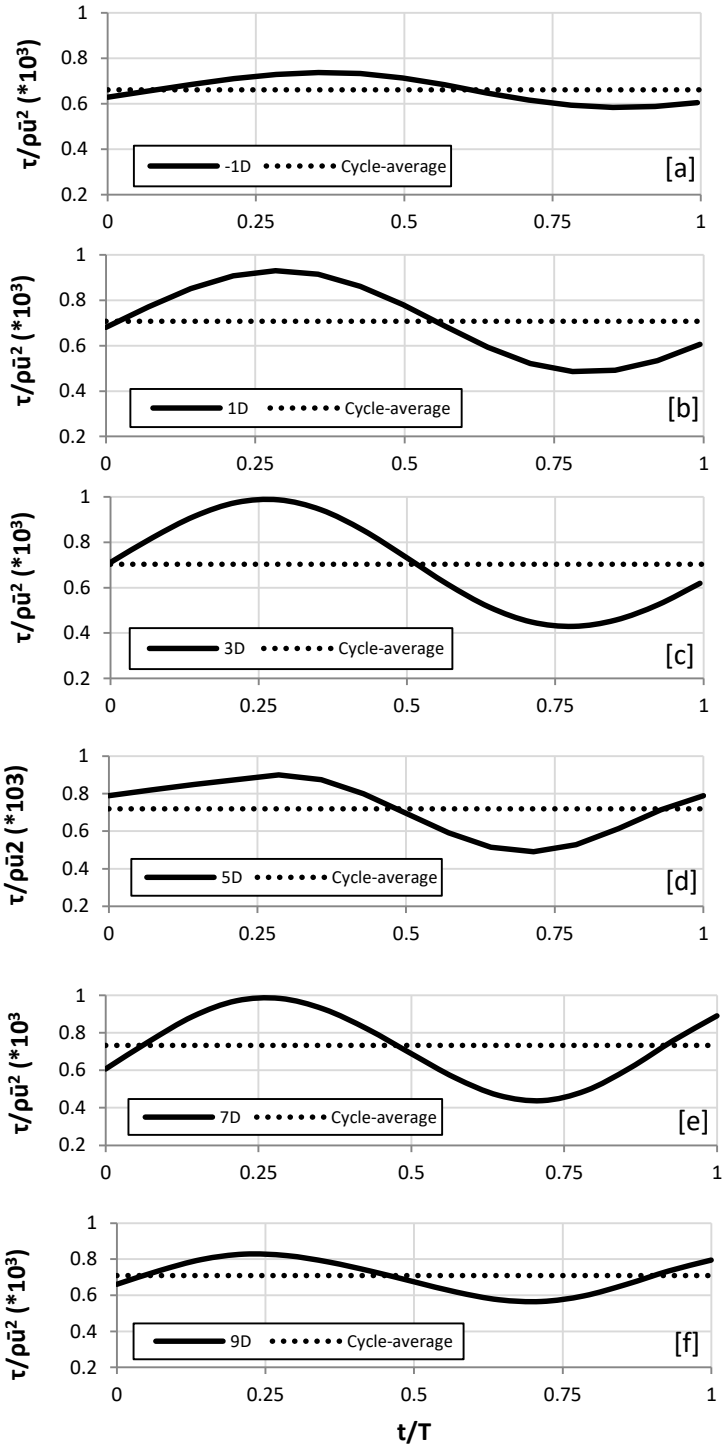

Figure 6-82 - Shows the shear stress for one wave-cycle at [a] -1D, [b] 1D, [c] 3D, [d] 5D, [e] 7D and [f] 9D downstream at bed centreline.

.

Figure 6-83 shows the wave-period averaged shear stresses along the channel centre at x = -5D, -1D, 1D, 2D, 3D, 4D, 5D, 7D, 9D and 11D. Similar to streamwise wave case, shear stresses increase significantly as the flow approaches the turbine. The shear stress under the turbine-affected region (x > 0D) shows a different feature than that found in the streamwise waves case. The variation between shear stresses is more or less small behind the turbine. It can be seen that at x = 7D, the shear stress increases diverting the descending trend.

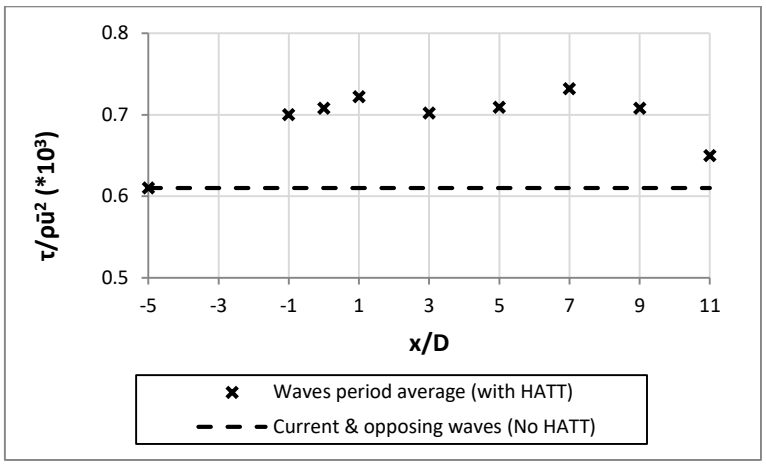

Figure 6-83 – Shows the wave-period averaged bed shear stress along the channel centreline.

Figure 6-84 presents the contours of instant shear stresses across the channel bed when the turbine is under wave crest (90º) and wave trough (270º). It is clearly seen that the turbine increases the shear stress near the bed immediately behind the structure with a prolonged tail in the high stress region (A). Such a feature persists even when the trough propagates downstream until 6D although the magnitude reduces (A').

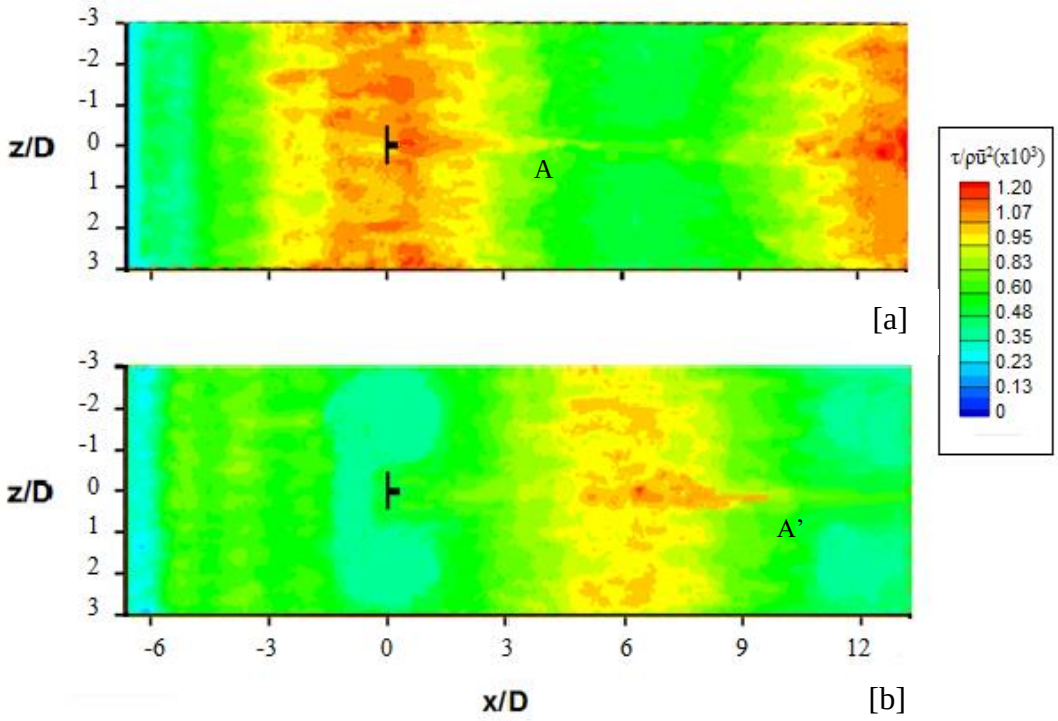

Figure 6-84 – Plan view: contour maps of shear stress on channel bed when angle at turbine location is [a] trough [b] crest.

6.5.4 Steady and unsteady flows comparison

Figure 6-85 compares the vertical profiles of wave-period-averaged velocity magnitude for steady current alone, streamwise and opposing waves combined with current conditions at, 1D, 2D, 3D and 4D sites. Overall, the three cases show similar flow behaviour. However, it is clear that the flow speed reduction at the turbine-affected region reduces in the presence of waves, especially for streamwise waves.

For the streamwise waves, two behaviours are seen. At y/D > 2.5 for 1D and 2D, the accelerated flow created by the turbine suppresses the influence of waves by increasing the flow speed above the turbine and eliminating the flow reduction that is normally seen near the surface as shown in Figure 6-56. However, at 3D and 4D, the turbine impact reduces and the wave's effect dominates to show lower flow speeds near the surface than that found for current alone cases.

For opposing waves, the flow speed in the surface layer is always higher when compared to streamwise waves and current alone cases.

The bed boundary layer has been affected considerably, particularly for the streamwise wave case where the accelerated flow dominates the boundary process and the wave-current interaction almost disappeared.

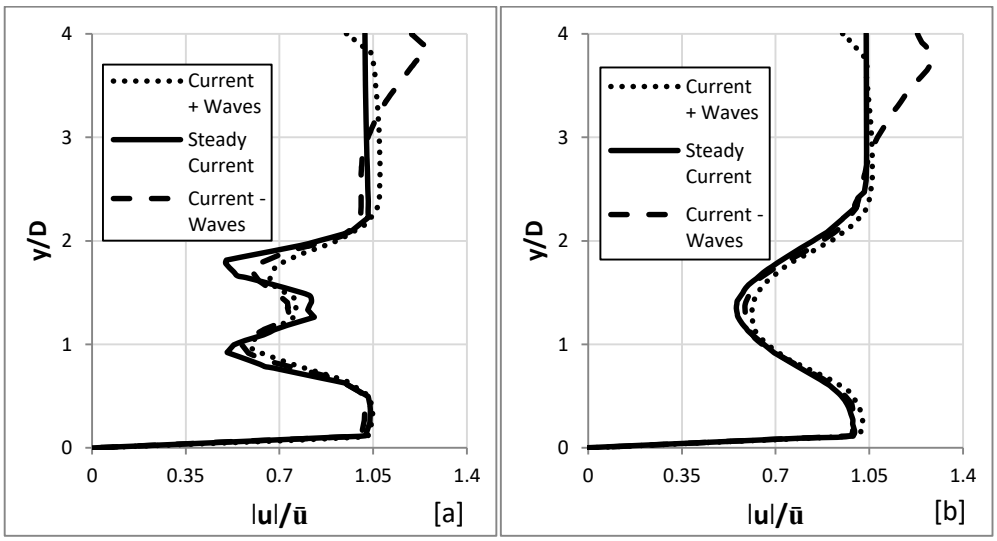

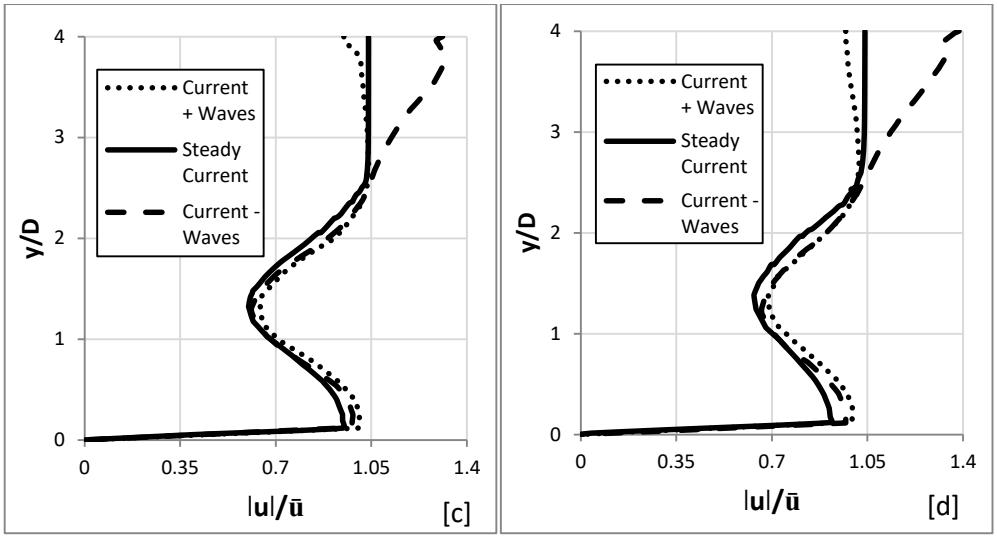

Figure 6-85 - Comparison between vertical profiles of wave-period averaged velocity magnitude of current + wave, current – waves and steady current at [a] 1D, [b] 2D, [c] 3D and [d] 4D (centreline).

Figure 6-86 shows the wave-period averaged velocity magnitude across the width of the channel. In the region where the turbine is present, the results are similar to those from the velocity vertical profiles. The flow velocity increases at the turbine section at 1D, and continues to be higher than the steady flow condition. The increase in flow speed is about 10%. However, the overall distribution is similar to that in the steady current. The turbine-affected region is limited within -0.5 < z/D < 0.5. The lateral mixing is not noticeably affected.

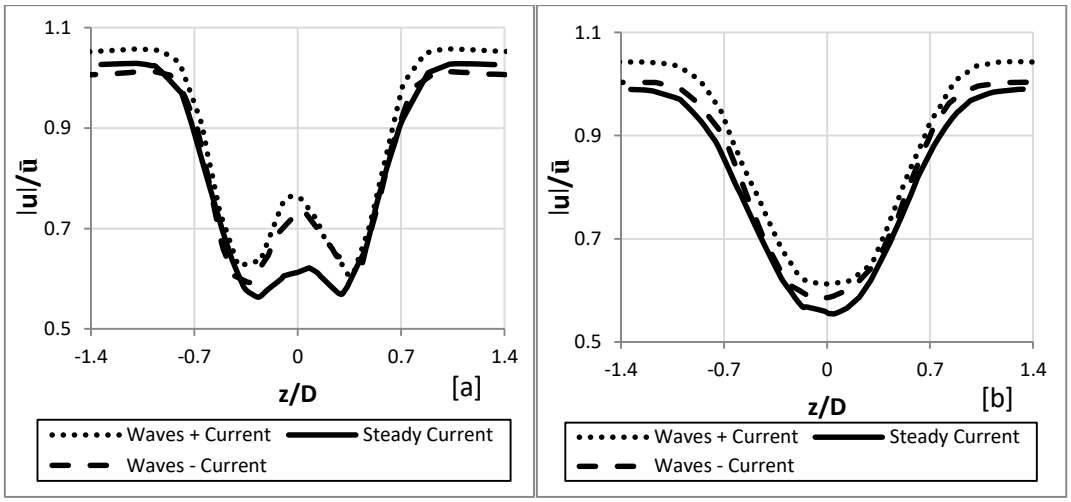

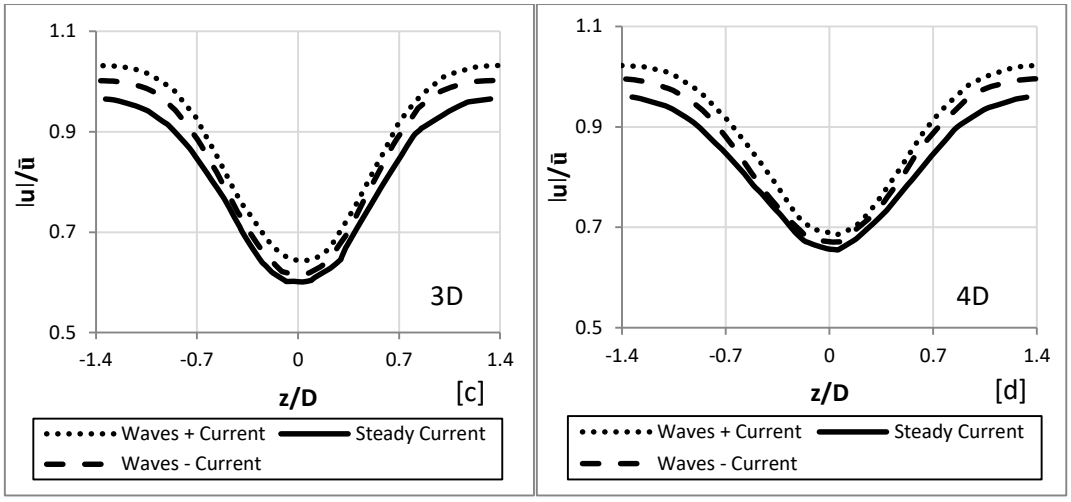

Figure 6-86 – Comparison between horizontal profiles of wave period averaged velocity magnitude of current + wave, current – waves and steady current at [a] 1D, [b] 2D, [c] 3D and [d] 4D (centreline).

Overall, the impact of waves in this scenario is not significant due to the strong current speed in comparison with the waves ($\frac{U_\delta}{\bar{u}} = 0.33$**)**. In addition, the turbine is allocated close to the bed which reduces the wave-turbine interaction. It is important to recognise in most realistic applications this would be the case.

Figure 6-87 compares the vertical profile of wave-period averaged TKE for current only and current +/- waves. At the upper surface layer, a strong increase in TKE value is seen where maximum TKE appear nearer to the surface, being directly affected by the wave kinematics.

This behaviour is consistent along the channel length and for both wave conditions. For current only condition, the TKE preserves a constant value that is lower when compared with wave conditions. At the turbine-affected region, it is found that the presence of waves increases the TKE further. Similarly, a noticeable increase is seen at the bed boundary layer.

Furthermore, it is apparent that highest TKE is found with streamwise wave. The total TKE produced exceeds the opposing wave condition by approximately 71% at 1D. This dominance is also seen in the upper surface layer, as this layer becomes directly affected by the turbine-induced turbulence and therefore overtaking opposing wave's impact here. However, this impact reduces further downstream and higher TKE become stronger for

opposing waves as would be expected (more apparent at 3D). Moreover, the decay in TKE is less apparent; the maximum values remain at around 0.01 TKE/$\bar{u}^2$.

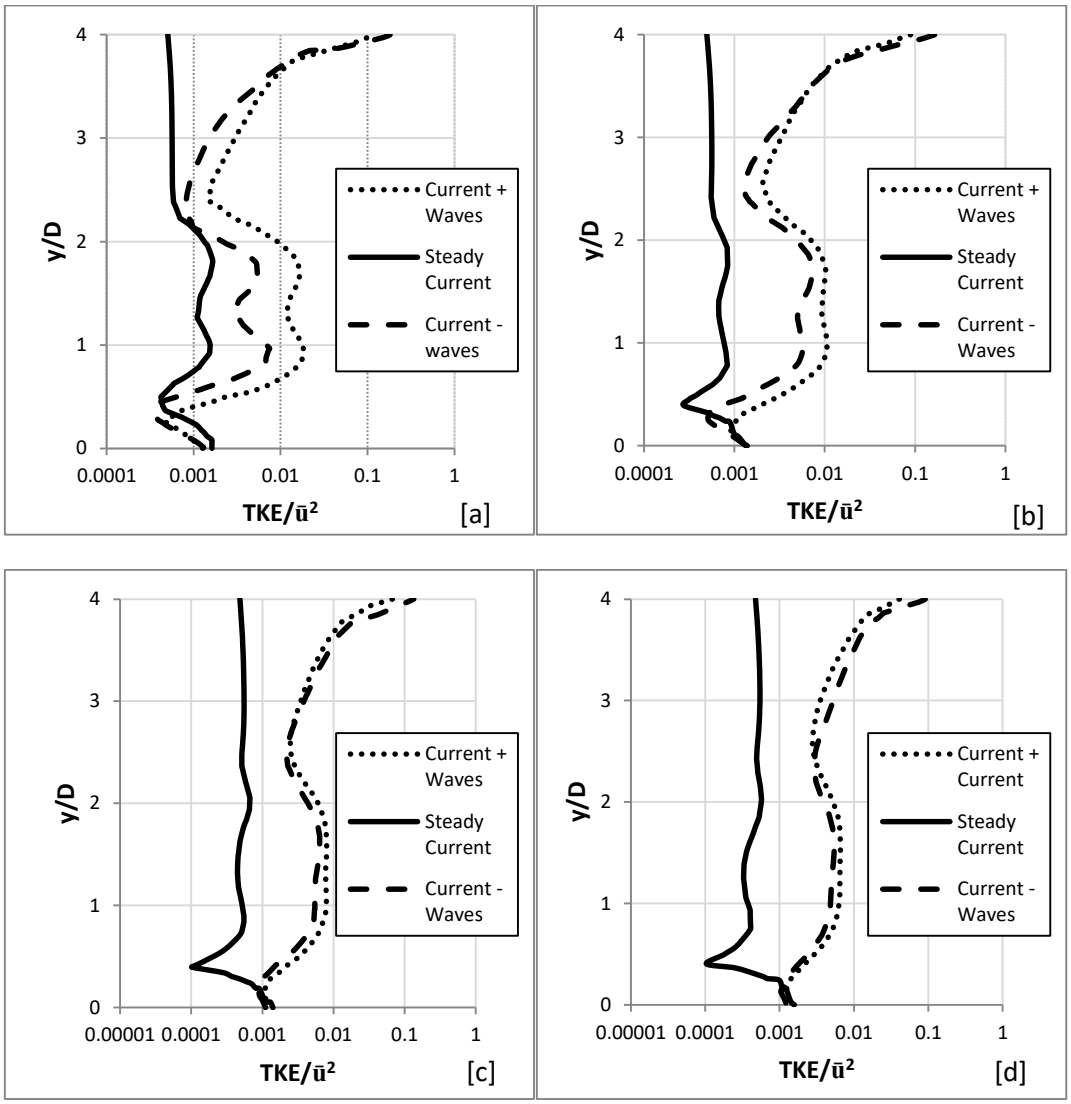

Figure 6-87 - Comparison between vertical profiles of wave-period averaged TKE of current + wave, current – waves and steady current at [a] 1D, [b] 2D, [c] 3D and [d] 4D (centreline).

There are three turbulence generation sources: the wave propagating along the surface, the turbine operation and the near bed boundary layer process. It is clear that each process dominates a different region of the water body and in the tested cases the presence of the waves affects directly on the overall turbulence level, not like in the current only condition. However, as mentioned earlier, there is turbulence energy transfer between the surface and the turbine-affected regions.

6.6 Summary

Based on the above investigations, these are highlights of the findings:

- It is found that in lower blockage conditions the wakes vertical and horizontal movements (alignment shift) tend to increase as well as its expansion range due to more space available.
- For higher blockage conditions, the wake velocity recovery is faster due to the generation of stronger turbulence in the wake that enhances the flow mixing.
- It was found that bed shear stress shows a double peak feature along the turbine centre line. This is due to the interaction of vortex and accelerated flow around the turbine that cause divergence and convergence of the flow trajectory.
- It is found that the strongest shear stresses happen within the 1^{st} turbine diameter downstream.
- Yawed turbines cause stronger velocity deficits near the hub but higher accelerations near the tips. Their wakes are normally recovered over shorter distances. Their wake tends to shift left and right which directly influences the bed shear stresses, showing more stress peaks. However, yawing turbine cause lower shear stresses on bed.
- Additional evidence was shown that the higher background turbulences the more enhanced wake recovery become.
- Scaling up the model showed very similar flow features to those found empirically.
- It was found that the increasing the background turbulence increased the turbulence behind the turbine exponentially
- It is also found that background turbulence will increase the bed shear stress.
- As expected, the elevation of the turbine directly influences the bed shear stress and therefore a compromise between the impact on bed shear stress and loading on structure should be considered.
- Additional evidence to experiment results that the turbine has a considerable influence on the wave height. With streamwise waves, the wave-period averaged drop is found to be 10% in the channel. Contrarily, opposing waves show an average increase 11% in the channel. In this study, it was found that maximum change in wave height appears at $x \approx 1D$ behind the turbine.

- It was found that near bed shear stress under the wave and current condition is affected in the presence of the turbine. The highest bed shear stresses are found approximately 1D behind the turbine. On average (along channel centre), during streamwise wave propagation the shear stress increases by 14% and during opposing waves 12% when compared to no turbine condition.
- The turbine-affected region clearly interferes with the wave characteristics. The turbine promotes the wave-induced turbulence.

6.7 References

ANSYS Fluent Theory Guide. (2010) ANSYS, INC. USA: Issue: 13.

Batten, W. M. J. Harrison, M. E. and Bahaj, A. S. (2013) Accuracy of the actuator disc-RANS approach for predicting the performance and wake of tidal turbines. *Philosophical transactions of the royal society,* vol. (371), Issue: 1985. pp.1-15.

Black & Veatch (2005) Phase 2 UK tidal stream energy assessments. The Carbon Trust, http://www.lunarenergy.co.uk/Userimages/PhaseIITidalStreamResourceReport.pdf [accessed 21 June 2014].

Dahl, J. M., Hover, F. S. and Triantafyllou, M. S. (2007) Resonant Vibrations of Bluff Bodies Cause Multivortex Shedding and High Frequency Forces. *Physical Research Letter,* vol. (99), Issue: 14. pp.144503.

Haans, W. (2011) *Wind turbine aerodynamics in yaw*, PhD. Thesis, University of Delft, Netherland.

Jordan, L. B., Simmons, S., McLelland, S., Murphy, B., Parsons, D. and Vybulkova, L. (2015) The Impact of Tidal Stream Turbines on 3D Flow and Bed Shear Stress Measured with Particle Image Velocimetry in a Laboratory Flume, *Proceedings of the 11th European Wave and Tidal Energy Conference (EWTEC),* Nantes, France.

Kemp, P. H. and Simon's, R. R. (1983) The interaction of waves and a turbulent current: waves propagating against the current. *Journal of Fluid Mechanics,* vol. (130), Issue: 1. pp.73 - 89.

Milne, I. A., Sharma, R. N., Flay, R. G. J. and Bickerton, S. (2013) Characteristics of the turbulence in the flow at a tidal stream power site. *Philosophical transactions of the royal society*, vol. (371), Issue:1985

Richmond, M., Thomon, J., Durgesh, V. and Polagye, B. (2011) Field measurements of turbulence for marine and hydrokinetic inflow conditions at Marrowstone Island. American Geophysical Union, Fall Meeting 2011, abstract #OS52A-06

Sun, X., Chick, J. P. and Bryden. I. G. (2008) Laboratory-scale simulation of energy extraction from tidal currents. *Journal of Renewable Energy,* vol. (33), Issue: 6. pp.1267-1274.

Tedds, S. C., Owen, I. and Poole, R. J. (2014) Near-wake characteristics of a model horizontal axis tidal stream turbine. *Journal of Renewable Energy,* vol. (63), pp.222-235.

Chapter 7 –Conclusions and Recommendations

7.1 Introduction

The central aim of this thesis is to understand the impact of a single turbine on a stream flow in a highly turbulent regime under natural wave-current conditions. The investigations were mainly focused in the near wake region. Initial tests took into account two different numerical methods to represent the turbine on a disk; actuator disk model (ADM) and virtual blade model (VBM). Subsequently, the VBM method was adopted in all the investigations under different natural occurring and turbine configuration conditions. It was important to model real tidal conditions in order to predict representative wake characteristics and impacts on the surrounding environment (stream bed and free surface).

The investigations covered experiment and field scale simulations and the results were normalised in order to be able to identify relations. The methods and techniques for setting up boundary and zone conditions, as well as the turbine representative models, were validated and verified across four different experiments. The models were mainly assessed based on flow velocity and turbulence kinetic energy and, in other cases, surface elevation (waves). It should be noted that the bed shear stresses were not directly validated since no experimental data were available. However, the flow velocity down to the bed was considered as a form of reliability indication. This chapter will present all the findings obtained from the investigations and will suggest possible future works. The present work was based on CFD modelling with special reference to tidal turbine operations. The findings of this study were divided into two parts, the CFD approach and the turbine impacts.

7.2 CFD Approach

In this study, the porous disk approach was employed to represent the turbine in a stream rather than the more detailed approach of having actual blades. This option was selected due to its simplicity, low computational cost and the numerous number of validation tests that had to be carried out (faster convergence). The assumption was that the impact from the rotating turbine was at a significant distance away from the blades. Therefore, the focus was on the temporally averaged flow field, rather than the instantaneous flow characteristic at the blades. In addition, the pressure change at the surface of the blades was assumed to be insignificant on the flow dynamic at 1D away from the turbine. The outcome of validation tests was satisfactory and certainly approve that these assumptions were acceptable.

Overall, high Reynold numbers were experienced in the open channel flow regimes, in addition, turbines induced the strongest turbulence in the flow, dominating any other sources of turbulence such as bed-induced turbulence. Consequently, the wall function approach was good enough to serve the purpose of these tests. This directly influenced the mesh density at the bed, where mesh sizes varied between 6mm and 24mm at the bed boundary, satisfying $30 < y^+ < 300$.

Taking into account the computational costs, time and most importantly the limitations of both turbine representation methods. The SST $k - \omega$ turbulence model was chosen as an appropriate RANS equation closure. Such an approach was able to reproduce the important turbine-induced wake features behind the turbine.

The turbines were assigned with 40 mesh nodes across their diameter to obtain high accuracy and reasonable number of mesh cells. Exceeding this number of nodes did not improve the results significantly in the wake region, but increased the running time considerably. Considering unsteady flow conditions (waves), 30 mesh nodes across the vertical wave height was ideal to capture the surface elevation accurately (see Chapter 4).

A number of validation tests were carried out, taking into account current alone and current with waves. In terms of current with waves, in the absence of the turbine, it was recognised that FLUENTs 14.5 was able to generate waves and capture their induced dynamics in the channel with an accuracy exceeding 95% in terms of velocity and wave height. In the presence of a turbine, it was found that the model was able to capture the velocity and TKE

profiles reasonably well. The accuracy of the predictions gradually improved as the flow moved away from the turbine. On average, the accuracy of computed results was found to be approximately 87%.

ANSYS FLUENT was able to simulate the flow in steady and unsteady states. The unsteadiness of the flow can be produced by generating waves at the inlet or by assigning background turbulence. In terms of the turbine representation method, VBM was initially developed for single phase and steady conditions. VBM was able to function with the wave as long as it was kept in the water phase and was able to respond to the changing behaviour of flow.

7.3 Major Findings

Comparison of static and rotational impacts on wake and bed (ADM and VBM)

Two numerical turbine representations were compared and validated against the experimental data conducted by Tedds (2014). The investigation was carried out in terms of velocity and turbulence kinetic energy. In terms of streamwise velocity, both ADM and VBM methods provided excellent accuracy of around 88% and 92% on average respectively. Although the computed velocities were slightly underestimated in both cases, the velocity distribution followed very well the experimental measurements by showing a "W" shape profile near the turbine ($0 \leq x/D \leq 4$). The VBM method, however, was able to capture the asymmetric nature of the flow velocity where the speed was 25% higher on the right-hand side of the turbine when looking from upstream. More importantly, the VBM was able to reproduce the vertical and cross-stream velocities reasonably well. The ADM method failed to capture the asymmetric nature of the flow and to represent vertical and cross-stream trajectories due to the absence of the rotational motion. Comparatively with the measured data, VBM overestimated the vertical velocity on average at around 17%, while underestimating the cross-stream velocity on average at around 15%.

In terms of turbulence, ADM and VBM both underestimated the turbulence kinetic energy by 17 % and 10% respectively. These underestimations were particularly found at the blade tips.

However, the computed TKE distributions followed well the measured data in both cases. In terms of unsteady flow conditions, FLUENT provided excellent accuracy of around 95% when generating currents with following and opposing waves. Employing VBM (turbine) in the channel, the accuracy of the turbine-induced flow velocity and TKE were found to be on average approximately 87%. These findings provide additional evidence that VBM was a robust method, although it preforms on a disk. It was expected from the start that VBM will produce better flow accuracy than that of ADM method (Mozafari, 2010), in this study, however, this accuracy dominance is quantified in terms of velocity and TKE.

It was found when examining the bed shear stresses for both methods (VBM and ADM) that rotational motion (VBM) imposed stronger shear stresses on the bed, providing extra features of the shear stress when compared to ADM. This is due to the generation of vortex which imposes a cross-stream flow component on the bed.

Turbine wake characteristics

It was clear that the flow starts to experience the presence of the turbine at 1D ~ 2D in front of the turbine where the flow speed starts to drop. Providing additional evidence, at the hub, the flow diffracts and accelerates through the gap between the blade-hub connectors and then quickly slows down. At the blades, the flow starts to form a vortex and eddies. At the turbine tip the flow swirls around the turbine and accelerates reaching maximum values of 1.5 times the mean inlet velocity. It was found that the accelerated flow swirling around the turbine edge recovers its velocity first. The flow streamwise velocity behind the turbine becomes asymmetric where it shows an increase of 25% on the right-hand side of the hub comparing with that on the left-hand side when looking from upstream (turbine rotation clockwise). Such asymmetric behaviour appears behind the turbine ($x > 0D$) when the vortex begins to form.

It was found in this study that this asymmetrical behaviour of the flow causes the wake to shift slightly to towards the left-hand side of the hub (looking from upstream) by an angle of $2^{\circ} \sim 5^{\circ}$.

Additional evidence was provided by this study with that found empirically by Bahaj et al. (2007) that the wake slightly shifts towards the bed due to the free surface effect. In terms of

vertical velocity, it was found that the flow velocity was always higher in the downward direction due to the influence of gravitational force.

The strongest turbulent kinetic energy was generated by the turbine. This happens due to the rapid velocity and pressure changes in the face of the turbine. Again, the TKE distributions follow an asymmetric pattern where it was always greater on the right side of the turbine, when looking from upstream, and at the bottom half of the channel depth. In these areas, the flow velocity magnitudes were found to be higher, due to the turbine rotatory direction and the influence of the stationary bed (wall) respectively.

Overall, it was found that the wake expands around 1.7D ~ 2.3D when the flow meets the turbine at a perpendicular angle and will continue to expand further downstream.

In this study, the transition from near to far wake fields has been defined by assessing the flow velocity and flow behaviour behind the turbine. In the region where the velocity deficit exceeded 40% of the ambient (inlet) flow velocity, this region was defined as the near wake. It was found that this region has been always in the first 5 diameters behind the turbine. However, anywhere beyond 5D was defined as far wake. Furthermore, the near wake region has always displayed reversed values of flow velocity (eddies) that dissipate beyond 5D behind the turbine.

Impact of turbine on bed shear stresses

The presence of the turbine was found to have a significant impact on the bed shear stresses. These bed stresses were initially experienced in front of the turbine approximately 1D in front. Behind the turbine, a double-peak feature was seen and these beds stresses persisted beneath the wake region. The reason for the first stress peak was due to the immediate increase of flow velocity behind the turbine that creates a strong velocity gradient. However, the second stress peak appears due to vortex generated by the turbine that clearly increases in magnitude to impose an additional cross-stream flow motion. Between the two peaks a slight drop in shear stress was seen due to the change in flow trajectory influenced by bed boundary. Beyond the second peak the wake starts to recover and the stresses on the bed gradually reduce. In general, stronger shear stresses were found due to faster flows found near the bed.

Influence of blockage ratio effects (5.3% and 16%)

It was found that at higher blockage conditions when compared to lower blockage conditions, the turbine experiences a stronger pressure change in the turbine face, which consequently causes the flow to accelerate faster around the turbine and produces stronger effects on the bed boundary, turbine-affected and upper surface layers. The flow squeezes through the hub-blade gap with higher velocity, but higher flow deficits were found behind the blades, showing the stronger vortex magnitude.

In high blockage conditions, it was found that these flow accelerations around the blade tip persist over a longer distance downstream up to approximately 4D, besides generating stronger turbulence, which enhances the mixing of flow and hence faster recovery of wake velocity. This was not the case for the lower blockage conditions, where the accelerated flow expands laterally and therefore dissipates faster, not creating strong velocity shear.

It was found that in lower blockage conditions the wakes vertical and horizontal movements (alignment shift) tend to increase when compared to the high blockage condition. In addition, it was observed that the wake expansion length also increased in lower blockage conditions due to more space available.

The impact of the wake on the bed shear stresses was found to follow a similar distribution across the channel centre for both cases. The results show a double-peak feature that varies in magnitude and distance on the bed. For high blockage conditions, the maximum shear stress was found to be 15% higher than that found for low blockage. Furthermore, the length of impact on the bed covers more ground, dissipating slower at around half the rate when compared to the low blockage case. This was due to the strong flow velocity and vortex magnitude found in the bed boundary layer. Furthermore, the bed shear stress was found to spread over a larger area when compared to the low blockage condition.

The surface elevation was also affected considerably in the high blockage case, in which the variation between the surface rise in front of the turbine and the surface drop behind the turbine was stronger. It was found that the difference between the two elevation states was higher by 34% than that found in the low blockage condition.

Influence of turbine yawing angle (0˚ and 45˚)

To test the effects of angle of current towards the turbine, this investigation focused on turbines with yaw angles of 0˚ and 45˚. These yaw angles provide a good test for an appropriate comparison, besides, increasing the yaw angle beyond 45˚ will directly and significantly reduce the power production, which would suggest not proceeding beyond it (Galloway et al., 2014).

It was found that when having the turbine at 45˚ yaw, the flow velocity distribution has clearly changed to show a "U" shape rather than the usual "W" shape. The flow undergoes stronger deficit near the hub area of around 6%, when compared to a straight turbine (yaw = 0˚). However, stronger acceleration around the turbine tip was found. The yaw angle leads to an asymmetrical behaviour in which the highest reduction appears on the side away from the main flow. The turbine exerts a smaller blockage effect against the flow and consequently the flow speed recovers in a shorter distance. Furthermore, the large area around the turbine was affected by the accelerated flow, which also enhances the wake recovery. This accelerated flow was found to dominate in the bed boundary layer where the flow velocity was much higher than that in the upper surface layer due to the free surface effect. However, the swirling flow beneath the turbine at 0˚ yaw was found to be more influential on the bed.

The flow vortex for the 0˚ yaw turbine seemed to be almost symmetrical in the channel in terms of vortex length and expansion. For the turbine with 45˚ yaw, however, the vortex length on the upstream side was found to be longer. On the other hand, the vortex expansion (in the lateral direction) was found to be greater on the downstream side.

Overall, the turbine-induced turbulent kinetic energy was found to be higher when the turbine was at 45˚ yaw. Such a difference was found across the entire channel, apart from the bed boundary layer where the turbulence under the 0˚ yaw turbine dominates. It was found that with the 45˚ yaw turbine, the TKE levels were higher on the downstream side, due to larger vortex expansion. The turbine yaw also amplifies the asymmetric nature of TKE across the water column where the TKE was significantly higher at the lower half of the turbine.

The turbine yaw had a different influence on the bed shear stress magnitude, on average; the bed shear stress was lower under the 45˚ turbine by approximately 27% along the centreline in comparison with 0˚ yaw turbine. The distribution was clearly different where four stress

peaks, besides the one immediately beneath the turbine, were seen at different locations to the left and right of the channel centre line with the 45˚ yaw turbine. These peaks follow the vortex path behind the turbine.

The surface elevation was also affected by the turbine yaw where the variation between rise and drop in front and behind the turbine was less by 35% on average, than that found in the 0˚ yaw turbine.

Influence of background turbulence (4% and 8%)

It was found that high turbulence backgrounds do not essentially influence the velocity distribution of flow around and behind the turbine. However, additional evidence shows they improve the mixing process significantly and consequently enhance the wake recovery. Flows with high background turbulence tend to alleviate the asymmetric characteristic of wake. Background turbulence demonstrates its strongest impact on the turbine-affected region where higher turbulent kinetic energy is generated. It appeared that the background turbulence intensity enhances the turbine effects and the turbulence generation in particular behind the turbine. It was found that the relationship between background turbulence and turbine-induced turbulence had an exponential nature.

The strength of background turbulence had been found to influence the bed shear stresses. With increasing background turbulence intensity, the bed shear stresses increase in front and much more behind the turbine.

Influence of turbine elevation (2h/3 and h/2)

Increasing the elevation of a turbine above the bed will increase the speed of flow around the turbine. This faster flow will produce stronger acceleration around the turbine and at the hub area and also leads to a stronger flow deficit behind the blades. The velocity distribution, however, remains as usual. In terms of TKE, similar distributions to those for the lower turbine elevations were seen in both the vertical and horizontal planes. However, magnitudes differ, especially across the water depth. Higher TKE was found for the turbine at mid-depth, on average, by 55%, close to the turbine (1D). As expected, the stresses were shown to be stronger at the bed, by around 65%, when the turbine was at two thirds of the water depth.

Influence of turbine on waves (streamwise and opposing waves)

Additional evidence from the modelling perspective confirmed that the presence of a turbine had an impact on waves shape. For streamwise waves, several behaviors were recognized in the case studied:

1. The wavelength was slightly extended by about 12% when compared with the original wavelength.
2. The wave height reduced by about 10% on average.
3. The presence of a turbine promoted non-linearity of waves.

For opposing waves, almost contrary behaviours of the wave form were seen:

4. The wavelength slightly decreased by about 11% when compared with the original wavelength.
5. The wave height on average increased by about 11%.

It was found that the waves alignment across the width of the channel was considerable deformed in the presence of a turbine. The wave tends to arc around the turbine region to form a crescent shape when looking top-down.

It was found that the turbine-induced TKE extends to the upper surface layer to interact with the upper layer under the free surface. In this study where wave-induced turbulence was negligible, it was found that the turbine-induced turbulence promotes the generation of such turbulence produced by the waves.

Influence of waves and current on wake characteristics and streambed

When turbines were employed in flows with propagating waves, it was found that the velocity distributions across the width and depth of the channel were very similar to those found in steady flow conditions. However, waves can still leave a noticeable signature on the intra-wave processes as shown in Chapter 6. In particular, the wake can interfere with the wave-induced oscillation immediately behind the turbine, causing flow speed reduction in the crest and trough region under the streamwise wave. In opposing waves, the flow speed

increases downstream as the wave was propagating from downstream to upstream of the turbine.

For streamwise waves, it was found that the velocity variation (spread) between different wave phases increases on moving away from the turbine. This means that the wave influence was suppressed by the turbine where strong flow transformation occurs. In the presence of opposing waves, however, a contrary process takes place as the velocity variation increases when approaching the turbine. This means that the wave influence was encouraged by the turbine when in the opposite direction of flow.

It was also found that not only do the values of flow velocity change, but also the elevation of the turbine-affected region. For streamwise waves, the velocity deficit drops slightly in elevation when the wave crest was above the area of interest and slight rise when the wave trough was at the area of interest. Therefore, the wake was continuously alternated its elevation (oscillating) in the presence of waves. A similar behaviour was seen for opposing waves, but with wake rising at wave trough and wake dropping at wave crest.

It was clear that the presence of waves (opposing or streamwise) enhances the wake recovery. This was seen across the depth and width of the channel. The presence of waves encourages stronger TKE generation in the flow regime. The highest TKE levels were found in the upper surface layer where the waves produce their strongest impact. Opposing waves always show their dominance in this region, however streamwise waves produce higher TKE in turbine-affected and bed boundary layers.

It was clear that in the presence of waves (no turbine), the bed shear stress was significantly increased when compared to current alone condition. It was found that the impact of streamwise waves on the bed shear stress was stronger than that from opposing waves since they produce a stronger flow velocity gradient in the bed boundary layer.

In the presence of a turbine, it was found that the highest bed shear stresses were approximately 1D behind the turbine when the wave crest was at the turbine loction, producing a 36% increase when compared to no turbine case. Such an increase reduces to 32% when the wave trough in above the turbine location. The wave-period averaged shear stress increases along the channel centre ($-5D < x < 10$) by 14% when compared with no turbine case. During opposing wave conditions, the highest shear stresses on the bed were found when the trough was at the turbine location, producing a 48% increase when compared

with no turbine. Such an increase reduces to 8% when the wave crest was above the turbine location. The wave-period averaged shear stress increases along the channel centre by 12% when compared with no turbine case.

It was found that the double-peak feature (bed shear stress) created behind a turbine in steady flow conditions remain when considering the intra-wave variation under the wave oscillation. In this study, it was found that the shear stress induced by the waves had a stronger imapct on the channel bed than that caused by the turbine itself.

.

Imapct of turbine on marine environment

It was clear that the turbine had a significant influence of the flow dynamics, causing a huge pressure change. As a result, it was seen that the free surface as well as the bed surface were directly influenced by these dynamic changes. This study would like to point out two points:

1. Turbines produced many physical processes that were complex in nature, accompanied by strong pressure jumps. Different marine species will be affected by these physical changes in different ways. Therefore, it will require to distinguish the reactions of species for that site to such adverse nature in order to able to predict the turbines impact on them.
2. It was found that turbines had a significant influence on the bed shear stresses where sediment transport is a function of shear stress. As a result, the turbines will directly influence sediment transport patterns and particles suspension. On the other hand, these strong shear stresses will possibly effect habitat and water turbity since many nutrient, contaminants and pollutant are attached to sediments.

7.4 Future Recommendation

This work can be improved in several ways, shown as follows:

- The turbine is set with a constant rotation speed (rpm) that does not change with the variation of flow velocity accordingly, i.e., unsteady state conditions. This is seen when waves are propagating across the channel where the flow velocity varies depending on the wave phase. This will cause over and under-predictions of the wake characteristics and their influence on the upper surface and bed boundary layers. A rotation speed correction code should be inserted in the VBM method to account for these changes in flow behaviours.

- The topography of the channel beds was flat (uniform) in all models run in this study. In real conditions however, bed surfaces are typically uneven and their impact on the flow behaviour in general are pronounced. It would be good practice to account for various bed arrangements such as wavy or sloping beds, since extra turbulence is induced from boundaries.

  In addition, different bed textures could be assessed by having different bed roughness's. Mignot et al. (2009) investigated characterises of near bed turbulences in a rough bed flow, finding that maximum TKE appears very close to the bed when the bed is fairly uniform. When the bed is rough (gravel), maximum TKE occurs at the crest of gravels. Turbulence intensity is maximized when the roughness nature is increased. Secondary flows in an open channel are significant in inducing turbulences. Wang (2008) investigated the characteristics of flow when exposed to six different bed forms, which lead to large longitudinal vortices. The ambient flow demonstrated the presence of pairs of counter-revolving vortices. The disruption caused by the bed added extra turbulences to the flow.

  These studies suggest that there is a possible interacting relationship between bed layers and turbine-affected regions. The authors' predictions were that wake characteristic would slightly change in terms of recovery speed and possibly the shape. Similarly, flow behaviour in the bed boundary layer and the bed shear stresses would be affected.

- Investigating the impact of turbines on sediment transport is an encouraging aspect to focus on. Sediment transport is a naturally occurring behaviour that will be affected by the obstruction to flows of turbines in streams. It was already found in this PhD study that turbines increase shear stresses on the bed when employed. This would directly influence the sediment transport and suspension in the vicinity.
- Increasing the mesh resolution at the bed boundary is essential to be able to simulate the flow at that region properly. The viscous and buffer layers should be counted in order to capture the flow which will influence the sediments. This will also require increasing of the strength of the turbulence model, i.e., LES or DNS.

- In the present work, the RANS turbulence model SST $k-\omega$ model is used based on the balance of computing costs and model accuracy. However, with increased availability of computing facility, it is more desirable to employ high order turbulence closure, and preferably LES and even DNS to resolve all the details of turbulence, without relying on the traditional turbulence model assumption. This is particularly useful when turbine simulation is required.

- The model can be extended to include multiple turbines, since higher power generation is achieved when turbines are placed in an array. Therefore, very often the impacts from such arrays are significant to the local hydrodynamics and environment.

7.5 References

Galloway, P. W., Myers, L. E. and Bahaj, A. S. (2014) Quantifying wave and yaw effects on a scale tidal stream turbine. *Journal of Renewable Energy,* vol. (63), pp.297-307.

Mignot, E., Barthelemy, E. and Hurther, D. (2009) Double-averaging analysis and local flow characterization of near-bed turbulence in gravel-bed channel flows. *Journal of Fluid Mechanics,* vol. (618), pp.279-303.

Wang, Z. (2008) *Turbulence-induced secondary flows in straight open channel with imposed transverse bed non-uniformities.,* Nanyang Technological University.